PHOTOELECTRON IMAGING AND PHOTOFRAGMENTATION OF MOLECULAR AND CLUSTER ANIONS

by

Dmitry Khuseynov

_____

A Dissertation Submitted to the Faculty of the

DEPARTMENT OF CHEMISTRY AND BIOCHEMISTRY

In Partial Fulfillment of the Requirements

For the Degree of

DOCTOR OF PHILOSOPHY

WITH A MAJOR IN CHEMISTRY

In the Graduate College

THE UNIVERSITY OF ARIZONA

2 0 1 4

THE UNIVERSITY OF ARIZONA
GRADUATE COLLEGE

As members of the Dissertation Committee, we certify that we have read the dissertation prepared by Dmitry Khuseynov, entitled Photoelectron Imaging and Photofragmentation of Molecular and Cluster Anions and recommend that it be accepted as fulfilling the dissertation requirement for the Degree of Doctor of Philosophy.

_____ Date: 16 April 2014
Andrei Sanov

_____ Date: 16 April 2014
Oliver Monti

_____ Date: 16 April 2014
Steven Schwartz

_____ Date: 16 April 2014
Dennis Lichtenberger

Final approval and acceptance of this dissertation is contingent upon the candidate's submission of the final copies of the dissertation to the Graduate College.

I hereby certify that I have read this dissertation prepared under my direction and recommend that it be accepted as fulfilling the dissertation requirement.

_____ Date: 16 April 2014
Dissertation Director: Andrei Sanov

STATEMENT BY AUTHOR

This dissertation has been submitted in partial fulfillment of the requirements for an advanced degree at the University of Arizona and is deposited in the University Library to be made available to borrowers under rules of the Library.

Brief quotations from this dissertation are allowable without special permission, provided that an accurate acknowledgement of the source is made. Requests for permission for extended quotation from or reproduction of this manuscript in whole or in part may be granted by the head of the major department or the Dean of the Graduate College when in his or her judgment the proposed use of the material is in the interests of scholarship. In all other instances, however, permission must be obtained from the author.

SIGNED: _____

Dmitry Khuseynov

ACKNOWLEDGEMENTS

I would like to thank Professor Andrei Sanov for being the best research advisor I have ever had the privilege to work for. His enthusiasm and appreciation of science were a constant inspiration for me to be a better scientist in all of the meanings of the word. I am infinitely thankful for his patience and support and for a great sense of humor about all of the pranks we played on him over the years.

I am very grateful to Professor Daniel Goebbert for being a great mentor and a friend during my first couple of years in the group. His endless patience in teaching me lab techniques and the science behind photoelectron imaging has helped to shape me as a researcher and as a teacher.

Thank you to my colleague Dr. Lori Culberson for being an awesome friend throughout the Ph.D. process, for encouraging me, and for all of the discussions we had about science and graduate life.

Thanks to Andrew Dixon for working with me on many experiments over the years, for proofreading a bulk of my dissertation and for our scientific discussions. Thanks to him, Chris Blackstone and Adam Wallace for being such positive new presences in the lab. Thanks to Dr. Kostyantyn Pichugin and Dr. Emily Grumbling for welcoming me in the lab and for their mentorship in the beginning of my graduate career.

Thanks to Matthew Fontana for his valuable help in the tetracyanoethylene experiment and to Daniel Dokuchitz for working with me on the fumaronitrile project. I couldn't have hoped for more responsible and enthusiastic mentees.

I am very appreciative of Mike Read and Kevin Bao of the electronic shop, and Ed Autz and Lee Macomber of the machine shop for their support and expertise. Without their help in fixing the equipment or designing new parts it would be impossible to improve or even maintain a working instrument.

Infinite thanks to graduate program coordinator Lori Boyd for her patience and kindness and for going above and beyond in assisting all of the graduate students in the program.

Thanks to my dissertation committee, Professors Andrei Sanov, Oliver Monti, Steven Schwartz, and Dennis Lichtenberger for their helpful feedback.

I would like to also acknowledge the Science Foundation of Arizona, the Technology and Research Initiative Fund in Imaging, the Galileo Fellowship, the University of Arizona, and the National Science Foundation for supporting and funding various aspects of my graduate education.

Thanks to all of my friends in the Chemistry and Biochemistry department and in the Tucson community.

Thanks to my brother, Artem Khuseynov, for his cooperation (and support). Probasch!

Finally, special thanks to Alex Petlick for her love and encouragement.

DEDICATION

To my family for their support and love, for keeping me grounded and teaching me how to find humor in every situation

Table of Contents

LIST OF FIGURES

LIST OF FIGURES - continued

LIST OF FIGURES - continued

LIST OF FIGURES - continued

LIST OF FIGURES - continued

LIST OF FIGURES - continued

LIST OF FIGURES - continued

using a low-pass Fourier filter, as described in the text. In (b), the 355 nm image and spectrum show two bands corresponding to the $X\,^3\mathrm{A}''$ and $A\,^3\mathrm{A}''$ states of HCCHO. The vertical dashed line indicates the approximate location of the $a^1\mathrm{A}$ state, expected based on the calculations described in the text.

Figure 11.4 (a) Fourier transform $F(q)$ of the experimental 532 nm photoelectron spectrum of $HCCHO^{\bullet-}$ in Figure 11.3(a). The Fourier spectrum is arbitrarily divided into the low-q (true signal) and high-q (noise) parts, shown as solid blue and red dotted lines, respectively. The high-q (noise) part is discarded in calculating the filtered spectrum shown in Figure 11.3(a). (b) The same Fourier spectrum as in (a), but plotted as a function of periodic spectral interval ω, related to signal frequency q by $\hbar\omega = 1/q$. $F(\omega)$ is obtained from $F(q)$ via a Jacobian transformation $F(\omega) = F(q)\,|dq/d\omega|$, with $|dq/d\omega| \propto q^2$. The blue solid and red dotted lines have the same meaning as in (a). Asterisks mark the same dominant vibrational peak at q = 17.7 eV^{-1} in (a), corresponding to ω = 456 cm^{-1} in (b), reflecting the average spacing of the partially resolved vibrational progression seen in the experimental spectrum in Figure 3(a).

Figure 11.5 Photoelectron images and spectra of vinoxide, H2CCHO$^-$, measured at (a) 532 and (b) 355 nm. The 532 nm spectrum shows the ground X $^2\mathrm{A}''$ state and a vibrational progression with the peaks labeled v = 0 – 5. The 355 nm spectrum also show the X $^2\mathrm{A}''$ state and the excited A $^2\mathrm{A}'$ state with a vibrational progression labeled v = 0 – 2.

Figure 11.6 Photoelectron image and spectrum of $CCO^{\bullet-}$ obtained at 355 nm. The $X\,^3\Sigma^-$, $a\,^1\Delta$, and $b\,^3\Sigma^+$ electronic states are observed, with the well-resolved vibrational progressions corresponding to the C=O stretch. Lower intensity peaks are due to the C=C stretch mode.

Figure 11.7 The lowest electronic states of HCCHO, $X\,^3\mathrm{A}''$, $a^1\mathrm{A}'$, and $A\,^3\mathrm{A}''$ in order of increasing energy. The primary resonance structures for each state are labeled to best describe the electron arrangement.

Figure 11.8 Relaxed potential energy surface scan of the HCCH dihedral for $HCCHO^{\bullet-}$ and ^{3}HCCHO calculated at the B3LYP/aug-cc-pVDZ level of theory. The predicted lowest-energy structure for $HCCHO^{\bullet-}$ is the *syn* geometry, while the *anti* structure is about 1 kcal/mol higher in energy. The lowest energy structure of ^{3}HCCHO is the *trans* isomer, with a barrier of about 3.5 kcal/mol separating the *cis* and *trans* isomers.

LIST OF FIGURES - continued

LIST OF FIGURES - continued

LIST OF FIGURES - continued

LIST OF TABLES

LIST OF TABLES - continued

LIST OF TABLES - continued

ABSTRACT

The electronic structure and photofragmentation dynamics of several molecular and cluster anions have been investigated in the gas phase via negative ion velocity-map imaging photoelectron spectrometer combined with tandem time-of-flight (TOF) mass spectrometry.

Photoelectron images and photofragmentation spectra are reported for the $O_{2n}^-(H_2O)_m$ cluster series at 532 nm. The results indicate that both pure oxygen clusters and their hydrated counterparts with $n \geq 2$ form a O_4^- core. The fragment autodetachment patterns observed for some of the clusters are indicative of the high vibrational excitation of the generated O_2^- fragment, which is explained via a proposed charge-hopping electronic excitation mechanism mediated by asymetric solvation of the nascent photofragments.

Photodissociation of nitromethane cluster anions, $(CH_3NO_2)_n^-$, has been explored at 355 nm and results were consistent with the parent clusters containing a monomer-anion core, $CH_3NO_2^-$, solvated by n-1 neutral nitromethane molecules. The $NO_2^-(CH_3NO_2)_k$ and OH^- fragments are described as a core-dssocitaion products, while the $(CH_3NO_2)_k^-$ fragments are attributed to recombination (caging) mechanism.

Negative ions of cyanoacetylene and cyanovinylidene were generated simultaneously via two competing H_2^+ abstraction channels of the O^- reaction with acrylonitrile. Their electronic structure was further characterized via photoelectron imaging spectroscopy. In contrast to unsubstituted acetylene, cyanoacetylene was shown to have a stable, adiabatically weakly bound anionic state and the vertical detachment

energy was measured experimentally. The key to the formation of this elusive species is the bent carbon skeleton of the acrylonitrile.

A photoelectron imaging investigation of the halogen- and cyano- substituted methyl radicals and corresponding carbenes has been performed on several mono- and hetero- substituted species – dicyanomethyl and chlorocyanomethyl radicals, $\cdot CH(CN)_2$ and $\cdot CHClCN$, and corresponding carbenes, NCCCN and CClCN. The results are discussed in comparison with the corresponding dichloro- species, focusing on the divergent effects of the halogen and pseudohalogen (CN) substitutions. A cooperative (captodative) interaction of the π-donor Cl and π-acceptor cyano groups favors the increased stability of the CHClCN radical, but a competition of the two substituents is observed in the singlet − triplet splitting of the carbene. The experimental results are consistent with high level ab-initio calculations using the spin- flip approach in combination with the coupled-cluster theory. The C-H bond dissociation energies were determined for several substituted methanes and discussed.

The mass-resolved anionic products of the reaction of O^- with acetaldehyde, H_3CCHO, are also studied using photoelectron imaging. The primary anionic products are vinoxide, H_2CCHO^-, formylmethylene anion, $HCCHO^-$, and ketenylidene anion, CCO^-. From the photoelectron spectra of $HCCHO^-$, the electron affinity of triplet (ground state) formylmethylene and the vertical detachment energy corresponding to the first excited triplet state are determined, but no unambiguous assignment for singlet HCCHO could be made. The elusive singlet is a key intermediate in the Wolff rearrangement, resulting in formation of ketene. The fast rearrangement associated with a large geometry change upon photodetachment to the singlet surface may be responsible

for the low intensity of the singlet compared to the triplet bands in the photoelectron spectrum. Several new thermochemical properties are determined, including C-H bond dissociation energies and heats of formation of several organic molecules and/or their anions.

Anions of two cyanosubstituted ehtylenes, TCNE, $(NC)_2C=C(CN)_2$, and fumaronitrile, NCHC=CHCN, have been produced in the gas phase and studied using photoelectron imaging and photofragmentation. Their electron affinities have been measured spectroscopically for the first time and photodissociation pathways have been reported for the bare species and their clusters. The fumaronitrile dimer anion has also been observed and studied. The results provide evidence of covalent bonding between two fumaronitrile moieties in the dimer $(C_4H_2N_2)_2^-$ anion.

Finally, a practical model is presented for describing the energy dependence of laboratory-frame photoelectron angular distributions in direct photodetachment from (in principle) any molecular orbital using linearly polarized light. A transparent mathematical approach is used to generalize the Cooper-Zare central-potential model to initial states of any mixed character. In the limits of atomic photodetachment or photoionization, the model reproduces the Cooper-Zare formula. In the case of electron emission from an orbital described as a superposition of *s*- and *p*-type functions, the model yields the previously obtained *s*-*p* mixing formula. The formalism is further advanced using the Hanstorp approximation, valid for anion photodetachment only, whereas the relative scaling of the partial wave cross-sections is assumed to follow the Wigner threshold law. The resulting model can be used to describe the energy dependence of photoelectron anisotropy for any atomic, molecular, or cluster anions. As

a benchmark case, we compare the predictions of the *p-d* variant of the model to the experimental results for NO^- photodetachment and show that the observed anisotropy trend is described well using physically meaningful values of the model parameters.

CHAPTER 1

GENERAL INTRODUCTION

Negative ions are involved in many natural, technological, and chemical processes and therefore are of great importance in a diverse range of disciplines, from chemistry and physics to biology and medicine.[11-13] Fundamental physical and chemical properties of isolated anions are strongly connected with their chemical reactivity and thus of vital importance for understanding of chemical bonding and simple chemical reactions. The reactivity of anions is also greatly influenced by the interactions with the chemical environment. In this regard, cluster anions present a perfect system for studying the effects solvent has on electronic properties and stability of the anion.[13,14] An understanding of these interactions can shed light on fundamental principles of microscopic solvation and chemical processes in condensed environments.

One of the most powerful spectroscopic techniques for studying the electronic structure of isolated molecular and cluster anions in the gas phase is photoelectron imaging spectroscopy.[15] It provides both the energetics of the photoelectrons and the information about the symmetries of the molecular orbital from which electrons originate. This chapter presents a general introduction to the field of negative ion photoelectron spectroscopy and in particular photoelectron imaging, followed by a brief overview of this dissertation.

Studying negatively charged anions is a challenging task both experimentally and theoretically. From the theoretical perspective, the calculation of negatively charged ions

is complicated by the highly diffused nature of the highest occupied orbital that contains an extra electron. This requires the inclusion of large basis sets with diffuse functions and the rigorous treatment of the electronic correlation which in turn demands higher computational power especially for larger anions. Experimental challenges are mostly concerned with the production of ions in sufficient quantities for the particular experiment, as well as with the anion lifetimes.

On the other hand, there are many experimental advantages in studying anions, as opposed to their neutral counterparts. First of all, anions are charged particles and therefore may be easily separated by mass-to-charge ratio using electric fields. This allows for the selective probing of the ion of interest. Additionally, the excess electron of an anion is much more weakly bound to the remaining neutral core compared to the neutrals or cations. Thus an electron photodetachment from the anions can be performed by a photon of much lower energies (visible or UV range), which simplifies the experiment (via use of commercially available light sources) and its interpretation.

Most importantly, anion photoelectron spectra contain information about the electronic states of the corresponding neutral, including the “dark” states which are typically forbidden in optical absorption spectroscopy on the neutral itself. The energy spectra allow for the accurate determination of many important chemical properties of the anion and the neutral, including electron affinities, vertical detachment energies, state ordering, and even vibrational frequencies for the observed electronic states of the neutral molecule. These experimentally determined properties can be further used in various thermochemical cycles to determine bond dissociation energies and reaction enthalpies.

Weakly-bound electrons in anions are also very sensitive to the chemical environment, thus probing the electronic structure of cluster anions provides the opportunity to study intermolecular interactions. In general, solvated anions, X^-Y_n consist of the core anion (X^-) surrounded by a solvent shell of neutral molecules (Y). As a result of the attractive charge-dipole or charge-quadrupole interactions between the ion and neutral species, solvated anions are more stable with respect to electron detachment. This leads to an increase in vertical detachment energies with the increasing size of the cluster, which allows for the simple calculation of the step-by-step solvation energy based on the shift in the corresponding band in photoelectron spectrum. Probing the electronic structure of the cluster anions as a function of size provides a systematic picture of the role of solvation on chemical structure and reactivity and effectively bridges the gap between gas- and condensed-phase chemistry.[16-23]

Historically, the imaging technique was originally introduced by Chandler and Houston[24,25] in 1987 for studying ionic photofragments. It was later improved and applied to photoelectrons by Eppink and Parker[26,27] with the introduction of a velocity mapping approach which allowed for reduced spatial blurring of photoelectron images by mapping the resulting electrons on the imaging detector based only on their velocity, regardless of their initial position within the laser-ion interaction volume. This instrumental approach revolutionized the photoelectron imaging turning it into a widely utilized technique with a variety of applications.[15]

The main advantage of photoelectron imaging over traditional photoelectron spectroscopy techniques is the ability to simultaneously measure both the photoelectron energy spectrum and photoelectron angular distributions (PADs), combining the power of

two well established techniques.[28] The PADs reflect the symmetry of the parent anion orbital,[29-32] and detachment from different orbitals is generally expected to yield different PADs.[15,33] In many cases, this allows for assignment of the multiplicity and the energy ordering of the electronic states based on the simple examination of PADs.

Additionally, the photoelectron angular distributions resulting from one-photon detachment are closely related to the differential photodetachment cross-sections.[34] Thus the PAD dependence on the electron kinetic energy, especially in the low-eKE regime, is of great importance. The relative simplicity with which PADs are obtained using photoelectron imaging spectroscopy allows for a fast experimental probe of this dependence, provided an access to a variety of laser sources. On the other hand, in order for proper interpretation of the photoelectron angular distribution, a thorough yet simple model based on the physics of the detachment process is required. This coupling of the experimental technique with the transparent and practical modeling of the angular distribution is one of the main goals of this dissertation.

We employ the power of photoelectron imaging to elucidate the electronic structure and electrostatic intermolecular interactions in a variety of molecular and cluster anion systems, and develop a new rigorous mathematical approach that allows for more transparent description of the photoelectron angular distributions for the detachment from any molecular orbital, thus providing better fundamental understanding of the electron detachment process and photon-anion interaction in general.

The rest of this dissertation is divided into fourteen chapters, with each chapter describing a gas-phase photoelectron imaging or photofragmentation study of the specific anionic system or a series of systems. Some of these studies have been published in peer-

reviewed journals while others are ongoing projects with interesting potential that have been pursued to some extent either experimentally or computationally.

Chapter 2 describes the experimental apparatus designed to perform the combined photoelectron imaging/photofragmentation experiments. A newly redesigned sample heater allowing for a wider range of possible study systems and in general increased ion production is described in great detail. Laser sources, along with data acquisition and analysis are also discussed.

The study on electronic structure and photochemistry of $[O_{2n}(H_2O)_m]^-$, n = 1 – 6, m = 0 – 1 cluster series is presented in Chapter 3. This is an extension of our previous study[19], investigating the nonadiabatic transitions in solvent environments and the overall effect of solvation on the photochemistry of these clusters. Experimental observations are explained via a proposed charge-hopping mechanism for electronic-to-vibrational energy transfer, mediated by asymmetric solvation of the nascent photofragments of the core O_4^- anion.

In Chapter 4 we report a photofragmentation study on nitromethane cluster anions $(NM)_n^-$, n = 1 – 6, conducted at 355 nm. Several photodissociation processes are observed resulting in the $NO_2^-(NM)_k$, OH^-, and $(NM)_k^-$, k < n, anionic fragments. The results are discussed based on the electronic structure of core monomer anion NM^- and the $NM^-(NM)_{n-1}$ structure of its clusters.

The results of a negative-ion photoelectron imaging experiment on cyano-substituted vinylidene and acetylene, :C=CHCN and HC=CCN respectively, are presented in Chapter 5. Both isomeric forms of the corresponding negative ions are

simultaneously produced in the gas phase via two competing H_2^+ abstraction reactions of $O^{\bullet -}$ with acrylonitrile. The stable anionic state of cyanoacetylene is observed experimentally for the first time and its adiabatic detachment energy is determined and discussed.

Chapters 6 through 8 deal with cyano- and halogen- substituted radicals and carbenes. In Chapter 6, the gas-phase bond dissociation energy of malononitrile, $CH_2(CN)_2$, is determined from the electron affinity of the corresponding dicyanomethyl radical, $\bullet CH(CN)_2$. In Chapter 8, bond dissociation energy of heterogeneously substituted methane, CH_2ClCN, is also determined using measured electron affinity of the corresponding methyl radical, $\bullet CHClCN$. The results are discussed in comparison with the properties of other substituted methanes and the effects halogen- and cyano-substituents have on radical stability. Chapters 7 and 8 present photoelectron imaging spectroscopy results on dicyanocarbene, $NCCCN^-$, and chlorocyanocarbene, $ClCCN^-$. The effects the substituents have on their ground state multiplicity as well as the magnitude of the singlet-triplet splitting are discussed.

In Chapters 9 and 10 we explore the photochemistry of cyanosubstituted ethylene radical anions, tetracyanoethylene ($(CN)_2C=C(CN)_2^-$) and fumaronitrile ($CNHC=CHCN^-$), in the gas phase via photoelectron imaging and photofragmentation mass-spectrometry. The solvation effects of water and argon on anion stability are also examined and reported along with the covalent bonding character of fumaronitrile dimer anion.

In Chapter 11 we employ the high reactivity of $O^{\bullet-}$ with acetaldehyde, H_3CCHO, to produce and characterize three reactive intermediates via photoelectron imaging: $HCCHO^{\bullet-}$, H_2CCHO^-, and $CCO^{\bullet-}$. Several new thermochemical properties are also determined. Among other things, new method of data analysis, based on a low-pass Fourier analysis filter is developed and discussed in detail. It allows for more accurate determination of electron affinity and vibrational spacing and is particularly useful for very noisy photoelectron spectra.

Low-lying excited states of cyclopentadienone are explored in Chapter 12. The corresponding anion of this highly unstable compound was observed in the gas phase for the first time and studied via photoelectron imaging.

In Chapter 13 we report a study on cyanobenzene anion, C_6H_5CN, and its clusters. The large dipole moment of the cyanobenzene molecule is sufficient for formation of the dipole bound anion. We observe this anion in the gas phase and, using photoelectron imaging spectroscopy, access and assign ground and several low-lying excited states of neutral cyanobenzene. We also report the effect of water solvation on anion stability and the formation of the cyanobenzene dimer anion.

Chapter 14 describes a new model for explaining the energy dependence of photoelectron angular distributions in one-electron, one-photon detachment from any molecular orbital. A general, yet transparent and practical mathematical approach is used to expand the Cooper-Zare central-potential model to molecular states of any mixed character. The model was further simplified for use on molecular anions using Hanstorp's approximation. Its predictions for the p-d mixing case were compared to experimental

results for the NO($X\,^2\Pi$, v′ = 2) ← NO^-($X\,^3\Sigma^-$, v″ = 0) photodetachment band and shown to reproduce the observed anisotropy trend with physically meaningful parameter values.

Finally, this dissertation concludes with description of several ongoing projects and ideas for future studies

.

CHAPTER 2

EXPERIMENTAL METHODS

2.1. Overview

All of the photoelectron imaging and photofragmentation experiments described in this dissertation were performed on a home-built experimental apparatus described in detail elsewhere[14]. In general, it consists of a pulsed ion source and a linear time-of-flight mass spectrometer (TOF-MS) succeeded by a reflectron time-of-flight mass spectrometer (ReTOF-MS). The schematic diagram of the instrument is illustrated in Figure 2.1. Linearly polarized laser pulse is time-tuned to interact with a mass selected anion of interested at the spatial focus of the linear TOF inducing photodetachment and/or photofragmentation. Resulting photoelectrons are detected with a velocity-map imaging (VMI) assembly[26], mounted perpendicular to the laser and ion beams propagation. Ionic photofragments can be detected at the focal plane of the reflectron.

2.2. Vacuum hardware

The instrument consists of three differentially pumped sections, as illustrated in Figure 2.1: the ion source chamber (Section I), time-of-flight region (Section II) and the detection region (Section III). The custom made source chamber with inner dimensions of 25"×24"×16" is held under vacuum by a Varian VHS-10 diffusion pump (5300 l/s), which is water cooled and backed up by an Edwards E2M40 rotary vane pump (~14 l/s). The TOF region is connected to the source chamber through a 4 mm diameter orifice and

is pumped with two Leybold, Turbovac 361 turbomolecular pumps (~400 l/s) which are also water cooled and backed in a parallel configuration by a single Leybold, Trivac D16B rotary vane pump (~5.3 l/s). The detection region is separated from the TOF by a pneumatic gate valve with a 4" opening and is pumped with a third Leybold, Turbovac 361 turbomolecular pump backed by a Leybold, Trivac D16B rotary vane pump.

The base pressures in each region are ~5×10^{-7} Torr (Section I), ~5×10^{-8} Torr (Section II), and 1–5×10^{-9} Torr (Section III). When experiments are being performed, the pressures raise to 1–5×10^{-5} Torr, 1–4×10^{-7} Torr, and 2–5 $\times10^{-8}$ Torr respectively. When the instrument is not in use, the detection region is sealed with pneumatic gate valve and the diffusion pump is turned off and closed with additional pneumatic gate valve (Vacuum Research Ltd., 10" ASA flanges).

2.3. Ion production

Neutral precursor vapor is seeded in the career gas (Ar, N_2O, O_2, etc.) with various backing pressures (20–40 psi) and supersonically expanded into the source chamber via a pulsed nozzle valve (General Valve, Series 99). The valve is opened by a solenoid-driven poppet (Kel-F or PEEK) and controlled by the IOTA ONE high speed valve driver (Parker Hannifin Corp., General Valve). The valve is pulsed at 20, 50 or 70 Hz, depending on the laser system used, and is opened for 100-300 μs of the total experimental cycle (200 ms).

About 5 mm away from the nozzle orifice, the supersonic gas jet is intersected with a 1 keV electron beam generated by the commercially available electron gun (Southwest Vacuum Devices, Inc., CE 3K/5U) via thermionic emission from a bent

tungsten filament cathode floated at 1 kV using Bertan 205B-03R power supply. Two sets of electrostatic deflector plates (supplied by two Agilent E3612A power supplies) and an Einzel lens (supplied by Bertan 205B-03R power supply) are used to vertically and horizontally steer and focus electron beam in order to maximize the overlap with the gas expansion.

High energy electrons ionize the gas cloud, producing relatively slow (< 1 eV) secondary electrons that can interact with the neutral species and produce metastable anions which in turn can be stabilized by one of the following processes[35]:

$$X + e^- + Y \rightarrow X^{-*} + Y \rightarrow X^- + Y^* \quad \text{(three-body stabilization)} \qquad (2.1)$$

$$(XY) + e^- \rightarrow (XY)^{-*} \rightarrow X + Y^- \quad \text{(dissociative attachment)} \qquad (2.2)$$

$$X_n + e^- \rightarrow [X_n]^{-*} \rightarrow [X_{n-m}]^- + mX \quad \text{(evaporative cooling)} \qquad (2.3)$$

Thus produced ions have a high density of approximately 10^9 cm^{-3} and are able to drift relatively long distances in vacuum without significant ion loss. This allows for reactive formation of other anionic species via low-energy ion-neutral collisions[36].

There is an obvious limitation to the type of neutral precursor that can be used in this experiment, due to low vapor pressure of many solid and liquid samples under standard temperature conditions. In many cases it results in low (sometimes even undetectable) ion production and inability to perform the experiments. In order to address this issue, the heated sample holder has been implemented, employing the well-known dependence of vapor pressure on temperature. The schematic diagram of it is presented in Figure 2.2. The commercially available band heater (MB-1, OMEGA Engineering Inc.,

1" ID, 1.5" width, 120 V, 150 W) is secured around the stainless steel sample holder (Swagelok) and managed by the external controller (Dwyer Instruments, Series 32B). The temperature is monitored via washer thermocouple (K-Type, Omega Engineering Inc.) placed in between the heater and a sample holder. All materials employed in the design have low outgassing rates and can be used under high vacuum conditions. By heating the sample above the room temperature (available temperature range varies with the sample) we effectively raise the vapor pressure resulting in higher ion production. This allows for a much wider variety of samples that can be studied.

2.4. Linear time-of-flight mass spectrometer

The expanding gas jet is directed between two parallel plates: the extraction plate and the ground electrode of the acceleration stack. About 2 ms after the nozzle is fired (~18 cm downstream from the nozzle), the repeller plate is pulsed with a negative voltage (tunable between 0 and –950 V) by a Directed Energy Inc., PVM-4210 pulse generator module with a fast rise/fall time (< 20 ns) and the anions are extracted from plasma into a Wiley-McLaren type TOF-MS described in detail elsewhere[37]. The extracted anions enter an acceleration stack consisting of 10 circular electrodes (1/32" thick, 3.0" OD, 1" ID opening). The plates are connected by 1MΩ high precision resistors, with the first plate grounded and the last plate floated with a ~2.5 kV potential (supplied by Bertan 205A-05R power supply).

Two sets of deflector plates (supplied by two Agilent E3612A power supplies) are used to steer the anion beam. An Einzel lens, consisting of three 1.5" OD, 1.5" long stainless steel cylinders, is used to transversely focus the ion beam. The middle electrode

is set to a decelerating +900–1100 V (supplied by Bertan 205B-03R power supply), while the outer ones are at the float voltage (~2.5 kV). After leaving the Einzel lens the ions are referenced back to the ground potential by means of a fast potential switch (<25 ns rise/fall time) as described previously[38]. It is operated by a high voltage pulse generator (Directed Energy, Inc., model PVX-4140), timed to only be at float voltage for a short duration of time (10-30 μs), defined by the delay generator (Stanford DG535). This allows for ions of certain mass-to-charge ratio range to pass through without changing their kinetic energy.

The ions are detected at the end of time-of-flight tube by a 25 mm diameter chevron-configured dual microchannel plate (MCP) detector with a metal anode (Burle, Inc.). A 70 wires-per-inch mesh (Precision Eforming, LLC, with 90% maximum transmission) connected to a ground potential is placed couple of millimeters in front of the detector in order to shield the MCP field from the rest of the flight tube. The signal output from the detector is further amplified (Phillips Scientific, model 6931, DC-100 MHz) and monitored with a 300 MHz digitizing oscilloscope (Tektronix Inc., model TDS3032). The spectra can be averaged over 512 experimental cycles and transferred to a computer through a GPIB interface (National Instrument, Inc.) and saved using home-made LabView software.

The acquired spectra can be converted from the time-of-flight to the mass-to-charge scale using empirical equation:

$$t = a\left(\frac{m}{z}\right)^{1/2} + t_0, \tag{2.4}$$

where t is the time-of-flight for the ion with the mass m and charge z. By identifying two separate peaks in the mass spectrum, we can use their mass-to-charge ratios, m_1/z and m_2/z and corresponding time-of-flights, t_1 and t_2, as a calibration. System of two equations allows for the determination of a and t_0 parameters:

$$a = \frac{t_1 - t_2}{\sqrt{m_1} - \sqrt{m_2}}, \tag{2.5}$$

$$t_0 = \frac{t_2\sqrt{m_1} - t_2\sqrt{m_2}}{\sqrt{m_1} - \sqrt{m_2}}. \tag{2.6}$$

This conversion is also implemented in the same home-made LabView program, allowing for faster mass spectrum analysis and peak identification.

2.5. Laser systems

The ion of interest is intersected perpendicularly by a linearly polarized laser beam traveling in the same horizontal plane as ion beam. One of the three commercially available laser systems were used in our experiments: Nd:YAG nanosecond laser system (Spectra Physics Inc., model Quanta-Ray Lab 130-50), Ti:Sapphire femtosecond laser system (Spectra Physics, Inc.), and tunable nanosecond dye laser (Continuum).

The Nd:YAG laser system typically yields ~8 ns width pulses at 1064 nm with 50 Hz repetition rate. The fundamental output can be frequency doubled, tripled or quadrupled using necessary crystals for higher harmonic generation. Maximum power available are on the order of 320, 120, 50, and 15 mJ/pulse for the 1064 nm, 532 nm, 355 nm, and 266 nm outputs respectively. However, only a fraction of the maximum output is typically used for the experiments in order to eliminate the possibility of a two photon processes.

The femtosecond system provides ~80 fs width pulses at 780 nm with 1 kHz repetition rate. The beam can be frequency-doubled using a Super Tripler (Optronics) in which the beam is focused, collimated, and directed through a 0.2 mm thick, double-antireflection-coated (400 nm/ 800 nm) type I β-barium borate (BBO) crystal (MiniOptic Technology, Inc.). Maximum laser powers available are approximately 1000 and 300 μJ/pulse for the fundamental and frequency-doubled (390 nm) outputs respectively.

The final laser system consists of a dye oscillator and two dye amplifier cells (ND6000, Continuum), externally pumped by an Nd:YAG laser system (Surelite II-20, Continuum). The system generates ~5 ns width pulses with a 20 Hz repetition rate. Maximum laser powers available for the pump laser are 250 and 120 mJ/pulse for the second (532 nm) and third (355 nm) harmonics respectively. The power output from the dye laser is highly dependent on the conversion efficiency of the dye used. In the work presented in this dissertation we used Rhodamine 640 (612 nm, 40 mJ/pulse), LDS 821 (812 nm, 40 mJ/pulse), which were also frequency doubled using appropriate crystals to produce 306 nm (6 mJ/pulse) and 406 (2 mJ/pulse) respectively.

The timing of the laser is controlled by the Stanford delay generator. The delay between the laser flash lamps trigger and firing (Q-Switch) is tuned to achieve required power output. The timing of the Q-Switch opening is scanned to overlap in time only with the selected ion of interest. A good overlap is achieved by maximizing the neutral signal at the in-line MCP, which are observed by applying high enough voltage to the reflectron deflecting all charged species. If no neutrals are observed for a particular wavelength or ion, the overlap is optimized by monitoring and maximizing the photoelectron signal in real time.

2.6. Reflectron time-of-flight mass spectrometer

The photofragment-ion mass-spectra are recorded using a single-stage linear-field reflectron mass spectrometer, described in detail previously[37]. The reflectron assembly consists of a ground stainless steel electrode (4.173" OD, 1/32" thick) with a 0.315" diameter aperture, followed by 26 stainless steel circular electrodes (3.15" OD, 1/32" thick) with a 2.025" diameter opening. All plates are connected by 1.0 MΩ high precision resistors with rear plate connected to a high-voltage power supply (Bertan, 205A-05R), defining the reflectron voltage (V_f).

After ions are reflected they are detected by an off-axis chevron-type dual MCP detector (Burle, Inc.). The detector is placed in a thin stainless steel box in order to shield the primary ion beam from the detector voltages. A grid (5 wpi, InterNet, Inc.) is placed at the opening of the detector with a +20 Volts bias applied to it to discriminate against low energy electrons. The signal output from the detector is amplified (Phillips Scientific, model 6931, DC-100 MHz), monitored and averaged over 512 experimental cycles with oscilloscope (Tektronix Inc., model TDS3032) and transferred to a computer for data analysis. The signal is recorded with laser off as well and subtracted from the original spectrum to ensure that the detected fragment is real and only originates from ion-laser interaction.

Typically, parent ions (with mass m_p) are initially refocused by the reflectron onto an off-axis MCP detector by optimizing the reflectron voltage V_p. Fragment ions (with mass m_f) are then focused on the same off-axis detector, with the same arrival time as the parent ions before, by setting the reflectron retarding potential to

$$V_f = V_p \left(\frac{m_f}{m_p}\right) \quad (2.7)$$

The entire photofragment ion mass spectrum is recorded by scanning the reflectron potential.

2.7. Photoelectron imaging

Photoelectron images are recorded using the velocity-map[26] imaging[24] assembly, that consists of four oxygen-free high conductivity copper plates, 1/32" thick, with a 1" diameter opening. The top three electrodes have a 1" spacing between them and are modeled after the similar setup described in detail previously[39]. There is an additional electrode at the bottom (1.6" apart) which is added for photofragment imaging capability. In this prospective experiment, first laser pulse initiates the photochemistry, launching the anion onto dissociative potential. The resulting anionic fragments are reflected and mass-selected via reflectron mass spectrometer and second laser pulse is used to photodetach electrons from photofragments[14].

In a typical imaging experiment for photoelectrons originating from parent anions, second to bottom electrode is at the 100–400 V negative potential (provided by the Hewlett-Packard, 6516A power supply), the middle plate is grounded, and the top electrode is in contact with the floated electron flight tube at a positive potential of 200–800 V. The bottom plate is not used and kept at ground potential. The ratio of the positive to negative voltages is optimized for best focusing conditions and kept constant with typical values of 1.99–2.02. The magnitude of the voltages affects the speed of the electrons and therefore the size of the image, with larger voltages resulting in smaller

image size. A μ-metal shield surrounds the entire imaging assembly in order to contain the electric fields that can otherwise alter the electron trajectories.

The electrons are detected by a 40 mm position sensitive dual-chevron MCP detector coupled with a P43 phosphor screen (Burle, Inc.). To discriminate against the noise, two MCP surfaces are kept at a low gain mode with only a 1 kV difference (+2 kV for the first surface and +3 kV for the second), with an additional 1kV pulse (Directed Energy Inc., PVM-4150) provided only for a 100-200 ns time window after laser firing. The phosphor screen is kept at +6.5 kV (provided by Burle PF 1054 power supply). A fine electroformed nickel mesh (333 wpi, Precision Eforming, LLC., 70% maximum transmission) is placed ~0.65" prior to the first MCP of the detector in order to screen the photoelectrons from the detector voltages.

The photoelectron images are recorded by a charge-coupled device (CCD) camera and accumulated for ~10^5–10^6 experimental cycles. Two different cameras were used in this dissertation, Dalsa Inc. DS-1A-01M30 CamLink with 1 Megapixel (1024×1024) resolution and thermoelectrically cooled Photometrics CoolSnap MYO with 2.8 Megapixels (1940×1460) resolution. A modified version of the DAQ46 acquisition program developed by Neumark group[14] was used with the Dalsa camera, while Cool Image software[11] was used with Photometrics camera.

A three dimensional reconstruction of the two dimensional images is performed using an inverse Abel transform as implemented in BAsis Set EXpansion (BASEX) program[40]. The well-characterized[41,42] photodetachment transition of O^- atomic anion (unresolved O^- ($^2P_{3/2,1/2}$) → O ($^3P_{2,1,0}$) + e^-) is used as a calibration of the resulting

spectra, which allows for the following simple equation for conversion between the velocity and energy domains:

$$\left(\frac{eKE_{O^-}}{v^2_{O^-}(pixels)}\right) = \left(\frac{eKE_i}{v^2_i(pixels)}\right), \tag{2.8}$$

where eKE_i is the electron kinetic energy of the *i*-th electron.

The angular distributions (PADs) are obtained by integrating over a specific radius range for a particular angle, using the Betacalc program[11]. The experimental anisotropy parameter β is obtained by a least-squares fit to the Cooper-Zare model[29,30] in the form

$$I(\theta) = a[1 + \beta P_2(\cos\theta)] \tag{2.9}$$

where $I(\theta)$ is the probability of an electron emission at an angle θ, $P_2(cos\theta)$ is the second-order Legendre polynomial, β is the anisotropy parameter, and a is a proportionality constant.

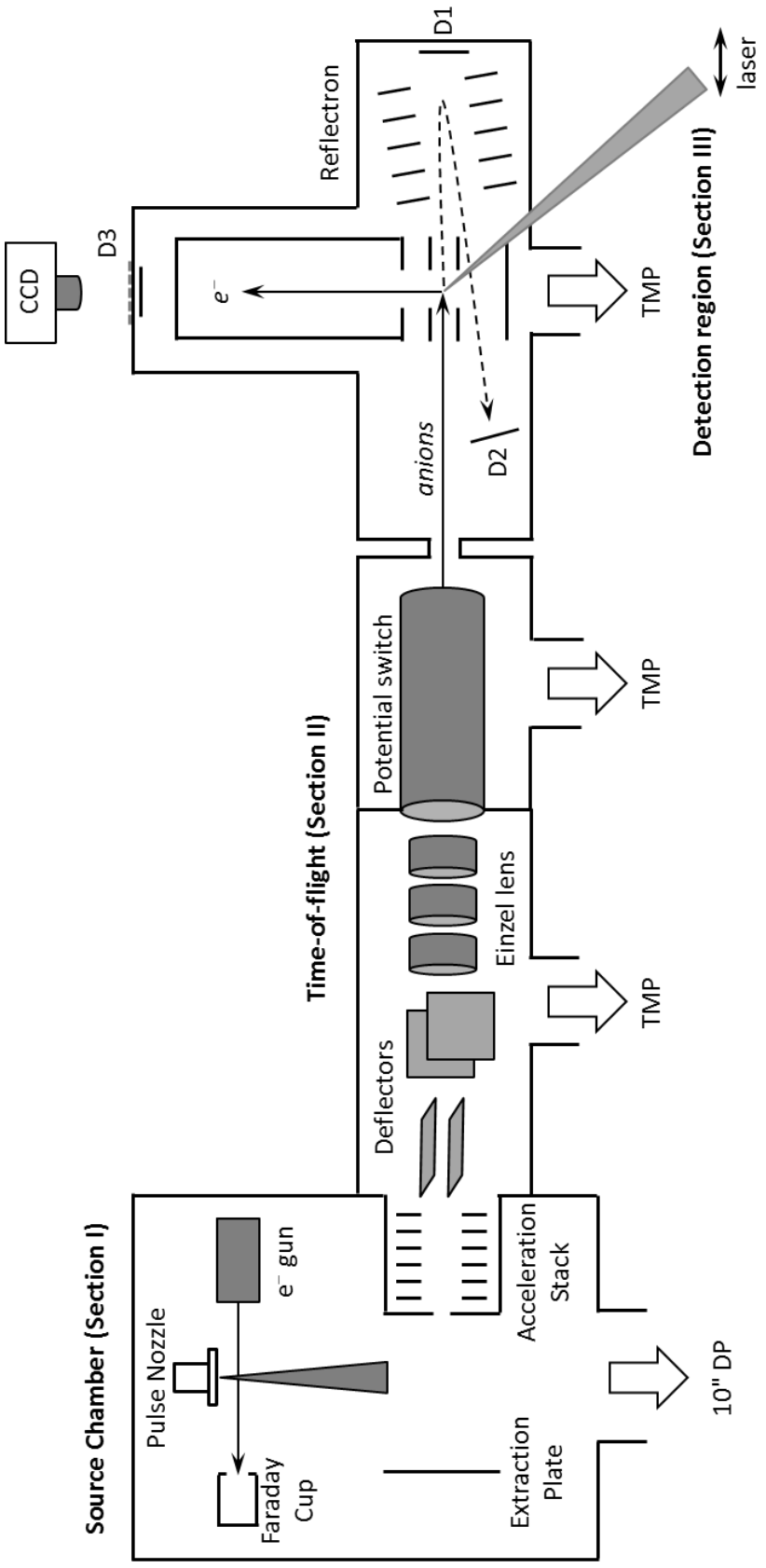

Figure 2.1 Schematic diagram of the experimental apparatus. All major parts are labeled, see text for further details. DP: diffusion pump, TMP: turbo-molecular pump, D1: in-line ion/neutral detector, D2: off-axis ion detector, D3: photoelectron imaging detector.

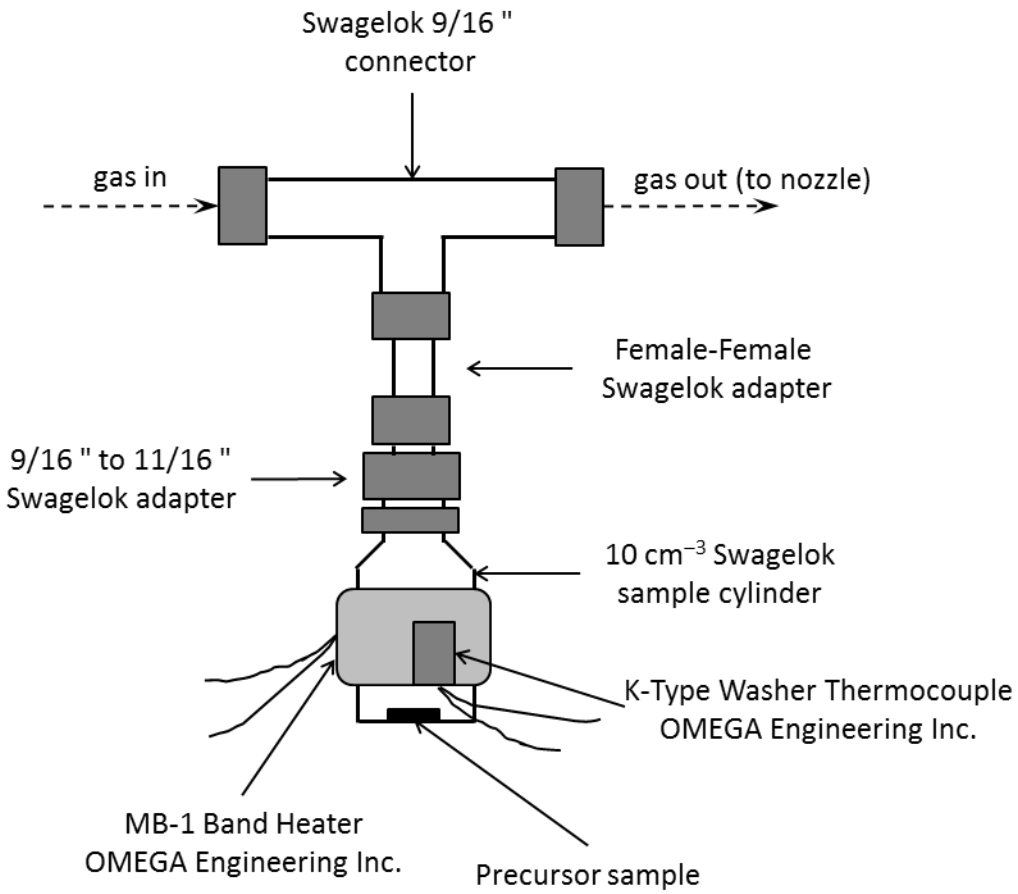

Figure 2.2 Schematic diagram of the sample heater design. See text for the details.

CHAPTER 3

OXYGEN CLUSTER ANIONS REVISITED: SOLVENT-MEDIATED DISSOCIATION OF THE CORE O_4^- ANION WITHIN $O_{2n}^-(H_2O)_m$ CLUSTERS

3.1. Introduction

Experiments on cluster anions examine molecular-level interactions implicated in the chemistry of condensed environments.[13,43,44] Interactions of ions with solvent molecules perturb the electronic structure and may facilitate a variety of pathways and mechanisms for chemical reactions. This aspect of solvation plays a particularly important role for the reactions involving nonadiabatic transitions between electronic states.

Superoxide O_2^- and its clusters, particularly O_{2n}^-, have complicated photochemistry due to the existence of numerous low-lying electronic states. These clusters have long been considered perfect subjects for reaction dynamics studies, with several accounts of such studies available in the literature,[38,45-49] including particularly exhaustive investigations by Continetti and coworkers.[50,51] The experiments on both pure oxygen clusters, O_{2n}^-, and their hydrated counterparts, $O_{2n}^-(H_2O)_m$,[19,50,52] supported by theoretical studies,[4,53] showed that all species with $n \geq 2$ form an O_4^- core anion. The relatively high binding energy of O_2 to O_2^- (0.455 ± 0.22 eV)[54] indicates partial covalent character in O_4^-.[4,45,50] As one specific example, the recent infrared spectra from the Johnson group[55] suggest the existence of two isomeric O_6^- structures, both corresponding to a mostly neutral O_2 solvent molecule bound to the O_4^- core. The O_4^- anion itself is

described as two $O_2^{-1/2}$ moieties with weak covalent bonding between them.[4,50]

In our previous work,[19] we examined the effect of hydration on the oxygen cluster anions using photoelectron imaging and photofragment mass-spectroscopy of $[O_{2n}(H_2O)_m]^-$, n = 1–4, m = 0–3 at 355 nm. We confirmed that the identity of the O_4^- core anion is preserved for both the pure-oxygen and heterogeneously hydrated clusters with $n \geq 2$. Fragmentation of these clusters yielded predominantly the O_2^- and $O_2^-(H_2O)_n$, $n < m$, anionic products, while the presence of low-electron kinetic energy autodetachment features in the photoelectron images indicated that the fragments were vibrationally excited.

In the present work, we extend our previous study[19] and report photoelectron spectra and anionic photofragmentation pathways of $[O_{2n}(H_2O)_m]^-$, n = 1–6, m = 0–1 at 532 nm. This wavelength is particularly important in understanding the photodynamics, because the only dissociation channel in the core O_4^- accessible in this regime yields vibrationally cold $O_2^-(X\,^2\Pi_g)$ and electronically excited $O_2(a\,^1\Delta_g)$.[48,49] In a cluster environment, these nascent products may undergo nonadiabatic transitions leading to the opening of the electronically relaxed reaction channel. These transitions and the overall effect of solvation on the photochemistry of these clusters are the primary focus of this work. As in the previous work,[19,50] we observe intense autodetachment bands for O_6^- and larger O_{2n}^- parent anions, as well as some of their hydrated counterparts. Autodetachment is attributed to vibrationally excited ($v \geq 4$) O_2^- fragments formed along the electronically relaxed core dissociation asymptote. In order to explain the experimental observations, we propose a charge-hopping mechanism for electronic-to-vibrational energy transfer, mediated by asymmetric solvation of the nascent $O_2^-(X\,^2\Pi_g) + O_2(a\,^1\Delta_g)$

photofragments of the core O_4^- anion.

3.2. Experimental section

The experiments were performed using a pulsed reflectron time-of-flight mass-spectrometer equipped with a photoelectron velocity-map[26] imaging[24,25] detector that has been described in detail elsewhere.[37]

Neat O_2 gas with 20 psi backing pressure was expanded into a high-vacuum chamber through a pulsed supersonic nozzle (General Valve Series 9), operated at a 50 Hz repetition rate. Cluster ions were synthesized by secondary electron attachment upon interaction of the gas jet with a 1 keV electron beam. The anions were accelerated to a kinetic energy of about 3 keV and focused in a laser interaction region, where the ion beam was crossed with a linearly polarized pulsed laser beam. The second harmonic of the Nd:YAG (yttrium aluminum garnet) laser was used to produce 532 nm radiation with an 8 ns pulse width and a 20–30 mJ/pulse power. Parent ions were detected using a microchannel plate (MCP) detector (Burle, Inc.) mounted at the end of flight tube. Two types of experiments were performed in the laser interaction region: photoelectron imaging and photofragmentation.

In the imaging measurements, electrons were projected onto a 40 mm diameter MCP detector coupled with a phosphor screen (Burle, Inc.) using static electric fields within the velocity-map imaging assembly. Images were recorded with 1 megapixel charge-coupled device camera and were typically accumulated for ~10^4 – 10^5 experimental cycles. Kinetic energy and angular distributions of the photodetached electrons were obtained via inverse Abel transform[25,56] as implemented in the BASEX program.[40] The kinetic energy scale was calibrated using the well-known

photodetachment transition of O^-.[41,42]

Photofragment ions were detected by using a single-stage linear-field reflectron. Parent ions with mass m_p were initially refocused to the off-axis MCP detector and the signal was optimized by varying the reflectron potential V_p. Fragment ions with mass m_f can be than focused on the same off-axis detector, with the same arrival time as the parent ions, by reducing the reflectron voltage to $V_f = V_p(m_f/m_p)$. Photofragment mass-spectra were recorded by scanning reflectron potential.

3.3. Results

In this section we present the photoelectron imaging data and photofragmentation spectra for oxygen-water anion clusters, $[O_{2n}(H_2O)_m]^-$, $n = 1 – 6$, $m = 0 – 1$, recorded at 532 nm laser wavelength. The images are obtained using the same experimental conditions and shown on the same velocity-mapping voltages scale. However, the image intensity scales are tuned arbitrary for the best perception of each individual image features and thus do not represent the absolute photodetachment cross-section. Photofragmentation spectra were recorded at the same detector voltages and are presented on consistent intensity scales.

3.3.1. Photoelectron imaging spectroscopy

Photoelectron images of the $[O_{2n}(H_2O)_m]^-$, $n = 1 – 6$, $m = 0 – 1$ cluster anions were recorded using linearly polarized 532 nm radiation. Figure 3.1 shows several representative images, corresponding to the pure and monohydrated O_2^-, O_4^-, O_6^- and O_{10}^- ions. The photoelectron spectra obtained from all images recorded in this study, including those shown in Figure 3.1, are presented in Figure 3.2. The spectra are plotted

versus electron binding energy (eBE), calculated from electron kinetic energy (eKE) as eBE = $h\nu$ – eKE.

The two well-resolved progressions A and B in the photoelectron spectrum of O_2^- are attributed to vibrations in the ground and first excited electronic states of neutral O_2, the $X\,^3\Sigma_g^-$ and $a\,^1\Delta_g$ states, respectively.[3] The vibrational structure of both electronic bands is also apparent in the raw photoelectron image of O_2^- shown in Figure 3.1. As both bands have been the subjects of several previous investigations,[3,19,47,48,57-59] they will not be discussed here. The broad bands in the photoelectron spectra of O_4^-, O_6^-, and O_8^- (Figure 3.2) are attributed to direct dissociative photodetachment of the O_4^- core of these clusters via the overall $O_4^- \rightarrow 2O_2(X\,^3\Sigma_g^-) + e^-$ pathway.[19,48,50,60] Similar to the first band in the O_2^- spectrum, these bands are labeled A, because they too correspond to the formation of O_2 molecules in the ground electronic state. The higher-energy dissociative photodetachment channel, $O_4^- \rightarrow O_2(X\,^3\Sigma_g^-) + O_2(a\,^1\Delta_g) + e^-$, is not observed at 532 nm (Figure 3.2), as it was in the 355 nm spectrum.[19,48]

The maximum of band A in the O_4^- spectrum is shifted to higher binding energy, relative to the most intense O_2^- peak, by approximately 0.6 eV, as indicated by the green horizontal arrow in Figure 3.2. The shift reflects the approximate $O_4^- \rightarrow O_2(X\,^3\Sigma_g^-) + O_2^-(X\,^2\Pi_g)$ dissociation energy and its magnitude is indicative of the weakly covalent bonding character between two diatomic moieties in O_4^-.[4,19,53,61] The much smaller shift of band A in the O_6^- spectrum, compared to O_4^-, is attributed to electrostatic solvation interactions in the $O_4^-(O_2)_{n-2}$, $n > 2$ structures.

In the spectra of O_6^- and larger O_{2n}^- clusters (Figure 3.2), we observe series of

sharp low-eKE peaks labeled with lower-case letters (a, b, …). These peaks correspond to the well-defined isotropic rings near the respective image centers (see, for example, the O_6^- and O_{10}^- images in Figure 3.1). These features are assigned to autodetachment of vibrationally excited O_2^- photofragments.[19,50]

The effect of a single water molecule on electron photoemission can be seen in the right columns of Figures 3.1 and 3.2, where the results for the $O_{2n}^-\cdot H_2O$ clusters are presented. Two intriguing aspects of these results are immediately apparent. First, the autodetachment features a – c are markedly weaker or altogether absent for the monohydrated clusters. Second, the photoelectron intensity for the larger species, for example, $O_6^-\cdot H_2O$ and $O_{10}^-\cdot H_2O$, is spread over greater effective images areas, compared to the smaller clusters, such as $O_2^-\cdot H_2O$. (All photoelectron images in Figure 3.1 are shown on the same velocity scale.) This visually striking observation is counterintuitive, as under otherwise unchanged conditions one expects the average eKE and hence the effective areas of photoelectron images to decrease with increasing cluster size, due to solvation-induced stabilization of the cluster anions.[13,44] The larger effective image areas reflect the presence of higher-eKE spectral bands, which upon close examination can be seen in the images of all larger clusters studied in this work: O_{2n}^-, $n \geq 4$, and $O_{2n}^-\cdot H_2O$, $n \geq 3$.

These bands are particularly prominent in the hydrated cluster-anion images and spectra, $O_{2n}^-\cdot H_2O$, $n \geq 3$. For these species, the bands in question are vibrationally resolved (Figure 3.2) and exhibit predominantly perpendicular photoelectron angular distributions (Figure 3.1). The observed vibrational pattern and the characteristic angular distributions are fingerprints of O_2^- photodetachment. To stress this conclusion, the

photoelectron spectrum of $O_{10}^-\cdot H_2O$, shown in the corresponding panel of Figure 3.2 in blue, is superimposed with the spectrum of O_2^- (red), reproduced from the top-left panel of the figure. The agreement between the larger-eKE $O_{10}^-\cdot H_2O$ band and the O_2^- spectrum is unmistakable. Therefore, the high-eKE/low-eBE bands in the photoelectron spectra of O_{2n}^-, $n \geq 4$, and $O_{2n}^-\cdot H_2O$, $n \geq 3$, are attributed to the photodetachment of O_2^- formed in the photofragmentation of the respective parent clusters, a net two-photon process. This conclusion was further supported by photoelectron imaging results for the same ion obtained using two different laser fluences, 0.8×10^{-4} and 1.2×10^{-4} W/cm^2 (data not shown here). The image taken with higher laser power shows significant increase in the relative O_2^- photodetachment bands intensity, consistent with a two-photon process.

3.3.2. Photofragment mass-spectrometry

The same series of mass-selected anions, $[O_{2n}(H_2O)_m]^-$, $n = 2 – 6$, $m = 0$ and 1, was studied using photofragment mass-spectroscopy. The 532 nm spectra are presented in Figure 3.3. For the unhydrated ($m = 0$) O_{2n}^-, $n = 2–5$, species, O_2^- is the only anionic photofragment observed, with O_4^- appearing for $n = 6$. The monohydrated ($m = 1$) clusters studied yield both O_2^- and $O_2^-\cdot H_2O$. The branching ratio of these fragments varies from cluster to cluster, as evident in Figure 3.3, albeit not dramatically. In addition, the $O_{2n}^-\cdot H_2O$ clusters with $n \geq 4$ yield small but detectable quantities of O_4^- photofragments.

3.4. Discussion

In addition to direct dissociative photodetachment (band A), the photoelectron

spectra of pure-oxygen clusters O_{2n}^-, $n \geq 3$, as well as some of their monohydrated counterparts, $O_{2n}^- \cdot H_2O$, display low-eKE features (peaks a – c in Figure 3.2). These peaks correspond to isotropic rings close to the centers of the photoelectron images (Figure 3.1). Their spectral positions do not shift as a result of solvation by O_2 or hydration. These properties are signs of an indirect detachment process and we assign features a – c to autodetachment from O_2^- photofragments. Similar features have been observed by Continetti and coworkers at 355 and 532 nm,[50] as well as in our previous work at 355 nm.[19]

The assignment of the autodetachment features to O_2^- fragments is further (indirectly) supported by the photofragmentation data presented in Figure 3.3. For the O_{2n}^-, $n \geq 3$ series, O_2^- is the only anionic fragment observed at 532 nm. At the same time, progressions of O_2^- autodetachment features a – c are prominent in the corresponding photoelectron spectra (Figure 3.2). For the hydrated series, $O_{2n}^- \cdot H_2O$, $n \geq 3$, the O_2^- fragment branching ratio decreases with increasing n, which parallels the disappearance of the autodetachment features in the $O_{10}^-(H_2O)$ and $O_{12}^-(H_2O)$ photoelectron spectra.

We will focus on one key result of this work, expanding on the previous observations by Continetti and coworkers,[50,51] namely, the intense autodetachment of O_2^- fragments observed for O_6^- and larger O_{2n}^- species at 532 nm, contrasting its marked absence for O_4^-. This result is seemingly at odds with another experimental fact, that O_2^- photofragments are produced for all of these parent ions (Figure 3.3). Similar experiments at 355 nm do show significant fragment autodetachment signal for O_4^-, but the autodetachment yield is surprisingly enhanced for O_6^-.[19,50]

Autodetachment is expected for vibrationally excited O_2^- fragments, since the

vibrational levels with $v \geq 4$ lie higher in energy than the ground electronic and vibrational state of neutral O_2.[45,50] The above observations suggest that at both 355 and 532 nm the O_2^- fragments, on average, have a higher degree of internal (vibrational) excitation when they are formed from O_6^-, via an overall $O_6^- \rightarrow O_2^- + 2O_2$ process, compared to the $O_4^- \rightarrow O_2^- + O_2$ dissociation. This conclusion contrasts statistical expectations, since O_6^- dissociation involves more degrees of freedom, compared to O_4^-.

Based on the previous experimental[19,45,50,51] and theoretical[4,53] studies, the O_{2n}^- and $O_{2n}^- \cdot H_2O$, $n \geq 2$ species are well described as covalently bound O_4^- anions, solvated by the remaining neutral molecules. The O_4^- anion is, in turn, described as two $O_2^{-1/2}$ moieties with weak covalent bonding between them, arranged in a rectangular (D_{2h}) structure shown in Figure 3.4(b).[4,50] In this structure, corresponding to the $X\,^2A_u$ electronic state, the excess electron is shared between the respective $\pi_g^*(2p)$ orbitals of the two equivalent diatomic moieties.[4] The antibonding character of $\pi_g^*(2p)$ is responsible for the greater bond length in O_2^-, compared to neutral O_2 [Figures 3.4(a) and (c)]. Delocalizing the additional $\pi_g^*(2p)$ electron between two $O_2^{-1/2}$ moieties in O_4^- should lead to each of the $O_2^{-1/2}$ bonds being shorter than the O_2^- bond.

Based on this qualitative expectation alone, one might propose a naive explanation for the enhanced vibrational excitation and, hence, autodetachment of O_2^- photofragments ejected from O_6^-, compared to those resulting from unsolvated O_4^- dissociation. The extent of charge delocalization in O_6^-, even though it is described as nominally $O_4^- \cdot O_2$, is likely to be more significant than in O_4^-. That is, a more appropriate description for O_6^- might be $O_2^{-(1-\delta)/2}O_2^{-(1-\delta)/2}O_2^{-\delta}$, with $0 < \delta << 1$. The

reduced populations of the diatomic antibonding $\pi_g^*(2p)$ orbitals in the core anion should translate into shorter O–O bonds, which, in turn, would result in a greater geometry change imparted on an O_2^- fragment ejected impulsively from O_6^-. This would be consistent with a greater degree of O_2^- fragment vibrational excitation and, hence, auto-detachment in the O_6^- case, compared to O_4^-.

However, the $O_2^{-1/2}$ bond length in O_4^- is predicted to be much closer to that in neutral O_2 than in O_2^- (see Figure 3.4), indicating that the excess electron in O_4^- contributes mainly to the bonding between the two $O_2^{-1/2}$ moieties. Therefore, further charge delocalization in O_{2n}^-, $n \geq 3$ can result in only a miniscule reduction in the $O_2^{-(1-\delta)/2}$ bond length. Such a small geometry change cannot explain the drastic difference in the 532 nm fragment autodetachment channel in O_6^- versus O_4^-. A more detailed analysis of the electronic structure is therefore required to explain the experimental observations.

The ground state of O_4^-, as well as its first two excited states, $A\,^2B_{3g}$ and $B\,^2B_{2g}$, correlate asymptotically with the lowest $O_2(X\,^3\Sigma_g^-) + O_2^-(X\,^2\Pi_g)$ dissociation limit.[4,50] However, 532 nm excitation from the $X\,^2A_u$ state accesses the higher-lying $^2B_{3g}$ state, $C\,^2B_{3g}$, which correlates to the electronically excited $O_2(a\,^1\Delta_g) + O_2^-(X\,^2\Pi_g)$ channel.[4] At the CASSCF/ICCI level of theory,[4] there is a large vertical energy gap (1.77 eV) between the two $^2B_{3g}$ states.

In agreement with these predictions, the only anionic photodissociation pathway in O_4^- observed in this wavelength region yields vibrationally cold $O_2^-(X\,^2\Pi_g)$ and electronically excited $O_2(a\,^1\Delta_g)$.[48,49] Specifically, 86% of the O_2^- products at 523.6 nm

are formed in the ground vibrational state, with 14% in v = 1.[48] Hence, most available energy in O_4^- photodissociation in this regime is tied up in the electronic excitation of O_2.

At shorter wavelength, both the $O_2^-(X\,^2\Pi_g) + O_2(a\,^1\Delta_g)$ and $O_2^-(X\,^2\Pi_g) + O_2(X\,^3\Sigma_g^-)$ channels are accessed in O_4^- dissociation, with the latter channel resulting in vibrationally hot (autodetaching) anionic products.[19,48,49] As pointed out by one of the reviewers of this paper, the very specific energy partitioning observed in the vicinity of 532 nm may be driven by an O_4^- vibronic resonance.[49,62] Away from this possible resonance, O_4^- dissociation is less state specific, accessing a broader range of available electronic and vibrational product channels. In our past work, for example, this manifested in the appearance of fragment autodetachment peaks in the unsolvated O_4^- spectra at 355 nm.[19] However, the mere increase in the total available energy at 355 vs. 532 nm may also result in the formation of vibrationally excited O_2^- products, even in coincidence with electronically excited O_2.[48]

The above $O_4^- + 532\text{ nm} \rightarrow O_2^-(X\,^2\Pi_g) + O_2(a\,^1\Delta_g)$ channel is largely preserved in O_6^-, despite the presence of a third O_2 moiety.[51] However, the O_6^- cluster anion also exhibits the electronically relaxed channel, not observed for O_4^- at this wavelength. Whereas the core O_4^- dissociates into $O_2^-(X\,^2\Pi_g) + O_2(X\,^3\Sigma_g^-)$ with significant population of higher vibrational level of O_2^- ($v \geq 4$), and the overall cluster process described as $O_6^- \rightarrow O_2^-(X\,^2\Pi_g,\ v \geq 4) + 2O_2(X\,^3\Sigma_g^-)$. This pathway leads to autodetachment from the vibrationally excited O_2^- fragments, as seen both in the past work[19,45,50,51] and the results presented here (features a–c in Figure 3.2).

These findings indicate nonadiabatic transitions between the $O_4^- \rightarrow O_2(a\,^1\Delta_g) + O_2^-(X\,^2\Pi_g)$ and $O_2^- + O_2(X\,^3\Sigma_g^-)$ dissociation asymptotes occurring in the presence of

solvent molecules (i.e., in O_6^- and larger O_{2n}^- clusters). Such relaxation amounts to electronic-vibrational energy transfer, leaving a measurable fraction of the anionic fragments in vibrationally excited, autodetaching states ($v \geq 4$). Several explanations for the drastic change in the dissociation dynamics of O_6^-, compared to O_4^-, have been put forth, including a charge-transfer-to-solvent model, solvent-induced nonadiabatic coupling of the core O_4^- anion electronic states, and caging.[45,50]

Each of these mechanisms may contribute to the dissociation process and none can be clearly singled out. Based on the recent advances in cluster chemistry, we propose yet another, complementary view of the O_{2n}^- and $O_{2n}^- \cdot H_2O$, $n \geq 3$, dissociation process. Namely, the electronic excitation of the nascent fragments of the core O_4^- anion in 532 nm dissociation via the $C\,^2B_{3g}$ state,[4,49] may be transferred to the vibrational degrees of freedom by means of charge transfer from the nascent O_2^- to the counter fragment, the electronically excited O_2.

This mechanism is described as an overall $O_4^-(C\,^2B_{3g}) \rightarrow O_2^-(X\,^2\Pi_g) + O_2(a\,^1\Delta_g) \rightarrow O_2(X\,^3\Sigma_g^-) + O_2^-(X\,^2\Pi_g)$ process involving the nascent core photofragments. Similar solvent-assisted mechanisms were previously proposed for other in-cluster fragmentation processes, such as the spin-orbit quenching of $I(^2P_{1/2})$ photofragments of I_2^- photodissociation at 395 nm via an $I^- + I(^2P_{1/2}) \rightarrow I(^2P_{3/2}) + I^-$ mechanism[63-65] and $I^- + Br \rightarrow I + Br^-$ relaxation of IBr^- dissociation products in the presence of CO_2.[66,67]

The electron-hopping process proposed for the present case is illustrated at the molecular-orbital level in Figure 3.5(a), where the initial and final populations of the doubly degenerate $\pi_g^*(2p)$ HOMOs of both diatomic fragments (O_2^- and O_2) are shown, corresponding to the nascent $O_2^-(X\,^2\Pi_g) + O_2(a\,^1\Delta_g)$ fragments of $O_4^-(C\,^2B_{3g})$ dissociation

on the left and the electron-hopping products, $O_2(X\,^3\Sigma_g^-) + O_2^-(X\,^2\Pi_g)$, on the right.

Energetically, the charge-transfer is made possible by asymmetric solvation in the cluster environment, as illustrated in the qualitative diagram in Figure 3.5(b). For given internal states, the $O_2^-\cdots O_2$ and $O_2\cdots O_2^-$ fragment pairs are degenerate only in the absence of solvent or in a symmetric solvent environment. In the more common case of asymmetric solvation, the fragment pair corresponding to a more solvated anion will, in general, be more stable than the same pair (same internal states) with the solvent in closer proximity to the neutral fragment.

For the purpose of illustration, let $X\cdot(O_2^-\cdots O_2)$ represent asymmetric solvation of the $O_2^-\cdots O_2$ fragment pair with neutral solvent molecules X preferentially located on the anion, O_2^-, side. The $X\cdot(O_2^-\cdots O_2)$ state is degenerate with its mirror-image counterpart, the $(O_2\cdots O_2^-)\cdot X$ state, which is obtained by inversion of the coordinates of all nuclei and electrons in the system. However, should charge transfer occur in either of these two states without change in the solvent configuration, a transition described as $X\cdot(O_2^-\cdots O_2) \rightarrow X\cdot(O_2\cdots O_2^-)$ or $(O_2\cdots O_2^-)\cdot X \rightarrow (O_2^-\cdots O_2)\cdot X$, respectively, the energy of the cluster will increase in both cases (assuming the internal states of the "new" O_2 and O_2^- are the same as those of the initial respective species).

In general, the energy of a fragment pair is dependent not only on the O_2 and O_2^- internal states, but also on solvation asymmetry or the "solvent coordinate". In the above illustration, the opposite directions along this coordinate correspond to the $X\cdot(\ldots)$ and $(\ldots)\cdot X$ solvent configurations, which we shall refer to, for brevity, as "left" and "right". The overall state of the solvated pair is thus described by both the charge localization, $O_2^-\cdots O_2$ or $O_2\cdots O_2^-$, and the solvent coordinate, ranging from $X\cdot(\ldots)$ to $(\ldots)\cdot X$.

As illustrated pictorially in Figure 3.5(b), the $O_2^-\cdots O_2$ pair energy increases along the solvent coordinate from left to right, i.e., from $X\cdot(O_2^-\cdots O_2)$ to $(O_2^-\cdots O_2)\cdot X$, while the opposite is true for $O_2\cdots O_2^-$. Specifically, Figure 3.5(b) illustrates asymmetric solvation of the nascent $O_2^-(X\,^2\Pi_g, v = 0) + O_2(a\,^1\Delta_g, v' = 0)$ fragment pair and several charged-switched, electronically relaxed $O_2(X\,^3\Sigma_g^-, v' = 0) + O_2^-(X\,^2\Pi_g, v = 0–5)$ states. The energy of the former pair increases along the solvent coordinate from left to right, i.e. from $X\cdot(O_2^-\cdots O_2)$ to $(O_2^-\cdots O_2)\cdot X$, while the energy of each of the latter charge-switched states decreases in the same direction.

In explaining the observed O_2^- autodetachment, we are concerned with the formation of $O_2^-(X\,^2\Pi_g, v \geq 4)$ photofragments. The green arrow in Figure 3.5(b) indicates a possible pathway, specifically for the formation of O_2^- in $v = 4$: $O_2^-(X\,^2\Pi_g, v = 0) + O_2(a\,^1\Delta_g, v' = 0) \rightarrow O_2(X\,^3\Sigma_g^-, v' = 0) + O_2^-(X\,^2\Pi_g, v = 4)$. In the absence of solvent (or for symmetric solvation), the energy gap between the initial and final states of this process is in excess of 0.4 eV. The corresponding gaps are smaller for higher vibrationally excited final states, but even the $v = 4$ gap, indicated in Figure 3.5(b), can be bridged for certain solvent configurations on the left side of the solvent-coordinate axis. It could be argued that just one solvating O_2 molecule might not be sufficient to achieve an $O_2^-(X\,^2\Pi_g, v = 0) + O_2(a\,^1\Delta_g, v' = 0)$ and $O_2(X\,^3\Sigma_g^-, v' = 0) + O_2^-(X\,^2\Pi_g, v = 4)$ resonance in the O_6^- cluster dissociation. However, due to the large geometry difference between O_2 and O_2^- (see Figure 3.4), both O_2 and O_2^- fragments are likely to be vibrationally excited as a result of an $O_2^- + O_2 \rightarrow O_2 + O_2^-$ charge hopping. Vibrational excitation shifts the $O_2(X\,^3\Sigma_g^-, v' > 0) + O_2^-(X\,^2\Pi_g, v)$ levels in Figure 3.5(b) to higher

energies, making the described electron-hopping transitions more plausible, particularly for highly vibrationally excited final states.

The proposed pathway leads to vibrationally excited $O_2^-(X\,^2\Pi_g)$ products, as the initial electronic excitation of O_2 is converted to vibrational excitation of O_2^- (same molecular moiety). The vibrational excitation of O_2^- is manifest as autodetachment bands in the photoelectron data, as the $O_2^-(X\,^2\Pi_g,\ v \geq 4)$ levels are embedded in the detachment continuum. This pathway is due to dissociating O_4^- interacting with the solvent. As might be expected, it does not take over the dissociation process completely, but competes with the "original", electronically excited but vibrationally cold $O_2^-(X\,^2\Pi_g)$ + $O_2(a\,^1\Delta_g)$ channel (the only channel in 532 nm dissociation of unsolvated O_4^-).

We finally note that the greatest fragment autodetachment intensity, relative to the direct photodetachment bands, is observed for O_{2n}^-, $n \geq 3$. The autodetachment is significantly weaker for the hydrated $O_{2n}^-\cdot H_2O$ species (see Figure 3.2), consistent with the greater solvation-induced stabilization in these clusters, which is due to the high solvent binding energy of water (~0.7 eV), compared to O_2 (~0.1 eV).[19] It is, however, intriguing that no clear autodetachment signatures are observed for $O_4^-\cdot H_2O$, while the $O_6^-\cdot H_2O$ spectrum does show autodetachment peaks (see the right column in Figure 3.2). Combined with the results for the unhydrated O_{2n}^- cluster anions (left column in Figure 3.2), this observation suggests that at least one solvent O_2 molecule is necessary for fragment autodetachment to occur, while a single H_2O by itself does not have the same effect. This may be due to the particulars of the corresponding cluster structures (if, for example, H_2O binds to O_4^- in a symmetric manner, while O_2 does not). It seems, however, more likely that a solvent O_2, due to its chemical nature and positive electron

affinity, plays a more direct role in the proposed electron-hopping process, possibly acting as a transfer bridge between the nascent $O_2^- \cdots O_2$ fragments. A similar role was proposed recently for CO_2 mediating the fragment relaxation process in $IBr^- \cdot CO_2$ dissociation.[66,67] Time-resolved measurements on some of the $O_{2n}^-(H_2O)_m$ clusters, particularly on O_6^-, would go a long way to either confirm or disprove this speculation.

3.5. Conclusion

The electronic structure and photochemistry of $O_{2n}^-(H_2O)_m$, n = 1 – 6, m = 0 – 1 cluster anions has been investigated using photoelectron imaging and photofragment mass-spectroscopy at 532 nm. Both pure oxygen clusters and their hydrated counterparts with $n \geq 2$ form an O_4^- core anion. Fragmentation of these clusters yields predominantly O_2^- and $O_2^- \cdot H_2O$ anionic products, with the addition of O_4^- fragments for larger clusters. The fragment autodetachment patterns observed for O_6^- and larger O_{2n}^- species, as well as some of their hydrated counterparts, indicate that the corresponding O_2^- fragments are formed in excited vibrational states ($v \geq 4$). Yet surprisingly, the unsolvated O_4^- anion itself does not show fragment autodetachment. Excitation at 532 nm promotes the core O_4^- anion to a dissociative state that leads to the $O_2^-(X\,^2\Pi_g) + O_2(a\,^1\Delta_g)$ dissociation channel. It is hypothesized that in a cluster environment, interaction with the solvent results in nonadiabatic electronic quenching of the nascent fragment pair via a charge-hopping mechanism $O_2^-(X\,^2\Pi_g) + O_2(a\,^1\Delta_g) \rightarrow O_2(X\,^3\Sigma_g^-) + O_2^-(X\,^2\Pi_g)$. This process, mediated by solvent asymmetry and possibly a bridging role played by solvent O_2 molecules, leads to vibrationally excited $O_2^-(X\,^2\Pi_g)$ products.

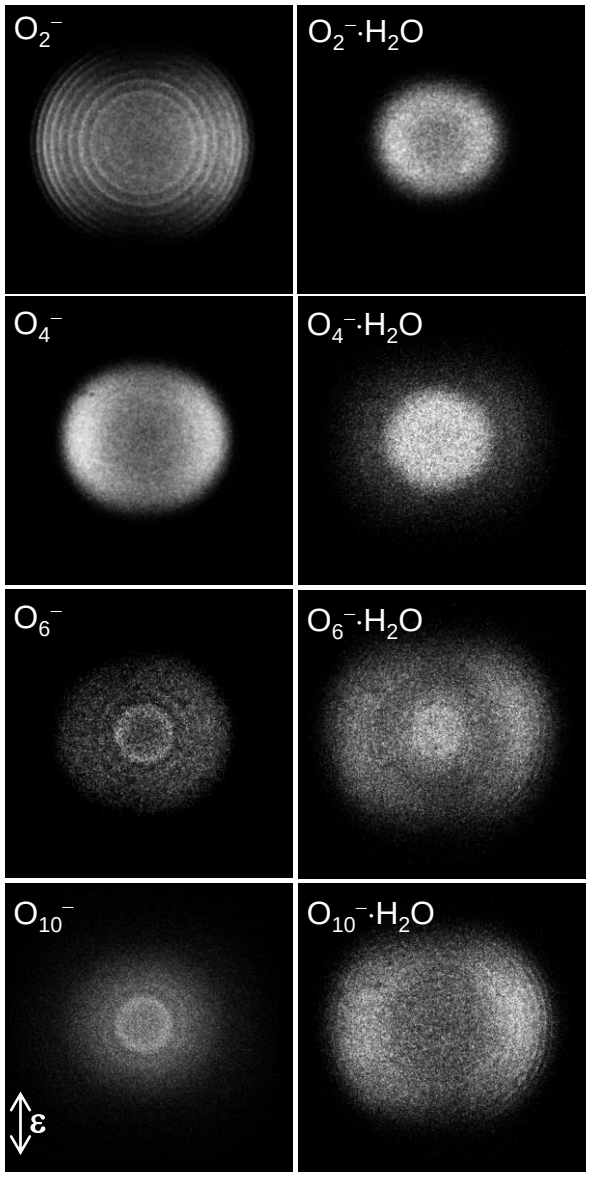

Figure 3.1 532 nm photoelectron images of representative $O_{2n}^-(H_2O)_m$ clusters anions. All images were recorded under the same experimental conditions and shown on the same velocity scales.

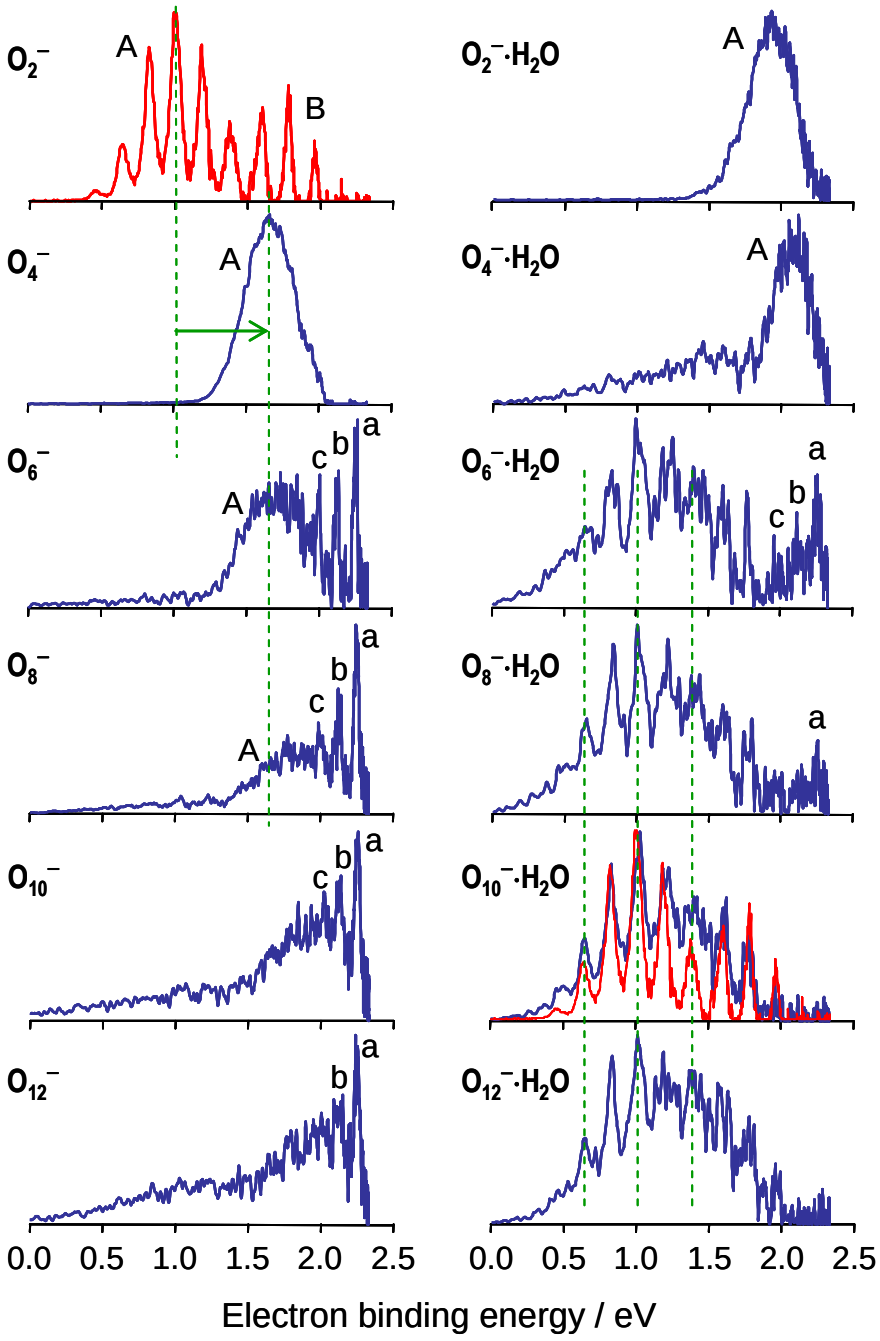

Figure 3.2 532 nm photoelectron spectra of $[O_{2n}(H_2O)_m]^-$, n = 1 - 6, m = 0 – 1 obtained from the images shown in Figure 1. Labels A and B correspond to the formation of O_2 in the ground $X\,^3\Sigma_g^-$ or first excited $a\,^1\Delta_g$ states, respectively, via direct photodetachment (for n = 1) or O_4^- dissociative photodetachment (for $n \geq 2$).

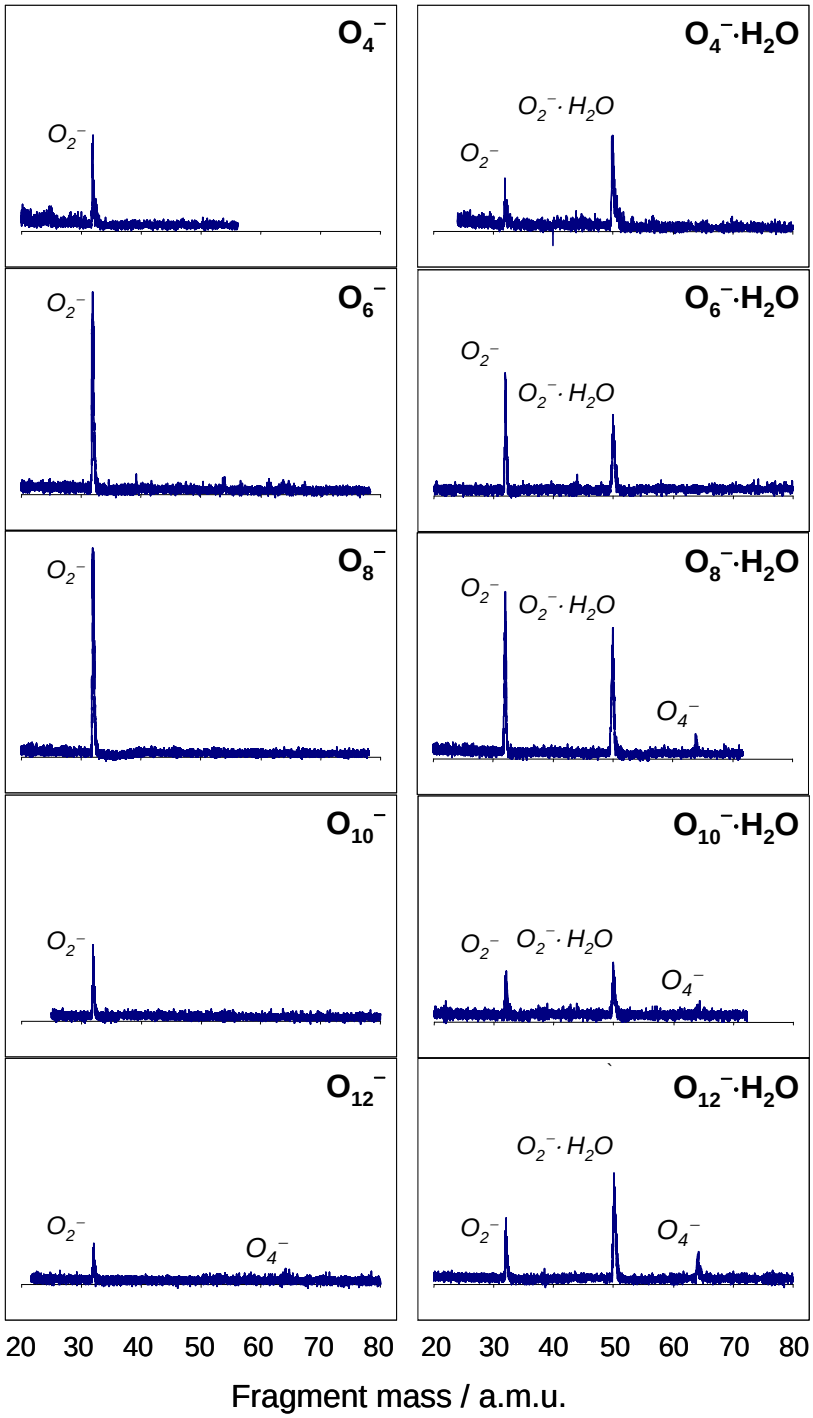

Figure 3.3 532 nm photofragmentation mass spectra for $O_{2n}^{-}(H_2O)_m$, n = 2 – 6, m = 0 – 1. Spectra were recorded at the same detector voltages and are presented on consistent intensity scales.

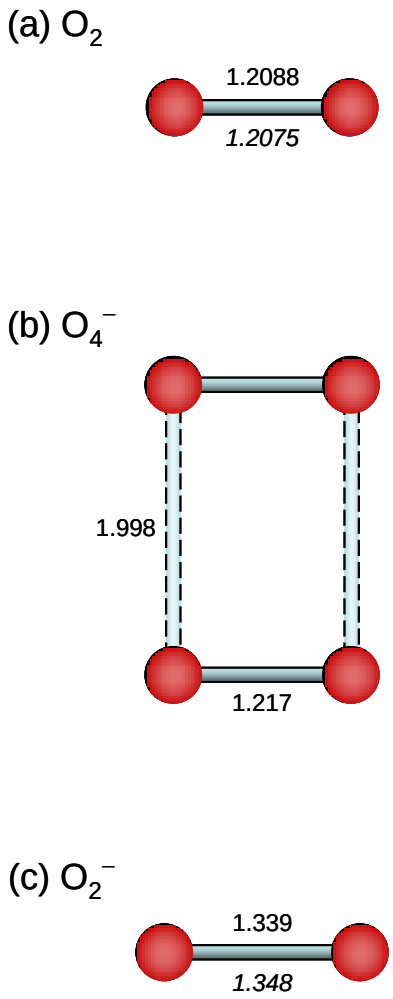

Figure 3.4 The equilibrium structures of (a) O_2, (b) O_4^-, and (c) O_2^-. Bond lengths are indicated in Ångstroms. The Roman-type values are from CCSD(T)/aug-cc-pVTZ calculations. For comparison, the numbers in italics are experimental measurements (Refs. [1,2] for O_2 and Ref. [3] for O_2^-). The O_4^- structure is from Ref. [4]

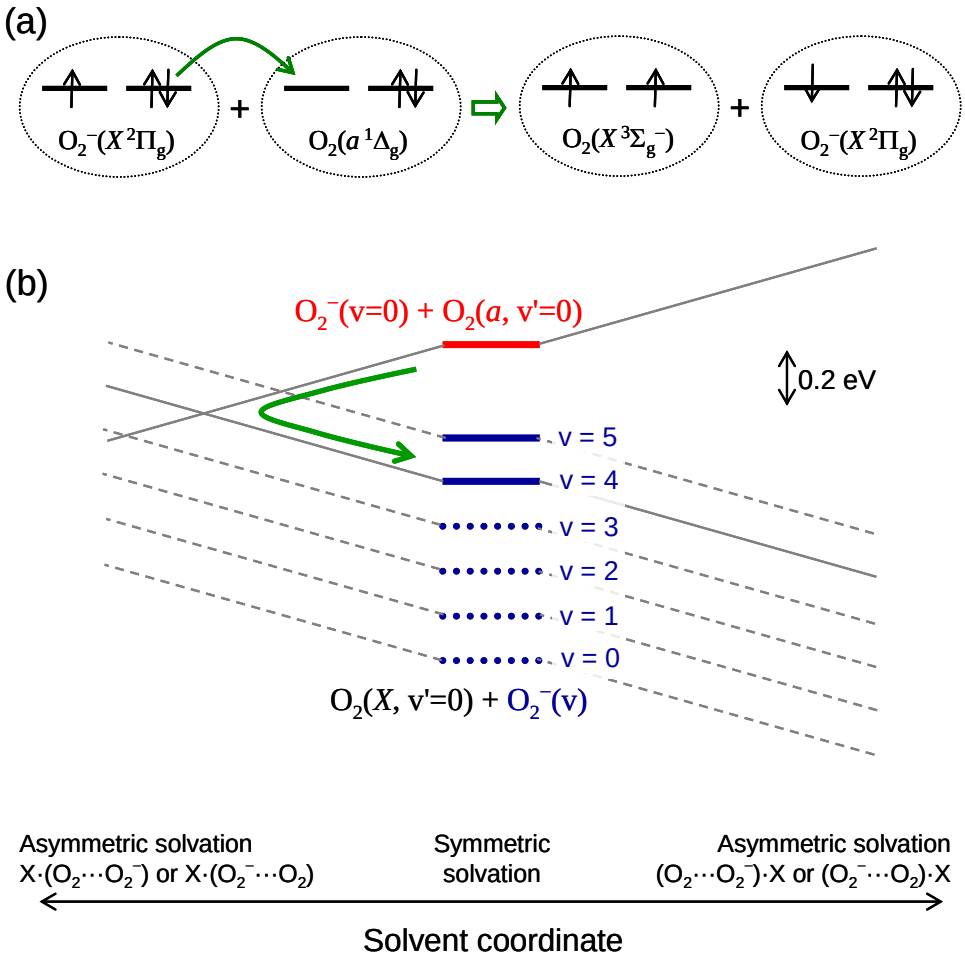

Figure 3.5 (a) Molecular-orbital level illustration of the $O_2^-(X\,^2\Pi_g)$ + $O_2(a\,^1\Delta_g)$ → $O_2(X\,^3\Sigma_g^-)$ + $O_2^-(X\,^2\Pi_g)$ relaxation process via electron-hopping. The initial and final populations of the doubly degenerate $\pi_g^*(2p)$ HOMOs of O_2^- and O_2 are shown, corresponding to the nascent fragments of O_4^- dissociation on the left and the electron-hopping products on the right. **(b)** Illustration of the proposed electron-hopping mechanism, induced by asymmetric solvation. The vertical double arrow shows the approximate energy scale of the diagram. See the text for details.

CHAPTER 4

PHOTODISSOCIATION OF NITROMETHANE CLUSTER ANIONS

4.1. Introduction

Nitromethane, CH_3NO_2, is known for its rich and complex chemistry, which is largely due to the nitro group. The unique properties of this substituent are dictated by the electronegative nature of the constituent atoms, a large molecular dipole moment, and a resonant π system interacting with the non-bonding lone pairs of electrons on the oxygen atoms. An important property of nitromethane (NM) is its propensity to form negative ions in the gas phase by electron attachment.[68-73] The mechanism of electron attachment to NM has been studied using a number of techniques, primarily involving collisions with electrons, alkali, or high-Rydberg atoms.[68-72] The reverse process, electron detachment from NM^-, has also been studied in detail by negative-ion photoelectron spectroscopy.[70,74,75]

These experiments have revealed that electron attachment to NM forms valence NM^- anion via an initial electron-molecule complex, a gateway dipole-bound state that involves a diffuse Rydberg-type orbital protruding from the CH_3 group. In the neutral and dipole-bound anionic states, the C–NO_2 group is nearly planar, but in the valence-bound anion these atoms are found in a non-planar arrangement, with the nitrogen at the apex of a pyramidal structure. Theoretical studies have suggested that in the neutral CH_3NO_2 molecule distortion from the planar C–NO_2 structure stabilizes the vacant π^* orbital on the NO_2 group. In the anionic form, distortion from the planar arrangement

localizes the electron in this π^* orbital, yielding the valence anion.[68,70,76]

Electron collision experiments have shown that nitromethane not only forms anions, but also undergoes anionic fragmentation. Recent studies investigated dissociative electron attachment to NM over a range from 0 to 16 eV.[77,78] The major fragments observed were NO_2^-, O^-, OH^-, CN^-, and CNO^-, along with several minor products: $CH_2NO_2^-$, $CHNO_2^-$, CH_2NO^-, H_2NO^-, CH_3^-, CH_2^-, CH^- and H^-. Most of the fragment anions were observed at electron collision energies between 5 and 10 eV and had low relative intensities, but two important fragments had noticeably different appearance energies: NO_2^-, with a maximum intensity at around 0.62 eV, and OH^-, which had a pronounced maximum near 0 eV. Most fragmentation channels are believed to occur via dissociative electron attachment, but OH^- is thought to form via a bimolecular process.

Little is known about cluster anions containing nitromethane. Wincel measured the solvation energies of NM^- containing clusters, and binding energies of several other anions solvated by NM.[79] Another study focused on the photodissociation of $X^-\cdot NM$ (X = I or Br) clusters and three types of fragment ions, X^-, NM^-, and NO_2^-, were observed by photofragment action spectroscopy.[80] For the $I^-\cdot NM$ cluster, the NM^- fragment was most intense at photon energies of 3.59 eV. The I^- and NO_2^- fragments also had sharp peaks at 3.59 eV, but exhibited additional structure at higher photon energies, corresponding to excitation of the $-NO_2$ vibrations. In the ground state of the $X^-\cdot NM$ clusters, the excess electron is localized on the halogen atoms, while the nitromethane molecules play the role of (neutral) solvent. The mechanism for formation of either X^- or NO_2^- photofragments in these systems can be interpreted in a manner similar to an S_N2 reaction. A more recent study of hydrated NM^- showed typical stepwise increases in

electron binding energy, until $NM^-(H_2O)_6$, which showed a low energy feature attributed to a "dual dipole-bound" anion. Photofragmentation of the clusters at 2134 nm indicated the dipole bound $NM^-(H_2O)_6$ was converted to a valence bound fragment $NM^-(H_2O)_3$.[81]

Although NM^- is a relatively small molecule, it has proven to be a challenging system for electronic structure calculations. The difficulty of obtaining reliable theoretical descriptions of NM^- is highlighted in a comprehensive theoretical study of the electron affinity of NM, where various levels of theory give values ranging from -0.126 eV to 0.595 eV,[82] compared to the experimental result of 0.172 ± 0.006 eV.[74] Theoretical studies have examined direct dissociation of $CH_3NO_2^-$ to $CH_3 + NO_2^-$.[83,84] The dissociation barrier was calculated to be 0.35 eV,[83] but a more recent study placed the barrier height at about 0.78 eV.[84] The potential isomerization to CH_3ONO^- with subsequent fragmentation to $CH_3O^- + NO$ has also been explored and found to be much less favorable. The ground state of $CH_3NO_2^-$ is $^2A'$, while that of CH_3ONO^- is $^2A''$, so the transformation is nonadiabatic. On the $^2A''$ surface, the rearrangement involves a large potential barrier, calculated to be 2.59 eV.[83] Furthermore, another study questioned the stability of the CH_3ONO^- isomerization product, as some levels of theory predict an unstable isomer.[84]

In this paper, we report several fragmentation processes in the photodissociation of nitromethane cluster anions, $(NM)_n^-$, n = 1–6, at 355 nm. In contrast to the past work on $X^-\cdot NM$ clusters,[80] the charge in $(NM)_n^-$ is localized on an NM molecule; hence, nitromethane plays the dual role of an anionic solute and neutral solvent. The photochemistry of the core anion, NM^-, is due to the excess electron occupying the antibonding π^* orbital. Transition energies from this orbital to other low-energy

antibonding orbitals are lower, compared to transitions in neutral NM, which involve non-bonding or π electrons. At 355 nm, the photochemistry of $(NM)_n^-$ is initiated by photoabsorption by the core anion, NM^-, without competing dissociation of neutral NM molecules. The dominant NM^- dissociation process is the breaking of the C–N bond to yield the NO_2^- + CH_3 products.[84] These products are analogous to those in the photodissociation of neutral NM at 271–193 nm, where photon energies are sufficient to initiate the dissociation process in the neutral.[85-89]

4.2. Experimental and theoretical methods

The experiments were performed using a tandem time-of-flight reflectron mass-spectrometer described in detail elsewhere.[37] Cluster anions are generated in a pulsed (50 Hz) supersonic expansion of nitromethane vapor in Ar carrier gas with a backing pressure of 20 psi. The expansion is crossed with a 1 keV electron beam, which produces slow electrons from collisions with the gas. The desired cluster anions are formed by dissociative attachment of slow secondary electrons to neutral nitromethane clusters. A Wiley-McLaren time-of-flight mass spectrometer separates the ions according to their mass-to-charge ratio. The third harmonic (355 nm, 20 mJ/pulse) of a Nd:YAG laser (Quanta Ray, Lab 50, 8 ns pulse duration) intersects the ions prior to the reflectron stage. Fragment ions are detected by scanning the reflectron potential while monitoring the ion intensity with a dual microchannel plate detector. Typically, 512 mass-spectral traces are averaged for each fragment ion. The mass-spectra reported in this work are composites of the scanning steps.

Electronic structure calculations were carried out with the Gaussian 03 suite of programs,[90] using density functional theory (DFT) with the 6-311++G(3df,3pd) basis set.

The geometry of the anion in the ground state was optimized and normal mode analysis confirmed that the structure found was indeed a stationary point (all frequencies were real). Excited states were treated at the optimized geometry of the anion, either explicitly or by using the time-dependent density functional theory (TD-DFT) approach.[91-93]

4.3. Results

A representative time-of-flight mass spectrum of the parent anions formed by electron attachment to nitromethane clusters is shown in Figure 4.1. The nitromethane cluster anions, $(NM)_n^-$, are the dominant species observed. The *m/z* = 46 peak, just below the n = 1 peak, is assigned to NO_2^-, while most of the low-intensity peaks neighboring the intense $(NM)_n^-$ peaks correspond to hydrated clusters. The most intense peak in the spectrum corresponds to the dimer anion, $(CH_2NO_2)_2^-$, followed by the monomer anion, $CH_2NO_2^-$, while the larger clusters steadily decrease in intensity with increasing size. The formation of NO_2^- from dissociative electron attachment is consistent with the previous electron attachment studies of NM, where NO_2^- was the major fragment ion observed even at low electron kinetic energies.[77,78] Clusters of NO_2^- with NM have negligible intensity in our primary (parent-ion) mass-spectra.

The 355 nm photofragment-ion mass spectra for $(NM)_n^-$, n = 1–6, are shown in Figure 4.2. With increasing parent cluster size, n, the maximum of the fragment intensity distribution shifts to higher-mass fragments. The dominant fragments observed for the smaller clusters are described by the general formula $NO_2^-(NM)_k$, while the larger clusters preferentially form the $(NM)_k^-$, $k < n$, fragment ions.

The observed photofragments suggest the following reaction pathways:

$$(NM)_n^- + h\nu \rightarrow (n-k-1)NM + CH_3 + NO_2^-(NM)_k \quad (4.1)$$

$$\rightarrow (n-1)NM + CH_2NO + OH^- \quad (4.2)$$

$$\rightarrow (n-k)NM + (NM)_k^- \quad (4.3)$$

All of these pathways are energetically accessible in the photodissociation of $(NM)_n^-$ with 3.5 eV photons. The mass-spectral peaks corresponding to the anionic photofragments formed via these pathways are labeled in Figure 4.2. The first process (Eq. 4.1, red labels in Figure 4.2) implies dissociation of NM^- within $(NM)_n^-$ to produce NO_2^-, which may remain associated with additional NM solvent molecules. The second reaction (Eq. 4.2, green label in Figure 4.2) is the formation of OH^-. This fragment is observed only for the NM^- and $(NM)_2^-$ parent ions. Solvated OH^- fragments are not seen in quantities sufficient for unambiguous identification. The third type of fragmentation reaction is NM solvent evaporation (Eq. 4.3, blue labels in Figure 4.2).

We will refer to the anionic fragments formed via Eqs. 4.1 and 4.2 as core-dissociation fragments, while the $(NM)_k^-$ ions formed via Eq. 4.3 will be described as "caged" photofragments. The fractional yield of the caged photoproducts tends to increase with increasing size of the parent $(NM)_n^-$ clusters. The combined yield of all $(NM)_k^-$ fragments, relative to the total anionic fragment yield, is plotted in Figure 4.3(a) as a function of the parent cluster size, n. The values shown were obtained by integrating the corresponding fragment peak intensities. The fractional yield of the caged fragments reaches about a half for $n = 6$. By analogy with the trends seen in other cluster systems,[43,63,94-98] one expects the caged fragment fraction to increase further for larger $(NM)_n^-$ clusters.

Figure 4.3(b) shows ⟨NM lost⟩, the average numbers of (intact) neutral NM molecules evaporated in the core-dissociated and caged photofragments, respectively, also plotted versus the parent cluster size, n. In calculating ⟨NM lost⟩ for the core-dissociation channels, the number of evaporated NM in Eqs. 4.1 and 4.2 equals $(n - k - 1)$ and $(n - 1)$, respectively. For caged fragments, the quantity plotted represents the average of $(n - k)$, per Eq. 4.3. The ⟨NM lost⟩ values for both the caged and core-dissociated channels display approximately linear trends, increasing with n, but are generally lager for the caged fragments.

4.4. Discussion. Dissociation mechanisms

4.4.1. Overview

We will show that the experimental observations are consistent with each $(NM)_n^-$ cluster having an NM^- core anion, i.e. the cluster structures are best described as $NM^-(NM)_{n-1}$. It is the NM^- cluster core that absorbs the excitation photon. With no evidence of stable (electron-bound) excited states of NM^-,[75] the excitation of bare NM^- results in direct photodetachment or an anionic resonance $[NM^-]^*$, which may, in turn, decay by either autodetachment or fast dissociation. In clusters, $[NM^-]^*$ may be stabilized by solvation, decreasing the probability of autodetachment in favor of solvent-enabled chemistry.[99] Focusing on the anionic fragmentation channels, $[NM^-]^*$ is expected to yield the dominant $CH_3 + NO_2^-$ fragments. In clusters, the $CH_3 + NO_2^-$ photofragment recombination (caging)[64,94,95,100] may occur or, alternatively, $[NM^-]^*$ may relax via direct energy transfer to the solvent network. Both processes will be followed

by NM solvent evaporation, resulting in the overall reaction described by Eq. 4.3.

It is instructive to compare the photodissociation of NM^- to that of neutral nitromethane. A number of groups have studied the vacuum-UV (~ 271–193 nm) photodissociation of this molecule.[85-89] Recent theoretical studies have suggested the excited state decays through an S_3/S_2 conical intersection, which ultimately yields the $NO_2 + CH_3$ products.[101] In the present study, we observed a similar dissociation, specifically, cleavage of the C–N bond in NM^-. Neutral OH formation, which would be analogous to the OH^- channel in the anion, has not been seen in NM dissociation. However, CH_3O + NO rearrangement products were observed in infrared multi-photon dissociation studies.[102]

4.4.2. Electronic states

Compared to neutral NM, electronic excitation of the anion and, consequently, NM^- dissociation can be induced with lower energy photons. In the $X\,^2A'$ ground state of NM^-, the unpaired electron occupies the π* (11a′) orbital localized primarily on the nitro group.[75] Thus, in contrast to the photodissociation of neutral NM, which occurs via the $\pi^*(NO_2) \leftarrow \pi(NO_2)$ or $\pi^*(NO_2) \leftarrow \sigma(CN)$ transitions,[103] the π* orbital is occupied in the anion and it is this unpaired electron that is photochemically active in our study. The relatively high energy of this orbital is responsible for the smaller electronic excitation gaps in the anion, while its π* character leads to a non-planar anion structure and a slight increase of the NO_2 bond lengths in NM^-, compared to NM.

The three lowest-energy, same-spin unoccupied orbitals at the equilibrium geometry of NM^- are 12a′, 13a′, and 7a″, as indicated by the UB3LYP/6-311++G(3df,3pd)

calculations. Excitation of the 11a′ electron to one of these orbitals yields the A^2A′, B^2A′, and C^2A″ excited states, respectively. The 12a′ and 13a′ orbitals both have some antibonding σ* character along the C–N bond; hence, the A^2A′ and/or B^2A′ states are expected to be important in NM^- dissociation to $CH_3 + NO_2^-$. On the other hand, 7a″ is a C–H σ* type orbital; the C^2A″ state may, therefore, play a role in the OH^- fragment formation.

To gain insight into the roles of NM^- excited states in photodissociation, we surveyed the energy differences between the ground and excited electronic states using several theoretical methods. Within a one-electron Koopman's theorem approach, the vertical transition energies between the 11a′ HOMO and the 12a′, 13a′, and 7a″ orbitals of the anion were estimated at 1.66, 2.58, and 2.69 eV, respectively. Alternatively, the TD-DFT method yields transition energies of 1.02, 1.83 and 1.98 eV, corresponding to the A^2A′, B^2A′, and C^2A″ excited states respectively. This method also predicts the oscillator strengths for the A^2A′ and B^2A′ states to be much larger than that for the C^2A″ state. The C^2A″ state energy could be calculated explicitly, because it involves electron promotion to an orbital of different symmetry. The calculation yielded 2.37 eV for the $X \rightarrow C$ vertical transition energy. As the large discrepancies between the computed values illustrate, excited states are notoriously difficult to model; however, the qualitative predictions are still useful. To put the accuracy of the above predictions in an experimental perspective, we attempted photodissociation of NM^- and $(NM)_2^-$ at 532 nm (2.33 eV) and did not observe any anionic fragments. This suggests that the dissociative excited states lie > 2.33 eV (vertically) above the NM^- minimum.

4.4.3. $CH_3NO_2^- \setminus CH_3 + NO_2^-$

In a recent study of collisions between oriented nitromethane molecules with sodium atoms, qualitative potential energy curves were used to explain the mechanism of $CH_3 + NO_2^-$ formation.[68,69] A repulsive $^2A'$ potential was proposed to play a primary role in dissociative electron transfer. This state would correlate with the electronic ground states of the CH_3 and NO_2^- fragments. Building on this work, in Figure 4.4 we show qualitative potential energy curves for NM^- dissociation, based primarily on our findings. Direct cleavage of the C–N bond in the ground electronic state of the anion yields CH_3 and NO_2^-, but this NO_2^- fragment is in the excited $^3B_1$ state. The ground state of NO_2^- is $^1A_1$, in which all electrons are paired, while the ground state of CH_3 is $^2A_2''$. Since covalent bond formation between the fragments in these states is not possible, the $NO_2^-(X\,^1A_1) + CH_3(X\,^2A_2'')$ potential is repulsive.

The excited states of the methyl radical are much higher in energy and can safely be ignored in this discussion, while the adiabatic difference between the $X\,^1A_1$ and $a\,^3B_1$ states of NO_2^-, calculated at the UB3LYP/6-311++G(3df,3pd) theory level, is 1.95 eV. This value corresponds to the gap between the two anion curves in the asymptotic limit in Figure 4.4. The adiabatic C–N dissociation energy of NM^- can be calculated using the following thermochemical cycle:

$CH_3NO_2^- \rightarrow CH_3NO_2 + e^-$	$EA(CH_3NO_2) = 0.172$ eV	(Ref. [74])
$CH_3NO_2 \rightarrow CH_3 + NO_2$	BDE = 2.64 eV	(Ref. [104])
$NO_2 + e^- \rightarrow NO_2^-$	$-EA(NO_2) = -2.273$ eV	(Ref. [105])

$$CH_3NO_2^- \rightarrow CH_3 + NO_2^- \qquad \text{BDE} = 0.54 \text{ eV} \qquad (4.4)$$

The resulting BDE($H_3C–NO_2^-$) = 0.54 eV is indicated in Figure 4.4. We also show in Figure 4.4 the potential minimum for neutral NM, which lies 0.172 eV above NM^-,[74] and the repulsive excited state for photodissociation of NM to CH_3 and NO_2, which lies (vertically) beyond the 3.5 eV photon energy used in our experiment. In the fragment limit, UB3LYP/6-311++G(3df,3pd) calculations put $NO_2(X\,^2A_1)$ 2.23 eV above $NO_2^-(X\,^1A_1)$, in good agreement with the 2.273 eV experimental value of adiabatic electron affinity of NO_2.[105]

It follows from the diagram in Figure 4.4 that dissociation to CH_3 and NO_2^- on the repulsive $[NM^-]^*$ surface is possible, provided the fragments separate rapidly beyond the crossing of the neutral and anion potential curves. Since we observe these anionic fragments experimentally and no major autodetachment features are present in the photoelectron spectrum of NM^- at 355 nm,[75] the dissociation must indeed be faster than autodetachment. This is reasonable, because the timescale for autodetachment is generally nanoseconds or longer,[106] whereas dissociation on a repulsive potential should be complete on a shorter timescale.

4.4.4. $CH_3NO_2^-$ \ OH^- + CH_2NO

Formation of OH^- was previously reported in dissociative electron attachment to nitromethane, with a sharp onset near zero electron kinetic energy.[71,77,78] In our experiment, OH^- is formed in low relative intensity in photodissociation of NM^- and $(NM)_2^-$. The corresponding rearrangement process may occur in either the ground or one of the excited electronic states of NM^-. In particular, the $C\,^2A''$ state corresponds to a

C–H σ* ← π* excitation, which may be responsible for the C–H bond cleavage necessary for the formation of OH^- from $CH_3NO_2^-$. Previous theoretical results have also shown a small amount of σ* character on the methyl group in the HOMO of NM^-, suggesting the C–H bonds may be slightly weakened in the anion.[74] Our calculations agree with the earlier studies, and we find the C–H bonds are slightly longer in NM^- compared to NM, a likely indication of a weaker bond.

The possibility of the $CH_3NO_2^- \rightarrow OH^- + CH_2NO$ reaction in the ground electronic state should also be considered. In Figure 4.5, we show the energetics for this reaction, calculated at the B3LYP/6-311++G(3df,3pd) level of theory. We find the reaction leads directly to the $OH^- + CH_2NO$ products, with no stable intermediate structure. The transition state is calculated to be 1.83 eV higher in energy than $CH_3NO_2^-$, well within the energy available due to photon absorption, but much larger than the energies for electron detachment or solvent evaporation. The products energy is about 1.03 eV higher relative to $CH_3NO_2^-$.

4.5. Discussion. Solvation effects.

The solvent evaporation (binding) energies for $(NM)_n^- \rightarrow (NM)_{n-1}^- + NM$, determined in a previous experiment,[79] are listed in Table 4.1. The binding energy of $(NM)_6^- \rightarrow (NM)_5^- + NM$ was not measured, but the values for $n < 6$ show a linear trend versus cluster size and extrapolating the available data to $n = 6$ provides an estimate of the binding energy of approximately 0.26 eV. Combining the sequential solvation energies, the complete solvent evaporation energy from the largest cluster in the present study, $(NM)_6^- \rightarrow 5NM + NM^-$, can be calculated to be approximately 2.3 eV.

Taking into account the 3.5 eV photon energy, there is sufficient energy to completely remove all solvent molecules from the largest cluster anion investigated in this study. Including the additional 0.54 eV for NM^- dissociation (per Eq. 4.4), complete solvent evaporation *and* core dissociation of $(NM)_6^-$ to yield an unsolvated NO_2^- requires about 2.8 eV. Although this is less than the 3.5 eV nm photon energy, no bare NO_2^- fragments are observed from $(NM)_6^-$, or even $(NM)_5^-$. However, these parent clusters do yield $NO_2^-(NM)_k$, $0 < k < n$. The largest parent cluster for which the unsolvated NO_2^- fragments are unambiguously detected is $(NM)_4^-$ (see Figure 4.2).

If we compare the binding energies in Table 4.1 to the dissociation energy of NM^-, we find that NM^- core dissociation is energetically more favorable compared to solvent evaporation for $(NM)_2^-$ and $(NM)_3^-$, assuming the dissociation energy is largely unaffected by solvation. This is consistent with the intense $NO_2^-(NM)_k$ fragments observed for $(NM)_2^-$ and $(NM)_3^-$. The first solvent evaporation for $(NM)_4^-$, however, is slightly lower in energy compared to NM^- core dissociation. Therefore, based on the relative energies alone we might expect a shift towards caged fragments (pure solvent evaporation) for $(NM)_n^-$, $n \geq 4$. At the same time, from a mechanistic point of view, since caging occurs via energy transfer from $[NM^-]^*$ to the solvent system, its probability is expected to increase when the core anion is surrounded by a large number of solvent molecules. This expectation is in agreement with the caging probability trend seen in Figure 4.3(a).

From Figure 4.3(b), we note that more solvent NM molecules are evaporated from the clusters in the caged vs. core-dissociated product channels. This is because the energy available for solvent evaporation in the latter case is reduced by the amount spent

on dissociating the core-anion bond. Although no asymptotic convergence is achieved in Figure 4.3(b) within the cluster size-range studied, the difference in ⟨NM lost⟩ between the caged and core-dissociated products, Δ⟨NM lost⟩, is ~ 1 for n = 5-6. Consulting Table 4.1, Δ⟨NM lost⟩ of ~ 1 corresponds to roughly 0.5 eV in solvent evaporation energy — comparable to the adiabatic C–N BDE of NM^-.

4.6. Conclusion and future directions

We presented the first experimental study of the photodissociation of the $(NM)_n^-$, NM = CH_3NO_2, n = 1–6, cluster anions at 355 nm. Three types of fragmentation processes are observed, giving rise to the $NO_2^-(NM)_k$, OH^-, and $(NM)_k^-$, $k < n$, anionic fragments. The results are consistent with the model of $(NM)_n^-$ clusters involving a monomer-anion NM^- core, as implied by an $NM^-(NM)_{n-1}$ structure. The $NO_2^-(NM)_k$ and OH^- fragments formed from these clusters are described as core-dissociation products. The $(NM)_k^-$ fragments, on the other hand, are attributed to energy transfer from an initially excited $CH_3NO_2^-$ into the solvent network or a core-dissociation—recombination (caging) mechanism. As with other, previously studied cluster families, the fraction of caged photofragments shows an overall increase with increasing cluster size. The low-lying $A\,^2A'$ and/or $B\,^2A'$ electronic states of the core NM^- anion are believed responsible for photoabsorption leading to dissociation to NO_2^- based fragments. The $C\,^2A''$ state of NM^- is likely responsible for the OH^- pathway.

Further study of $(NM)_n^-$ dissociation is necessary to extend the range to larger clusters (n > 6). As with other strongly solvated cluster systems,[43,63,94,96,98] we expect the caging fraction to approach 1 in the limit of large clusters. Similarly, the ⟨NM lost⟩

versus *n* trends (Figure 4.3b) for both caged and core-dissociated channels is expected to plateau in the limit of large *n*. These anticipated results will provide insight into the structural motifs and energetics of the $(NM)_n^-$ clusters, illuminating the transition to "bulk" properties.[13,43,44] Calculations of cluster structures will be helpful in examining the detailed intermolecular interactions controlling fragmentation and photodetachment dynamics.

Table 4.1 Relevant reaction energetics.

Reaction	Energy (eV)	Ref
$(NM)_2^- \rightarrow NM + NM^-$	0.659 ± 0.009	79
$(NM)_3^- \rightarrow NM + (NM)_2^-$	0.556 ± 0.013	79
$(NM)_4^- \rightarrow NM + (NM)_3^-$	0.451 ± 0.022	79
$(NM)_5^- \rightarrow NM + (NM)_4^-$	0.364 ± 0.009	79
$(NM)_6^- \rightarrow NM + (NM)_5^-$	0.26[a]	This work
$NM^- \rightarrow NM + e^-$	0.171 ± 0.006	74
$CH_3NO_2 \rightarrow CH_3 + NO_2$	2.640	104
$NO_2^- \rightarrow NO_2 + e^-$	2.2730 ± 0.0050	105
$CH_3NO_2^- \rightarrow CH_3 + NO_2^-$	0.54[b]	This work

a) Estimated from linear extrapolation of dissociation energies (see text).

b) Per Equation 4.

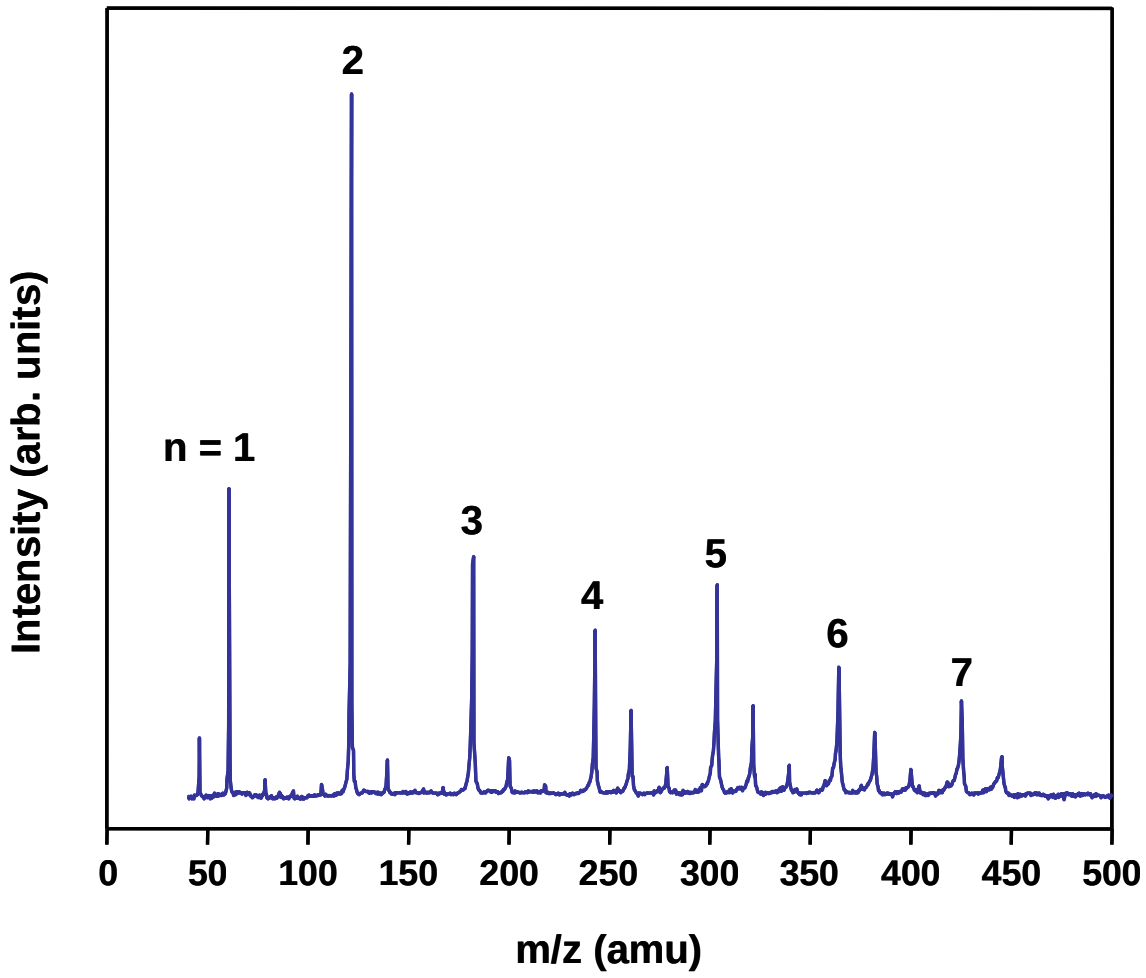

Figure 4.1 Representative time-of-flight mass spectrum of parent ions formed by electron attachment to NM clusters in the ion source. The major $(NM)_n^-$ peaks are labeled. Other peaks correspond to hydrated ions and $NO_2^-(NM)_n$ clusters.

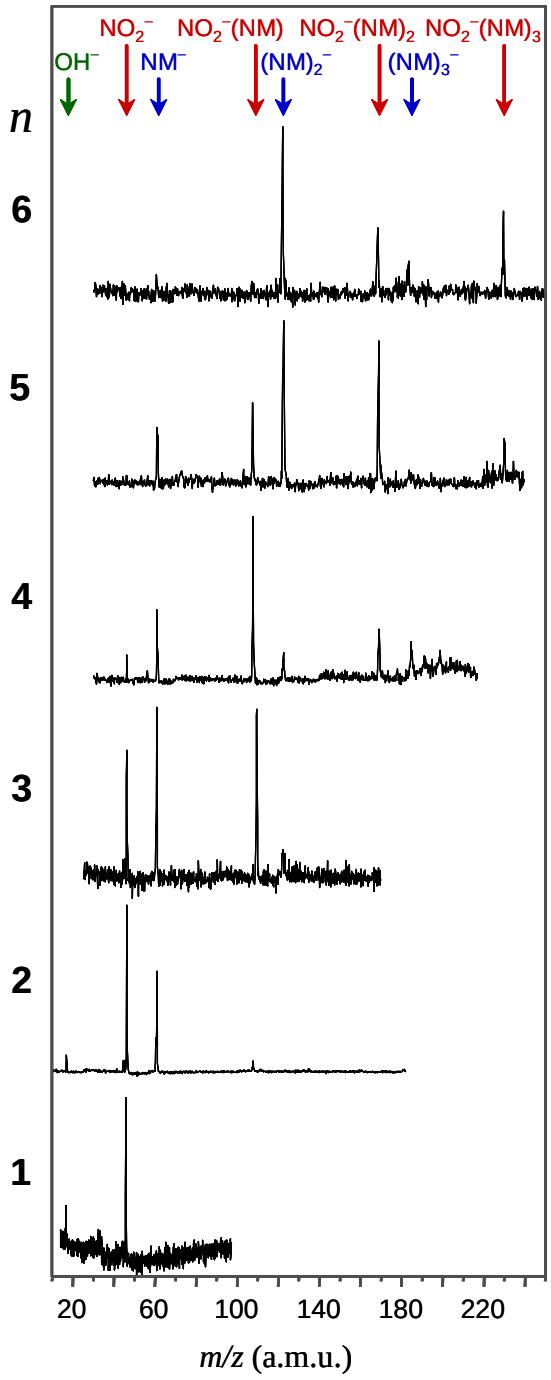

Figure 4.2 355 nm photodissociation mass spectra of $(NM)_n^-$, n = 1 – 6. Peak assignments are indicated along the top of the figure, where the green arrow represents OH^-, red labels are for $NO_2^-(NM)_k$ fragments and blue labels show the $(NM)_k^-$ species.

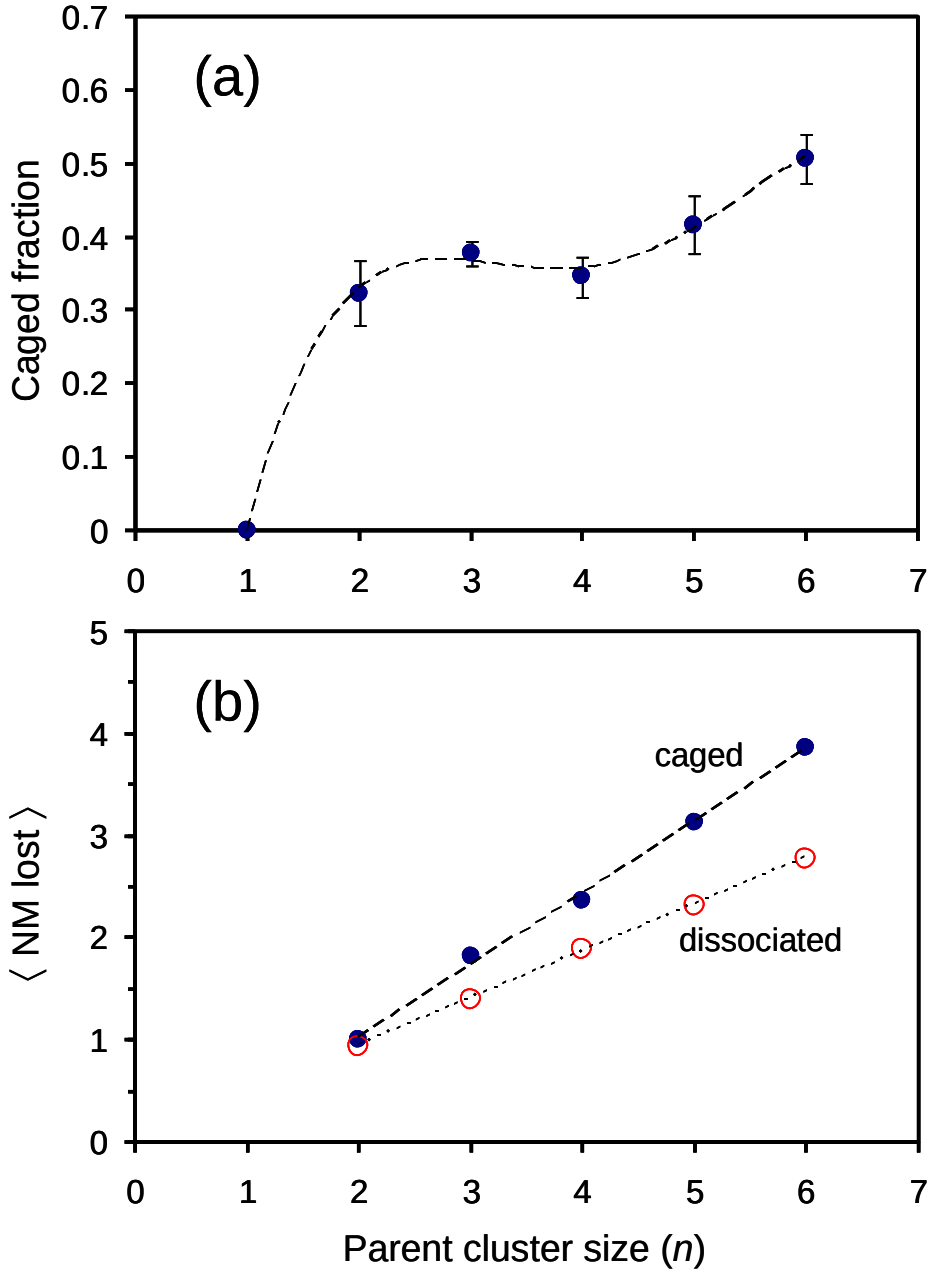

Figure 4.3 Cluster size dependent trends for (a) the fraction of $(NM)_k^-$ (caged) products, and (b) the average number of NM molecules lost within the caged and core-dissociated products (closed and open circles, respectively), as functions of parent cluster size, *n*. The dashed curve in (a) is a polynomial fit to the data intended to guide the eye. The dashed lines in (b) represent linear regressions of the corresponding datasets.

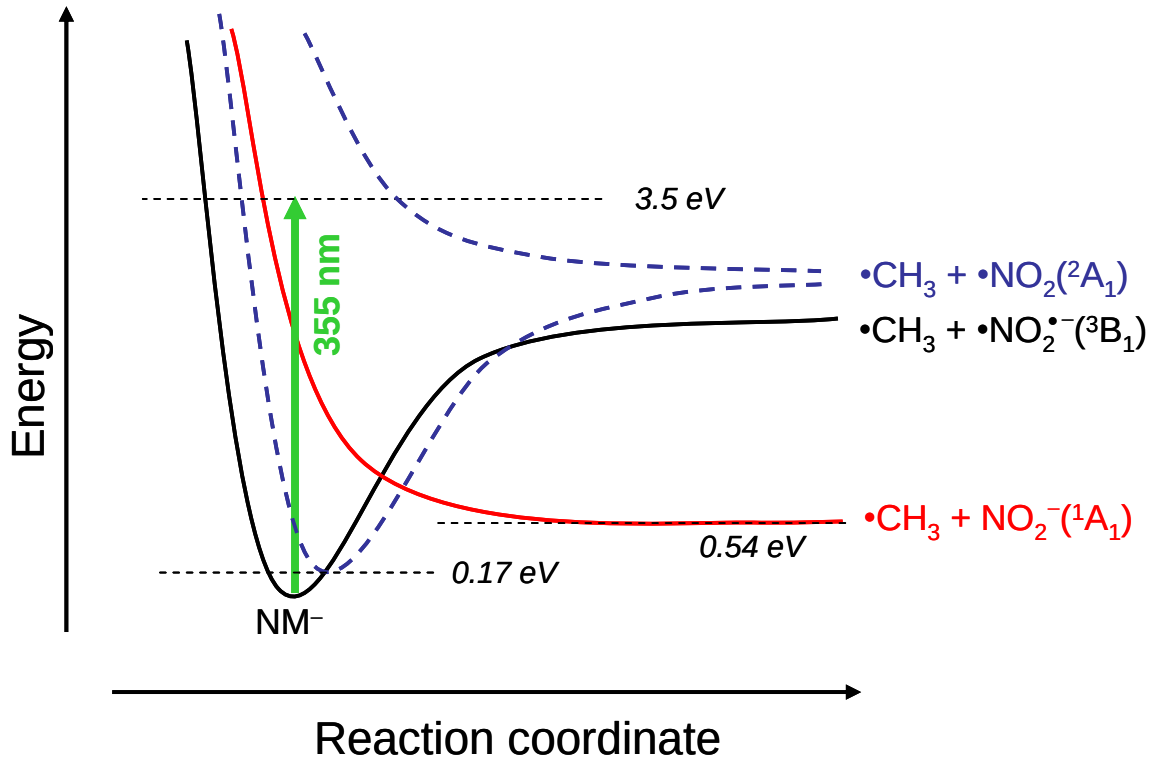

Figure 4.4 Schematic potential energy curves for the dissociation of NM^- into CH_3 and NO_2^-. The energy scale is not linear. Direct dissociation along the C–N bond yields NO_2^- with two unpaired electrons, indicated as $\bullet NO_2^{\bullet -}$, in the $^3B_1$ state (black curve). The ground state of NO_2^-, $^1A_1$, is lower in energy and corresponds to the repulsive dissociation curve shown in red. The ground and dissociative states of neutral NM are indicated by the dashed blue lines.

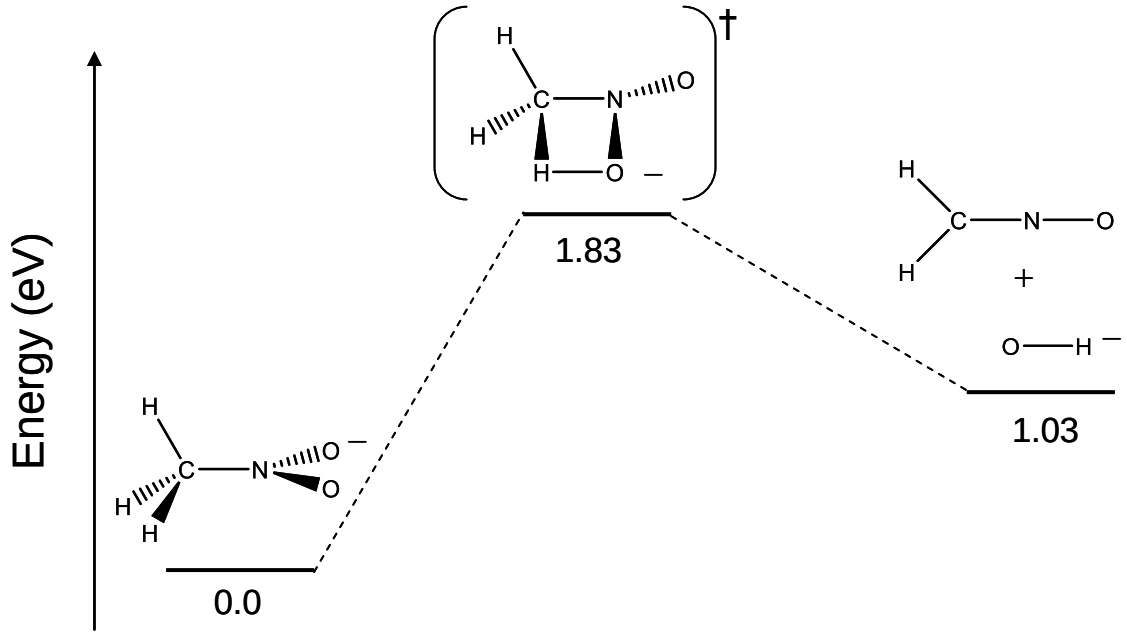

Figure 4.5 Reaction profile for formation of OH^- from $CH_3NO_2^-$, calculated at the B3LYP/6-311++G(3df,3pd) level of theory. The transition state corresponds to formation of a 4-membered intermediate which leads to direct loss of OH^-.

CHAPTER 5

PHOTOELECTRON IMAGING OF CYANOVINYLIDENE AND CYANOACETYLENE ANIONS

5.1. Introduction

Photoelectron spectroscopy of negative ions has been used extensively to study reactive intermediates that shape the composition of our planet and the Universe. A classic example is the chemistry of vinylidene, :C=CH_2, which undergoes a rapid 1,2-Hydrogen atom shift to the more stable acetylene structure, HC≡CH, with only a small (2 ± 1 kcal/mol) potential barrier.[107-113] In contrast to the neutral, the ground state of the $C_2H_2^-$ anion corresponds to the vinylidene geometry, CCH_2^-, while the acetylene anion, $HCCH^-$, is unstable. Thus, photodetachment of $C_2H_2^-$ provides access to the reactive (vinylidene) part of the neutral potential energy surface, where the $CCH_2 \rightarrow$ HCCH rearrangement ensues on a timescale $\leq$ 0.2 ps.[107,108]

In the present work, we use negative-ion photoelectron imaging to examine cyano-substituted vinylidene and acetylene, :C=CHCN and HC≡CCN, respectively. The relative energetics of the two neutral structures are qualitatively similar to those of vinylidene and acetylene, and so one might expect the behavior of cyanovinylidene to be comparable to that of vinylidene. Namely, CCHCN is expected to undergo rearrange-ment to the more stable HCCCN structure, with only a small (2.2 kcal/mol) barrier predicted by calculations.[114] Small rearrangement barriers are also found for other substituted vinylidenes, such as fluoro-, *tert*-butyl-, and vinyl-vinylidenes, which have

been studied by both photoelectron spectroscopy[115-117] and theory.[118,119] Qualitative analysis suggests that the properties of cyanovinylidene should be similar to those of fluorovinylidene, since the CN substituent acts as a pseudo-halogen. On the other hand, the conjugated π system with the CN substituent might also result in similarities to vinyl-vinylidene.

Due to the electron affinity of the CN group, the cyanovinylidene and cyanoacetylene anion structures are affected by the substitution to a greater extent than the corresponding neutrals. In stark contrast to acetylene, the cyanoacetylene anion, $HCCCN^-$, is in fact a stable species.[5,120] The large dipole moment and the unsaturated π system of HCCCN are responsible for the predicted existence of dipole-bound and valence anionic states.[5] These states have attracted attention not only because of their exotic fundamental properties, including the possible coupling between the dipole-bound and valence states of the anion,[5] but also because dissociative electron attachment to cyanoacetylene (involving these states) may play a role in the formation of carbon-rich and CN-containing negative ions in extraterrestrial environments.[120-125] However, until recently[120] $HCCCN^-$ had eluded definitive experimental detection – not only in space, but also in the laboratory. Despite the general interest in reactive intermediates, cyanovinylidene has also not been studied by anion photoelectron spectroscopy.

We demonstrate the simultaneous formation of $CCHCN^-$ and $HCCCN^-$, providing access (via photodetachment) to both the cyanovinylidene and cyanoacetylene sides of the CCHCN → HCCCN rearrangement reaction. The two isomeric forms of the anion are generated via the competing channels of O^- reaction with acrylonitrile, $H_2C{=}CHCN$. The vinylidene form of the anion is formed via the 1,1-H_2^+ abstraction pathway, while the

valence anions of cyanoacetylene are formed via the *cis*- and/or *trans*-1,2-H_2^+ abstraction channel(s).[120]

The cyanovinylidene anion was indicated in a previous study of the reaction of O^- with 2-deuteroacrylonitrile (H_2C=CDCN),[126] but no evidence for the simultaneous formation of the cyanoacetylene anion had been reported. However, $HCCCN^-$ was once proposed in electron attachment to acrylonitrile, but that assignment has also not been confirmed.[127] The key to the formation of the elusive anion of $HCCCN^-$ in the present work is the bent –Ċ=Ċ–C≡ skeleton of the reactant acrylonitrile, contrasting the corresponding linear arrangement in neutral HCCCN.[120] High-level *ab initio* calculations by Sommerfeld and Knecht predicted a roughly w-shaped equilibrium geometry of valence $HCCCN^-$, which is adiabatically stable with respect to electron detachment by only 50 meV.[5] However, the large geometry difference between $HCCCN^-$ and HCCCN results in a sizable vertical detachment energy (VDE) of the anion, VDE = 1.04 eV, as determined by photoelectron spectroscopy.[120] This experimental determination is compared to the theoretical prediction of 1.25 eV.[5]

In this work, we characterize the stable valence anions of cyanovinylidene and cyanoacetylene by means of photoelectron imaging spectroscopy at 532 and 355 nm. The two anion isomers exhibit drastically different photoelectron spectra: a broad, unstructured band with no identifiable origin for $HCCCN^-$ and a resolved vibrational progression assigned to $CCHCN^-$. We examine the energetics of the two anion species revealed by their photoelectron spectra and model the vibrational progression in $CCHCN^-$ using a Franck-Condon simulation based on the parallel-mode approximation and the Duschinsky algorithm.[128]

5.2. Experimental arrangement

The experiments were performed using a pulsed time-of-flight mass spectrometer with a velocity-map imaging detector that has been described previously.[37] Anions were generated by the reaction of O^- with acrylonitrile.[126,129] Acrylonitrile vapor was entrained in neat N_2O carrier gas with a backing pressure of 20 psi and expanded into high vacuum through a pulsed supersonic nozzle (General Valve, Inc., series 99) operating at a 50 Hz repetition rate. The expanding gas was crossed with a 1 keV electron beam, which produced slow secondary electrons by collisions with the neutral gas molecules. Dissociative electron attachment to N_2O generated O^-, which in turn reacted with acrylonitrile via the 1,1- or 1,2-H_2^+ abstraction channels to form the cyanovinylidene and cyanoacetylene anions, respectively.[120]

Thus formed negatively charged ions were extracted into a pulsed time-of-flight mass spectrometer and after acceleration to 3 keV entered a field-free region of the instrument, where the mass-selected *m/z* = 51 ions were irradiated with a linearly polarized output of a Nd:YAG laser (Spectra Physics, Inc., model Lab-50). The laser output was frequency doubled or tripled to produce 532 or 355 nm pulses, with a pulse width of ~8 ns and pulse energies of 30 and 10 mJ, respectively. Static electric fields within a velocity-map[26] imaging[24] assembly projected the photodetached electrons onto a position sensitive detector and the resulting images were captured with a 1 megapixel camera. In all measurements, the laser polarization axis was set parallel to the detector plane. A typical dataset included ~10^5 experimental cycles. The final images reported here are the compositions of three to four such data sets.

The nascent three-dimensional photoelectron distributions, which are cylindrically

symmetric with respect to the laser polarization axis (z), were reconstructed from the photoelectron images using the inverse Abel transformation implemented in the BASEX program.[40] The electron kinetic energy (eKE) scale was calibrated using the known detachment energy of O^-.[42] The photoelectron spectra were obtained by integrating Abel-inverted photoelectron images with respect to the angular coordinate, while integration over a radial range yielded the photoelectron angular distributions (PADs) for the corresponding transitions. The PADs were analyzed to determine the values of the photoelectron anisotropy parameter β, which uniquely describes the angular distribution in a one-photon photodetachment transition.[29,30]

5.3. Electronic structure and Franck-Condon simulations

Electronic structure calculations were carried out at the B3LYP/aug-cc-pVDZ, MP2/aug-cc-pVDZ and CCSD(T)/6-311++G** levels of theory using the Gaussian 03 program package.[130] The geometries for the anion and neutral ground and excited states were optimized with normal mode analysis to confirm the structures corresponded to true potential minima. The energies of the neutral ground and excited states were also calculated at the optimized anion geometry in order to obtain estimates of the vertical detachment energies.

In order to simulate photoelectron spectra from the results of *ab initio* or density-functional theory calculations, we developed a program for calculating Franck-Condon factors of polyatomic molecules, which adopts the general procedure described by Duschinsky.[128] In this approach, the normal modes for the anion are expressed in generalized coordinates $\mathbf{Q'}$, while the coordinates for the neutral are expressed as $\mathbf{Q}$. The two sets of coordinates are related by the Duschinsky rotation matrix $\mathbf{J}$ and a

displacement vector **K**:[128]

$$\mathbf{Q}' = \mathbf{J}\cdot\mathbf{Q} + \mathbf{K} \tag{5.1}$$

We calculate **J** and **K** from normal coordinates and geometries using the methods outlined by Chen and coworkers[131] for converting Gaussian output from Cartesian coordinates to the generalized coordinates in a home-written LabView program. Evaluation of the multi-dimensional overlap integrals is a well-known, but generally complicated problem.[131,132] We simplify it by making the parallel mode approximation, where **J** is set equal to the identity matrix **I**. The Franck-Condon factors then simplify to a set of one-dimensional integrals:[133]

$$\left\langle v_1' v_2' v_3' \ldots v_n' \middle| v_1'' v_2'' v_3'' \ldots v_n'' \right\rangle^2 = \prod_{i=1}^{n} \left\langle v_i' \middle| v_i'' \right\rangle^2 , \tag{5.2}$$

where v_i' and v_i'' are the numbers of excitation quanta in mode *i* of the neutral and anion, respectively. The main advantage of the parallel mode approximation, compared to evaluation of the multi-dimensional overlap integrals, is realized when one considers combination bands. Using the parallel mode approximation, these integrals reduce to products of the one-dimensional overlap integrals.[133] Assuming all vibrations to be harmonic, we evaluate the integrals in Eq. (5.2) numerically for an arbitrary number of vibrational modes *n*.

Since the **J** matrix is approximately unitary, multiplying both sides of Eq. (5.1) by $\mathbf{J}^\mathbf{T}$ yields $\mathbf{J}^\mathbf{T}\mathbf{J} \approx \mathbf{I}$. Similarly, $\mathbf{J}^\mathbf{T}\mathbf{K} = \mathbf{K}'$, where $\mathbf{K}'$ is a set of effective displacement vectors weighted by the magnitude of the diagonal matrix elements J_{ii}. The vibrational modes of the anion and neutral do not necessarily follow the same ordering, and multiple modes of the anion may match a single mode of the neutral (and *vice versa*), leaving the remaining modes unassigned.[133] We manually assign the vibrational modes to maximize

the overlap of the two states, which guarantees the best description within the parallel mode approximation.

The validity of the parallel mode approximation is verified by inspecting the Duschinsky matrix, **J**. The matrix describes the extent of mixing between vibrational modes of the same symmetry between two or more states, where off-diagonal elements indicate the extent to which different states mix.[131,132] If the diagonal elements are all close to 1, the parallel mode approximation is valid, whereas if any diagonal element is significantly less than 1, the full multi-dimensional calculation may be required. In our simulations of the photoelectron spectrum of $CCHCN^-$, the diagonal elements were close to 1, indicating that the parallel mode approximation is reasonable for this system. The approximation's validity is due to the similar equilibrium geometries of the cyanovinylidene anion and the corresponding neutral. The same approximation breaks down in the case of $HCCCN^-$, because of the vastly different equilibrium geometries of the anion and the neutral.

5.4. Experimental results and spectroscopic assignments

The 532 and 355 nm photoelectron images and the corresponding photoelectron spectra for the *m/z* = 51 anions ($CCHCN^-$ and $HCCCN^-$) are shown in Figure 5.1. While the 532 nm data were included in our preliminary report,[120] the 355 nm results are presented here for the first time. Both images show two distinct features. In the 532 nm image, the outer band, A, peaks in the direction parallel to the laser polarization axis, while the inner feature, B, consisting of several well-resolved vibrational bands, peaks in the perpendicular direction. In the 355 nm image, the bands are shifted to higher eKE and, owing to the decrease in absolute energy resolution with increasing eKE, the

vibrational bands comprising feature B are less resolved, compared to the 532 nm image.

The 532 and 355 nm photoelectron spectra are plotted in Figure 5.1 versus electron binding energy (eBE). The two spectra are in excellent agreement. The first three vibrational peaks of band B are assigned labels 0, 1, and 2, appearing in parentheses in the text and Table 5.1. The origin transition, B(0), is centered at eBE = 1.85 eV in the 532 nm spectrum and 1.83 eV in the 355 nm spectrum. The origin of band B is therefore determined to be at eBE = 1.84 ± 0.01 eV. The origin transition corresponds to the most intense peak in the vibrational progression. Its energy, therefore, corresponds to both the adiabatic electron affinity of the neutral and the vertical detachment energy (VDE) of the anion.

The above experimentally determined value agrees with the VDE = 1.85 eV predicted at a high level of theory for the cyanovinylidene anion.[5] We therefore assign band B to the photodetachment of $CCHCN^-$. This assignment is further supported by the Franck-Condon analysis in Sec. 5.3 below. We also note that cyanovinylidene anions were previously observed in the reaction of O^- with acrylonitrile,[126] but the photoelectron spectrum of $CCHCN^-$ is discussed here for the first time.

The broad and structureless band A in Figure 5.1 shows an onset at eBE ≈ 0.5 eV and a maximum at 1.04 ± 0.05 eV. The latter corresponds to the vertical detachment energy of the anion. Since band A is lower in energy relative to band B, it is attributed to a different species. With support from the theoretical predictions in Sec. 5.5, band A is assigned to the cyanoacetylene form of the anion, $HCCCN^-$.[120]

The energetics and the anisotropy parameters determined for the different spectral features are summarized in Table 5.1. At 532 nm, band A ($HCCCN^-$) shows a slightly

parallel PAD with a β value of 0.32, while the vibrational features of band B ($CCHCN^-$) are perpendicular in character, with β values of approximately –0.40. Larger uncertainties are associated with the 355 nm β values due to the poorer signal to noise of the data, but the opposite signs of β for bands A and B are also discerned in the 355 nm results.

5.5. Discussion

5.5.1. Cyanovinylidene and cyanoacetylene structures and energetics

Figure 5.2 shows the geometries of $CCHCN^-$ (bottom left), $HCCCN^-$ (bottom right), the CCHCN singlet (S) and triplet (T) states (middle and top left, respectively), and the ground (singlet) state of HCCCN (middle right). In addition, the transition state (TS) for cyanovinylidene → cyanoacetylene rearrangement is also shown (top right inset). All structures were optimized at the B3LYP/aug-cc-pVDZ level of density-functional theory (DFT). MP2/aug-cc-pVDZ calculations give similar structures. The geometry of cyanovinylidene (S) shown in Figure 5.2 is very similar to the structure determined using a combination of the Brueckner coupled cluster and DFT methods, BCCSD(T)/cc-pVTZ and B3LYP/aug-cc-pVTZ.[125] The cyanoacetylene anion structure is qualitatively similar to that predicted at the CCSD(T)/aug-cc-pVDZ level of theory,[5] although some of the bond angles are not reproduced very well by the DFT.

The relative energies for the different cyanovinylidene and cyanoacetylene structures obtained using various levels of theory are summarized in Table 5.2. Figure 5.3 shows an energy diagram, which is based primarily on the DFT results, supplemented by the relevant experimentally determined values (this work) and the G3(MP2) and

CCSD(T) results of Sommerfeld and Knecht.[5] The diagram is intended as a survey of the relevant structures and energy levels. The deficiencies of the inexpensive DFT calculations should not mask the important qualitative features of the potential energy landscape, as the quantitative details can be adjusted wherever higher-level ab initio results are available.[5,114,125]

All energies in Table 5.2 and Figure 5.3 are in electron-volts relative to the HCCCN (S) ground state. The black and red lines in Figure 5.3 correspond to the neutral and anion structures, respectively. As expected, cyanovinylidene corresponds to a shallow local minimum on the neutral potential energy surface for the 1,2-H atom shift to the more stable cyanoacetylene structure. According to the B3LYP/aug-cc-pVDZ prediction, the transition state (TS) for the CCHCN (S) → HCCCN (S) rearrangement lies only 0.02 eV above the CCHCN minimum. Although the rearrangement barrier is expected to be small, it is evident that its height is underestimated by the DFT calculation, as both MP2 (Table 5.2) and CCSD(T) (Table 5.2 and Ref. [114]) predict barrier heights of about 0.09 eV (2.2 kcal/mol).[114]

On the anion surface, the two isomers are separated by a large potential barrier, corresponding to the anionic transition state (TS^-). The DFT calculations indicate that the cyanoacetylene anion is more stable than the cyanovinylidene anion, contrasting the relative energetics of unsubstituted acetylene and vinylidene. The same calculations predict an adiabatic electron affinity of 0.46 eV for neutral cyanoacetylene and a VDE of 1.40 eV for the corresponding anion. The CCSD(T)/aug-cc-pVDZ calculations have indicated an adiabatic electron affinity of 0.05 eV and a VDE of 1.25 eV.[5] Comparing these results, we are inclined to believe that the DFT exaggerates the stability of

$HCCCN^-$ relative to HCCCN, as well as, probably, relative to $CCHCN^-$. However, the overall features of the energy diagram in Figure 5.3, especially the existence of stable $HCCCN^-$, are not in doubt.[5,120]

The adiabatic electron affinity of HCCCN cannot be determined from the photoelectron spectra of $HCCCN^-$, since the corresponding band in Figure 5.1, band A, shows no identifiable origin. This is due to the large geometry difference between the equilibrium $HCCCN^-$ and HCCCN structures (Figure 5.2). However, the above theoretical values for the anion VDE compare reasonably well with the experimental result of 1.04 ± 0.05 eV, especially considering that the electronic structures of weakly bound anions are notoriously difficult to model theoretically.

The purple dashed lines in Figure 5.3 correspond to the $CCHCN^-$, *trans*-$HCCCN^-$, and *cis*- $HCCCN^-$ anion structures obtained from acrylonitrile via the vertical 1,1-H_2^+, *trans*-1,2-H_2^+, and *cis*-1,2-H_2^+ abstraction processes (so labeled in the Figure), respectively. These structures, referred to as the vertical abstraction geometries, are derived from the equilibrium structure of acrylonitrile with the two indicated hydrogen atoms, plus a charge, removed without changes to other bond lengths or angles (see also Figure 5.1 in Ref. [120]). Unstable with respect to geometry relaxation, the vertical abstraction structures correspond to the sudden limit of anion formation by H_2^+ abstraction from acrylonitrile. Although the sudden approximation is admittedly crude, it provides useful guides for estimating the nascent $CCHCN^-$ and $HCCCN^-$ excitations.

The *trans*-1,2-H_2^+ vertical abstraction geometry of $HCCCN^-$ is rather similar to the equilibrium *trans* structure of $HCCCN^-$. This structural similarity is the key to the formation of the $HCCCN^-$ anion.[120] The vertical *cis*-1,2-H_2^+ abstraction process, on the

other hand, yields the anion in the initial *cis* configuration. The DFT calculations did not locate a local $HCCCN^-$ minimum corresponding to a *cis* geometry. That is, while *cis*-$HCCCN^-$ is vertically stable with respect to electron detachment, we expect it to be unstable with respect to rearrangement to the *trans* form of the anion. Therefore, regardless of the mechanistic details, the 1,2-H_2^+ abstraction reaction should ultimately yield $HCCCN^-$ anions in their equilibrium *trans* configuration.

On the other hand, the nascent energies of $CCHCN^-$ and $HCCCN^-$ formed by vertical 1,1-H_2^+ and 1,2-H_2^+ abstraction from acrylonitrile are estimated to be significantly lower than the barrier separating the cyanovinylidene and cyanoacetylene minimum energy forms of the anion (Figure 5.3). We therefore predict that the $CCHCN^-$ and $HCCCN^-$ products of the O^- + H_2CCHCN reaction do not interconvert into one another.

5.5.2. Analysis of $CCHCN^-$ spectrum

Calculations (summarized in Table 2) predict the adiabatic electron binding energy of the cyanovinylidene anion, $CCHCN^-$, is in the range of 1.65 to 2.06 eV. These predictions are in good agreement with the origin of band B in the photoelectron spectra in Figure 5.1 observed at 1.84 ± 0.01 eV. A comparison with the previously reported spectra of other substituted vinylidenes provides further support for this band's assignment. Table 5.3 gives a summary of the eBEs and photoelectron anisotropy parameters determined for the anions of vinylidene, fluorovinylidene, vinylvinylidene, and cyanovinylidene. Since the cyano group acts as a pseudo-halogen, we might expect the electron affinity of singlet cyanovinylidene (1.84 ± 0.01 eV) to be comparable to that

of the $X\,^1\mathrm{A}'$ state of fluorovinylidene. The latter was determined to be 1.718 eV.[115]

Since no higher-energy bands are observed in the photoelectron spectra in Figure 5.1, the first excited state of cyanovinylidene ($a\,^3\mathrm{A}'$) must lie outside the experiment's energy range. The 3.49 eV energy of 355 nm photons combined with the 1.84 eV electron affinity of the ground singlet state give a 1.65 eV lower bound for the singlet-triplet splitting. The theoretical results summarized in Table 5.2 support this conclusion.

The features of band B in Figure 5.1 support its assignment to the cyanovinylidene anion. The optimized $CCHCN^-$ and CCHCN (S) structures shown in Figure 5.2 are not considerably different. In fact, the optimized geometries of both singlet and triplet cyanovinylidene resemble the corresponding anion structure. The most noticeable change upon anion photodetachment to the singlet occurs in the CCH bond angle, which decreases by 13°. The predicted structural similarity is consistent with the sharp onset of band B and the appearance of a defined vibrational progression. These properties contrast with the broad and unstructured band A, which corresponds to a large geometry change expected in the photodetachment of $HCCCN^-$.

The predicted similarity of the optimized $CCHCN^-$ and CCHCN (S) structures makes this system suitable for Franck-Condon simulations in the parallel-mode approximation. We used this approach, as described in Sec. 5.3, in conjunction with the results of the B3LYP/aug-cc-pVDZ calculations for $CCHCN^-$ and CCHCN (S) to simulate the photoelectron spectrum of the cyanovinylidene anion. The simulated stick spectrum was convoluted with a Gaussian function to reproduce the observed peak widths and shifted to overlap the band origin in the experimental spectrum. The simulated spectrum is shown in Figure 5.4, where it is compared to the 532 nm

experimental spectrum (band B, reproduced from Figure 5.1).

The two spectra are in good overall agreement, confirming the validity of the spectral assignment, although the intensities of the higher-order vibrational peaks are not well reproduced. As the simulated spectrum does not involve any fitting parameters, other than a shift of the transition's origin, an instrumental peak broadening factor and a scaling factor for frequencies, an exact agreement cannot be expected. The discrepancies are most likely due to the use of the parallel mode approximation used instead of calculating the full multi-dimensional overlap integrals. Although the full Franck-Condon treatment would likely result in a better fit, our simulation procedure is adequate for assigning the vibrational progression of band B to the $X\,^1\mathrm{A}'$ state of cyanovinylidene.

The major progression in the simulated spectrum in Figure 5.4 corresponds to the calculated (unscaled) CCH bend frequency of 924 cm^{-1}. By comparing the optimized geometries in Figure 5.2, the CCH bond angle decreases noticeably upon electron detachment from $CCHCN^-$ to the $X\,^1\mathrm{A}'$ state of CCHCN. The average peak spacing in both the 355 and 532 nm spectra in Figure 5.1 is in agreement with the calculated frequency. All vibrational modes were included in the simulation, but only the CCH bend shows appreciable intensity in our spectrum.

The lifetimes of reactive intermediates can be estimated by lineshape analysis. In the previous studies of vinylidenes,[108,115,117] this is done by first modeling the lineshapes corresponding to the triplet state to determine the rotational temperature of the ions and then using the result to simulate the rotational profile for the singlet state. The remaining peak width, unaccounted for by the rotational contribution, is attributed to lifetime broadening. In the present experiment, the triplet state is not observed and the rotational

temperature of the ions is not known. If we assume that the full width at half-maximum of the B(0) peak in the 532 nm photoelectron spectrum in Figure 5.1 (~45 meV) is due to lifetime broadening, the lower limit for the lifetime of cyanovinylidene is estimated to be ~30 fs.

This limit is consistent with the previous studies of vinylidene, which found lifetimes of 20 – 200 fs.[108] However, it does not take into account the instrumental response and the rotational envelope of the transitions. In the studies of other ions with similar energetics under similar experimental conditions, we found linewidths of about 20–25 meV. As a very crude estimate, it can be assumed that a similar lineshape accounts for the instrumental and rotational profiles of the $CCHCN^-$ transitions. The effect of lifetime broadening can then be estimated by deconvoluting a 25 meV wide lineshape function from a 45 meV wide envelope of the B(0) transition. Using Gaussian lineshape functions, this procedure yields a lifetime broadening of 35–40 meV, corresponding to a ~35 fs lifetime – only slightly increased compared to the initial estimate. We caution, however, that the rotational constants and temperatures can differ significantly for different ions, so this estimate is still only a lower limit for the lifetime of cyanovinylidene.

5.5.3. Photoelectron angular distributions

The photoelectron angular distributions may serve as additional indicators of the nature of the initial anion and final neutral electronic states. The PADs reflect the symmetry of the parent orbitals from which the electrons are ejected. Both $CCHCN^-$ and $HCCCN^-$ have planar equilibrium geometries, corresponding to the C_s symmetry point

group and in both cases the highest-occupied molecular orbitals (HOMO) transform under the a′ irreducible representation. In general, parallel PADs are usually expected in the photodetachment from totally symmetric orbitals. Among the C_s point group examples, in the previous study of vinoxide detachment from the a′ orbitals yielded parallel PADs ($\beta > 0$), while detachment from the a″ orbitals yielded perpendicular distributions ($\beta < 0$).[134] The same trend was recently demonstrated for the nitromethane anion.[75]

In the present work, the positive β values observed for band A (Table 5.1) are consistent with the above arguments, considering the a′ symmetry HOMO of $HCCCN^-$. However, the PADs for band B ($CCHCN^-$) are predominantly perpendicular in character ($\beta < 0$), even though the band is also assigned to electron detachment from the a′ symmetry HOMO. The apparent discrepancy is due to the low symmetry of the C_s point group, where two of the three orthogonal coordinate vectors transform as the non-degenerate representation a′. The limitation of the symmetry-based approach can be heightened to the extreme, if one considers an asymmetric molecule (C_1 point group), in which *all* orbitals transform under the same, nominally "totally symmetric" representation. Photodetachment transitions in such anions may still produce PADs of different characters and perpendicular ($\beta < 0$) transitions are not forbidden by any means, while the symmetry analysis becomes trivial and obsolete in such a case. Hence, the strict symmetry-based PAD analysis, proven to be quite powerful for C_{2v} and higher-symmetry species,[15,32,33] is less useful in systems of reduced symmetry. Even though its utility has been demonstrated in some C_s symmetry cases,[75,134] the present contradictory examples of $CCHCN^-$ and $HCCCN^-$ emphasize the need for other approaches.

The perpendicular PADs observed for $CCHCN^-$ (band B, Table 5.1) are not surprising, if we compare the reported β values with those obtained for other vinylidenes. Table 5.3 lists the anisotropy parameters reported for the photodetachment of the vinylidene,[108] fluorovinylidene,[115] and vinylvinylidene[116] anions, in comparison to cyanovinylidene. In all available cases, photodetachment to the ground neutral state displays perpendicular PADs ($\beta < 0$). Both fluorovinylidene and vinylvinylidene have C_s symmetry structures with a′ symmetry HOMOs, consistent with the present case of cyanovinylidene. Vinylidene anion has C_{2v} symmetry, and the lowest photodetachment transition originates from a b_2 orbital. Group symmetry analysis for the C_{2v} point group correctly predicts the perpendicular nature of the PAD in this case.[32]

Finally, for *all* vinylidene anions in Table 5.3, the HOMOs are qualitatively described as carbon π^*2p orbitals in the plane of the molecule, which are similar in character to the π_g^* (d_{xy}-like) HOMO of O_2^-. The photodetachment of superoxide is known to yield predominantly perpendicular angular distributions,[19,57,135] lending additional support for the interpretation of the present cyanovinylidene results.

5.6. Conclusions

The cyanoacetylene and cyanovinylidene anions are generated simultaneously via the competing 1,1-H_2^+ and 1,2-H_2^+ abstraction channels of O^- reaction with acrylonitrile. Via photodetachment, the two isomeric forms of the anion, separated by a large (~2 eV) potential energy barrier, provide access to both the reactant and the product sides of the neutral cyanovinylidene → cyanoacetylene rearrangement reaction.

Using photoelectron imaging spectroscopy at 532 and 355 nm, the adiabatic electron affinity of cyanovinylidene ($X\,^1A'$) is determined to be 1.84 ± 0.01 eV, while the

first excited state ($a\,^3\mathrm{A}'$) lies at least 1.65 eV higher. Using electronic structure calculations, the equilibrium geometry of $CCHCN^-$ is predicted to be rather similar to that of neutral cyanovinylidene. The major vibrational progression in the $X\,^1\mathrm{A}' \leftarrow X\,^2\mathrm{A}'$ photoelectron spectrum of $CCHCN^-$ is attributed to the excitation of the CCH bending mode. The spectral features are reproduced reasonably well using a Franck-Condon simulation under the parallel-mode approximation, while a crude lineshape analysis gives a lower bound for the cyanovinylidene rearrangement lifetime of ~30–35 fs.

In contrast to unsubstituted acetylene, cyanoacetylene has a stable anionic state. The valence $HCCCN^-$ structure,[5] which had until recently eluded experimental detection,[120] is adiabatically weakly bound with respect to electron detachment,[5] but has an experimentally determined vertical detachment energy of 1.04 ± 0.05 eV.

Table 5.1 Photoelectron band energies and anisotropy parameter (β) values determined from the $CCHCN^-$/$HCCCN^-$ photoelectron images shown in Figure 5.1. The anisotropies are average values, uncertainties are standard deviations.

Band	Wavelength (nm)	eBE (eV)	eKE (eV)	β
A	532	1.04	1.29	0.32 ± 0.04
	355	1.04	2.45	0.06 ± 0.04
B(0)	532	1.85	0.48	-0.40 ± 0.04
	355	1.83	1.66	-0.47 ± 0.15
B(1)	532	1.97	0.36	-0.42 ± 0.04
	355	1.94	1.55	-0.30 ± 0.20
B(2)	532	2.06	0.27	-0.32 ± 0.08
	355	2.03	1.46	-0.10 ± 0.13

Table 5.2 Calculated energies (in eV) of various cyanovinylidene and cyanoacetylene neutral and anion structures determined at different levels of theory. The corresponding structures are shown in Figure 5.2, with the exception of HCCCN (T) and TS^-.

Structure	Electronic State	B3LYP aug-cc-pVDZ	MP2 aug-cc-pVDZ	CCSD(T) 6-311++G**	CCSD(T) aug-cc-pVDZ
$CCHCN^-$	$^2A'$	–0.04	0.72	0.46	n/a
CCHCN (S)	$^1A'$	2.03	2.37	2.15	n/a
CCHCN (T)	$^3A'$	3.90	4.78	3.90	n/a
TS	$^1A'$	2.05	2.28	2.23	n/a
HCCCN (S)	$^1\Sigma_g$	**0.00**	**0.00**	**0.00**	**0.00**
HCCCN (T)	$^3A''$	3.60	n/a	n/a	n/a
$HCCCN^-$	$^2A'$	–0.46	0.22	n/a	–0.05
TS^-	$^2A'$	2.08	n/a	n/a	n/a
Source		this work	this work	this work	Ref. [5]

Table 5.3 Electron binding energies and photoelectron anisotropies observed in the photodetachment of the vinylidene, fluorovinylidene, vinylvinylidene, and cyanovinylidene anions.

Neutral Molecule Electronic State	Wavelength (nm)	Electron Binding Energy (eV)	Anisotropy Parameter, β	Source
H_2CC				
X^1A_1	351.1	0.490	-0.51	
a^3B_2	351.1	2.555	+1.45	Ref. [108]
b^3A_2	351.1	3.244	-0.5	
HFCC				
X^1A'	351.1	1.718	n/a	Ref. [115]
b^3A'	351.1	3.076	+1.1	
C_4H_4				
X^1A'	351.1	0.914	-0.10	Ref. [116]
a^3A'	351.1	3.038	+0.95	
CCHCN				
X^1A'	355	1.83	-0.399	This work

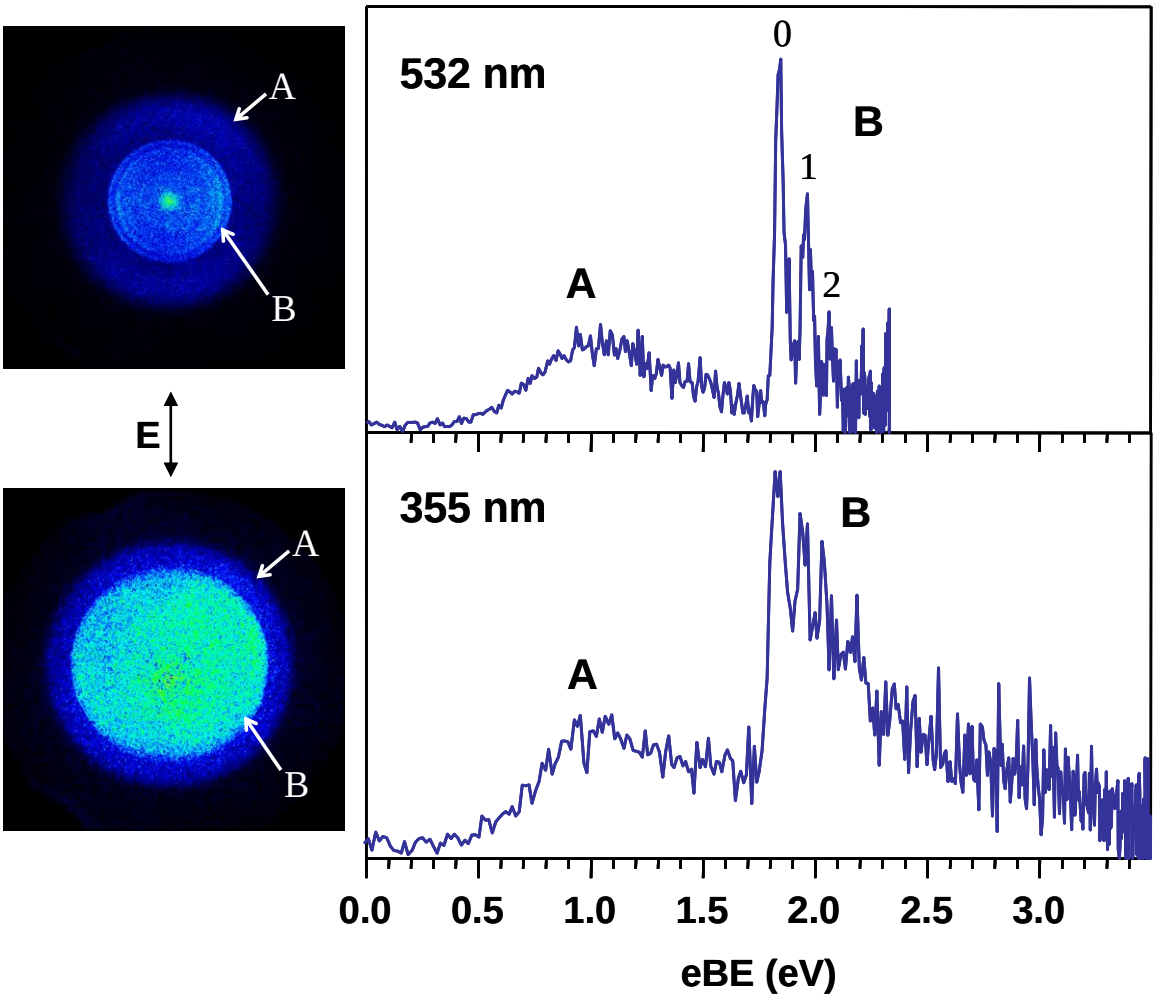

Figure 5.1 Photoelectron images and spectra of $HCCCN^-$ and $CCHCN^-$ obtained at 532 and 355 nm. The laser polarization axis is vertical in the plane of the images. Bands A and B (the vibrational transitions of band B are labeled 0, 1 and 2) are assigned to the photodetachment of $HCCCN^-$ and $CCHCN^-$, respectively. The spectral peak energies and photoelectron anisotropy parameters are summarized in Table 5.1

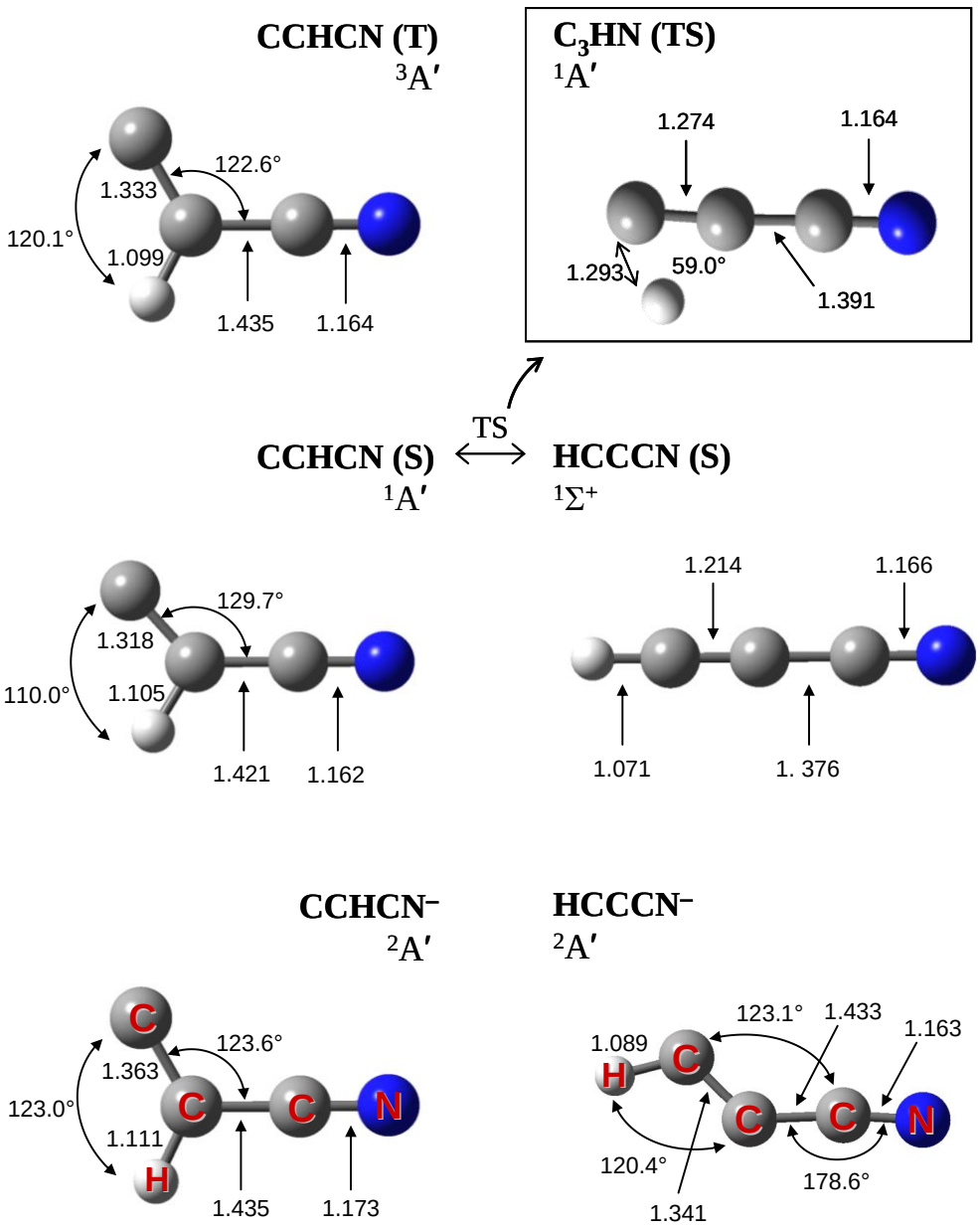

Figure 5.2 Optimized structures of $CCHCN^-$ and $HCCCN^-$, CCHCN and HCCCN ground state singlets (S), and the excited state triplet (T) of CCHCN. The inset in the top right shows the predicted geometry of the transition state (TS) on the singlet potential energy surface for the cyanovinylidene → cyanoacetylene rearrangement. All structures shown are from the B3LYP/aug-cc-pVDZ calculations. The bond lengths are indicated in Angstroms. The corresponding state energies are summarized in Table 5.2.

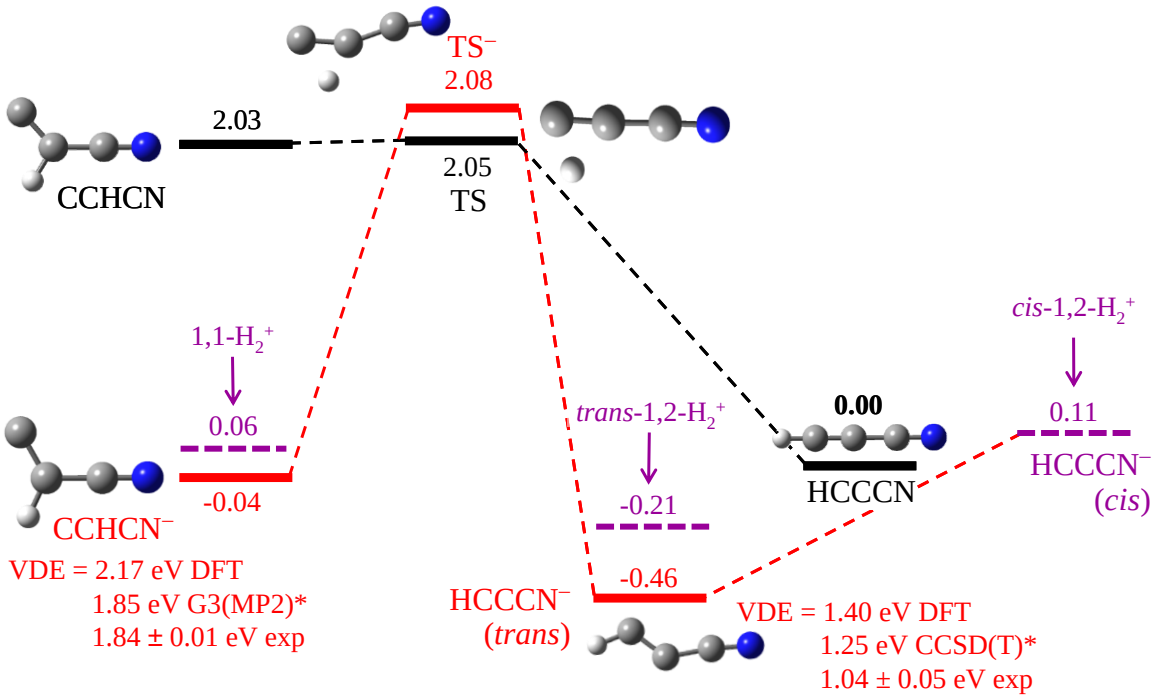

Figure 5.3 A schematic diagram (not to scale) showing the relative energies of different cyanovinylidene and cyanoacetylene anion and neutral structures. Geometric details of most structures are found in Figure 5.2. The diagram is based on the results of the B3LYP/aug-cc-pVDZ calculations, supplemented by the relevant experimentally determined values (marked "exp") and the G3(MP2) and CCSD(T)/aug-cc-pVDZ results from Ref. [5] (marked with asterisks). The energies are indicated in electron-volts, relative to the ground state of HCCCN. The black and red lines correspond to the neutral and anion structures, respectively. The purple dashed lines correspond to the $CCHCN^-$, *trans*-$HCCCN^-$, and *cis*-$HCCCN^-$ anion structures obtained from acrylonitrile via the vertical (sudden) 1,1-H_2^+, *trans*-1,2-H_2^+, and *cis*-1,2-H_2^+ abstraction processes, respectively.

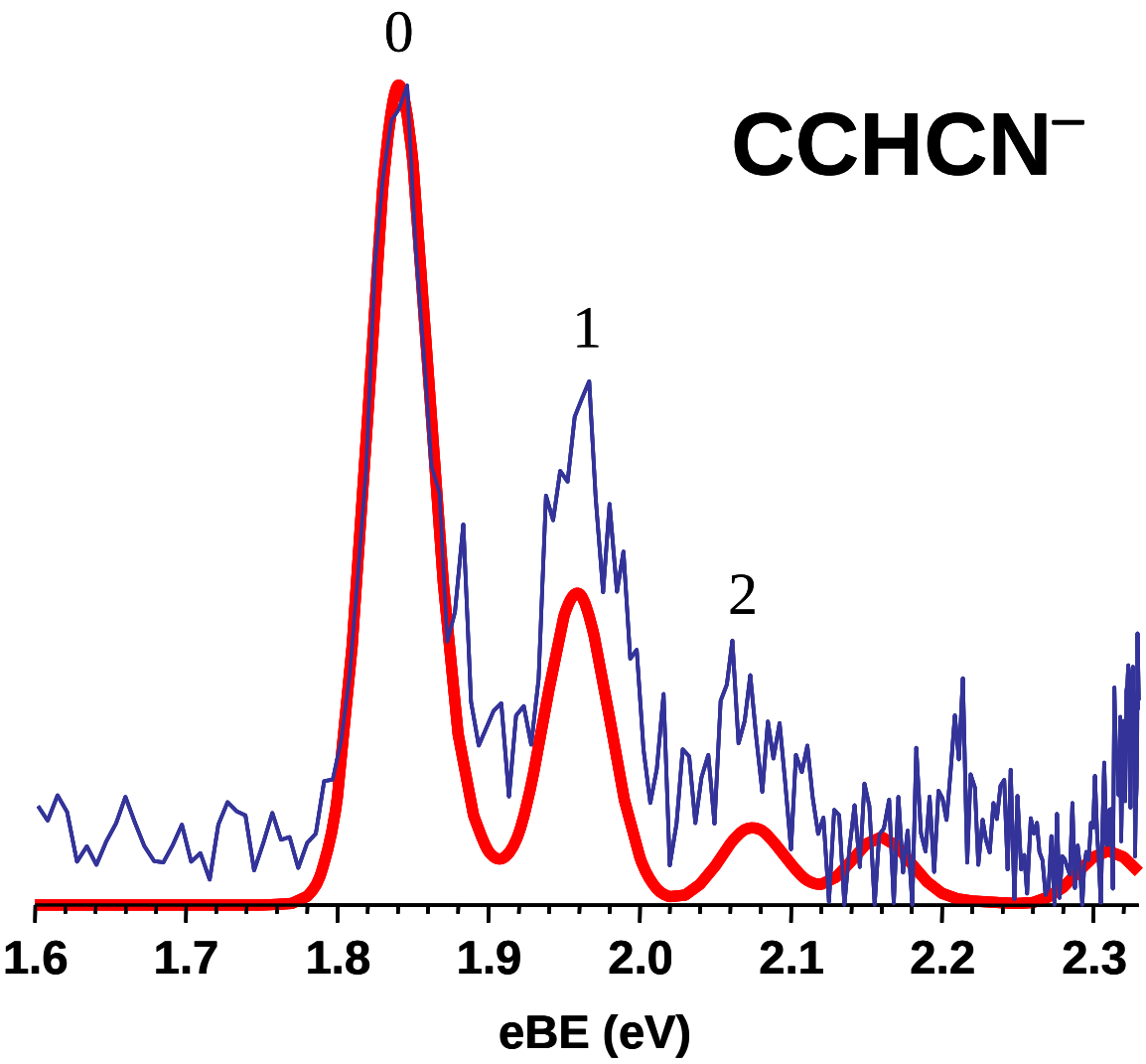

Figure 5.4 Bold red line: simulated photoelectron spectrum of $CCHCN^-$. Thin blue line: the corresponding experimental spectrum (band B at 532 nm, reproduced from Figure 5.1). The simulated spectrum was calculated using the B3LYP/aug-cc-pVDZ molecular parameters for $CCHCN^-$ and CCHCN (S). The initial stick spectrum, calculated using the parallel mode approximation, as described in the text, was shifted to match the experimental band origin and convoluted with a Gaussian function to reproduce the experimental spectrum shown in the figure.

CHAPTER 6

THE C-H BOND DISSOCIATION ENERGY OF MALONONITRILE

6.1. Introduction

The CN group is often regarded as a pseudohalogen due to its large electronegativity. However, halogens are π donors, while the CN group is not, and acts more like an aryl group in an extended π system. This critical difference between the CN group and halogens is revealed in the C-H bond energies of substituted methanes.[136]

In this letter we report the gas-phase C-H bond dissociation energy of malononitrile, $CH_2(CN)_2$, determined from the electron affinity of the corresponding dicyanomethyl radical, $^{\bullet}CH(CN)_2$. The results are discussed in comparison with the properties of methane (CH_4), acetonitrile (CH_3CN), and cyanoform [$CH(CN)_3$]. This CN-substituted series is in turn compared to halogenated methanes, such as CH_nF_m ($n + m = 4$). We find a clear contrast in how the C-H bond energies are affected by the π donating halogens with the resonance stabilization offered by the CN group.

6.2. Experimental methods

The electron affinities of $\bullet CH(CN)_2$ and $\bullet CH_2CN$ were measured using a previously described negative ion[35] velocity map[26] photoelectron imaging[24] spectrometer.[37] The $CH(CN)_2^-$ and CH_2CN^- ions were generated by the proton-abstraction reaction of O^- with malononitrile or acetonitrile, respectively. Mass-selected anions were photodetached using the third (355nm) or second (532 nm) harmonic of a Nd:YAG (yttrium aluminum garnet) laser with pulse energies of 10-20 mJ and an 8 ns

pulse width. Photoelectron images were analyzed following published procedures.[40] The photoelectron spectra were calibrated using the known electron affinity of O^-.[41]

6.3. Results and discussions

The 355 nm photoelectron image and the corresponding spectrum obtained for $CH(CN)_2^-$ are shown in Figure 6.1(a). For comparison, the photoelectron image and the corresponding spectrum of CH_2CN^-, measured at 532 nm, are displayed in Figure 6.1(b). In both cases, the photoelectron angular distributions peak in the direction perpendicular to the laser polarization axis, characteristic of detachment from carbon 2*p* type orbitals.[15,33]

In the $CH(CN)_2^-$ case, we observe a single, remarkably narrow band at an electron binding energy eBE = 2.88 ± 0.01 eV, which corresponds to electron affinity (EA) of $^{\bullet}CH(CN)_2$. Calculations[90] at the B3LYP/aug-cc-pVDZ level of theory predict an EA of 2.92 eV, in good agreement with the experimental value.

The CH_2CN^- spectrum shows a short vibrational progression with a sharp origin, corresponding to an electron affinity of 1.53 ± 0.01 eV. This spectrum is in good agreement with a previous study of CH_2CN^-, which yielded an EA of 1.543 ± 0.014.[137] The most intense spectral peak in Figure 6.1(b) is the transition origin, while all other bands (spaced by ~ 700 cm^{-1}) correspond to the excitation of the umbrella mode of $^{\bullet}CH_2CN$.[137] Our B3LYP/6-311++G(3df,3pd) calculations[90] on $^{\bullet}CH_2CN$ predict an umbrella mode frequency of 684 cm^{-1} and electron affinity of 1.57 eV, in good agreement with the experimental data.

The comparison of the $CH(CN)_2^-$ and CH_2CN^- photoelectron spectra in Figure 6.1 highlights the absence of a discernable vibrational progression in the $CH(CN)_2^-$ case.

This observation suggests that the $CH(CN)_2^-$ anion and the $^{\bullet}CH(CN)_2$ neutral must have very similar geometries. To support this conclusion, we optimized the geometries of $CH(CN)_2^-$ and $^{\bullet}CH(CN)_2$ at the B3LYP/aug-cc-pVDZ level of theory.[90] The resulting structures are shown in Figure 6.2. Both $CH(CN)_2^-$ and $^{\bullet}CH(CN)_2$ are predicted to have planar structures of C_{2v} symmetry, with a $^1A_1$ electronic state for the anion and a $^2B_1$ ground state for the neutral radical. The anion and neutral structures are indeed essentially identical at this level of theory, with the most noticeable difference being in the CCC bond angle, which is predicted to decrease by 1.2° upon electron detachment.

In contrast, CH_2CN^- is known to be non-planar (C_s symmetry), while the corresponding neutral radical has a planar structure.[137] This geometry difference is responsible for the vibrational progression in the photoelectron spectrum of CH_2CN^- seen in Figure 6.1(b). The striking difference between the planar geometry of $CH(CN)_2^-$ and the non-planar structure of CH_2CN^- is attributed to decreased electron density on the central carbon atom in the presence of two CN groups. The Mulliken analysis of $CH(CN)_2^-$ in Figure 6.2 indicates a large positive charge on the central carbon, which favors a planar geometry. A similar calculation for CH_2CN^- shows a negative Mulliken charge (–0.536) on the central carbon. To put the relationship between geometry and charges in perspective, the carbon in CH_3^+ is positively charged and the ion is planar, while in CH_3^- the carbon is negatively charged and the anion is non-planar. While these arguments are not new,[138] this subtle result highlights inductive effects typically associated with the pseudohalogen (electronegative) nature of the CN group, which is electron withdrawing in the σ system.

The experimental electron affinity of $^{\bullet}CH(CN)_2$ allows us to calculate the C-H bond

enthalpy (DH_{298}) of malononitrile using the general acidity/electron affinity cycle:[139]

$$DH_{298}(R\text{-}H) = \Delta_{acid}H_{298}(RH) + EA(R^{\bullet}) - IE(H^{\bullet}) + [\text{thermal correction}], \qquad (6.1)$$

In this equation, $\Delta_{acid}H_{298}(RH)$ is the gas-phase acidity of a closed-shell molecule, $EA(R^{\bullet})$ is the electron affinity of the corresponding radical, and $IE(H^{\bullet})$ = 313.6 kcal/mol is the ionization energy of atomic hydrogen.[140] The small thermal correction, is a set of heat capacity integrals from 0 to 298 K corresponding to RH, R^-, H and H^+. This correction is generally smaller than 0.3 kcal/mol and is hence absorbed by larger experimental uncertainties.[141] Neglecting the [thermal correction] term in Eq. (6.1) and using the known acidity of malononitrile, $\Delta_{acid}H_{298}[CH_2(CN)_2]$ = 335.8 ± 2.1 kcal/mol,[142] and the experimental EA of dicyanomethyl radical, $EA[^{\bullet}CH(CN)_2]$ = 2.88 ± 0.01 eV, we find the C-H bond dissociation energy of malononitrile $DH_{298}[H\text{-}CH(CN)_2]$ = 88.7 ± 2.1 kcal/mol. Similar calculation for acetonitrile, with $\Delta_{acid}H_{298}(CH_3CN)$ = 372.9 ± 2.1 kcal/mol (from Ref. [143]) and $EA(^{\bullet}CH_2CN)$ = 1.53 ± 0.01 eV (as determined here), gives $DH_{298}(H\text{-}CH_2CN)$ = 94.6 ± 2.1 kcal/mol. This result is within the uncertainty of the previously reported value, 94.2 ± 2.0 kcal/mol.[137]

Thus determined bond dissociation energy of malononitrile, 88.7 ± 2.1 kcal/mol, is small compared to typical C-H bond energies of neutral closed-shell organic molecules. In general, bond energies reflect the stability of the corresponding radicals: smaller DH_{298} values translate into greater radical stability. As a reference, the bond dissociation energy of methane, $DH_{298}(H\text{-}CH_3)$ = 104.9 ± 0.4 kcal/mol,[139] is significantly larger than the corresponding values for acetonitrile and malononitrile. In the methyl radical, the unpaired electron is localized on the carbon atom and receives no additional stabilization. For comparison, the bond energies of molecules producing "stable" radicals, such as

toluene, $DH_{298}(H\text{-}CH_2C_6H_5)$ = 89.8 ± 0.6 kcal/mol, and propene, $DH_{982}(H\text{-}CH_2CHCH_2)$ = 88.8 ± 0.4 kcal/mol are similar to those of acetonitrile and malononitrile.[139] The lower $DH_{298}(H\text{-}CH_2CN)$ of acetonitrile reflects stabilization of the unpaired electron in the cyanomethyl radical through π resonance with the CN group. In dicyanomethyl radical, the additional CN group further stabilizes the unpaired electron via increased resonance interaction, resulting in the even lower C-H bond dissociation energy of the parent molecule, malononitrile.

Although the CN group is often regarded as a pseudohalogen, radical stabilization in $^{\bullet}CH_2CN$ and $^{\bullet}CH(CN)_2$ is not due to electron withdrawing properties of CN shared with atomic halogens, but is manifested in the π system. Therefore, similar halogenated methanes are *not* resonance stabilized, as halogens are π-donors. For the case of $H\text{-}CH_nF_m$ (n+m = 3), we find $DH_{298}(H\text{-}CH_2F)$ = 103.2 ± 1.0 kcal/mol, $DH_{298}(H\text{-}CHF_2)$ = 106.4 ± 0.7 kcal/mol and $DH_{298}(H\text{-}CF_3)$ = 106.7 ± 1.0 kcal/mol, thus the bond energies *increase* with sequential halogen substution.[144,145]

While the DH_{298} difference between CH_4 and CH_3CN is about 16 kcal/mol, the difference between CH_3CN and $CH_2(CN)_2$ is about 6 kcal/mol, indicating a moderate increase in resonance stabilization with the addition of the second CN group. Based on this trend, we hypothesize that cyanoform, $CH(CN)_3$, should have an even smaller C-H bond dissociation energy, because of additional resonance stabilization in the resulting radical, $^{\bullet}C(CN)_3$. While difficult to isolate,[146,147] $CH(CN)_3$ may have one of the weakest C-H bonds for a closed-shell neutral organic molecule.

Finally, we calculate the heats of formation of the $^{\bullet}CH_2CN$ and $^{\bullet}CH(CN)_2$ radicals:[139]

$$\Delta_f H_{298}(R^{\bullet}) = DH_{298}(RH) + \Delta_f H_{298}(RH) - \Delta_f H_{298}(H^{\bullet}). \quad (6.2)$$

Using $\Delta_f H_{298}(H^{\bullet})$ = 52.103 ± 0.003 kcal/mol,[148] $\Delta_f H_{298}[CH_2(CN)_2]$ = 63.64 ± 0.24 kcal/mol,[149] and the C-H bond dissociation energy of malononitrile determined here, we find $\Delta_f H_{298}[^{\bullet}CH(CN)_2]$ = 100.2 ± 2.1 kcal/mol. For comparison, using $\Delta_f H_{298}(CH_3CN)$ = 17.70 ± 0.09 kcal/mol [150] and our value of $DH_{298}(H\text{-}CH_2CN)$, find $\Delta_f H_{298}(^{\bullet}CH_2CN)$ = 59.8 ± 2.0 kcal/mol, in good agreement with the previous studies, which yielded 59.7 ± 2.0 kcal/mol [137] and 58.5 ± 2.2 kcal/mol.[151]

6.4. Conclusions

In summary, the electron affinity of dicyanomethyl radical, EA = 2.88 ± 0.01 eV, was measured by photoelectron imaging of the $CH(CN)_2^-$ anion. This result was used to obtain the C-H bond dissociation energy of malononitrile, $DH_{298}[H\text{-}CH(CN)_2]$ = 88.7 ± 2.1 kcal/mol, and the heat of formation of the resulting radical, $\Delta_f H_{298}[^{\bullet}CH(CN)_2]$ = 100.2 ± 2. kcal/mol. The C-H bond dissociation energy of malononitrile is smaller than that of most closed-shell neutral organic molecules, including methane and acetonitrile. The bond weakness is attributed to resonance stabilization of the unpaired electron in $^{\bullet}CH(CN)_2$.

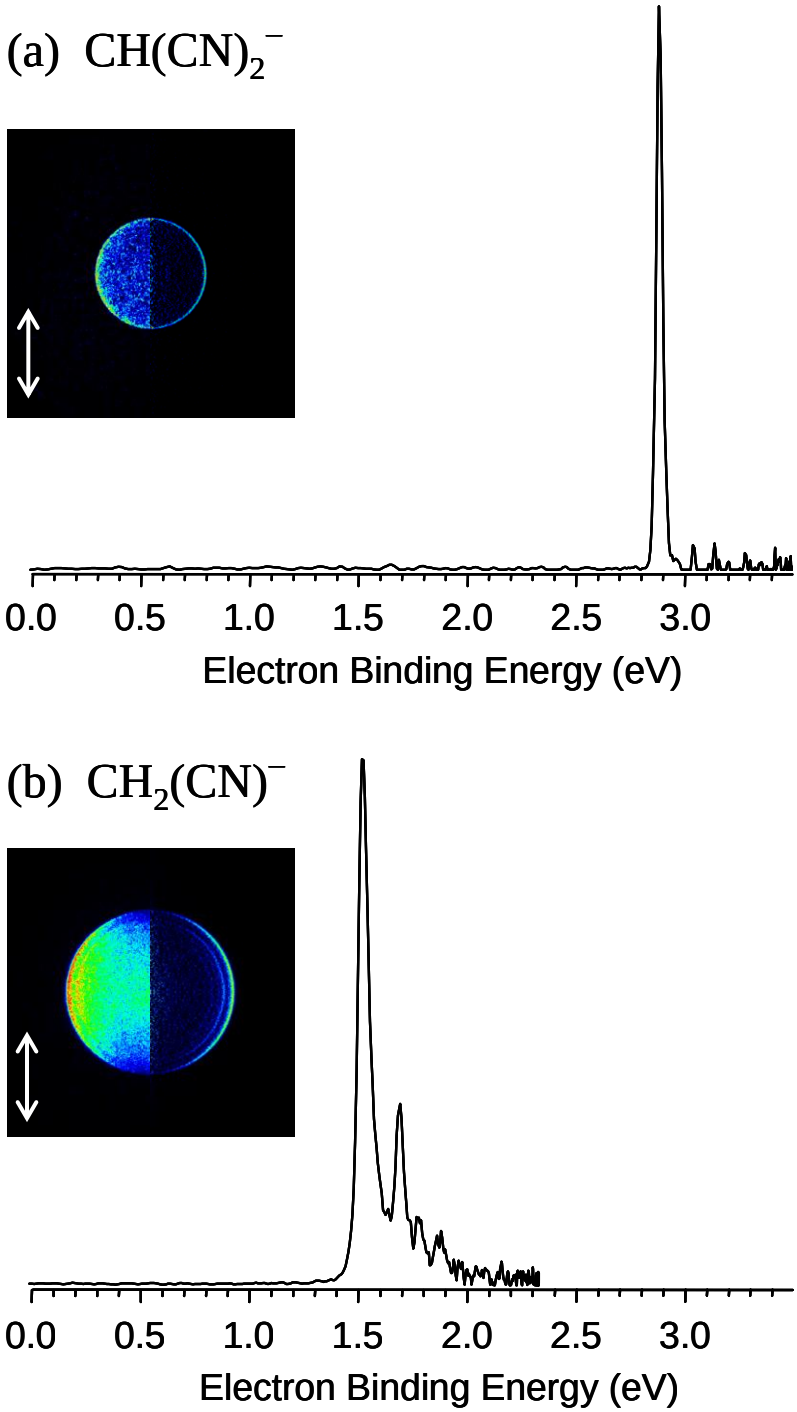

Figure 6.1 Photoelectron images and corresponding spectra of (a) $CH(CN)_2^-$, measured at 355 nm, and (b) CH_2CN^-, measured at 532 nm. The composite images show the raw (left side) and reconstructed data (right). The double arrows indicate the laser polarization direction.

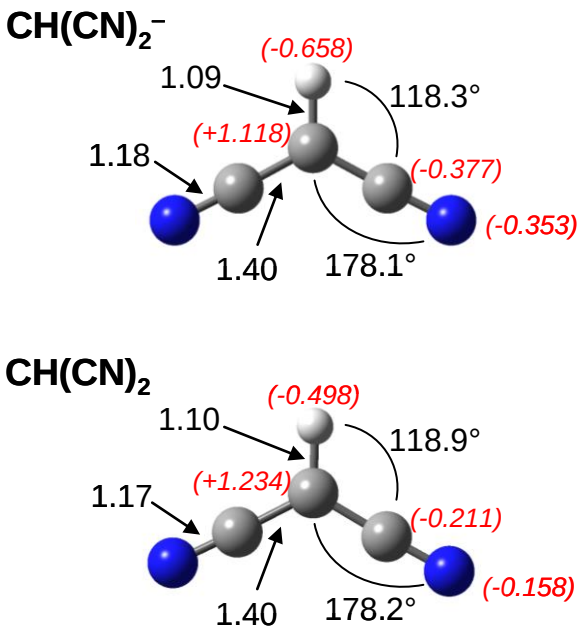

Figure 6.2 Geometries of $CH(CN)_2^-$ and $CH(CN)_2$ optimized at the B3LYP/aug-cc-pVDZ level of theory. Both structures are planar and belong to the C_{2v} symmetry point group. Bond lengths are in Angstroms. Values in parentheses are Mulliken charges.

CHAPTER 7

PHOTOELECTRON IMAGING OF NCCCN⁻: THE TRIPLET GROUND STATE AND THE SINGLET-TRIPLET SPLITTING OF DICYANOCARBENE

7.1. Introduction

Carbenes have long attracted attention as intermediates in chemical reactions. It is well known that substituents R_1 and R_2 on a carbene, $R_1{-}C{-}R_2$, determine the electronic ground state and singlet-triplet energy splitting. The simplest carbene, CH_2, has a triplet ground state,[152,153] with the two same-spin non-bonding electrons occupying different, slightly non-degenerate non-bonding *p* orbitals on the carbon atom to alleviate exchange repulsion.[154] In contrast, carbenes with π-donor substituents, particularly the halocarbenes, CHX and CX_2 (X = F, Cl, and Br), with the probable exception of CI_2, have singlet ground states.[155] In these systems, the energy splitting between the non-bonding orbitals is increased, compared to CH_2, as a result of π-electron donation by the halogen atoms. On the other hand, many carbenes with extended π systems, such as diarylcarbene and acetylene carbene, have triplet ground states stabilized by π conjugation.[156-158]

While nominally considered a "pseudohalogen", a cyano-substituent CN does not act as a π donor, and therefore affects carbenes more like the aryl or acetylenic groups. Indeed, cyanocarbene, HCCN, has a triplet ground state,[154,156-167] with a relatively large singlet-triplet splitting of 11.9 ± 0.4 kcal/mol (0.516 ± 0.017 eV).[159] It is expected that adding another cyano-substituent to give dicyanocarbene, NCCCN, should further

stabilize the triplet ground state and increase the singlet-triplet splitting.

In this work, we report a combined experimental and computational study of the structures and energetics of the electronic states of NCCCN. An *a priori* assessment of the electronic structure is shown in Figure 7.1. Structure 1 (at the bottom of the figure) shows a valence-bond picture of the $NCCCN^-$ anion in the ground state. Just above it (2) are the corresponding depictions of the excited electronic state of $NCCCN^-$ at the bent and linear geometries. The linear structure is included, because the excited-state anion obtained by vertical excitation from the bent ground state is expected to relax towards the linearity (as discussed below). The neutral triplet state and two singlets are depicted in the top portion of the Figure (structures 3, 4, and 5, respectively).

These representations (1–5) show the valence *p* orbitals of carbon and nitrogen atoms. For the anion ($^2B_1$ ground state), there are three electrons on the central carbon atom, with two electrons in the $a_1(\sigma)$ orbital and one electron in the $b_1(\pi)$ orbital. The anion is stabilized by incorporating more *s* orbital character into the doubly occupied orbital, which is favored in the bent geometry. Detachment of an a_1 electron yields the $^3B_1$ or $^1B_1$ neutral state (transitions $1 \rightarrow 3$ and $1 \rightarrow 5$ in Figure 7.1, respectively), with one electron in each *p* orbital of the central carbon atom. The electronic structure of the triplet state is examined more closely in Figure 7.2, which shows that the *p* electrons of the central carbon atom can participate in π bonding with both CN groups and several linear resonance structures can be drawn. The bottom resonance structure depicted in Figure 7.2 is nominally a biradical form of the carbene, where the spin-density is partially separated onto both terminal nitrogens, while the top resonance structure places both unpaired electrons on one of the terminal nitrogens and is nominally a nitrene. However,

it has been shown that the isoelectronic diacetylene carbene, HCCCCCH,[157,158] is best represented as two acetylenic groups connected to divalent carbon, HCC–$\dot{\underset{\dot{}}{C}}$–CCH, with most of the unpaired electrons density localized on the central carbon. This may also be the case for NCCCN. Detachment of the b_1 electron from the anion (transition 1 → 4 in Figure 7.1) gives the $^1A_1$ state of the carbene, which has a bent structure similar to the anion.

In a more general context, the electronic structure of *linear* NCCCN highlights important aspects of this molecule. In linear NCCCN, the two non-bonding electrons occupy a pair of degenerate π_u orbitals, resulting in three different possible electronic configurations: $^3\Sigma_g^-$, $^1\Delta_g$, and $^1\Sigma_g^+$, listed in order of increasing energy. However, NCCCN is subject to Renner-Teller distortion (Figure 7.3), which results in bent (C_{2v} symmetry) molecular structures and changes the state labels to $\tilde{X}\,^3B_1$, $\tilde{a}\,^1A_1$ + $\tilde{b}\,^1B_1$, and $\tilde{c}\,^1A_1$, respectively. In the non-linear regime, $\tilde{X}\,^3B_1$ is the ground state, $\tilde{a}\,^1A_1$ is a closed-shell singlet, $\tilde{b}\,^1B_1$ is an open-shell singlet and $\tilde{c}\,^1A_1$ is a higher energy closed-shell singlet, which will not be discussed further.

In a similar manner, the anion has three electrons in two non-bonding orbitals, which leads to a degenerate $^2\Pi_u$ state at the linear geometry. As with the neutral, the degeneracy is lifted by a Renner-Teller splitting, resulting in a $\tilde{X}\,^2B_1$ ground state and a $\tilde{A}\,^2A_1$ excited state. Similar to Figure 7.2, the $^2A_1$ state has resonance structures with π conjugation in the σ plane, which may result in a linear or quasi-linear structure. Qualitative potential energy curves based on the valence bond structures for $NCCCN^-$

and NCCCN with respect to the CCC bond angle are shown in Figure 7.3.

The important questions that remain to be answered for NCCCN concern the structures of the singlet and triplet states and the magnitude of the singlet-triplet splitting. A previous anion photodetachment study of the cyanocarbene, $HCCN^-$, dealt with many of the same structural issues.[159] For HCCN, the triplet state is quasi-linear, i.e. the bent structure is a potential minimum, while the linear form is a local maximum on the potential energy surface, but the low energy of this maximum (275 cm^{-1}) allows rapid interconversion of triplet HCCN. For the triplet ground state of dicyanocarbene (^{3}NCCCN, for brevity), the effect of two CN substituents must be taken into account, but by simple analogy we might expect ^{3}NCCCN to be also a linear or quasi-linear molecule. Compared to HCCN, the linear NCCCN structure should be more favored due to additional π conjugation offered by the second CN group. Moreover, the triplet state of isoelectronic HCCCCCH has been computed to be linear, suggesting that NCCCN should be linear, as well.[157,158]

There have been several previous studies of NCCCN.[168-172] A matrix isolation measurement indicated a linear triplet structure,[172] but the 193 or 254 nm radiation used in that study induced isomerization between several high-energy isomers, including cyclic structures. A mass-spectrometric study with ^{13}C labeled $NCCCN^-$ showed loss of carbon upon reionization, suggesting the carbon atoms are scrambled via these cyclic intermediates upon neutralization of the anion by high energy collisions.[170] Theoretical studies in the same work also suggested that the triplet is linear, corresponding to the $\tilde{X}\,^3\Sigma_g^-$ state, while the lowest-energy singlet, $\tilde{a}\,^1A_1$, and the anion, $\tilde{X}\,^2B_1$, are both bent at their respective optimized geometries.[170] Coupled-cluster calculations utilizing B3LYP

geometries predict the electron affinity (EA) of NCCCN($^3\Sigma_g^-$) to be 3.20 eV, while the energy splitting between the triplet and the closed-shell singlet state, $\tilde{a}\,^1A_1$, is calculated to be 0.47 eV. A more recent theoretical investigation by Kalcher[160] indicated an EA of 3.36 eV, and a singlet-triplet splitting ($\tilde{X}\,^3\Sigma_g^- \rightarrow \tilde{a}\,^1A_1$) of 0.35 eV, in fair agreement with the coupled-cluster results. As with the previous work, the triplet is predicted to be linear ($\tilde{X}\,^3\Sigma_g^-$).

Another study was reported by Nguyen and co-workers,[171] who utilized complete active-space perturbation theory (CASPT2) calculations, again with B3LYP geometries, to investigate the rearrangement of NCCCN. The ground state of NCCCN was found to be linear ($^3\Sigma_g^-$), with significant spin on the terminal nitrogens, which is consistent with partial biradical character, as indicated in Figure 7.2. Although the electron affinity was not calculated in their study, the singlet-triplet splitting was determined to be 0.32 eV. However, an important result of this study was that the linear open-shell singlet, $^1\Delta_g$, was calculated to be lower in energy than the bent closed-shell singlet, $^1A_1$. Therefore, although the magnitude of the singlet-triplet splitting reported by Nguyen and co-workers[171] is similar to the values reported previously, it corresponds to a different pair of electronic states ($^3\Sigma_g^- \rightarrow {}^1\Delta_g$ in Ref. [171] vs. $^3\Sigma_g^- \rightarrow {}^1A_1$ in the other works[160,170]). The $^3\Sigma_g^- \rightarrow {}^1A_1$ adiabatic excitation energy, on the other hand, was found to be 0.76 eV,[171] contrasting the 0.47 eV [170] and 0.35 eV [160] values reported by others.

A common theme in the studies described above is the use of geometries from density functional methods, and so it is not surprising that they all yielded linear geometries for the triplet state. This has not always been the case, however. In an early

study of NCCCN using self-consistent field methods, the optimized geometry of the triplet was calculated to be bent with a central CCC angle of 132.5°, while the corresponding singlet-state angle was determined to be 114.9°.[173] The interconversion barrier for the triplet state corresponding to the linear geometry was calculated to be 0.4 eV (9 kcal/mol). The calculation, however, did not include electron correlation, which is important in systems like this.[157]

The present paper reports the results of our negative-ion photoelectron imaging experiment and spin-flip coupled-cluster calculations on $NCCCN^-$ and NCCCN. The photoelectron spectrum of $NCCCN^-$ strongly resembles those that have been reported previously for other triplet ground-state carbenes, such as HCH and HCCN. The photoelectron band corresponding to formation of ^{3}NCCCN is broad and congested, suggesting a large geometry change upon electron detachment, as we would expect for the bent anion and linear or nearly linear ^{3}NCCCN. In contrast, the singlet feature is sharp, reflecting the similar geometries of the anion and the closed-shell singlet. The open-shell singlet is not observed at the photon energy used in the experiment. Theoretical studies find ^{3}NCCCN to be linear or quasi-linear, depending on the level of theory and basis set used in the calculation. The computed electron affinity and singlet-triplet splitting are consistent with the experimental results. Finally, in contrast to the previous CASPT2 results,[171] the closed-shell singlet state, $^1A_1$, is calculated to be lower in energy than the open-shell singlet state, $^1\Delta_g$.

7.2. Experimental and theoretical methods

7.2.1. The experiment and data analysis

All measurements were carried out using a negative-ion time-of-flight mass spectrometer equipped with a photoelectron imaging assembly, described in detail elsewhere.[37] Negative ions were synthesized by ion-molecule reactions in a pulsed supersonic expansion. The room-temperature vapor of malononitrile, $CH_2(CN)_2$, was seeded in N_2O carrier gas at a backing pressure of ca. 30 psi and expanded into vacuum through a pulsed supersonic nozzle (General Valve, Series 99) operated at a 50 Hz repetition rate. High-energy electron collisions produced slow secondary electrons, which formed O^- by dissociative electron attachment to N_2O. Dicyanocarbene anions were generated by the reaction of O^- with malononitrile:[6,170]

$$O^- + CH_2(CN)_2 \rightarrow H_2O + C(CN)_2^-. \qquad (7.1)$$

The ions were accelerated to 2.5 keV in a linear time-of-flight mass spectrometer. A collimated, pulsed, linearly polarized laser beam (third or fourth harmonics of a Spectra Physics, model Lab-50 Nd:YAG laser; 10 ns, 10 mJ at 355 nm, 0.05 mJ at 266 nm) intersected the ions of interest within a velocity-map[26] imaging[24] assembly. Photodetached electrons were accelerated by a series of electrodes onto a 40 mm diameter dual microchannel plate detector, coupled to a P43 phosphor screen (Burle, Inc.). The resulting images were recorded by a charge-coupled device camera. Typically, $10^4 – 10^5$ experimental cycles were accumulated for each reported image.

Due to the cylindrical symmetry with respect to the laser polarization axis, images can be reconstructed using the inverse Abel transform to yield the complete three-

dimensional photoelectron distributions.[25] The Abel inversion, as implemented in the BASEX program,[40] yields intensities in polar coordinates, $I(r,\theta)$, where r is the distance from the image center and θ is the angle with respect to the laboratory-frame laser polarization axis. Integration of intensities over θ yields photoelectron spectra. The energy scale was calibrated using the known photoelectron spectrum of O^-.[41,174] Integration over r yields photoelectron angular distributions.[29,30]

7.2.2. Theoretical methods

The low-lying electronic states of NCCCN were investigated using Krylov's spin-flip method[175-177] combined with coupled-cluster theory. The spin-flip (SF) approach incorporates the equation-of-motion methodology to calculate the energies of low-spin excited states, starting from the high-spin reference state and using the spin-flip excitation operator. Unlike low-spin states, the high-spin states are not affected by orbital degeneracies and can be accurately described by a single-reference method. In the case of NCCCN, we employ the unrestricted high-spin component of the triplet state as a reference and describe the singlets and the low-spin component of the triplet as "excited" states in the space of the single spin–flipping excitations:

$$\Psi^{s,t}_{M_S=0} = \hat{R}_{M_S=-1}\Psi^{t}_{M_S=1} \tag{7.2}$$

In Eq. (2), M_S is the projection of the total spin, $\Psi^{t}_{M_S=1}$ is the αα component of the triplet reference state. $\Psi^{s,t}_{M_S=0}$ represents the wave functions of the final singlet and triplet states, while $\hat{R}_{M_S=-1}$ is an excitation operator that flips the spin of one electron. A linear combination of the configurations that result from spin-flip within one of the singly-

occupied orbitals creates either the $m_s = 0$ triplet state, $(\alpha\beta + \beta\alpha)/\sqrt{2}$, or the open-shell singlet, $(\alpha\beta - \beta\alpha)/\sqrt{2}$. (Here, α and β are the usual one-electron spin-functions; the latter should not be confused with the photoelectron anisotropy parameter β). An orbital change that accompanies the spin-flip can be used to create the closed-shell singlet.

The geometries of the closed-shell singlet state and the triplet state were optimized at the (U)CCSD/cc-pVTZ level of theory, whereas the open-shell singlet state was optimized by using the spin-flip approach, SF-CCSD/cc-pVTZ. For geometry optimizations, Hartree-Fock orbitals were used as the orbital basis for the CCSD calculations. This potentially leads to a slight error due to spin-contamination in the wave functions. To minimize the contamination, B3LYP orbitals were used as the orbital basis for single-point calculations. Single-point energy calculations were carried out for all states using the SF-CCSD and SF-CCSD(T) methods.[177,178] The triplet energies used in this work are those for the $M_s = 0$ state, as recommended by Krylov.[179] The calculations were carried out using the QCHEM program package.[180]

7.3. Results

7.3.1. Photoelectron images and spectra

The 355 and 266 nm photoelectron images of $NCCCN^-$ are shown in Figure 7.4, along with the corresponding photoelectron spectra. The 266 nm spectrum in (a) shows two major overlapping features, labeled A and B. As illustrated in the Figure, the overall spectrum is well fit by a sum of two overlapping Gaussian functions (relatively broad for band A and narrow for band B). Band A peaks at a binding energy of 3.53 ± 0.02 eV and has an onset around 3.2 eV (as determined by the signal rising above the noise level in

the experimental spectrum). Feature B has a maximum at 3.72 ± 0.02 eV. The maximum positions are assigned as the vertical detachment energies (VDEs) of the corresponding transitions.

The analysis of the angular distributions is complicated by the overlap of the two bands. The anisotropy parameter for band A was obtained by analyzing the 266 nm photoelectron image in the range of eBE from 3.20 to 3.60 eV, effectively excluding the energy range of the band B Gaussian fitting function [see Figure 7.4(a)]. Band A's anisotropy was thus determined to be $\beta = 0.20 \pm 0.03$. The β value for band B could not be determined, because its entire spectral range includes significant overlap with feature A. The photoelectron angular distribution of the entire 266 nm image (bands A and B combined) is described by $\beta = 0.19 \pm 0.03$.

The 355 nm photoelectron image of $NCCCN^-$ in Figure 7.4(b) shows the onset of band A around eBE = 3.3 eV. Similar to the 266 nm spectrum, no vibrational structure is resolved. The 355 nm spectrum shows one additional feature, a weak outer band (labeled c) with a maximum at eBE = 2.88 ± 0.02 eV and an anisotropy value of $\beta = -0.16 \pm 0.10$. Scanning the photodetachment laser pulse timing along the m/z = 64 ($NCCCN^-$) and 65 peaks and adjusting the instrument mass-resolution (which controls the degree of overlap between neighboring m/z peaks), conclusively showed that feature c belongs to the m/z = 65 anion, $HC(CN)_2^-$, formed in the ion source from the same precursor used in this study. Band c position is in excellent agreement with the recently measured value of electron affinity of dicyanomethyl radical, 2.88 ± 0.01 eV.[6] Therefore, this band will not be further discussed here.

7.3.1. Theoretical results

7.3.1.1. Molecular geometries

Theoretical calculations were carried out on the triplet, open-shell singlet, closed-shell singlet, and the radical anion states of dicyanocarbene. The optimized bond lengths and bond angles are given in Table 7.1. The geometries of the singlet states are consistent with the previous results for this system,[160,170,173] as well as other similar carbenes (e.g., HCCN and $H_3CCCCCCH$).[158,159] The closed-shell singlet ($\tilde{a}\,^1A_1$) structure is strongly bent (CCC bond angle 118°), similar to other simple closed-shell carbenes, including methylene.[153] Similarly, the open-shell singlet ($\tilde{b}\,^1B_1$) optimizes to a linear geometry ($\tilde{b}\,^1\Delta_g$), as shown previously by Nguyen and co-workers.[171]

The structure of the triplet state is more challenging to determine. At the (U)CCSD/cc-pVTZ level of theory, it is found to be slightly non-linear, with a CCC bond angle of 168.4° (Table 1). The large bond angle in the triplet state is typical for carbenes. However, the question remains whether ^{3}NCCCN is truly bent. The triplet state of the isoelectronic diacetylenic carbene, HCCCCCH, has been found to be linear.[157] Similarly, whereas triplet cyanocarbene, HCCN, appears to be non-linear, spectroscopic studies indicate that it is quasi-linear, with an electronic potential barrier at linearity that is lower than the zero-point vibrational level.[159,161] We find that the optimized geometry of ^{3}NCCCN is highly sensitive to the basis set and the extent of correlation included in the calculation. For example, the CCC bond angles optimized at the CCSD level of theory using the cc-pVDZ, cc-pVTZ and cc-pVQZ basis sets are 155.6°,168.4°, and 172.0°, respectively, indicating that the triplet state structure approaches linearity as the basis set

size is increased.

In order to investigate the effect of additional correlation, we carried out single-point calculations at the SF-CCSD and SF-CCSD(T) levels with the cc-pVTZ basis set for a series of triplet state geometries optimized at the CCSD/cc-pVTZ level with the CCC bond angle fixed at selected values between 155° and 180°. The resulting energies were compared to those determined at the same level of theory with the same basis set for the fully optimized CCSD/cc-pVTZ geometry (∠CCC = 168.4°). The results are listed in Table 7.2. Although the energy differences are small, lower energy structures (compared to the fully optimized CCSD/cc-pVTZ geometry) are found with different levels of theory. The difference is likely due to using B3LYP orbitals as opposed to HF orbitals for the CCSD basis in the single point calculations.

Based on the SF-CCSD/cc-pVTZ results, the linear geometry is approximately 40 cm^{-1} higher in energy than the CCSD/cc-pVTZ fully relaxed structure. The SF-CCSD(T)/cc-pVTZ calculations suggest that the linear geometry is a very shallow minimum, 6.6 cm^{-1} more stable than the CCSD/cc-pVTZ fully relaxed structure with ∠CCC = 168.4°. When diffuse functions are included in the calculation (the aug-cc-pVTZ basis set), the linear geometry is favored at both the SF-CCSD and SF-CCSD(T) levels of theory, by 54.9 and 81.2 cm^{-1}, respectively.

While these energy differences are too small to draw any conclusions about the shape of the potential energy surface, the results indicate that there is very little energy difference between the linear and bent geometries. Therefore, the ^{3}NCCCN geometry is likely best described as quasi-linear. The small energy differences over a wide range of geometries suggest the CCC bending vibration undergoes large-amplitude motion.

7.3.1.2. State ordering and energies

The calculated relative energies of the triplet, closed-shell singlet, and open-shell singlet states of NCCCN are listed in Table 7.3. The ground state is determined to be the triplet, as has been reported previously.[160,170] However, in contrast to the results of Nguyen and co-workers,[171] we find the lowest-energy singlet to be the closed-shell state, which is 0.1 – 0.3 eV (depending on the level of theory) more stable than the open-shell singlet state.

The predicted state ordering is consistent with the effects of the Renner-Teller coupling in the singlet state. As illustrated in Figure 7.3, the two singlet states are degenerate at the linear geometry. The Renner-Teller interaction causes the states to split upon distortion from linearity, with one state ($^1A_1$) going lower in energy, and the other state ($^1B_1$) going up in energy.[181] A separate CASPT2 calculation carried out by Hrovat and Borden also supports the conclusions obtained here.[182] At the CASPT2(14,14)/aug-cc-pVTZ level of theory, the closed-shell singlet is found to lie adiabatically 0.69 eV higher in energy than the triplet state, whereas the energy of the open-shell singlet is found 0.74 eV above the triplet. These values are in excellent agreement with the SF-CCSD(T)/aug-cc-pVTZ results in Table 7.3. Most importantly, these calculations confirm that the closed-shell singlet is the preferred singlet state, as expected for the Renner-Teller system.

7.3.1.3. Electron Affinities

The adiabatic electron affinity of ^{3}NCCCN was calculated at the CCSD(T)/aug-cc-pVTZ and B3LYP/aug-cc-pVTZ levels of theory. The CCSD/cc-pVTZ geometry

reported in Table 7.1 was used for the anion in the couple-cluster calculations, whereas the linear geometry (Table 7.2) was used for the triplet state. Fully optimized geometries were used for the B3LYP calculations. The predicted and experimentally determined EA values for NCCCN are summarized in Table 7.4, where they are compared to those obtained by similar methods for HCCN. The electron affinities predicted by both CCSD(T) and B3LYP are in good agreement with the experimental measurements for both NCCCN and HCCN.[159]

The third column in Table 7.4 shows the electron affinity of ^{3}NCCCN obtained using an isodesmic approach[183] based on the energetics of the electron transfer reaction

$$NCCCN^- + {}^3HCCN \rightarrow {}^3NCCCN + HCCN^- \qquad (7.3)$$

and the known electron affinity of HCCN.[159]

The electron binding energy of the singlet state, shown in the last column in Table 7.4, was obtained by combining the EA calculated using the isodesmic approach with the singlet-triplet splitting calculated at the SF-CCSD(T)/aug-cc-pVTZ level of theory.

7.4. Discussion

7.4.1. Photoelectron spectrum assignment

Both $NCCCN^-$ and NCCCN have been previously studied experimentally and theoretically, but the singlet-triplet splitting and electron affinity of the neutral have not been measured. Initial assignment of features A and B in the photoelectron spectrum (Figure 7.4) can be made by comparison to the spectrum of $HCCN^-$, which shows a similar broad absorption at low eBE, corresponding to the triplet neutral state, and a sharp

feature at higher eBE, assigned to the closed-shell singlet.[159] Substituting a CN group for the H to form $NCCCN^-$ yields a photoelectron spectrum similar to that of $HCCN^-$, but the observed features are shifted to higher binding energy. The large increase in eBE reflects the pseudo-halogen nature of the CN group, and its ability to stabilize negative ions.[6,120,184] Therefore, band A in the $NCCCN^-$ spectra in Figure 7.4 is assigned to the $\tilde{X}\ ^3B_1/^3\Sigma_g^- \leftarrow \tilde{X}\ ^2B_1$ photodetachment transition, while band B is attributed to $\tilde{a}\ ^1A_1 \leftarrow \tilde{X}\ ^2B_1$.

The quantitative comparison of the measured spectra with the theoretical predictions provides support for this assignment. NCCCN ($\tilde{X}\ ^3B_1$ or $^3\Sigma_g^-$) is best described as a quasi-linear molecule with a small barrier at the linear geometry. The large geometry change resulting from a transition from the anion structure to ^{3}NCCCN results in a broad photoelectron band, consistent with band A in Figure 7.4. The location of band A's origin is not clear. Examining the spectra in Figure 7.4 (a) and (b), we estimate that the band onset appears around eBE = 3.25 ± 0.05 eV. This is consistent with the computed electron affinity values for NCCCN, which range from 3.04 to 3.36 eV depending on the method and basis set used (Table 7.4). There is no identifiable vibrational progression in either the 266 or the 355 nm spectrum. The fundamental frequency of the CCC bending vibration, which is the primary mode expected to be excited in the bent-to-linear transition, has been measured to be 102 cm^{-1}.[172] This mode is expected to be strongly anharmonic. This low-frequency vibration, along with other modes make it impossible to resolve any structure within band A. However, the vertical detachment energy corresponding to the triplet state is readily determined as VDE = 3.53

± 0.02 eV. This value compares favorably with the VDE = 3.47 eV predicted for $NCCCN^-$ at the B3LYP/aug-cc-pVTZ level of theory.

In contrast to the NCCCN ground state, the optimized geometry of the closed-shell singlet, $\tilde{a}\,^1A_1$, is very similar to that of the anion (Table 7.1). Therefore, the $\tilde{a}\,^1A_1 \leftarrow \tilde{X}\,^2B_1$ transition is expected to yield a limited Franck-Condon progression with an intense feature at the origin. The sharp feature at high eBE in the 266 nm spectrum in Figure 7.4(a) (feature B) is consistent with such a transition. The band maximum at eBE = 3.72 ± 0.02 eV is assigned as the adiabatic detachment energy corresponding to the $\tilde{a}\,^1A_1$ state of NCCCN. This result compares remarkably well with the computed values summarized in the last column of Table 7.4.

The open-shell singlet state of NCCCN is calculated to be 0.74–0.82 eV (17–19 kcal/mol) higher in energy (adiabatically) than the triplet, which corresponds to an approximately 4.0 eV adiabatic detachment energy. Although the adiabatic transition is (barely) within the 266 nm (4.66 eV) photon energy range, it is not observed in our photoelectron spectra due to the poor Franck-Condon overlap expected for this bent-to-linear transition. The vertical detachment energy for this transition is predicted to fall well outside the photon energy range of the experiment because the Renner-Teller splitting results in a rapid increase in the energy of the open-shell singlet state with CCC bending.

7.4.2. Electron affinity and Singlet-Triplet splitting of NCCCN

It is difficult to determine the adiabatic electron affinity and the singlet-triplet splitting in NCCCN experimentally, because no features associated with the origin the

triplet band (A) can be assigned. The best estimate of the band onset obtained by rather subjective inspection of the spectra in Figure 7.3 places the electron affinity at EA ≤ 3.25 ± 0.05 eV.

Greater confidence in the above experimental estimate is achieved by fitting the triplet band using a Franck-Condon simulation function. In our analysis, we used the anion and triplet geometries and frequencies calculated at the B3LYP/aug-cc-pVDZ level. Higher-level calculations do not necessarily yield better fits due to the approximations used in the modeling procedure. Namely, in order to avoid having to evaluate the multidimensional overlap integrals of vibrational wavefunctions, the simulation uses the parallel-mode approximation and assumes harmonic oscillators, as described in detail elsewhere.[184] Several important limitations of this method should be recognized. First, the $NCCCN^-$ anion is bent, while the ^3NCCCN neutral is quasi-linear. Therefore, one rotational mode of the anion becomes a vibration in the neutral. To simplify the analysis, we opted to optimize the ^3NCCCN geometry with an CCC angle arbitrarily fixed at 175° to allow overlap of all vibrational modes. Second, band A has no resolved vibrational progression with which to compare simulated progressions. Third, the use of the parallel-mode approximation may be questioned in this case, as it is most appropriate for small geometry changes, which is hardly the case in $^3NCCCN \leftarrow NCCCN^-$ photodetachment. Finally, the potential energy surface for CCC bending is highly anharmonic, so evaluating overlap integrals of these principal Franck-Condon active modes requires additional computational effort.

In fitting the triplet band, we matched the band A maximum and shape in the 266 nm spectrum by scaling vibrational energies and convoluting all peaks with Gaussian

functions of variable width.[185] Although this procedure is admittedly crude, it produces a satisfactory fit; an example is shown in Figure 7.5. The parameters used to model the 266 nm spectrum also produce a satisfactory fit of the onset of band A in the 355 nm spectrum, after accounting for differences in resolution. Our simulation for band B confirms this feature is a vertical transition to the ground vibrational state of ^{1}NCCCN.

The predicted intensity at the origin is negligible, as one expects for a weak transition resulting from a large change in geometry. Still, this fitting procedure yields an adiabatic electron affinity of EA = 3.20 ± 0.05 eV, which is an improvement compared to the upper-limit estimate (EA ≤ 3.25 ± 0.05 eV) obtained by simply inspecting the spectra (see Table 7.4). Using this value in conjunction with the origin of the singlet band at 3.72 ± 0.02 eV, we estimate the singlet-triplet ($\tilde{a}\,^1A_1 \leftarrow \tilde{X}\,^3B_1/^3\Sigma_g^-$) splitting in NCCCN as ΔE_{ST} = 0.52 ± 0.05 eV (12.0 ± 1.2 kcal/mol). This estimate compares well with the theoretical value of 13.9 kcal/mol obtained with SF-CCSD(T)/cc-pVTZ, the highest level of theory employed in this study.

7.5. Conclusions

The photoelectron imaging study of $NCCCN^-$ reveals two bands in the photoelectron spectrum, corresponding to a triplet ground state ($\tilde{X}\,^3B_1$ or $^3\Sigma_g^-$) and an excited closed-shell singlet state ($\tilde{a}\,^1A_1$). Theoretical calculations show the triplet is either quasi-linear or linear. The triplet potential energy surface for CCC bending is flat and therefore sensitive to the choice of theoretical method and basis set. In contrast, the closed-shell singlet has a geometry very similar to the anion. Correspondingly, the singlet state is characterized by a sharp feature in the photoelectron spectrum, whereas the triplet

state is represented by a broad congested band. The best estimate of the origin of the triplet band, supported by Franck-Condon modeling, yields an adiabatic electron affinity of NCCCN, EA = 3.20 ± 0.05 eV. The adiabatic electron binding energy of the closed-shell singled state is measured to be 3.72 ± 0.02 eV, while the singlet-triplet ($\tilde{a}\,^1A_1 \leftarrow \tilde{X}\,^3B_1/^3\Sigma_g^-$) splitting is determined as ΔE_{ST} = 0.52 ± 0.05 eV (12.0 ± 1.2 kcal/mol).

The second CN group on NCCCN does not significantly alter the singlet-triplet gap compared to cyanocarbene [ΔE_{ST}(HCCN) = 0.516 eV].[159] Although we had predicted increased triplet stabilization based on the valence bond pictures in Figure 7.1. For comparison, the difference in singlet-triplet splittings of HCH and HCCN is about 0.39 eV,[153,159] a clear example of resonance stabilization. Our work illustrates an important point, however, that ΔE_{ST} is the magnitude of the singlet-triplet gap – and is only indirectly related to resonance stabilization of unpaired electrons in one of the states. Thus, one possible explanation for the similar ΔE_{ST} of NCCCN and HCCN, is that, while the triplet ground state of NCCCN might have increased resonance stabilization, the Renner-Teller splitting on the singlet surface drives the relative energy of the singlet state down as well, so the relative energy gap between the singlet and triplet states remains approximately unchanged.

7.6. Acknowledgements

This work was supported by the U.S. National Science Foundation under grants CHE-0713880 (A. Sanov) and CHE-0454874 and CHE-0808964 (P. Wenthold). Calculations were carried out using the resources from the Center for Computational Studies of Open-Shell and Electronically Excited Species (http://iopenshell.usc.edu), directed by Professor Anna Krylov and supported by the National Science Foundation through the CRIF:CRF

program. We thank Professor Lyudmila Slipchenko for assistance with the electronic structure calculations and Dr. David Hrovat and Professor Weston T. Borden for providing the results of their CASPT2 calculations.

Table 7.1 Optimized geometries of $NCCCN^-$ and NCCCN electronic states.[a]

	C-C Bond Length (Å)	C-N Bond Length (Å)	CCC Bond Angle	CCN Bond Angle
Anion ($\tilde{X}\,^2B_1$) [b]	1.379	1.173	119.3°	173.7°
Triplet ($\tilde{X}\,^3B_1/^3\Sigma_g^-$) [b]	1.320	1.179	168.4°	178.2°
Closed-shell singlet ($\tilde{a}\,^1A_1$) [b]	1.383	1.165	118.2°	173.1°
Open-shell singlet ($\tilde{b}\,^1\Delta_g$) [c]	1.318	1.168	180°	180°

[a] Determined at the (U)CCSD/cc-pVTZ level of theory.

[b] The CCCN dihedral angle is 180°.

[c] The open-shell state was optimized by using the SF approach.

Table 7.2 NCCCN triplet ($\tilde{X}\,^3B_1$) state energy (in cm^{-1}) as a function of CCC bond angle, relative to the energy of the relaxed structure ($\angle CCC = 168.4°$).[a]

∠CCC	Method and basis set			
	SF-CCSD cc-pVTZ	SF-CCSD(T) cc-pVTZ	SF-CCSD aug-cc-pVTZ	SF-CCSD(T) aug-cc-pVTZ
155°	0.2	113.2		
160°	–16.2	46.1		
165°	–2.0	11.0		
170°	3.7	0.9		
175°	16.9	7.5		
180°	21.9	–6.6	–54.9	–81.2

[a] Relative state energies were calculated using B3LYP orbitals. Geometries were optimized at the UCCSD/cc-pVTZ level of theory, using HF orbitals and holding the CCC bond angle fixed.

Table 7.3 Relative adiabatic state energies (in eV) obtained with the NCCCN geometries shown in Table 8.1, unless noted.

NCCCN state	Method and basis set			
	SF-CCSD cc-pVTZ	SF-CCSD(T) cc-pVTZ	SF-CCSD aug-cc-pVTZ	SF-CCSD(T)[a] aug-cc-pVTZ
Triplet ($\tilde{X}\,^3B_1/^3\Sigma_g^-$)	0.0	0.0	0.0	0.0
Closed-shell singlet ($\tilde{a}\,^1A_1$)	0.667	0.603	0.702	0.650
Open-shell singlet ($\tilde{b}\,^1\Delta_g$)	0.945	0.820	0.876	0.746

[a] Using the linear structure for the triplet.

Table 7.4 Adiabatic electron affinities (binding energies) for ^{3}HCCN, ^{3}NCCCN, and ^{1}NCCCN (in eV).

	^{3}HCCN	**^{3}NCCCN**	**^{3}NCCCN** per Eq. (3)	**^{1}NCCCN** [a]
CCSD(T)/aug-cc-pVTZ [b]	1.94	3.04	3.10	3.71[c]
				3.75[d]
B3LYP/aug-cc-pVTZ	2.02	3.10	3.08	3.68[c]
				3.73[d]
RCCSD(T)/aug-cc-pVTZ		3.20 [e]		3.67 [e]
ACPF/aug-cc-pVTZ		3.36 [f]		
Experimental	2.003 ± 0.014 [g]	≤ 3.25 ± 0.05 [h]		3.72 ± 0.02 [h]
		3.20 ± 0.05 [i]		

[a] Adiabatic electron binding energy of NCCCN($\tilde{a}\,^1A_1$).

[b] Using the geometries shown in Table 8.1 for $NCCCN^-$, and the linear geometry (Table 8.3) for the triplet; HCCN geometries were calculated at the CCSD/cc-pVTZ level of theory.

[c] Obtained by combining the EA from the isodesmic calculation (previous column) with the SF-CCSD(T)/cc-pVTZ singlet-triplet splitting from Table 8.3.

[d] Obtained by combining the EA from the isodesmic calculation (previous column) with the SF-CCSD(T)/aug-cc-pVTZ singlet-triplet splitting from Table 8.3.

[e] Reference [170], RCCSD(T)/aug-cc-pVTZ//B3LYP/6-31+G(d).

[f] Reference [160].

[g] Reference [159].

[h] This work, obtained by inspection of the photoelectron spectra in Figure 8.3.

[i] This work, determined from the Franck-Condon simulation of the 266 nm photoelectron spectrum, as shown in Figure 8.4.

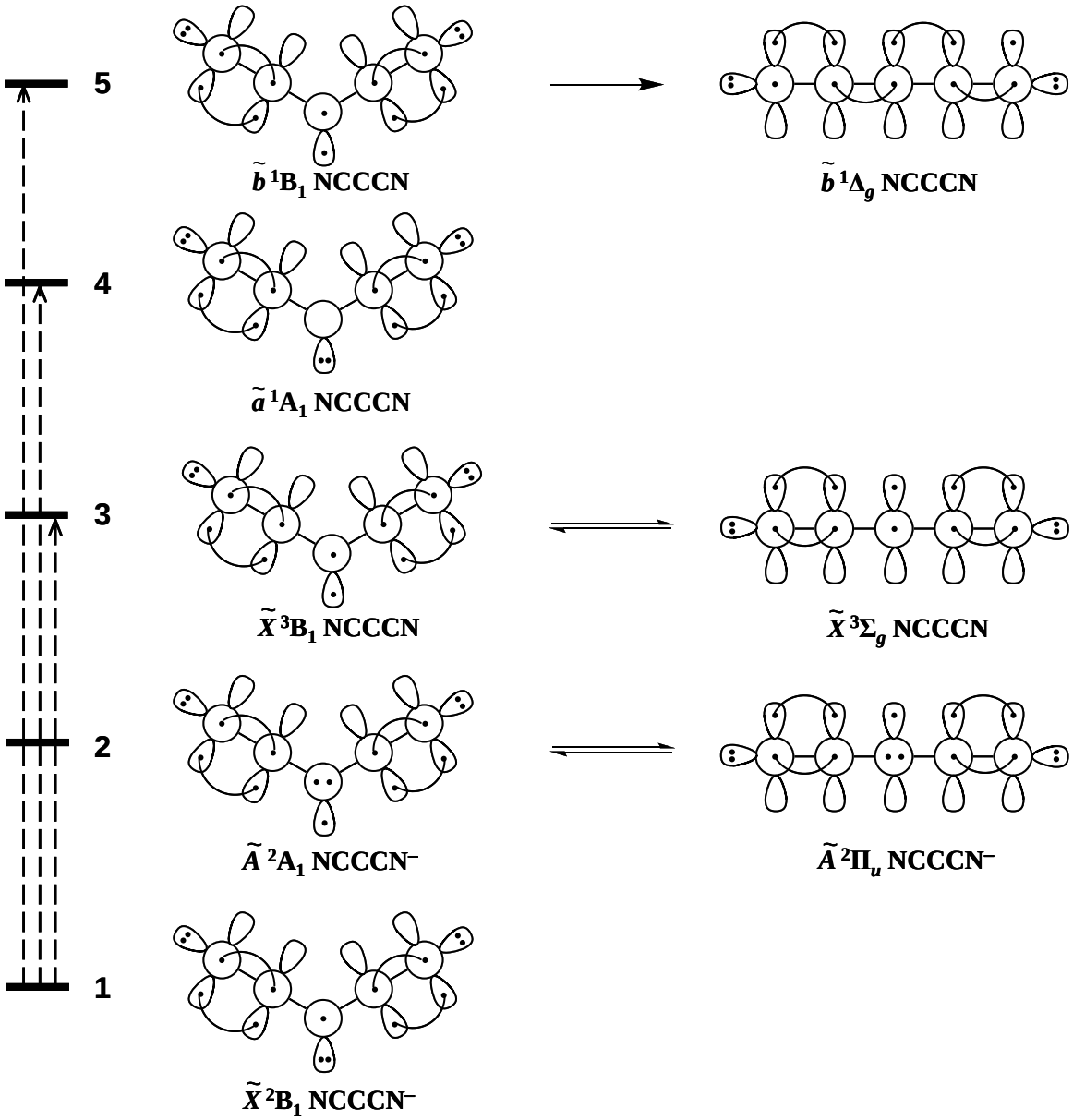

Figure 7.1 Valence bond pictures of the π bonding and low lying electronic states of NCCCN$^-$ and NCCCN.

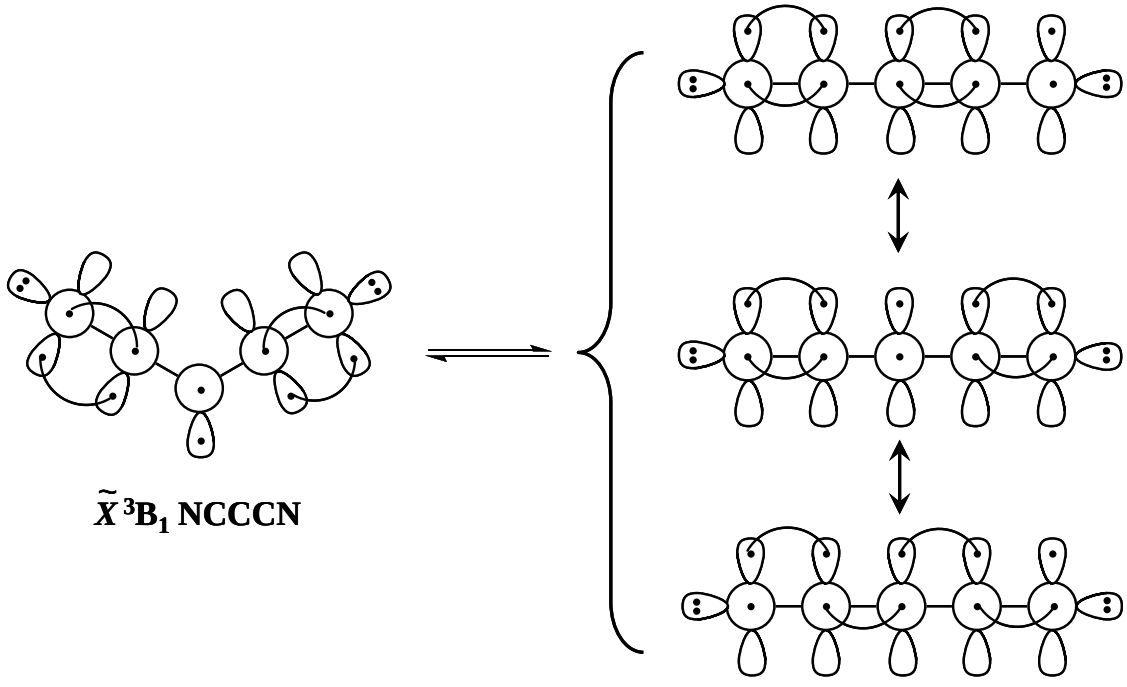

Figure 7.2 Valence bond pictures of the π bonding of ^{3}NCCCN. The double arrow indicates equilibrium between the bent / linear geometries, while the three resonance structures at the linear geometry (bottom to top: biradical, carbene, and nitrene) suggest this is the most stable geometry.

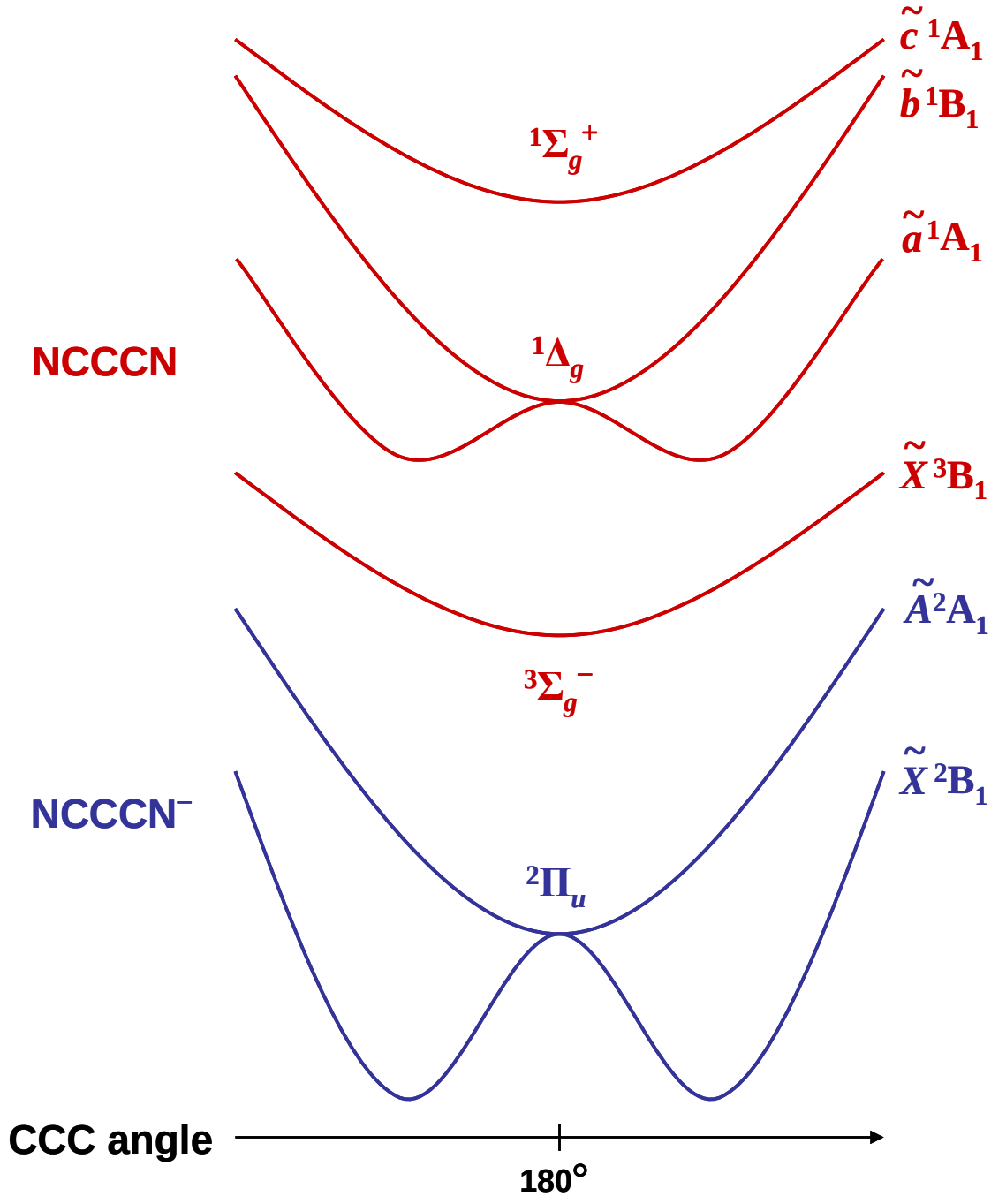

Figure 7.3 Qualitative potential energy curves of NCCCN$^-$ and NCCCN as functions of the CCC bond angle based on the valence bond structures shown in Figure 7.1.

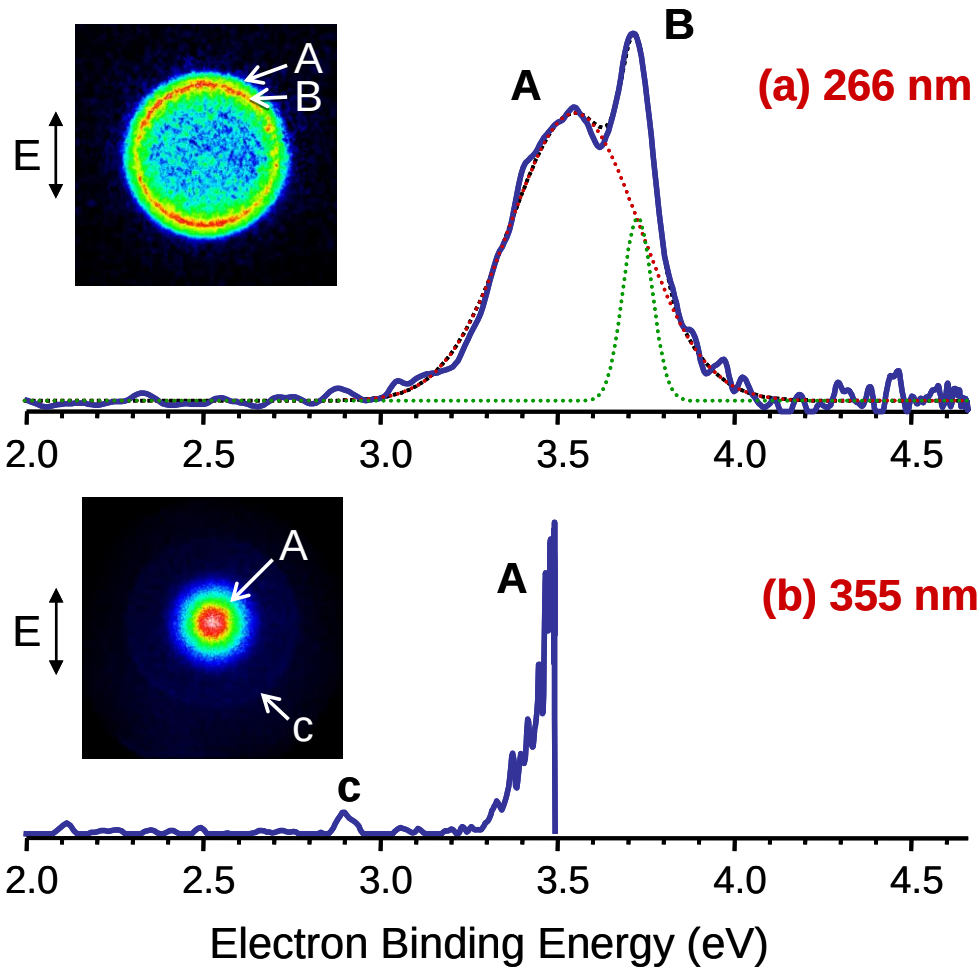

Figure 7.4 Photoelectron images and spectra of $NCCCN^-$ obtained at 266 nm (a) and 355 nm (b). The double arrows indicate the direction of laser polarization. Features A and B in the 266 nm spectrum are fit by two Gaussian functions (red and green dotted lines, respectively), which represent the Franck-Condon envelopes of the NCCCN ← $NCCCN^-$ photodetachment transitions. Band A is assigned to the $\tilde{X}\,^3B_1/^3\Sigma_g^-$ ← $\tilde{X}\,^2B_1$ transition with VDE = 3.53 ± 0.02 eV. Band B is assigned to $\tilde{a}\,^1A_1$ ← $\tilde{X}\,^2B_1$, with VDE = 3.72 ± 0.02 eV. Weak feature c peaking at eBE = 2.88 ± 0.02 eV in the 355 nm spectrum is due to the photodetachment of the $HC(CN)_2^-$ anion.[6]

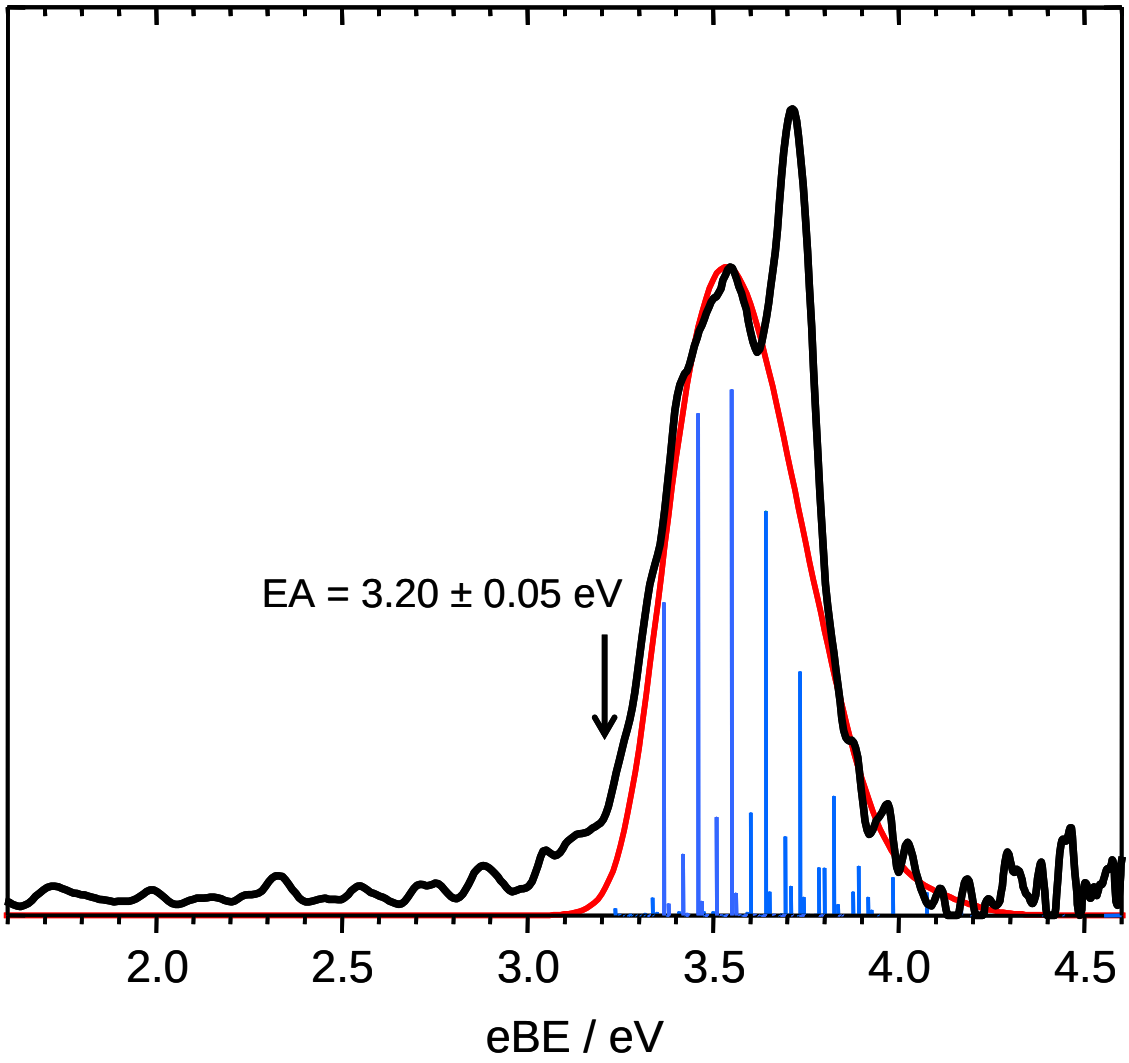

Figure 7.5 Simulation of band A using a Franck-Condon fitting procedure and geometries and frequencies obtained from B3LYP/aug-cc-pVDZ calculations. The black solid line is the experimental spectrum reproduced from Figure 7.3(a). The red line is the convoluted fit from the simulation. The blue vertical lines are the calculated Franck-Condon factors. The arrow indicates the adiabatic electron affinity obtained by fitting the Franck-Condon simulation to the experimental spectrum.to the photodetachment of the $HC(CN)_2^-$ anion.[6]

CHAPTER 8

HETEROGENEOUS SUBSTITUTION EFFECTS IN CHLOROCYANOMETHYL RADICAL AND CHLOROCYANOCARBENE

8.1. Introduction

Methyl radicals ($\cdot CR_1R_2R_3$) and carbenes ($:CR_1R_2$) are fundamentally interesting species that play important roles as intermediates in chemical reactions. Their structures and stabilities vary depending on the properties of the substituents (R). The radical stability, related to the bond dissociation energy (BDE) of the corresponding closed-shell molecule, $\Delta H_{298}(H–CR_1R_2R_3)$, is affected by resonance and inductive effects of the substituents.[136,186] The canonical picture of a carbene is even more intricate, due to the existence of two nearly degenerate non-bonding σ and π orbitals on the central carbon atom occupied by two electrons.[154,187] The neighboring atoms affect the energy difference between these orbitals, determining the electron configuration ($\ldots\sigma^2\pi^0$ or $\ldots\sigma^1\pi^1$) and the multiplicity of the ground state of the carbene, as well as the magnitude of the singlet-triplet splitting.

Radicals and carbenes are well suited for studies using anion photoelectron spectroscopy.[188] The precursor anions can be formed in the gas phase using the well-documented H^+ or H_2^+ abstraction reactions of O^- with the corresponding closed-shell molecules.[189,190] With regard to carbenes, photoelectron spectroscopy affords an additional key advantage of accessing both the singlet and triplet states of the neutral species. For a canonical carbene, the anion lowest-energy electron configuration is $\ldots\sigma^2\pi^1$ and the lowest singlet

and triplet states of the neutral are accessed by detachment from the respective π and σ orbitals.[187] (Photodetachment from the σ orbital also accesses the open-shell …$\sigma^1\pi^1$ singlet state, which will be explicitly referred to as "the open-shell singlet". The short-hand designation "the singlet" is reserved for the closed-shell …$\sigma^2\pi^0$ singlet state.) With this in mind, photoelectron imaging proves to be especially advantageous, since the π and σ orbitals are generally expected to yield distinct photoelectron angular distributions (PAD) reflecting the symmetry properties of the non-bonding orbitals.[15,33] Thus, the multiplicity and energy ordering of the electronic states of carbenes can be assigned (in some cases) based on a simple examination of the PADs.

In this work, we focus on the effects of Cl and CN substituents on the properties of doubly-substituted methyl radicals and carbenes. The inductive effects attributed to both substituents increase the electron affinity (EA). In addition, π-electron donation by halogens increases the energy splitting between the non-bonding σ and π orbitals in chlorocarbenes, favoring a singlet ground state.[8,191] The cyano group is often referred to as a pseudohalogen, due to its high electronegativity and mono-valent reactivity. However, while true halogens act as π electron donors, the cyano group does not. Instead, conjugation of its π system with the non-bonding 2*p* (π) orbital on the central carbon stabilizes the triplet state of the carbene.[154,157,158,187] For this reason, in contrast to HCCl and CCl_2, the corresponding cyano-substituted carbenes, HCCN and $C(CN)_2$, have triplet ground states.[7,159,187]

We report a study of the heterogeneously substituted methyl radical, ·CHClCN, and the corresponding carbene, :CClCN. We show that the π-donor halogen and π-acceptor cyano groups have a cooperative (captodative) effect on the mixed radical stability and,

to the contrary, competing effects on the singlet-triplet splitting in the mixed carbene. We use negative-ion photoelectron imaging to examine the properties of CHClCN and CClCN and compare the findings to the corresponding dichloro- and dicyano- radicals and carbenes, focusing on the divergent effects of the halogen and pseudohalogen (CN) substitutions.

8.2. Experimental and theoretical methods

The experiments were performed using the negative-ion photoelectron imaging spectrometer described in detail elsewhere.[37] In brief, a precursor gas mixture at a backing pressure of 20–30 psi is expanded into vacuum through a pulsed supersonic nozzle (General Valve, Series 99) operated at a 50 Hz repetition rate. The expansion is crossed with a collimated 1 keV electron beam. The resulting anions are pulse-extracted into a linear Willey-McLaren[192] time-of-flight mass spectrometer and accelerated to 2.5 keV. The mass-selected anions are photodetached within a velocity-map[26] imaging[24] assembly using linearly polarized laser pulses timed to coincide only with the ions of interest. The second or third harmonics of a Spectra Physics, Inc. Lab-130 Nd:YAG (yttrium aluminum garnet) laser (10 ns pulse duration, 20 mJ/pulse at 532 nm, 5 mJ/pulse at 355 nm) were used to detach electrons.

The photodetached electrons are accelerated by a series of velocity-mapping electrodes onto a 40 mm position sensitive microchannel plate detector coupled to a P43 phosphor screen (Burle, Inc.). The resulting images are recorded by a charge-coupled device camera. Typically, ~10^6 experimental cycles are accumulated for each reported image. The images are analyzed using the inverse Abel transform implemented in the BASEX program[40] to yield the complete three-dimensional photoelectron distributions.[25]

The energy scale in the resulting spectra is calibrated using the well-known photodetachment transition of O^-.[41,42]

To generate the $CClCN^-$ and $CHClCN^-$ ions studied in this work, the precursor chloroacetonitrile, CH_2ClCN, vapor was seeded in an N_2O or O_2 carrier gas. Dissociative electron attachment to N_2O produced O^- radical anions, which in turn reacted with chloroacetonitrile to form chlorocyanomethylide ($CHClCN^-$) and chlorocyanocarbene ($CClCN^-$) anions via the respective H^+ and H_2^+ abstraction reactions. A representative mass-spectrum of the anions generated with CH_2ClCN seeded in N_2O is shown in Figure 8.1a. All chlorine-containing anions yield two dominant mass-spectral peaks each, with approximate 3:1 intensity ratios reflecting the natural abundances of the main chlorine isotopes, ^{35}Cl and ^{37}Cl. The $CClCN^-$ anion is expected at 73 and 75 a.m.u. The corresponding peaks in Figure 8.1a clearly violate the expected intensity ratio and most of the 75 a.m.u. intensity is attributed to a different species, possibly $HNO^-\cdot N_2O$. The 73 a.m.u. peak was used for the experiments on $CClCN^-$. The mass spectra in Figure 8.1 are plotted on arbitrary intensity scales. Although the 73 a.m.u. peak appears small in Figure 8.1a, sufficiently strong photodetachment signal was observed, as evidenced by the results in Section 8.4.

Similarly, $CHClCN^-$ is expected at m = 74 a.m.u., with a less-intense satellite peak at 76 a.m.u. When using a CH_2ClCN/N_2O reaction mixture (Figure 8.1a), the primary $CHClCN^-$ peak (74 a.m.u.) overlaps with the $NO^-\cdot N_2O$ or $N_3O_2^-$ ions.[193,194] Therefore, an O^- reagent source other than N_2O was necessary for experiments on $CHClCN^-$. The mass-spectrum displayed in Figure 8.1b was obtained using O_2 instead of N_2O. The 74 a.m.u. ions observed under these conditions were the target of $CHClCN^-$ experiments.

Electronic-structure calculations involving geometry optimizations at the coupled-cluster level of theory with single, double (and triple) excitations, CCSD and CCSD(T), were performed using the Gaussian 09 suites of programs.[195] The geometries for the anion and neutral ground and excited states were optimized, with the normal-mode analysis used to confirm that the structures corresponded to true potential minima.

The low-lying electronic states were explored using the equation-of-motion (EOM) spin-flip (SF) methodology[176,177,196,197] combined with the coupled-cluster theory, including diagonal triples corrections (dT).[198] All EOM-XX-CCSD(dT) calculations (XX = SF or IP) were carried out using the Q-Chem 4.0 software package.[199]

8.3. Chlorocyanomethyl radical

The 355 and 532 nm photoelectron images of $CHClCN^-$ are shown in Figure 8.2 alongside the corresponding spectra. All spectra in this work are plotted with respect to electron binding energy eBE = $h\nu$ – eKE, where $h\nu$ is the photon energy and eKE is electron kinetic energy.

8.3.1. Vertical detachment energy of chlorocyanomethylide

The 355 nm photodetachment band is fitted with a Gaussian, shown in Figure 8.2a as a grey curve. The fit used the part of the experimental spectrum falling within the full-width-at-half-maximum interval. The maximum position of the fitted Gaussian is assigned as the vertical detachment energy of $CHClCN^-$, VDE = 2.39 ± 0.04 eV. The origin of the band, corresponding to the adiabatic EA of the neutral radical, is not immediately apparent.

The 532 nm photodetachment band (Figure 8.2b) corresponds to the same

transition. To account for the low-eKE effects expected near the energetic cutoff at eBE = $h\nu$ = 2.33 eV, the 532 nm spectrum was fitted with the modified Gaussian function (shown in grey):

$$P(\text{eBE}) = C(h\nu - \text{eBE})^{1/2}\exp[-(\text{eBE} - \text{VDE})^2/w^2], \quad (8.1)$$

where w is a width parameter and C is a normalization coefficient. Equation (8.1) assumes a Gaussian Franck-Condon profile and approximates the electronic cross-section scaling using a Wigner-like[200] pre-factor $(h\nu - \text{eBE})^{1/2} = \text{eKE}^{1/2}$, where the 1/2-power dependence reflects the assumed contribution of *s* partial waves. This assumption is strictly justified only for low-eKE electrons,[201] but previous modeling with similar approaches was successful in describing broad photoelectron bands.[202,203]

Due to the low-eKE intensity scaling, the maximum position of the 532 nm spectrum is shifted with respect to the VDE determined from the 355 nm spectrum. It is for this reason that the 355 nm spectrum provides for a more reliable determination of the VDE. Hence, the 532 nm spectrum in Figure 8.2b was fitted using Eq. (8.1) by adjusting w for best fit, while the VDE value was fixed at that determined from the 355 nm spectrum. The resulting fit curve is overlaid with the experimental spectrum in Figure 8.2b.

Calculations for the ground states of $CHClCN^-$ and CHClCN yielded the equilibrium geometries shown in Figure 8.3, with the bond lengths and angles given in the caption. The structures were optimized[195] at the CCSD level of theory using Dunning's augmented correlation-consistent polarized valence triple-ζ basis set (aug-cc-pVTZ). The significant geometry change expected upon electron detachment from $CHClCN^-$ (non-planar pyramidal to trigonal planar) is consistent with the broad and

congested photoelectron bands in Figure 8.2.

The VDE of $CHClCN^-$ and the EA of CHClCN were obtained from single-point calculations with a variety of methods and basis sets, using the optimized anion and neutral geometries shown in Figure 8.3. In all calculations, the VDE is defined as the energy difference between the neutral and anion states at the anion equilibrium geometry, while the EA is the energy difference between the respective neutral and anion equilibrium structures. The results are summarized in Table 8.1. For the couple-cluster calculations, the Hartree-Fock (HF) orbital bases were used by default. However, some of the CCSD values in Table 8.1 were calculated[199] using unrestricted B3LYP orbitals, to minimize the effect of spin-contamination. In addition, single-point EOM-IP-CCSD calculations[197] were carried out[199] for the optimized structure of the anion; the resulting VDE values are also included in Table 8.1.

The best (highest-level/largest basis) estimates of both the VDE and the EA were obtained from the CCSD(T)/aug-cc-pVTZ calculations. The corresponding VDE = 2.40 eV agrees perfectly with the experimental result, VDE = 2.39 ± 0.04 eV.

8.3.2. Electron affinity of the chlorocyanomethyl radical

The adiabatic EA of CHClCN cannot be determined directly from the data in Figure 8.2, because the band origin is not obvious in the spectra. An estimate using the following approximation can be obtained based on the experimentally determined anion VDE = 2.39 ± 0.04 eV:[191]

$$EA \approx VDE + (EA_{calc} - VDE_{calc}) , \qquad (8.2)$$

where EA_{calc} and VDE_{calc} are the adiabatic EA of CHClCN and the VDE of $CHClCN^-$,

respectively, derived from theory calculations. Equation (8.2) assumes that the errors in the calculated EA and VDE values are similar, i.e. the shift between the VDE and adiabatic EA (attributed to the anion-neutral geometry difference) can be reliably evaluated by theory.

As seen in Table 8.1, both EA_{calc} and VDE_{calc} vary substantially depending on the theory level and the basis set used. However, per Eq. (8.2), the EA estimate is dependent on the difference between the two computed properties, rather than their individual values, and the variation of the difference is less significant. In the following analysis, we will use the best theory result, CCSD(T)/aug-cc-pVTZ, which is also in agreement with the experimentally determined VDE. Substituting the corresponding value of (EA_{calc} – VDE_{calc}) = –0.53 eV into Eq. (2), the electron affinity of chlorocyanomethyl radical is determined as EA = 1.86 ± 0.08 eV. The error-bars are a combination of the experimental uncertainty in the VDE and the deemed to be on the order of chemical accuracy (~ 1 kcal/mol)[204] uncertainty of the theory result. Thus determined EA value and the corresponding confidence interval are indicated in Figure 8.2. This result constitutes the first determination of the CHClCN radical EA using spectroscopic data.

To further support the above EA determination, the low-pass filter Fourier analysis, described previously,[205] was performed on both spectra shown in Figure 8.2. The "clean" spectra (shown only for 532 nm spectrum in red) revealed the onset of the transition at approximately 1.8 eV, as determined by the signal rising above the noise level, in agreement with the above EA estimate. The same analysis yielded a vibrational period of 450 ± 50 cm^{-1}, which we attribute to the umbrella mode excited upon photodetachment due to the anion-neutral geometry difference.

8.3.3. The C-H bond dissociation energy of chloroacetonitrile.

The above determination of EA(CHClCN) makes it possible to evaluate the C–H bond enthalpy of chloroacetonitrile using the general acidity/electron affinity cycle:[136]

$$DH_{298}(R–H) = \Delta_{acid}H_{298}(RH) + EA(R) – IE(H) + [\text{thermal corrections}] \quad (8.3)$$

In this equation, $\Delta_{acid}H_{298}(RH)$ is the gas-phase acidity of the closed-shell molecule, EA(R) is the electron affinity of its radical, and IE(H) = 313.6 kcal/mol (13.60 eV) is the ionization energy of atomic hydrogen.[144] Using the published acidity of chloroacetonitrile, $\Delta_{acid}H_{298}(CH_2ClCN)$ = 357.7 ± 2.0 kcal/mol,[206] and the EA of the corresponding radical, EA(CHClCN) = 1.86 ± 0.08 eV = 42.9 ± 1.8 kcal/mol, as determined above, while neglecting the small (usually ~ 0.3 kcal/mol) thermal corrections term, we find the C–H BDE of chloroacetonitrile to be DH_{298}(H–CHClCN) = 87.0 ± 2.7 kcal/mol.

The BDE is related to the stability of the resulting radical, with smaller DH_{298} values corresponding to greater radical stability. The above BDE for chloroacetonitrile is smaller than the C–H bond energies of many closed-shell molecules. For comparison, the BDEs of several halogen and cyano-substituted methanes are summarized in Table 8.2.[6,136,145,207] The corresponding radical stabilization energies (RSE), calculated as the difference between the BDE of methane and that of the corresponding substituted molecule, are also included in the table.

The relative stabilities of the substituted radicals are determined by a combination of inductive and resonance effects. Both halogens and CN are strong electron-withdrawing groups with respect to the molecular σ system, destabilizing the electron-deficient

radical center. However, with respect to the π system halogens act as electron donors, while the CN group stabilizes the radical via resonance interaction, by donating its π system to the extended molecular framework.[136,186] It is for this last reason that the BDEs of CH_3CN and $CH_2(CN)_2$ are both progressively smaller, in comparison to methane.[6,207]

While the extent of the π donation or resonance stabilization depends on the overlap between the orbitals on the substituent and the radical center,[186] the magnitude of the inductive effect depends on the substituent's electronegativity. In fluoro-substituted methanes, the σ withdrawing and π donation effects are nearly balanced out, as all four $CH_{4-n}F_n$ species (n = 0–3) have similar C–H BDEs (Table 8.2). However, replacing F with less electronegative Cl results in an increased stability of the chloromethyl radicals, as reflected in the RSE($CH_{4-n}Cl_n$) values.

The C–H BDE of CH_2ClCN, determined in this work, corresponds to an RSE of 17.9 ± 2.7 kcal/mol. This is almost twice as large as the corresponding CH_2Cl_2 value (9.2 ± 0.6 kcal/mol),[145] but similar to that for $CH_2(CN)_2$ (16.2 ± 2.1 kcal/mol).[6] Moreover, the effect of the mixed CN and Cl substitution on the radical stability is comparable to (if not greater than) the sum of the separate single substitutions, RSE(CH_3CN) + RSE(CH_3Cl) = 15.5 ± 2.1 kcal/mol. These findings suggest that the mixed CHClCN radical benefits from a cooperative interaction of the unsaturated π resonance attributed to CN, and the π donation due to Cl. A captodative combination of these effects yields a radical of increased stability.[208]

8.4. Chlorocyanocarbene

The results for $CClCN^-$ (355 nm) are shown in Figure 8.4b, where they are

presented in comparison with the corresponding data for (a) CCl_2^- (355 nm)[209] and (c) $C(CN)_2^-$ (266 nm).[7] The results in (b) are new, while the "reference" data in (a) and (c) are not. The CCl_2^- dataset (a) is similar to the one reported by us recently, albeit in a different context.[209] These imaging results are fully consistent with the higher-resolution photoelectron spectrum reported by Lineberger and co-workers.[8] The $C(CN)_2^-$ data in (c) are adopted from our earlier work.[7]

The bulk of the following discussion (Sections 8.4.2–8.4.6) is concerned only with the new $CClCN^-$ results, while the comparison to CCl_2^- and $C(CN)_2^-$ is found in Section 8.5.2. However, first (in Section 8.4.1) we present a brief discussion of the qualitative insight gained from the CCl_2^- data, which helps set the stage for the assignment of the $CClCN^-$ bands.

8.4.1. Carbene anion imaging on the example of dichlorocarbene

The CCl_2^- data in Figure 8.4a is a particularly instructive case of carbene spectroscopy, because the characters of the σ and π carbene orbitals are immediately apparent in the PADs of the two clearly separated CCl_2^- photodetachment bands. Since the σ orbital (nominally an in-plane sp^2 hybrid) is totally symmetric with respect to the symmetry operations of the molecular point group,[15] and because of its significant *s* character,[209] the σ^{-1} PAD (triplet carbene) is notably parallel with respect to the laser polarization axis (vertical in Figure 8.4). On the other hand, the PAD of the π^{-1} channel, (singlet carbene) is perpendicular, characteristic of a *p*-like initial state.

The above qualitative analysis is not unique to dichlorocarbene. In general (and with due caution), in the moderate-eKE regime, we expect photodetachment from the σ

non-bonding orbital of a carbene anion (the triplet channel) to yield a predominantly parallel PAD. In the photodetachment from the π orbital (the singlet channel), a predominantly perpendicular PAD is expected.[188] Thus, given resolved singlet and triplet bands, photoelectron imaging of carbenes allows the assignment of the transitions (and hence the ground-state multiplicity of the carbene), based on qualitative examination of raw photoelectron images.

8.4.2. CClCN⁻ band assignments

A similar analysis is now applied to CClCN. The spectrum in Figure 8.4b consists of two main overlapping features, which we expect to correspond to the lowest-energy singlet and triplet states of CClCN. These states are ^{1}A′: …$(15a')^2(4a'')^0$ and ^{3}A″: …$(15a')^1(4a'')^1$, where 15*a*′ and 4*a*″ are CClCN's canonical σ and π carbene orbitals. Although the band separation in Figure 8.4b is not as good as in the CCl_2 case (Figure 8.4a), it is good enough to see that the outer (lower-eBE) band in the $CClCN^-$ image has a slightly perpendicular PAD, while the more intense higher-eBE transition comes with a clearly parallel angular distribution. Based on these qualitative PADs, following the arguments laid out in Section 4.0, we assign the lower-eBE band to the closed-shell singlet state of CClCN (^{1}A′), while the higher-eBE transition is assigned to the triplet state (^{3}A″). As an aside, a similar analysis could not be applied in the dicyanocarbene case, because the overlap of the singlet and triplet bands in the $C(CN)_2^-$ photoelectron image made it impossible to resolve even the qualitative character of the corresponding PADs.[7]

Figure 8.4b also reveals a possible additional transition, appearing as a weak central

spot in the image and distinguishable as a shoulder (marked *) near the spectral cutoff. If indeed distinct from the $^3A''$ band, this transition could correspond to the open-shell singlet state $^1A''$: …$(15a')^1(4a'')^1$. The plausibility of this assignment is argued in Section 8.4.6.

The photoelectron spectrum in Figure 8.4b has been modeled as a sum of three bands: a simple Gaussian for $^1A'$ and modified Gaussians (Eq. 8.1) for the $^3A''$ and (*) bands, which are close to the energetic cutoff. The resulting fit to the experimental spectrum is shown in Figure 8.4b. From the fit, the VDE corresponding to the $^1A'$ band is 2.76 ± 0.05 eV, with an onset of the transition observed around 2.5 eV. The VDE corresponding to the $^3A''$ state is 3.25 ± 0.05 eV. These results are included in Table 8.3.

8.4.3. Anion and neutral geometries

Ab initio calculations were performed for the anion and the singlet and triplet states of the neutral carbene. The geometries were optimized[195] at the CCSD level of theory with the aug-cc-pVTZ basis set. The resulting structures of the $^2A''$ ground state of the anion and the closed-shell singlet ($^1A'$) and the triplet ($^3A''$) states of the neutral are shown in Figure 8.5. All three equilibrium structures are planar, but differ in detail, particularly the bond angle at the carbene center. The anion geometry is closest to that of the singlet, with a small difference in the bond angle, but a notable change in the C–Cl bond length. The triplet structure has a more open carbene bond angle, with a 30° difference with respect to the anion. The optimized geometry of the open-shell singlet, $^1A''$, is not included in the figure, but expected to be most similar to the $^3A''$ geometry.

Based on these structures, we expect a broad Franck-Condon envelope for the

triplet band, more so than the singlet. Thus, although the experimental VDE of the triplet is ~0.5 eV higher than that of the singlet (see Figure 8.4b), the difference in the adiabatic electron affinities (equal to the singlet-triplet splitting, $\Delta E_{S\text{-}T}$) is expected to be significantly smaller, i.e. $\Delta E_{S\text{-}T} < 0.5$ eV. The origin of the triplet band is not observed in Figure 8.4b, not only due to the overlap with the singlet, but also possibly because of a small Franck-Condon factor corresponding to the 0-0 transition. Hence, the EA of the triplet carbene and $\Delta E_{S\text{-}T}$ cannot be estimated based on the experimental results alone. A higher-resolution spectrum with detailed Franck-Condon modeling would be helpful.[8] From the available data, no definite conclusion can be drawn even about the *sign* of the singlet-triplet splitting.[210]

8.4.4. Electron affinity and vertical detachment energy

The adiabatic EAs of the $^1A'$ and $^3A''$ states of the CClCN carbene, as well as the corresponding anion VDEs were computed[195] using the coupled-cluster theory. In addition to full geometry optimizations at the CCSD level, single-point CCSD(T)/aug-cc-pVTZ calculations were carried out[195] for the CCSD/aug-cc-pVTZ optimized geometries. The VDEs were also computed[199] directly using the EOM-IP-CCSD(dT) method, using the above anion geometry. The results are summarized in Table 8.3.

The calculated VDE values, corresponding to detachment to both the $^1A'$ and $^3A''$ states, are in good agreement with the peak energies in the experimental spectrum (Figure 8.4b). In particular, we note the excellent agreement of the CCSD/aug-cc-pVTZ results with the experiment (2.792 eV and 3.254 eV vs. 2.76 ± 0.05 eV and 3.25 ± 0.05 eV for the $^1A'$ and $^3A''$ VDEs, respectively). Inclusion of the triple excitations, CCSD(T), does

not improve the predictions, possibly because the triples are included without the corresponding geometry relaxation. A good agreement with the experimental values is also observed for the EOM-IP-CCSD(dT)/aug-cc-pVTZ results (2.738 eV and 3.306 eV vs. the above experimental VDEs). With the EOM-IP-CCSD method, inclusion of the diagonal triples correction (dT)[198] lowers the VDE values, while increasing the basis set size from double to triple-ζ has an opposite effect.

The calculated EA values for the closed-shell singlet carbene (Table 8.3) also agree very well with the observed onset of the ^{1}A′ band in Figure 8.4.

8.4.5. The singlet-triplet splitting of chlorocyanocarbene

Per Section 4.3, at the relaxed geometry of the anion, singlet CClCN is expected to lie (vertically) ~0.5 eV lower than the triplet. This prediction is in excellent agreement with the experimental results in Figure 8.4b, where the ^{1}A′ band peaks 0.5 eV below the ^{3}A″ band maximum. The calculations further predict that the relaxed geometry of the singlet is more similar to that of the anion than the triplet state's structure (see Figure 8.5). Accounting for the geometry relaxation, the singlet and the triplet states of CClCN are nearly degenerate, with a very small adiabatic energy gap. The CCSD/aug-cc-pVTZ calculations (Table 8.3) predict a slightly negative $\Delta E_{S\text{-}T} = -0.063$ eV (i.e., the triplet is below the singlet), while inclusion of the triples correction, CCSD(T), results in a positive $\Delta E_{S\text{-}T} = 0.080$ eV (the triplet higher than the singlet).[210]

The above predictions were obtained within a single-reference formalism. Taking into account the multiconfigurational nature of cyanocarbenes, we adopt a more appropriate description, based on the spin-flip method.[176,177,196,197] Although also rooted in a

nominally single-reference formalism, the EOM-SF strategy allows to calculate the energies of the low-spin excited states starting from a robust high-spin reference, thus providing a more accurate description of the multiconfigurational target states.[197] We use the high-spin (M_S = 1) component of the ^{3}A″ state of CClCN as a reference to describe the closed- and open-shell singlet states, ^{1}A′ and ^{1}A″, as well as the low-spin (M_S = 0) component of the ^{3}A″ state itself. All target states are described with single spin-flip excitations of the reference, as apparent from their leading electron configurations included in Figure 8.5.

The SF calculations were carried out[199] with the aug-cc-pVTZ basis set for each of the three CClCN geometries shown in Figure 8.5, corresponding to the CCSD/aug-cc-pVTZ optimized structures of the anion, the closed-shell singlet, and the triplet. As the use of HF orbitals indicated significant spin contamination in the wave functions, unrestricted B3LYP orbitals were used for the EOM-SF-CCSD calculations, taking advantage of the relative insensitivity of coupled-cluster theory to the choice of orbital bases. Typical spin expectation values $\langle S^2 \rangle$ = 2.02–2.04 were achieved for the triplet reference, compared to the 2.25–2.35 range resulting from the unrestricted HF orbitals. As recommended by Krylov,[179] the energy of the M_S = 0 component of the ^{3}A″ state, rather than that of the M_S = 1 reference, was used for calculating the singlet-triplet energy gaps.

The results are summarized in Figure 8.5. For each of the three geometries studied, the vertical ordering of the ^{1}A′, ^{3}A″(M_S = 0), and ^{1}A″ states is indicated, with the energies given relative to the lowest state *at that* geometry. Two energy values are given for each of the target states: the EOM-SF-CCSD results (in plain font) and those including the

non-iterative diagonal triples corrections (dT)[198] (in bold). The dominant electron configurations for each of the target states are also indicated, with the orbitals shown corresponding to the two non-bonding carbene orbitals, 15a' (σ) and 4a'' (π). The open-shell target states, i.e. the open-shell singlet, ^{1}A″, and the M_S = 0 component of the triplet, ^{3}A″, are described as linear combinations of the two dominant configurations shown. As always, the symmetric (with respect to exchange) spin combination corresponds to the triplet state, while the anti-symmetric – to the open-shell singlet.

The findings for the anion geometry can be compared directly to the experimental results. The photoelectron spectrum from Figure 8.4b is reproduced on the left margin of Figure 8.5, with the bands aligned to coincide approximately with the corresponding neutral states. Both the experiment and theory show that at this geometry the ^{1}A′ state of CClCN is lower in energy than the ^{3}A″ state. The experimentally determined difference between the two VDEs (0.49 ± 0.07 eV, per Table 8.3) is in agreement with the vertical singlet-triplet gap predicted by the calculations. We find again (as in Section 8.4.4) the EOM-SF-CCSD result (0.47 eV) to agree slightly better with the experiment than that including the triples correction (0.59 eV), but both values fall within or very close to the uncertainty range.

By comparing the absolute energies of the target states at different geometries, the adiabatic relaxation energy of the closed-shell ^{1}A′ state relative to the anion geometry, as well as the adiabatic singlet-triplet splitting of the carbene are determined (Figure 8.5 and Table 8.3). With the highest-level/largest basis set used EOM-SF-CCSD(dT)/aug-cc-pVTZ method, we obtain $\Delta E_{S\text{-}T}$ $\Delta E_{S\text{-}T}$ = 0.010 eV. This estimate is small in magnitude, consistent with the CCSD(T)/aug-cc-pVTZ results. The positive sign of $\Delta E_{S\text{-}T}$ implies

that the singlet, $^1A'$, is the ground state of the carbene.

While these conclusions are consistent with the experimental spectrum, the predicted magnitude of $\Delta E_{S\text{-}T}$ is so small that, for practical purposes, the singlet and triplet states should be viewed as nearly degenerate. This is especially true, considering how far apart these states are in the configuration space.

8.4.6. The open-shell singlet of CClCN

The results in Figure 8.5 also shed light on the plausibility of assigning the weak near-zero-eKE feature (*) in Figure 8.4b to the open-shell singlet state of CClCN. The VDE of the $^2A'' \rightarrow {}^1A''$ transition was calculated as the VDE of $^2A'' \rightarrow {}^3A''$, determined by the EOM-IP-CCSD method, combined with the EOM-SF-CCSD excitation energy of the $^1A''$ state relative to the $^3A''$ ($M_S = 1$) reference. The results are included in Table 8.3. Although the predicted VDE > 4 eV is significantly above the 3.5 eV photon energy, the $^2A'' \rightarrow {}^1A''$ transition is expected to have a broad Franck-Condon envelope, similar to the $^2A'' \rightarrow {}^3A''$ band in Figure 8.4b, as follows from the common orbital components, $\ldots(15a')^1(4a'')^1$, of the $^3A''$ and $^1A''$ wavefunctions.

The results in Table 8.3 and Figure 8.5 suggest that even at the $^3A''$ geometry the $^1A''$ carbene lies at or just above ~3.5 eV (obtained as the adiabatic EA of the high-spin component of the $^3A''$ state combined with the EOM-SF excitation energy of $^1A''$ relative to the triplet reference). Full geometry relaxation of the $^1A''$ state will lower the energy further and hence we expect adiabatic EA($^1A''$) ≤ 3.5 eV. Therefore, it is indeed possible that the weak band (*) in the proximity of the energetic cutoff in Figure 8.4 is due to the open-shell carbene. Future experiments at higher photon energy may clarify this

assignment.

8.5. Summary and conclusions

8.5.1. Results summary

The observed VDE of $CHClCN^-$, 2.39 ± 0.04 eV, is in excellent agreement with the CCSD(T)/aug-cc-pVTZ prediction of 2.40 eV. The significant geometry change predicted for the detachment transition (non-planar pyramidal anion → trigonal planar neutral) is consistent with the broad photoelectron band observed in the experiment. The adiabatic EA of the chlorocyanomethyl radical is determined as 1.86 ± 0.08 eV. This result is the first determination of the EA using spectroscopic data.

From the above EA(CHClCN) and the acidity/affinity cycle, the C–H BDE of chloroacetonitrile is determined, DH_{298}(H–CHClCN) = 87.0 ± 2.7 kcal/mol. The corresponding radical stabilization energy (due to the mixed Cl and CN substitution) is 17.9 ± 2.7 kcal/mol.

Photoelectron imaging of $CClCN^-$ reveals two main transitions, assigned to the closed-shell singlet ($^1A'$) and the triplet ($^3A''$) states of the CClCN carbene. The respective VDEs are 2.76 ± 0.05 eV and 3.25 ± 0.05 eV. A hint of the low-energy tail of a third, higher-energy band is present in the data, tentatively assigned to the open-shell singlet ($^1A''$) state of the carbene. The experimental results are in good agreement with the theoretically predicted singlet-triplet vertical energy gap at the anion geometry, but inconclusive with regard to the adiabatic state ordering and the magnitude of the singlet-triplet splitting in CClCN. *Ab initio* calculations, using the spin-flip approach in combination with the coupled-cluster theory, predict that the $^1A'$ and $^3A''$ states are near-

degenerate adiabatically, with the $^1A'$ state just below $^3A''$ ($\Delta E_{S\text{-}T} \approx 0.01$ eV).

8.5.2. The Cl vs. CN substitution effects

The EAs of substituted radicals and carbenes increase with the Cl and/or CN substitution, commensurate with the substituents' electronegativity. More intricate effects are observed in the intramolecular charge distributions and the relative energies of the radical and carbene π orbitals.

One important observation concerns the structure of the $CHClCN^-$ anion. To put it in perspective, most substituted methylides, including $CHCl_2^-$,[8] exhibit similar pyramidal structural motifs. To the contrary, $CH(CN)_2^-$ is planar, as is the corresponding radical, $CH(CN)_2$.[6] The planar geometry is attributed to the strong electron-withdrawing properties of the cyano-substituent, as even in the anion, the central carbon atom in $CH(CN)_2^-$ is positively charged.[6]

With the drastically different geometries of $CHCl_2^-$ and $CH(CN)_2^-$, the structure of the mixed anion, $CHClCN^-$, is not obvious *a priori*, but the results presented here indicate that $CHClCN^-$ is similar to $CHCl_2^-$, rather than $CH(CN)_2^-$. It too has a non-planar equilibrium geometry, with a negative charge on the central carbon (Figure 8.3). For further insight, consider that the singly-substituted anion $NCCH_2^-$ is also non-planar, in contrast to $CH(CN)_2^-$.[6,207] Substituting a π-donor Cl for one of the hydrogens in $NCCH_2^-$ pushes the resulting anion towards $CHCl_2^-$, reinforcing the non-planar bonding motif with a negative charge on the central carbon. Thus, among the doubly substituted methylides, the structural properties of $CHClCN^-$ are similar to those of $CHCl_2^-$, rather than $CH(CN)_2^-$.

An opposite trend is seen in the stabilities of the corresponding radicals, determined by the substituent effects on their singly occupied π HOMOs. As determined in this work, CHClCN is significantly more stable than $CHCl_2$, but is similar in this regard to $CH(CN)_2$. The Cl substituent is thus more effective in stabilizing a doubly-substituted radical when accompanied by CN, rather than a second Cl.

Moreover, the effect of the heterogeneous CN and Cl substitution is similar to, and may even be greater than, the sum of the respective first substitutions, as seen by comparing RSE(CH_2ClCN) to RSE(CH_3Cl) + RSE(CH_3CN) (Table 8.2). This is remarkable, because substitution effects are generally not additive, with the incremental effect of the second substituent usually smaller than that of the first. This is clearly borne out, for example, by the RSE values for $CH_{4-n}Cl_n$ and $CH_{4-n}(CN)_n$ in Table 8.2. The results of this work suggest cooperative (captodative) interaction of Cl and CN, whereas the unsaturated π resonance (due to CN) combined with the π donation (due to Cl) yields a mixed doubly-substituted radical of increased stability.

The effects of substitution on the ground-state multiplicity and the singlet-triplet splitting in the halo- and cyano-carbenes are summarized in Table 8.4.[7,8,153,159,188,211] For CCl_2, CClCN, and $C(CN)_2$, the relative ordering of the singlet and triplet states (which is related to, but not the same as the ordering of the spectral bands in Figure 8.4) is shown schematically in Figure 8.6.[7,8]

Unlike the corresponding radicals and their anions, chlorocyanocarbene does not resemble either dichlorocarbene[8] or dicyanocarbene.[7] Instead, the mixed species is intermediate between the two homogeneously substituted carbenes. In CCl_2, π donation by the halogen atoms destabilizes the non-bonding $2p(\pi)$ orbital on the carbene center,

thus favoring the …$\sigma^2\pi^0$ configuration and a singlet ground state.[187] In $C(CN)_2$,[8] the CN substituent has an opposite effect, stabilizing the π orbital via resonance interaction, so that the …$\sigma^1\pi^1$ configuration and a triplet ground state are favored.[7,187] In CClCN, the π donation by the halogen, on the one hand, and π resonance stabilization by CN, on the other, result in a near-degeneracy of the …$\sigma^2\pi^0$ and …$\sigma^1\pi^1$ configurations and the respective singlet and triplet states.

Other properties of the mixed CClCN carbene are also intermediate between its homogeneously substituted analogues. First, as shown in Figure 8.6, the respective electron affinities increase from CCl_2 to CClCN to $C(CN)_2$, as expected due to a combination of the inductive and π resonance properties of CN. Second, a similar trend is exhibited by the carbene bond angles. In all three systems in Figure 8.6, the carbene bond angle of the anion (A) is similar to that of the closed-shell singlet carbene (S), while the bond angle in the triplet (T), as well as in the open-shell $\sigma^1\pi^1$ singlet (not shown), is much more open. This trend is understood in terms of the electronic structure properties of carbenes[187] and the triplet-state bond angle in CClCN falls in between the respective triplets of CCl_2 and $C(CN)_2$.

In conclusion, the π-donor halogen and π-acceptor cyano groups exhibit a cooperative effect on the stability of the heterogeneously substituted radical and, to the contrary, competing effects on the singlet-triplet splitting in the mixed carbene.

Table 8.1 Adiabatic electron affinity (EA) of CHClCN and vertical detachment energy (VDE) of $CHClCN^-$ determined using different methods and basis sets. All values are in electron-volts.

Method	Basis set	EA	VDE	(EA_{calc} – VDE_{calc})
B3LYP [a]	aug-cc-pVDZ	1.93	2.44	–0.51
	aug-cc-pVTZ	1.89	2.46	–0.57
	6-311++G**	1.91	2.46	–0.57
	6-311++G(3df,3pd)	1.87	2.46	–0.59
CCSD [a]	aug-cc-pVDZ [b]	1.70	2.19	–0.49
	aug-cc-pVTZ	1.75	2.32	–0.57
	6-311++G** [b]	1.47	2.05	–0.58
	6-311++G(3df,3pd) [b]		2.30	
CCSD(T) [a]	aug-cc-pVDZ [b]	1.78	2.22	–0.44
	aug-cc-pVTZ	**1.87**	**2.40**	**–0.53**
	6-311++G** [b]	1.53	2.06	–0.53
EOM-IP-CCSD [b]	aug-cc-pVDZ		2.29	
	6-311++G**		2.20	
	6-311++G(3df,3pd)		2.46	
Experiment		1.86 ± 0.08 [c]	2.39 ± 0.04	

[a] The B3LYP, CCSD, and CCSD(T) values are calculated as the difference between the energies of the neutral and the anion (zero-point vibrational energy corrections are not included). For VDE calculations, both the neutral and the anion energies were computed for the anion equilibrium geometry. For adiabatic EA calculations, the respective neutral and anion equilibrium geometries were used. The geometries were optimized at the CCSD/aug-cc-pVTZ level (Figure 8.3). Theory values in bold correspond to the highest theory level and basis set.

[b] When indicated, B3LYP orbitals were used as the basis for single-point coupled-cluster calculations in order to reduce the effect of spin-contamination. In all other cases, the canonical HF orbitals were used. The absolute energy difference between the two approaches is ≤ 0.02 eV for the computed EA and VDE values and ≤ 0.01 eV for (EA_{calc} – VDE_{calc}).

[c] Estimated value determined using Eq. (8.2) and the CCSD(T)/aug-cc-pVTZ result for (EA_{calc}–VDE_{calc}).

Table 8.2 The C–H bond dissociation energies, DH_{298}(R–H), and the corresponding radical stabilization energies, RSE, of substituted methanes. All values in kcal/mol.

Compound	DH_{298}	Reference	RSE [a]
CH_4	104.9 ± 0.4	[136]	0
Fluoro-methanes:			
CH_3F	103.2 ± 1.0	[145]	1.7 ± 1.1
CH_2F_2	106.4 ± 0.7	[145]	–1.5 ± 0.8
CHF_3	106.7 ± 1.0	[145]	–1.8 ± 1.1
Chloro-methanes:			
CH_3Cl	100.1 ± 0.6	[145]	4.8 ± 0.7
CH_2Cl_2	95.7 ± 0.5	[145]	9.2 ± 0.6
$CHCl_3$	93.8 ± 0.6	[145]	11.1 ± 0.7
Cyano-methanes:			
CH_3CN	94.2 ± 2.0	[207], [6]	10.7 ± 2.0
$CH_2(CN)_2$	88.7 ± 2.1	[6] [b]	16.2 ± 2.1
$CH(CN)_3$	unknown		
Chlorocyanomethane:			
CH_2ClCN	87.0 ± 2.7	this work	17.9 ± 2.7

[a] The radical stabilization energies are calculated as RSE(R–H) = DH_{298}(CH_3–H) – DH_{298}(R–H).

[b] The C–H BDE of $CH_2(CN)_2$ was determined in Ref. [6] assuming IE(H) = 315.1 kcal/mol.[140] The BDE given here reflects the corrected value of 313.6 kcal/mol.[144] The revised DH_{298}[H–$CH(CN)_2$] value is within the uncertainty range of the original determination.

Table 8.3 Calculated VDEs of $CClCN^-$ corresponding to detachment to the $^1A'$, $^3A''$, and $^1A''$ states of the neutral, the adiabatic EAs of the singlet and triplet carbene, and the corresponding values of adiabatic singlet-triplet splitting ($\Delta E_{S\text{-}T}$). All values are given in eV, without zero-point energy corrections. The experimental VDE values, determined in this work, are included for comparison.

Method/basis set	VDE		Adiabatic EA			Adiabatic $\Delta E_{S\text{-}T}$ [a]
	$^2A'' \rightarrow {}^1A'$	$^3A''$	$^1A''$	$^1A'$	$^3A''$	
CCSD/aug-cc-pVDZ	2.773	3.278		2.536	2.489	–0.047
CCSD/aug-cc-pVTZ	2.792	3.254		2.575	2.512	–0.063
CCSD(T)/aug-cc-pVTZ [b]	2.721	3.331		2.551	2.631	0.080
EOM-IP-CCSD/aug-cc-pVDZ [b,c]	2.739	3.245				
EOM-IP-CCSD/aug-cc-pVTZ [b,c]	2.924	3.442				
EOM-IP-CCSD(dT)/aug-cc-pVDZ [b,c]	2.575	3.121				
EOM-SF-CCSD/aug-cc-pVDZ [b,c,d]			4.688[e]			0.0015
EOM-SF-CCSD(dT)/aug-cc-pVDZ [b,c,d]			4.241[e]			0.052
Experiment	2.76(5)	3.25(5)		~2.5		

[a] Negative sign of $\Delta E_{S\text{-}T}$ indicates that the triplet state lies adiabatically below the singlet, and vice versa.

[b] From single-point calculations carried out for CCSD/aug-cc-pVTZ optimized geometries of the anion and the neutral states (as appropriate), summarized in Figure 8.5.

[c] B3LYP orbitals were used as the basis for single-point coupled-cluster calculations in order to reduce the effect of spin-contamination (see the text for details).

[d] Calculations were performed starting from the high-spin (M_S = 1) reference, while the

singlet-triplet splitting was determined for the low-spin (M_S = 0) component of the triplet state, as recommended by the authors of Spin-Flip.[179,197]

[e] Calculated as the EOM-SF excitation energy of the ^{1}A″ state (the leading two-determinant configuration shown in Figure 8.5) relative to the ^{3}A″ (M_S = 1) reference, combined with the VDE of the ^{2}A″ → ^{3}A″ (M_S = 1) detachment transition determined using the corresponding EOM-IP method.

Table 8.4 The ground-state multiplicity and the singlet-triplet splitting (in eV) of halo- and cyano- carbenes. Positive $\Delta E_{S\text{-}T}$ values correspond to singlet ground states.

Carbene	Singlet/Triplet	$\Delta E_{S\text{-}T}$ / eV	Reference
CH_2	triplet	−0.390 ± 0.004	[188]
Halo-carbenes:			
CHF	singlet	0.646 ± 0.017	[153]
CHCl	singlet	0.18 ± 0.11	[153]
CCl_2	singlet	0.9 ± 0.2	[8]
Cyano-carbenes:			
HCCN	triplet	−0.516 ± 0.017	[159]
$C(CN)_2$	triplet	−0.52 ± 0.05	[7]
Chlorocyanocarbene:			
CClCN	(singlet) [a]	~0.01 [b]	this work

[a] The parentheses indicate that the experiment is inconclusive with regard to the ground-state multiplicity of CClCN, while the most advanced theory methods predict a singlet ground state. However, the predicted singlet-triplet splitting is small enough that the singlet and triplet states, separated significantly in the configuration space, should be viewed as effectively degenerate energetically.

[b] Theory estimate, consistent with the experimental results.

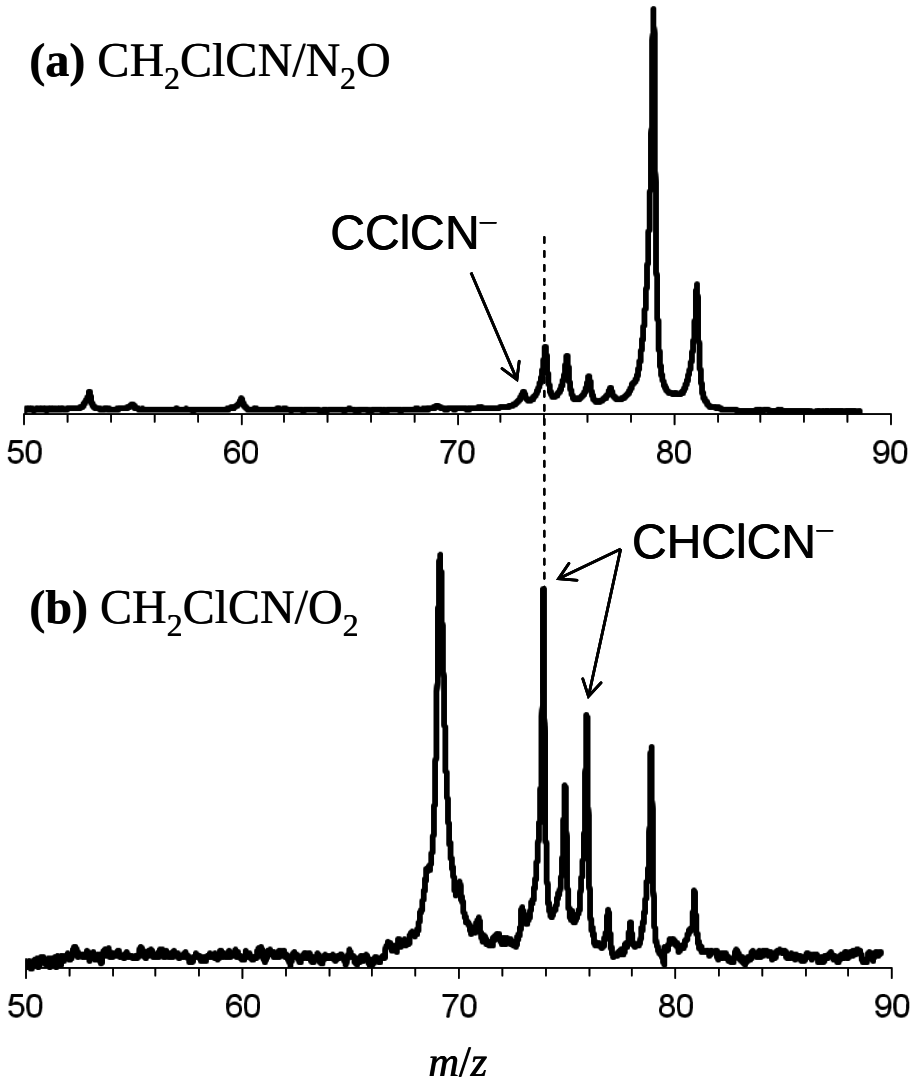

Figure 8.1 Representative time-of-flight mass spectra for (a) CH_2ClCN/N_2O and (b) CH_2ClCN/O_2 reaction gas mixtures. All chlorine-containing anions yield two dominant mass-spectral peaks each, due to two naturally abundant chlorine isotopes, ^{35}Cl and ^{37}Cl. The *m/z* = 74 and 76 a.m.u. peaks correspond to $CHClCN^-$, while *m/z* = 73 and 75 a.m.u. correspond to $CClCN^-$. Most of the 75 a.m.u. intensity, however, is attributed to a different species, possibly $HNO^-\cdot N_2O$.

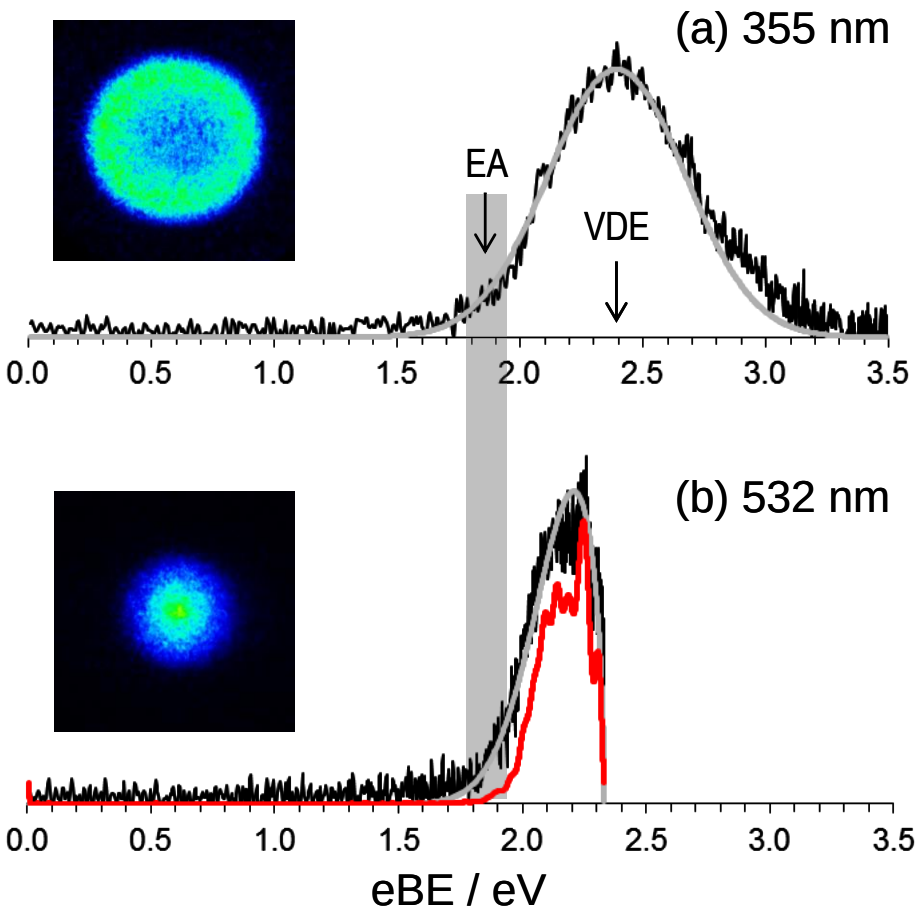

Figure 8.2 Photoelectron images and spectra of $CHClCN^-$ obtained at (a) 355 nm and (b) 532 nm. The grey curves are fits to the experimental data. The red curve in (b) is the "clean" spectrum obtained using the low-pass filter Fourier analysis, as described in the text.

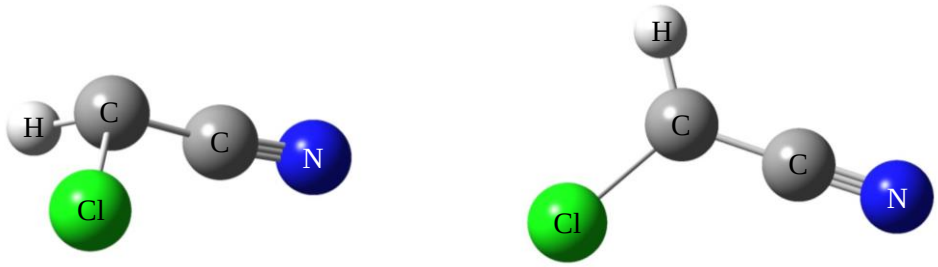

$CHClCN^-$ $CHClCN$

Figure 8.3 CCSD/aug-cc-pVTZ optimized geometries of $CHClCN^-$ and CHClCN. Anion structural parameters: R_{C-C} = 1.415 Å, $R_{C\equiv N}$ = 1.165 Å, R_{C-Cl} = 1.840 Å, R_{C-H} = 1.086 Å, ∠Cl–C–C = 110.1°, ∠Cl–C–H = 105.8°, ∠C–C–N = 174.5°, Dihedral(Cl–C–C–N) = 125.9°, Dihedral(H–C–C–N) =–116.8°. Neutral (planar): R_{C-C} = 1.396 Å, $R_{C\equiv N}$ = 1.172 Å, R_{C-Cl}=1.699 Å, R_{C-H} = 1.076 Å, ∠Cl–C–C = 120.4°, ∠Cl–C–H = 117.7°, ∠C–C–N =179.1°, Dihedral(Cl–C–C–N) = 180°.

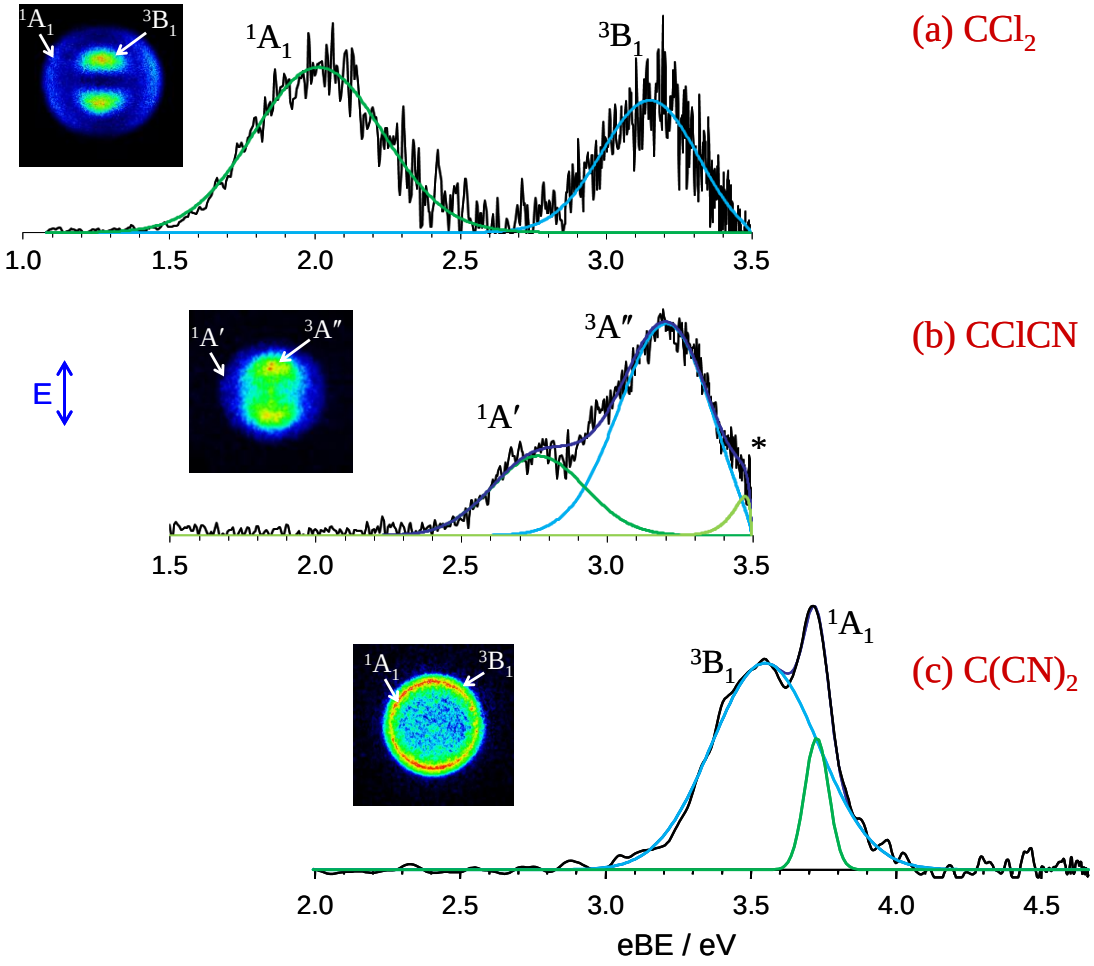

Figure 8.4 Photoelectron images and spectra of (a) CCl_2^- at 355 nm, (b) $CClCN^-$ at 355 nm, and (c) $C(CN)_2^-$ at 266 nm (adopted from earlier work).[7] Bands are fit with Gaussian or modified Gaussian functions (see the text for details). The singlet bands (S) are fit with green curves and correspond to the respective $^1A_1$ states of CCl_2 and $C(CN)_2$ and the $^1A'$ state of CClCN. The triplet bands are fit with blue curves and correspond to the $^3B_1$ states of CCl_2 and $C(CN)_2$ and the $^3A''$ state of CClCN.

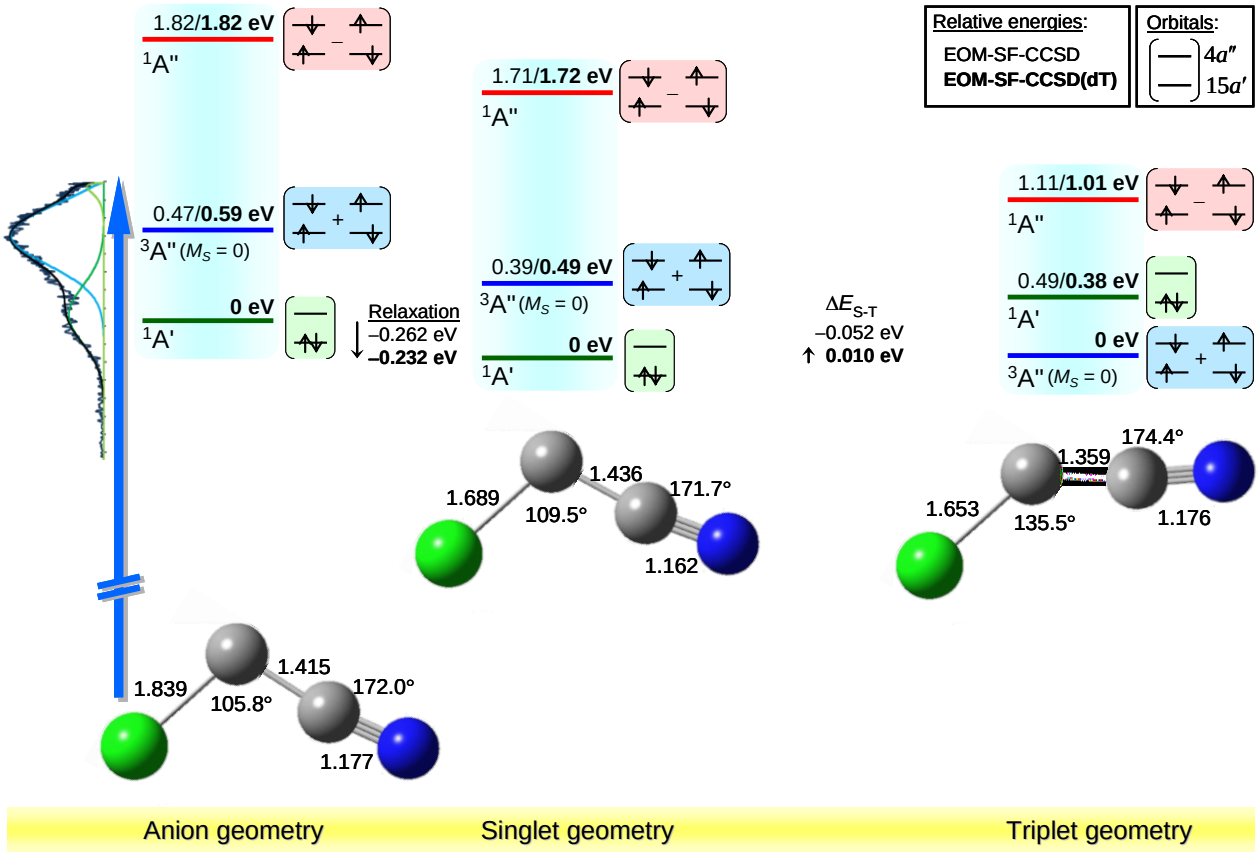

Figure 8.5. Manifolds of the low-lying electronic states of neutral CClCN, calculated using the EOM-SF-CCSD(dT)/aug-cc-pVTZ method for the equilibrium geometries of the anion, the singlet neutral, and the triplet neutral. The geometries were optimized at CCSD/aug-cc-pVTZ level of theory. The bond lengths are shown in Angstroms. For each of the three geometries, the vertical ordering of the 1A′, 3A″ (MS = 0), and 1A″ states is indicated, with the energies given relative to the lowest state at that geometry. Two energy values are given for each of the target states: the EOM-SF-CCSD results (in plain font) and those including the non-iterative diagonal triples corrections (dT) (in bold). The dominant electron configurations for each of the target states are also indicated, with the orbitals shown corresponding to the two non-bonding carbene orbitals, 15a′ (σ) and 4a″ (π).

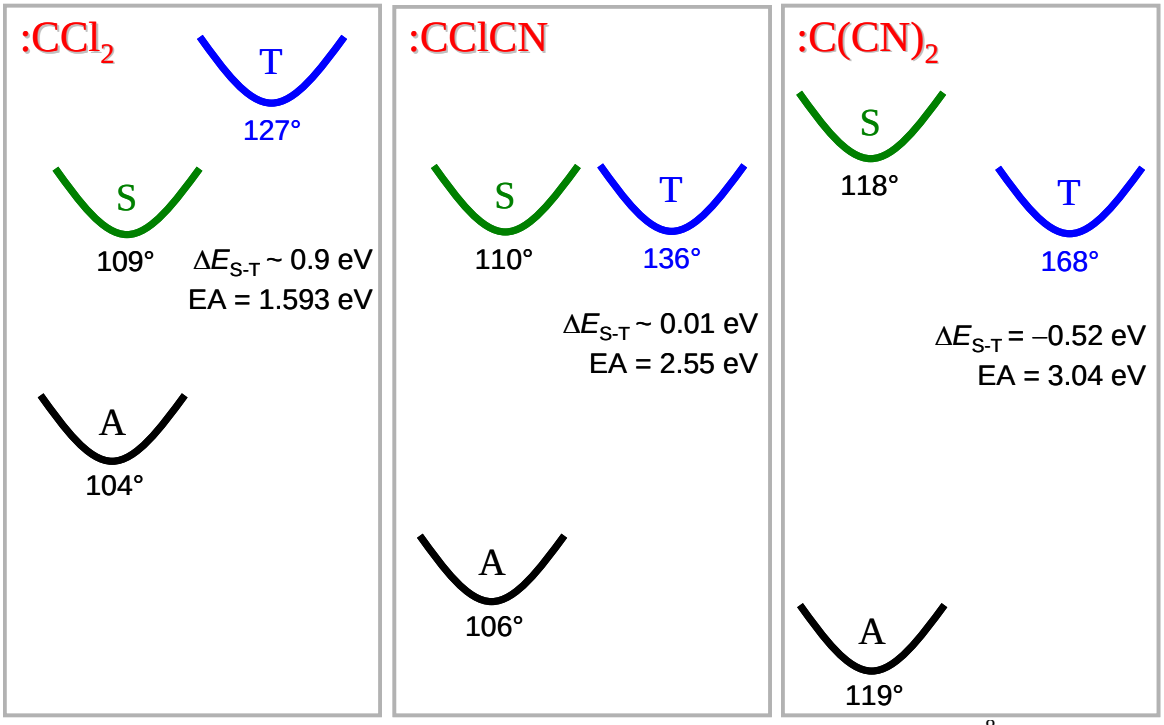

Figure 8.6 Relative ordering of the singlet (S) and triplet (T) states of CCl_2,[8] CClCN and $C(CN)_2$,[7] with the corresponding EAs, adiabatic singlet-triplet splittings (ΔE_{S-T}), and approximate carbene bond angles in both the neutral and the anion (A) states shown.

CHAPTER 9

PHOTOELECTRON SPECTROSCOPY AND PHOTOCHEMISTRY OF TETRACYANOETHYLENE RADICAL ANION IN THE GAS PHASE

9.1. Introduction

In the past decades, a considerable effort has been devoted to the preparation and study of molecule-based conductors, superconductors, and magnets. Electron-donor and electron-acceptor molecules play a major role in their development. One type of these molecules are organocyanides, which have been used extensively in materials chemistry due to their electron-acceptor properties and ability to form stable charge-transfer complexes and salts[212]. Thorough characterization of these molecules, especially their electron acceptance properties, is essential for understanding the bulk properties of the materials that contain them, as well as for the design of novel materials with enhanced characteristics.

Tetracyanoethylene (TCNE), the forerunner molecule in the class of strong electron acceptors[213], is well known for its highly conjugated π-system, which accounts for its unique reactivity[214]. The D_{2h} symmetry equilibrium structure of TCNE[9,10] is shown schematically in the inset in Figure 9.1. This molecule is an exceptionally strong dienophile[215]. It plays an integral role in many substitution and addition reactions, such as the Diels-Alder reactions[213], and is used as an oxidizing agent in the preparation of organic magnets, conductors[216], and superconductors[217]. It is also known to form stable charge-transfer complexes with many organometallic substrates, which makes it a key

component for study of electron-transfer reactions[218].

Despite the variety of applications in materials and organic chemistry[215], some key properties of TCNE and the corresponding reduced anion are still in question. For example, the adiabatic electron affinity (EA) of TCNE has been evaluated only indirectly through gas-phase electron-transfer equilibrium and the presently accepted value EA = 3.17 ± 0.20 eV[219] encompasses a broad uncertainty range. The molecular structure and stability of neutral and reduced TCNE have been studied theoretically[9,10], but the results vary significantly depending on the level of theory. For example, the MP2/aug-cc-pVDZ calculations predict EA = 2.17 eV, while CCSD/aug-cc-pVDZ (at the B3LYP/aug-cc-pVDZ optimized geometries of the anion and the neutral) yields EA = 3.00 eV[9].

In the present work, we generate the $TCNE^-$ radical anion in the gas phase and examine its photodetachment and photochemistry using photoelectron imaging and photofragment mass-spectroscopy. We report the first direct spectroscopic determination of the electron affinity of TCNE, significantly improving on the uncertainty of the previous result. We also examine the anion clustered with water or argon and report the solvation effects on the anion stability.

9.2. Experimental section

The experiments were performed using a tandem time-of-flight reflectron mass-spectrometer described in detail previously[37]. A sample holder with TCNE powder was heated to 150 °C in order to increase the vapor pressure. The resulting TCNE vapor seeded in an Ar carrier gas with a backing pressure of 20 psi was introduced into a high-vacuum chamber through a pulsed nozzle (General Valve, Series 9) operated at a repetition rate of 50 Hz. The supersonic expansion was crossed with a 1 keV electron

beam from an electron gun and anions were formed via secondary-electron attachment to neutral molecules and clusters[35]. Water clusters were formed from residual water vapor trapped in the gas lines.

The anions are extracted into a Wiley-McLaren time-of-flight spectrometer, where they are separated by the mass-to-charge ratio and detected with a microchannel plate (MCP) detector mounted at the far end of the flight tube. In the detection region of the instrument, the ion beam is intersected with a linearly polarized pulsed laser beam, synchronized in time with the ion of interest. The third (355 nm, 4 mJ/pulse) or fourth (266 nm, 2 mJ/pulse) harmonics of a Nd:YAG (Yttrium Aluminum garnet) laser (Quanta Ray, Lab 50, 8 ns pulse duration) was used in this work. Two types of experiments were performed: photoelectron imaging and photofragment mass-spectrometry.

Photoelectron images are recorded using a perpendicular (with respect to the ion beam) velocity-map[26] photoelectron imaging[24,25] assembly[37]. The photodetached electrons are projected onto a 40 mm diameter position sensitive MCP detector (Burle, Inc.) by means of the electric field defined by a series of velocity-map imaging electrodes. Raw images are recorded using a 1 megapixel charged-coupled device (CCD) camera and accumulated for ~10^6 experimental cycles. The reconstruction of the cylindrically symmetric (with respect to the laser polarization direction) three-dimensional probability distribution from the images is performed via inverse Abel transform[25] using the BASEX program[40]. The known photodetachment transition of O^-[41,42] was used to calibrate the electron kinetic energy (eKE) scale of the images. Photoelectron spectra were fit to sums of Gaussian functions using a standard algorithm for accurate determination of solvation energies. The corresponding photoelectron

angular distributions were not analyzed in this work.

The photofragment-ion mass-spectra were recorded using a single-stage linear-field reflectron[37]. The fragment masses were determined by scanning the reflectron retardation potential while monitoring the ion signal with an off-axis MCP detector, as described previously[19]. Typically, 512 time-traces are averaged for each ion fragment. Stitching the averaged traces together yields the final photofragmentation spectra presented here.

9.3. Results and discussions

A representative time-of-flight mass spectrum corresponding to the parent ions of interest is shown in Fig. 9.1. The photoelectron images of the bare $TCNE^-$ anion and the $TCNE^-\cdot Ar$ cluster obtained at 355 nm are presented in Fig. 9.2. The corresponding spectra, plotted versus electron binding energy, eBE $\equiv h\nu -$ eKE, are shown alongside the images (blue lines). The photoelectron images and spectra of $TCNE^-$, $TCNE^-\cdot Ar$ and $TCNE^-\cdot H_2O$ collected at 266 nm are shown in Fig. 9.3. All images exhibit notable noise and distortions, attributed to the low signal levels. On this account, no attempt was made to analyze the photoelectron angular distributions. The low-pass filter Fourier analysis, described previously[205], was performed on all data sets presented and the resulting "clean" photoelectron spectra, intended to guide the eye, are plotted in gray together with the raw data in Figs. 9.2 and 9.3.

The 355 nm $TCNE^-$ and $TCNE^-\cdot Ar$ photoelectron images in Fig. 9.2 reveal perceptible rings. In the corresponding spectra, the lower-eBE transitions are labeled collectively as band X. This band consists of at least four overlapping sub-bands, marked with ticks in the figure. These sub-bands are assigned to electron detachment from the ground state of the anion to the lowest vibrational levels (marked as 0–3) of the ground

electronic state of the neutral. The vibrational interval is estimated at ~500 cm^{-1}. From the position and width of the first peak in the 355 nm $TCNE^-$ spectrum, the adiabatic electron affinity of TCNE is determined as EA = 3.16 ± 0.02 eV. This is the first spectroscopic determination of this crucial property of TCNE. The result is in excellent agreement with the previous indirect determination of EA = 3.17 ± 0.20 eV[219], but reflects an order-of-magnitude smaller uncertainty range.

The low-eKE bands in the photoelectron spectra, labeled with lower case a and b in Fig. 9.2, are assigned to autodetachment from either $TCNE^-$ or one of the fragments produced in the photodissociation of the anion. The autodetachment peaks are less intense in the $TCNE^-\cdot Ar$ spectrum, consistent with the expectation that an Ar tagged cluster should be vibrationally cold, resulting in colder fragments.

The lowest-eBE bands in the 266 nm photoelectron spectra of $TCNE^-$, $TCNE^-\cdot Ar$ and $TCNE^-\cdot H_2O$ (Fig. 9.3) correspond to the same ground-state anion to ground-state neutral transition as in Fig. 9.2, so they are also labeled X. Due to the lower resolution for the higher kinetic energy electrons in 266 nm photodetachment, the low-frequency vibrational progression within the X band, partially resolved in Fig. 9.2, is not observed in Fig. 9.3. However, a higher-frequency progression with a ~2100 cm^{-1} interval is apparent in the 266 nm spectra. This progression is not observed in Fig. 9.2, because its second band (eBE ≈ 3.5 eV) is either greatly suppressed in the 355 nm spectra due to the threshold proximity or indistinguishable from the low-eKE autodetachment bands (a-b). We cautiously assign this progression to the CN stretch in neutral TCNE[220] Similar to 355 nm, the spectra in Fig. 9.3 exhibit sharp low-eKE peaks that do not shift as a result of solvation. These peaks are assigned to autodetachment of excited $TCNE^-$ or vibrationally

excited photofragments.

The $TCNE^{-}\cdot H_2O$ spectrum in Fig. 9.3 is shifted towards higher binding energy by about 0.35 eV. This shift defines the hydration energy that can be calculated from the thermodynamic cycle: $D_0(A^{-}\cdot X) = EA(A\cdot X) + D_0(A\cdot X) - EA(A)$. To a first approximation, $D_0(A\cdot X) = 0$, so $D_0(A^{-}\cdot X) = EA(A\cdot X) - EA(A)$. The above hydration energy of 0.35 eV is quite small compared to that of many smaller anions. For reference, the first hydration energy of O_2^{-} is 0.967 eV[221], while that of I^{-} is 0.46 eV[222]. We attribute the low first hydration energy to the delocalized-charge structure of $TCNE^{-}$[9,10] and its asymmetric solvation, whereas the water molecule is expected to be bonded to only one or at most two of the four electronegative CN groups, interacting effectively with only a fraction of the excess charge[223]. This interpretation finds further support in that no discernable solvation-induced shift is observed in the $TCNE^{-}\cdot Ar$ photoelectron spectra at either 355 or 266 nm. A typical Ar binding energy to a small anion is ~ 0.05 eV[224], which is greater than the resolution and uncertainty limit in Fig. 9.2. We expect that the Ar solvation energy may also be decreased significantly relative to the small-anion value, due to the large size and delocalized charge distribution of $TCNE^{-}$.

Figure 9.4 displays the photofragment-ion mass-spectra for $TCNE^{-}$ obtained at 355 and 266 nm. Three types of fragment ions are observed in different proportions at both wavelengths: CN^{-} (m = 26 a.m.u.) and the m = 102 and 76 a.m.u. ions corresponding to the loss of one or two CN groups from parent $TCNE^{-}$, respectively. The CN and 2CN loss fragments are indicated as –CN and –2CN, respectively in Fig. 9.4. This fragmentation pattern is consistent with the accepted structure of $TCNE^{-}$ (see the inset in Fig. 9.1). The CN^{-} channel dominates the fragmentation at 355 nm, but the double

dissociation (–2CN) fraction increases drastically at 266 nm compared to 355 nm, which may be accounted for by the greater available energy.

9.4. Summary

We reported the first spectroscopic determination of the adiabatic electron affinity of TCNE in the gas phase, EA = 3.16 ± 0.02 eV. This result represents an order-of-magnitude improvement in precision compared to the previous indirect determination [219]. Three anionic photofragmentation channels are observed for $TCNE^-$ at 355 and 266 nm: one yielding the CN^- fragment and the other two corresponding to the loss of one or two CN groups from the parent anion. The CN^- channel dominates the fragmentation at 355 nm, while the double-dissociation (–2CN) channel dominates the radical anion photochemistry at 266 nm.

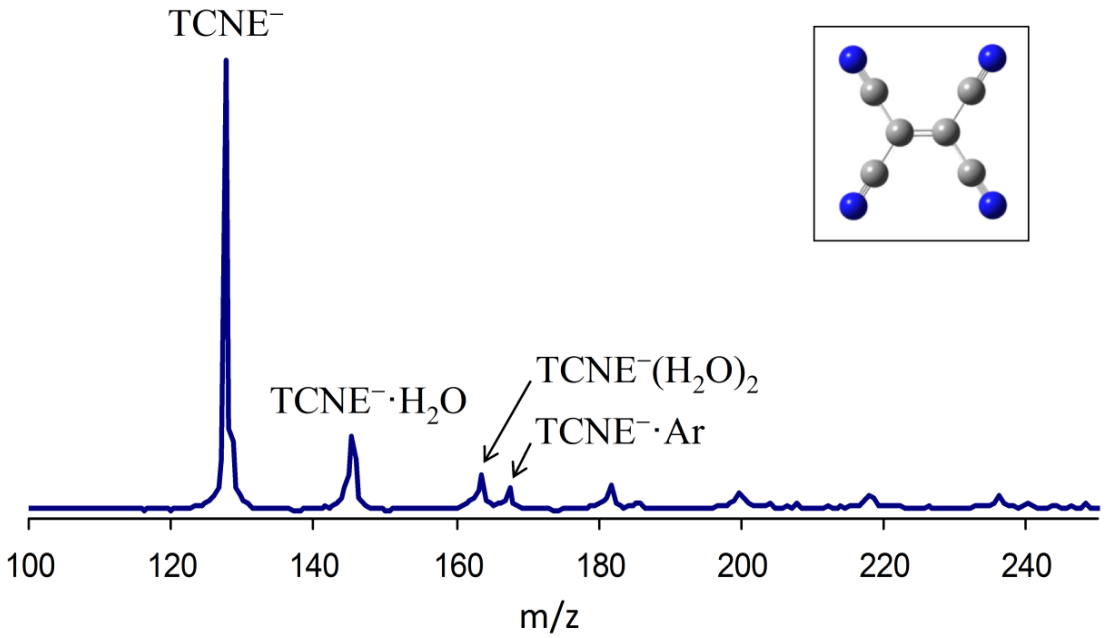

Figure 9.1. Representative time-of-flight mass spectrum. Inset shows the D_{2h} symmetry equilibrium structure of the neutral TCNE. The geometry of the anion is similar. See Refs.[9,10] for structural parameters.

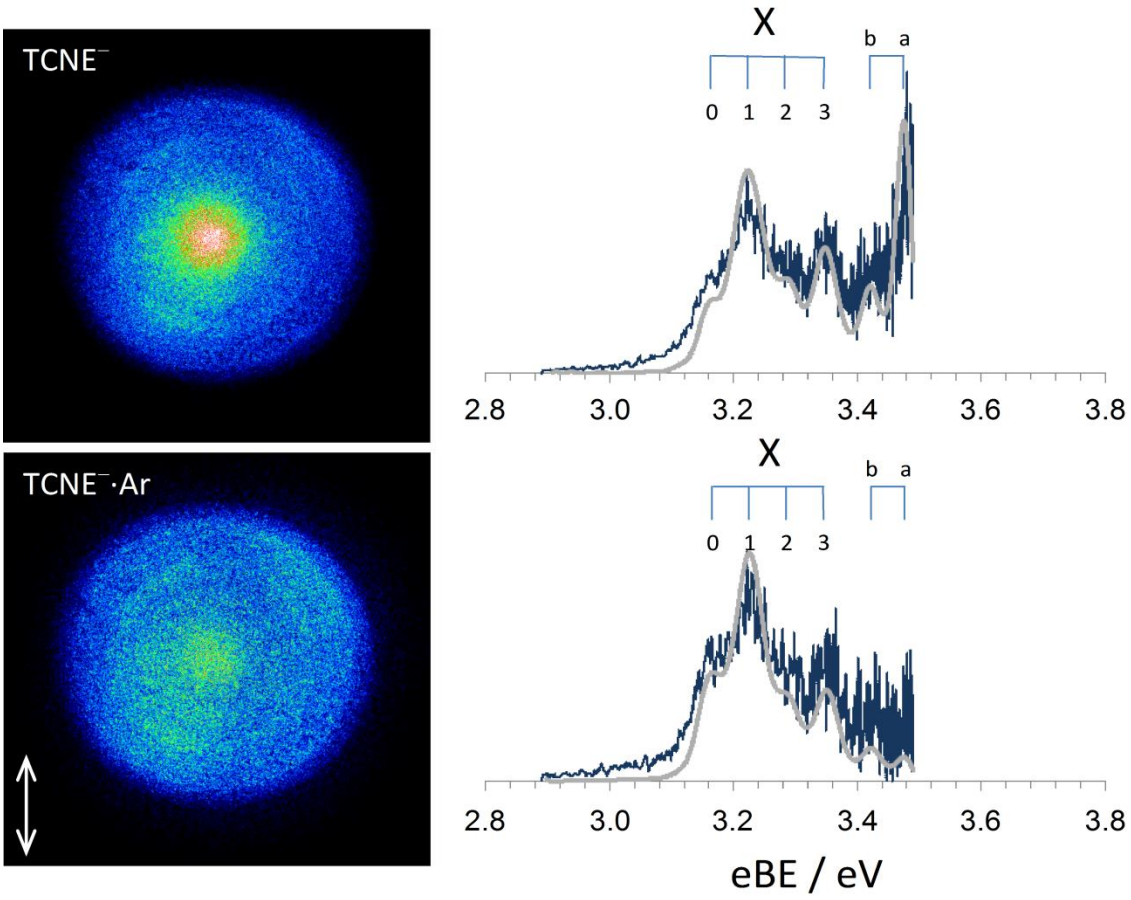

Figure 9.2 Photoelectron images and corresponding photoelectron spectra of $TCNE^-$ and $TCNE^-$·Ar cluster obtained at 355 nm. Vertical double arrow indicates the laser polarization direction. The experimental spectra are shown in blue. The gray curves are the result of a low-pass filter Fourier analysis. See the text for explanation of the spectral band assignments.

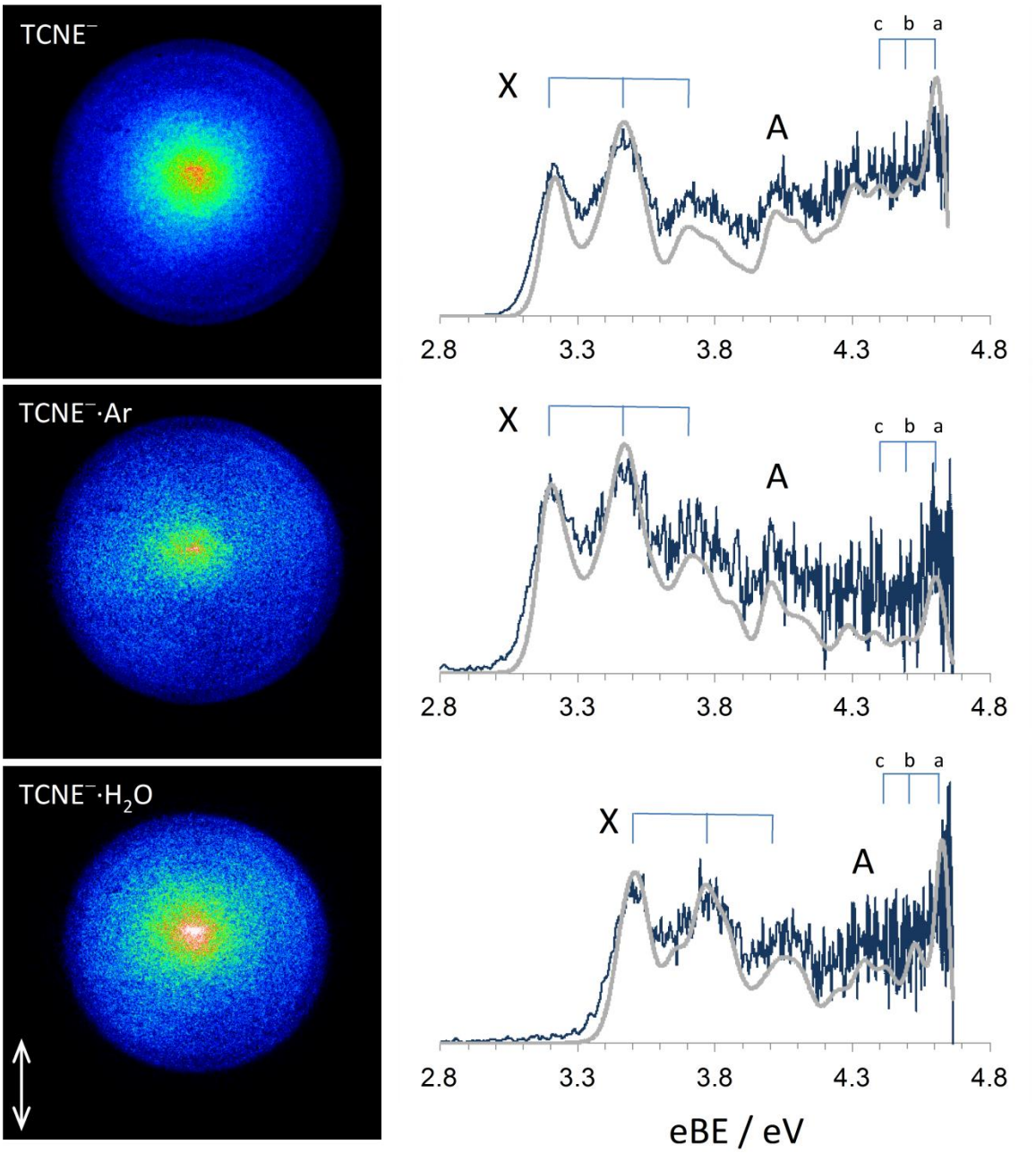

Figure 9.3 Photoelectron images and corresponding photoelectron spectra of $TCNE^-$, $TCNE^-\cdot Ar$, and $TCNE^-\cdot H_2O$ cluster collected at 266 nm. Vertical double arrow indicates the laser polarization direction. The experimental spectra are shown in blue. The gray curves are the result of a low-pass filter Fourier analysis. See the text for explanation of the spectral band assignments.

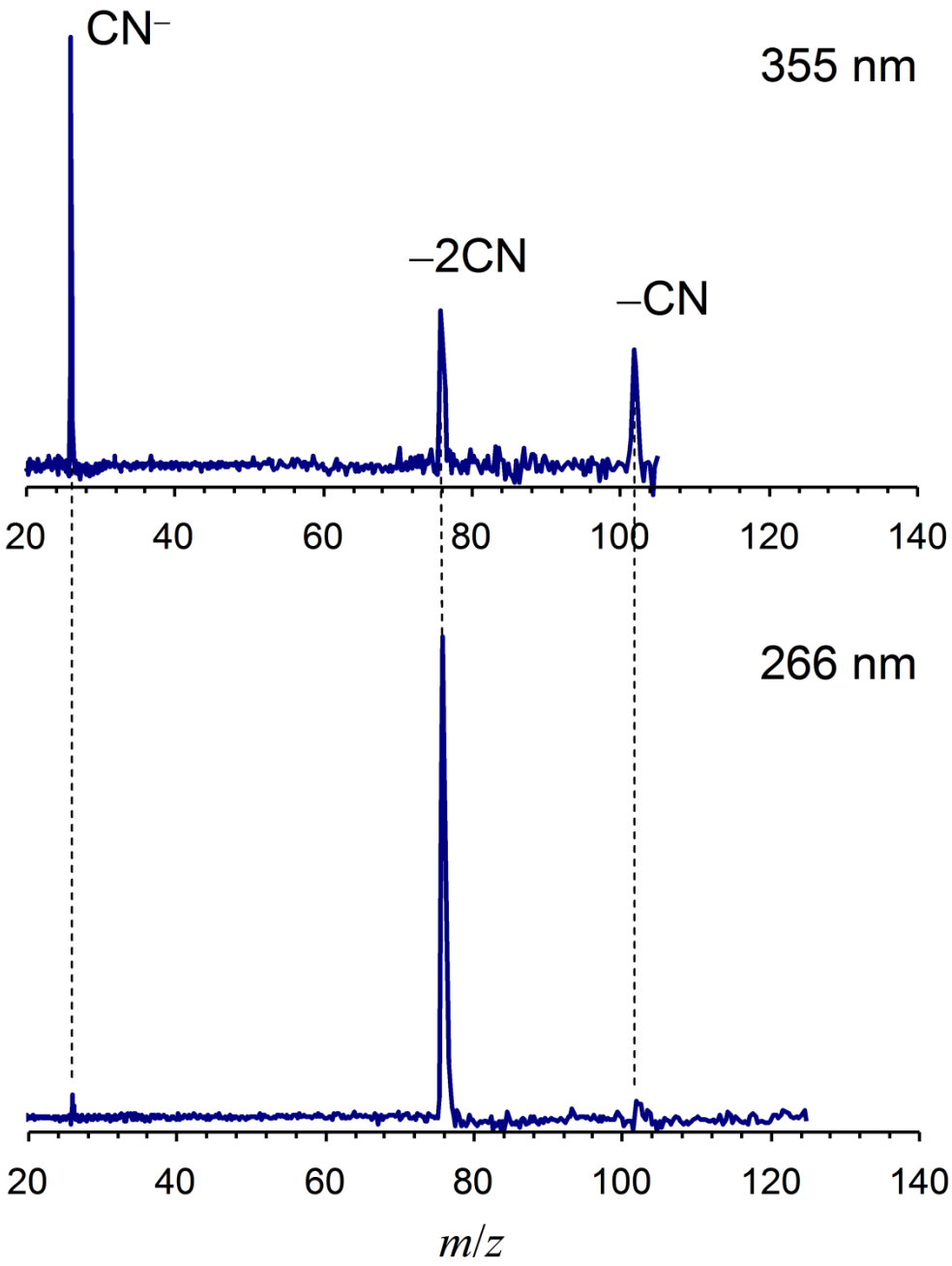

Figure 9.4 Photofragment-ion mass-spectra for TCNE obtained at 355 and 266 nm. –CN and –2CN indicate the m = 102 and 76 a.m.u. fragment anions, i.e., $C_2(CN)_3^-$ and $C_2(CN)_2^-$, corresponding to the loss of one or two CN groups from parent $TCNE^-$, respectively.

CHAPTER 10

PHOTOELECTRON IMAGING AND PHOTOFRAGMENTATION OF FUMARONITRILE RADICAL ANION IN THE GAS PHASE

10.1. Introduction

Fumaronitrile (trans-1,2-dicyanoethylene) is obtained from ethylene by the substitution of two cyano groups (CN) in the trans- position. In this manner it is an intermediate case between ethylene and fully substituted tetracyanoethylene (TCNE). The cyano group has a tremendous effect on the electronic properties of the molecule due to its electron withdrawing and π-conjugating properties. Each cyano group acts as an electron acceptor, analogous to the halogens. However, in contrast to the atomic halogens, cyano groups have unoccupied π orbitals that can conjugate with vinyl π system facilitating strongly bound anion states.

Electronic properties of cyano substituted ethylenes, and in particular doubly substituted trans-1,2-dicyanoethylene (fumaronitrile), have been studied experimentally and theoretically in the past. The commonly accepted experimental value of the electron affinity (EA) of fumaronitrile is 28.8 ± 2 kcal/mol (1.249 ± 0.087 eV) and was indirectly determined by measurement of the electron-transfer equilibrium $A^- + B = A + B^-$ with a pulsed electron high ion source pressure mass spectrometer.[219] The theoretical value of trans-dicyanoethylene EA has been calculated using density functional theory (DFT) quantum chemical calculations using five different gradient-corrected functionals with values ranging from 1.35 to 2.13 eV depending on the method used.[225]

The triplet energy of fumaronitrile was measured by laser flash photolysis technique using the Herkstroeter-Hammond method and was reported to be 59 ± 2 kcal/mol (2.56 ± 0.09 eV) higher in energy than a ground state singlet.[226] The triplet energy surface has a minimum at a bisected geometry; with a depth on the order of 9 kcal/mol with respect to H-C-CN rotation as determined by M06-2X/6-311+G(2d,p) calculations. The same calculations have concluded that the radical anion surface has minima in planar geometry and the barrier to geometric isomerization of 31.2 kcal/mol (1.353 eV).

In the present work, we generate the fumaronitrile radical anion in the gas phase and examine the electronic properties of its ground (singlet) and first excited (triplet) states via photoelectron imaging. We also gain some insight into photochemistry of fumaronitrile and its clusters using photofragment mass-spectrometry. We report the first direct spectroscopic determination of the electron affinity of fumaronitrile in its ground and first excited triplet states, significantly improving on the uncertainty of the previous result. We also examine the anion clustered with water, argon and fumaronitrile dimer and report the solvation effects on the anion stability.

10.2. Experimental and theoretical methods

The experiments were performed using a tandem time-of-flight reflectron mass-spectrometer described in detail previously.[37] A sample holder with crystalline fumaronitrile was mildly heated to 40 °C in order to increase the vapor pressure (0.635 mm Hg at 25 °C). The resulting fumaronitrile vapor was seeded in an Ar carrier gas (backing pressure of ~20 psi) and introduced into a high-vacuum chamber through a pulsed nozzle (General Valve, Series 9) operated at a repetition rate of 50, 70 or 20 Hz, depending on the laser system used. The supersonic expansion was crossed with a 1 keV

electron beam from an electron gun and anions were formed via secondary-electron attachment to neutral molecules and clusters.[35] Water clusters were formed from residual water vapor trapped in the gas lines.

The produced anions were further extracted into a Wiley-McLaren time-of-flight spectrometer, where they were separated by the mass-to-charge ratio and detected with a microchannel plate (MCP) detector mounted at the far end of the flight tube. In the detection region of the instrument, the ion beam was intersected with a linearly polarized pulsed laser beam, time tuned for the ion of interest. Three different laser systems were employed in this work. A Nd:YAG (Yttrium Aluminum garnet) laser (Quanta Ray, Lab 50, 8 ns pulse duration) was used for the second (532 nm, 10 mJ/pulse), third (355 nm, 4 mJ/pulse) or fourth (266 nm, 2 mJ/pulse) harmonics of the fundamental output. The 780 nm and 392 nm radiation (0.8 mJ/pulse, 100 fs pulses) was generated as the fundamental and second harmonic of an amplified Ti:sapphire laser system (Spectra Physics, Inc.) respectfully. The 612 nm radiation was the fundamental output of a Continuum, Inc. ND6000 Dye Laser system, pumped with second harmonic (532 nm, 20Hz) of Surelight II-20 Nd:YAG laser, operating on the Rhodamine 640 dye (20 mJ/pulse, ~10 ns duration pulses). The 306 nm light (5 mJ/pulse) was obtained by frequency doubling the above output of the dye laser. Two types of experiments were performed: photoelectron imaging and photofragment mass-spectrometry.

Photoelectron images are recorded using a perpendicular (with respect to the ion beam) velocity-map[26] photoelectron imaging[24,25] assembly.[37] The photodetached electrons are accelerated by a series of electrodes and projected onto a 40 mm diameter position sensitive MCP detector, coupled to a P43 phosphor screen (Burle, Inc.). The

resulting raw images are recorded using a charge-coupled device (CCD) camera and accumulated for ~10^5–10^6 experimental cycles. Two different cameras were used in this experiment (due to the longevity of the project), a Dalsa DS-1A-01M30 CamLink with 1 Megapixel resolution (Camera I) and thermoelectrically cooled Photometrics CoolSnap MYO with 2.8 Megapixels (Camera II). The camera used is indicated in figures where relevant, however results do not depend on the camera employed. Due to the cylindrical symmetry of the images with respect to the laser polarization direction, they can be reconstructed via inverse Abel transform[25] using the BASEX program[40] and three-dimensional probability distribution can be obtained.[25] The energy scale was calibrated using the well-known photoelectron spectrum of O^-.[41,42] The corresponding photoelectron angular distributions were not analyzed in this work.

The photofragment-ion mass-spectra were recorded using a single-stage linear-field reflectron[37]. The reflectron potential was scanned while monitoring the ion signal with an off-axis MCP detector to determine the fragment masses.[19] 512 time-traces were averaged for each ion fragment and the final photofragmentation spectra were obtained by combining them together.

Electronic-structure calculations involving geometry optimizations at the coupled-cluster level of theory with single and double excitations, CCSD, were performed using the Gaussian 09 suites of programs.[195] The low-lying electronic states of both the neutral and anion were explored using the equation-of-motion (EOM) ionization potential (IP)[177,227,228] and EOM- electronically excited (EE) methodologies, combined with the coupled-cluster theory, including diagonal triples corrections (dT).[198] All EOM-XX-CCSD(dT) calculations (XX = IP or EE) were carried out using the Q-Chem 4.0 software

package.[199]

10.3. Results and discussion

10.3.1. Experimental results

The photoelectron images of the bare $C_4H_2N_2^-$ anion obtained at different laser energies are presented in Fig. 10.1. The corresponding photoelectron spectra are plotted with respect to electron binding energy (eBE ≡ hν – eKE) and are shown together with the images. At 780, 612 or 532 nm, only the ground state of the neutral $C_4H_2N_2$ (X^1A_g) is accessible. Partially resolved vibrational progression is prominent with the vibrational frequency of 1610 ± 160 cm^{-1}, which is assigned to C=C stretch in agreement with previously measured and calculated vibrational spectra.[229,230] From the position and the width of the first peak in the 612 nm spectrum, the adiabatic electron affinity of $C_4H_2N_2$ is determined as EA = 1.21 ± 0.02 eV. This is the first direct spectroscopic determination of this important property of fumaronitrile. The result is in agreement with the previous indirect determination of EA = 1.249 ± 0.087 eV[219], but reflects a significant improvement in uncertainty.

For 392 nm and 355 nm laser pulses (photon energies of 3.16 eV and 3.49 eV respectively), images have very high intensity in the center which correspond to low eKE structureless features in the photoelectron spectra (labeled C in Figure 10.1). One might assume that this feature represents the first excited state of neutral fumaronitrile, however since there is no sign of it in the higher energy images (306 nm and 266 nm) this assignment does not hold. We preliminarily assign this feature to autodetachment from electronically excited fumaronitrile anion.

The first excited state of neutral $C_4H_2N_2$ (^3A) is accessible at the 306 and 266 nm images and corresponds to the broad transition in the spectra. Due to the broad and congested nature of the band, we can only estimate upper limit for the adiabatic binding energy of the transition ^3A state, EA (^3A) $\leq$ 3.78 eV, based on the first peak rising above the noise level in 306 nm spectra (see Figure 10.1). This is consistent with previous triplet energy determination,[226] whereas triplet energy was reported to be 2.56 ± 0.09 eV higher in energy than the ground state singlet, thus EA (^3A) = 3.77 ± 0.09 eV. Vertical detachment energy is assigned as the highest peak of the 266 nm band (supported by the Gaussian fit) to VDE = 4.05 ± 0.05 eV.

The photoelectron images and the corresponding photoelectron spectra of fumaronitrile cluster anions, $C_4H_2N_2^-$, $C_4H_2N_2^-\cdot(Ar)$, $C_4H_2N_2^-\cdot(H_2O)$, $C_4H_2N_2^-\cdot(H_2O)_2$, and $C_4H_2N_2^-\cdot(C_4H_2N_2)$, obtained at 532 nm, are presented in Figure 10.2. The spectrum of $C_4H_2N_2^-\cdot(Ar)$ is better resolved than bare $C_4H_2N_2^-$, because of colder temperature of Ar-tagged ions. The lowest eBE transition corresponds to the same ground-state anion to ground-state neutral transition and it is labeled A, due to possible loss of the C_{2h} symmetry associated with the solvent molecule. Vibrational progression is resolved for the ground state of neutral for all of the water clusters and it appears to be mostly unaffected by the solvation (~1600 cm^{-1}). Band assignments for all of the transitions are presented in Table 10.2.

The photoelectron spectra of fumaronitrile clusters are shifted towards higher binding energy. This shift reflects the solvation energy that can be calculated via the thermodynamic cycle: $D_0(A^-\cdot X) = EA(A\cdot X) + D_0(A\cdot X) - EA(A)$. To a first approximation, $D_0(A\cdot X) << D_0(A^-\cdot X)$, so $D_0(A^-\cdot X) = EA(A\cdot X) - EA(A)$. Solvation

energies for all the clusters studied in this work are presented in Table 10.3. The hydration energy (solvation energy of water) of 0.32 eV is significantly smaller than that of many smaller anions, but similar to $TCNE^-$ which has a hydration energy of 0.35 eV.[231] Similar to $TCNE^-$, we attribute the low first hydration energy to delocalized charge structure of fumaronitrile and asymmetric solvation, whereas the water molecule is bonded to only one of the CN groups, effectively interacting with only part of the charge. This finds further support in that second hydration energy (energy required for the reaction $C_4H_2N_2^-(H_2O)_2 \rightarrow C_4H_2N_2^-(H_2O) + H_2O$) has same value of 0.32 eV. This indicates that the second water molecule is bonded to another CN group, interacting with the partial charge of a similar magnitude.

The Ar solvation energy is also expected to be significantly decreased relative to the typical small-anion value (~0.05 eV).[224] Due to the limit in the resolution of our experiment, the band shift associated with Ar solvation cannot be discerned and only an upper limit of 0.02 eV can be assigned for solvation energy.

The maximum of band A in the $C_4H_2N_2^-\cdot(C_4H_2N_2)$ spectrum is shifted to a higher binding energy by a significantly higher value than the rest of the clusters, almost an electron-volt (0.94 eV). This shift reflects the approximate $(C_4H_2N_2)_2^- \rightarrow C_4H_2N_2^- + C_4H_2N_2$ dissociation energy and suggests covalent bonding between two fumaronitrile molecules. Thus the cluster should be referred to as $(C_4H_2N_2)_2^-$ rather than $C_4H_2N_2^-\cdot(C_4H_2N_2)$. However, the exact way these monomers bond cannot be discerned from our experiment and remains an open question which lies outside of the scope of this study.

Photofragment-ion mass-spectrometry was also performed on fumaronitrile and

its clusters at 355 and 266 nm. The CN^- mass fragment dominates the fragmentation at both wavelengths, with visible reduction of the signal for the clusters compared to bare fumaronitrile. However, the fragmentation pattern of the fumaronitrile dimer, $(C_4H_2N_2)_2^-$, is significantly different from other types of clusters. CN^- channel is considerably suppressed (if not gone) and the only photofragment detected is fumaronitrile monomer. This, again, points to the unique (with respect to other solvents) covalent bonding character of fumaronitrile with itself.

10.3.2. Computational results

Ab initio calculations were performed for the anion and the singlet and triplet states of neutral fumaronitrile. The geometries were optimized at the CCSD level of theory using Dunning's augmented correlation-consistent polarized valence triple-ζ basis set (aug-cc-pVTZ). The resulting structures of the ^2B_g ground state of the anion and the closed-shell singlet (^1A_g) and the triplet (^3A) states of the corresponding neutral are shown in the Figure 10.3. The anion and singlet geometries are both planar and very similar to each other with the biggest difference in C=C bond length. The optimized triplet geometry however is not planar, it is about 50° twisted around C=C bond.

On the basis of geometries, we expect relatively sharp transition for the singlet peak and a broad Franck-Condon envelope for the triplet. This is in agreement with experimental data (see Fig. 10.1), where low-eKE transition in the photoelectron spectrum is narrow with a resolved vibrational progression of 1610 ± 160 cm^{-1}, corresponding to C=C bond elongation in anion geometry compared to singlet. In contrast, transition corresponding to triplet is broad, consistent with large geometry

change. The EA of the triplet cannot be assigned accurately due to very small Franck-Condon overlap corresponding to 0-0 transition.

The adiabatic EAs of the ^1A_g and ^3A states of the neutral fumaronitrile, as well as the corresponding anion VDEs were computed[195] using the coupled-cluster theory. In addition, single-point CCSD(T)/aug-cc-pVTZ calculations were carried out[195] for the CCSD/aug-cc-pVTZ optimized geometries. The VDEs were also computed[180] directly using the EOM-IP-CCSD(dT) method, using the above anion geometry. The results are summarized in Table 10.4.

The calculated VDE values, corresponding to detachment to both the ^1A_g and ^3A states, are in good agreement with the peak energies in the experimental spectrum (Figure 10.1). In particular, we note the excellent agreement of the EOM-IP-CCSD(dT)/aug-cc-pVTZ results (1.295 and 4.027 eV vs 1.21±0.02 eV and 4.05±0.05 eV for the singlet and triplet VDEs respectively).

Electronically excited states of the anion were characterized using EOM-EE-CCSD(dT)/aug-cc-pVTZ. There is an excited state around 3.5 eV above the ground state. Photoexcitation to this state will result in autodetachment since it is embedded in the detachment continuum (excitation > EA). This is consistent with the high intensity peaks observed near the energy threshold for the 392 and 355 nm images (see Figure 10.1).

10.4. Conclusions

We reported the first spectroscopic determination of the adiabatic electron affinity of trans-1,2-dicyanoethylene (fumaronitrile) in the gas phase, EA = 1.21 ± 0.02 eV. This result represents an improvement in precision compared to the previous indirect determination.[219] The upper limit for the adiabatic binding energy of the triplet state was

estimated, EA (^{3}A) ≤ 3.78 eV, consistent with the previously reported value.[226] In support of experimental assignments, geometry optimization calculations were performed on the anion, and both singlet and triplet neutral species. The low-lying electronic states of both neutral and anion were calculated using the equation-of-motion (EOM) ionization potential (IP) and electronic excitation (EE) methodologies,[197] combined with the coupled-cluster theory, including diagonal triples corrections (dT).[198] The highest level/largest basis set used EOM-IP-CCSD(dT)/aug-cc-pVTZ yields 1.295 and 4.027 eV for the singlet and triplet vertical detachment energies in good agreement with experimentally assigned values.

We also performed photoelectron imaging and photofragmentation study of fumaronitrile cluster anions, $C_4H_2N_2^-\cdot(Ar)$, $C_4H_2N_2^-\cdot(H_2O)$, $C_4H_2N_2^-\cdot(H_2O)_2$, and $C_4H_2N_2^-\cdot(C_4H_2N_2)$. Reported solvation energies of water and Ar are significantly smaller than that of many smaller anions, but similar to the corresponding solvation energies of $TCNE^-$.[231] Similarly to $TCNE^-$, this attributed to delocalized charge structure of fumaronitrile and asymmetric solvation, whereas the water (or Ar) molecule is bonded to only one of the CN groups, effectively interacting with only part of the charge. In contrast, solvation energy of the fumaronitrile is on the order of an electron-volt, reflecting the approximate $(C_4H_2N_2)_2^- \rightarrow C_4H_2N_2^- + C_4H_2N_2$ dissociation energy and suggesting covalent bonding between two fumaronitrile molecules. There is only one photofragmentation channel for the fragmentation of bare fumaronitrile and its water and Ar clusters, yielding the CN^- fragment. It is significantly suppressed for the fumaronitrile dimer photochemistry, with appearance of another channel, resulting in the $C_4H_2N_2^-$ fragment. This supports the covalent bonding character between two fumaronitrile

moieties in the dimer anion. In the past, analogous dissociation channels were observed for example in the covalent dimer anions of CO_2, OCS, and CS_2.[202,232]

Table 10.1 Band assignment for the EA and VDE of two energetically available transitions, $C_4H_2N_2^-$ (^2B_g) → $C_4H_2N_2$ (X^1A_g) and $C_4H_2N_2^-$ (^2B_g) → $C_4H_2N_2$ (^3A)

Band	Wavelength (nm)	EA (eV)
^1A_g (v = 0)	780	1.23 ± 0.04
	612	**1.21 ± 0.02**
	532	1.21 ± 0.02
^1A_g (v = 1)	780	1.42 ± 0.04
	612	**1.41 ± 0.02**
	532	1.39 ± 0.02
^3A	306	≤ 3.78
	266	≤ 3.8
		VDE (eV)
^3A	266	4.05 ± 0.05

Table 10.2 Band assignment for the EA of the fumaronitrile cluster anions.

Cluster	Band maximum (eV)
$C_4H_2N_2^-$	1.21 ± 0.02
	1.41 ± 0.02
$C_4H_2N_2^-(Ar)$	1.20 ± 0.02
	1.40 ± 0.02
$C_4H_2N_2^-(H_2O)$	1.53 ± 0.02
	1.72 ± 0.02
$C_4H_2N_2^-(H_2O)_2$	1.85 ± 0.02
	2.06 ± 0.05
$C_4H_2N_2^-(C_4H_2N_2)$	2.15 ± 0.05

Table 10.3 Fumaronitrile cluster dissociation energies. The binding energy is derived from the thermochemical cycle $D_0(AX^-) = EA(AX) + D_0(AX) - EA(A)$, where EA = electron affinity and D_0 = dissociation energy. To a first approximation $D_0(AX) \approx 0$, so $D_0(AX^-) = EA(AX) - EA(A)$. Due to approximate nature of calculations we do not assign absolute uncertainties.

Reaction	Energy (eV)
$C_4H_2N_2^-(Ar) \rightarrow C_4H_2N_2^- + Ar$	<0.02
$C_4H_2N_2^-(H_2O) \rightarrow C_4H_2N_2^- + H_2O$	0.32
$C_4H_2N_2^-(H_2O)_2 \rightarrow C_4H_2N_2^-(H_2O) + H_2O$	0.32
$C_4H_2N_2^-(C_4H_2N_2) \rightarrow C_4H_2N_2^- + C_4H_2N_2$	0.94

Table 10.4 Calculated VDE and adiabatic EA corresponding to the detachment to the X^1A_g and ^3A_u states of the neutral

Method/basis set	VDE (eV)		Adiabatic EA (eV)	
	$^2B_g \rightarrow {}^1A_g$	$^2B_g \rightarrow {}^3A$	$^2B_g \rightarrow {}^1A_g$	$^2B_g \rightarrow {}^3A$
CCSD/aug-cc-pVDZ	1.212	3.789	0.999	3.279
CCSD/aug-cc-pVTZ	1.308	3.948	1.082	3.425
CCSD(T)/aug-cc-pVTZ	1.251	4.092	1.102	3.596
EOM-IP-CCSD/aug-cc-pVDZ	1.250	3.961		
EOM-IP-CCSD/aug-cc-pVTZ	1.395	4.168		
EOM-IP-CCSD(dT)/aug-cc-pVDZ	1.156	3.823		
EOM-IP-CCSD(dT)/aug-cc-pVTZ	1.295	4.027		
experiment	1.21(2)	4.05(5)	1.21(2)	≤3.78(5)

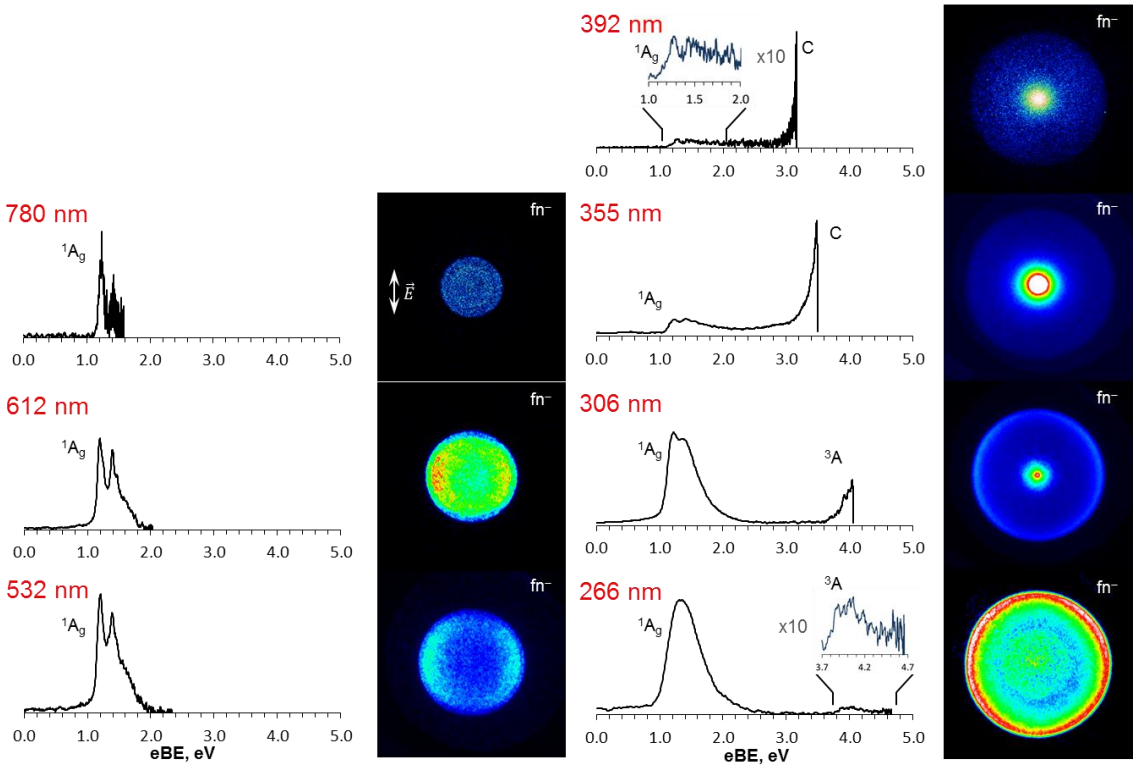

Figure 10.1 Photoelectron images and corresponding photoelectron spectra of $C_4H_2N_2^-$ collected at 780 (Camera I), 612, 532, 392, 355, 306 and 266 nm (Camera II). Vertical double arrow indicates the laser polarization direction. Energetically available transitions are labeled. For band assignment see Table 10.1.

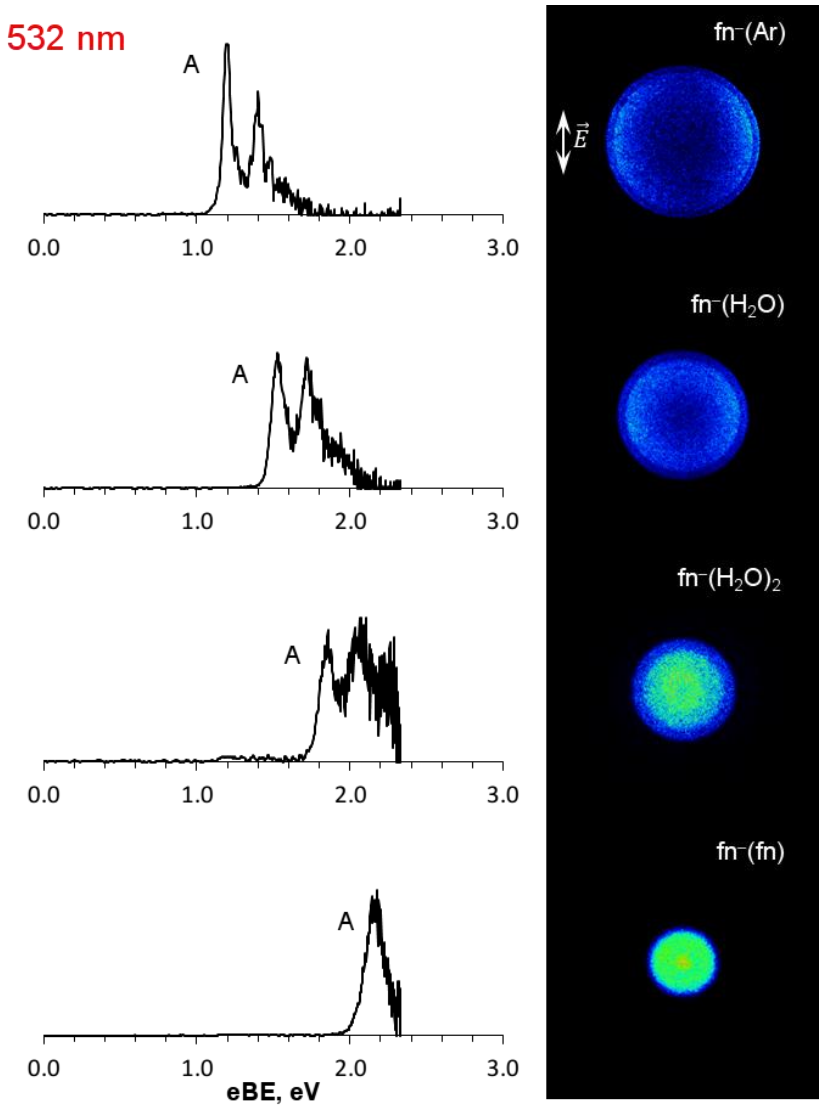

Figure 10.2 Photoelectron images and corresponding photoelectron spectra of $C_4H_2N_2^-$, $C_4H_2N_2^-\cdot(Ar)$, $C_4H_2N_2^-\cdot(H_2O)$, $C_4H_2N_2^-\cdot(H_2O)_2$, and $C_4H_2N_2^-\cdot(C_4H_2N_2)$ collected at 532 nm (Camera I). Vertical double arrow indicates the laser polarization direction. Energetically available transitions are labeled. For band assignment see Table 10.2.

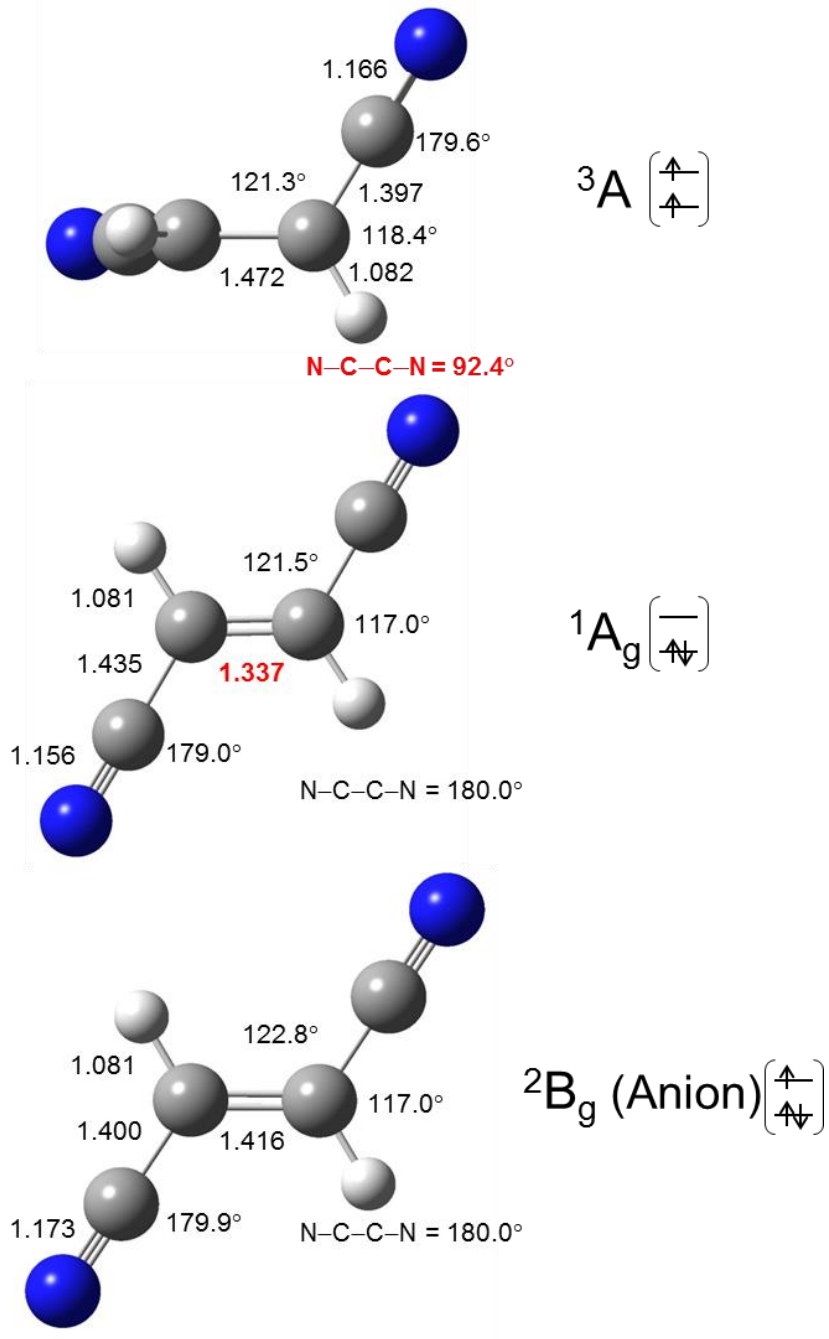

Figure 10.3 CCSD/aug-cc-pVTZ optimized geometries of ground ^2B_g state of anion, $C_4H_2N_2^-$, and singlet ^1A_g and triplet ^3A states of corresponding neutral. All the bond lengths are in Angstroms and angles are in degrees. Parameters with the largest difference between anionic and neutral structures are shown in bold red.

CHAPTER 11

THE O^- + ACETALDEHYDE REACTION PRODUCTS: SEARCH FOR SINGLET FORMYLMETHYLENE, A WOLFF REARRANGEMENT INTERMEDIATE

11.1. Introduction

The gas-phase reactivity of atomic oxygen radical anion ($O^{\bullet -}$) with organic molecules is well documented.[189,190,233-235] This anion primarily reacts with organics via H^+, $H^\bullet$, or $H_2^{\bullet +}$ abstraction, as indicated by the respective reactions:

$$O^{\bullet -} + RH \rightarrow OH^\bullet + R^- \quad (11.1)$$

$$O^{\bullet -} + RH \rightarrow OH^- + R^\bullet \quad (11.2)$$

$$O^{\bullet -} + HRH \rightarrow H_2O + R^{\bullet -} \quad (11.3)$$

These reactions are extremely useful, as they provide a convenient method for gas-phase synthesis of a number of important anion intermediates. Those intermediates can be characterized by spectroscopy, reactivity, or fragmentation in order to obtain their thermochemical properties, as well as molecular and electronic structures. However, one disadvantage of $O^{\bullet -}$ as a reagent is that it is often unselective toward the site of deprotonation, resulting in a complex mixture of isomers. Thus, $O^{\bullet -}$ is most useful as a reagent when a limited number of H atoms are available.

The reaction of $O^{\bullet -}$ with acetaldehyde, H_3CCHO, was examined previously by Grabowski and Melly using the flowing afterglow technique.[235] The products observed were H_2CCHO^- (34%), $HCCHO^{\bullet -}$ (32%), $OH^{\bullet -}$ (9%), $H_3CCO_2^-$ (15%), and HCO_2^-

(10%). The primary products correspond to the reactions (11.1) – (11.3), while the minor products result from the addition of $O^{\bullet -}$, followed by elimination.

Of the above products, particularly interesting is the formylmethylene anion, $HCCHO^{\bullet -}$. Electron detachment from this anion yields formylmethylene, an important carbene intermediate in the Wolff rearrangement.[236,237] This reaction is widely used in chemistry, especially in the synthesis of acids, ring contractions, and most importantly in the industrial process of photolithography.[236] Although formylmethylene could be found in several low energy electronic states (triplet and singlet), it is the singlet that is involved in the Wolff rearrangement.

The general mechanism of the Wolff rearrangement via a formylmethylene intermediate is shown in Figure 11.1. Typically, HCCHO, **1**, is generated by pyrolysis or photolysis of a diazoketone. The carbene undergoes a 1,2-H atom shift to form ketene, H_2CCO, **3**. Isotopic labeling studies have shown the carbon atoms in H_2CCO scramble, so an oxirene intermediate, **2**, has been proposed to explain experimental observations.

Although Figure 11.1 provides a plausible mechanism for the Wolff rearrangement, several experiments have indicated the reaction is controlled by additional factors, such as precursor geometry.[236-238] For example, photolysis of *syn* α-diazoketones leads preferentially to the formation of ketenes, while photolysis of *anti* α-diazoketones, such as 2,2,5,5-tetramethyl-4diazo-3-hexanone does not always lead to significant yields of ketene products.[238] Time resolved studies have indicated there are at least two decay processes related to the starting geometry of the keto-carbene intermediate.[239,240] A fast decay is consistent with a direct 1,2-H atom shift immediately upon photolysis. A slower component would imply the formation of a long-lived intermediate, such as oxirene or a

ketocarbene. A recent study found evidence for non-statistical behavior in the product ratio of the Wolff rearrangement due to a bifurcated potential energy surface.[241] Thus, the mechanism in Figure 11.1 is too general for this reaction.

In this paper, we report a photoelectron imaging study of the products from the reaction of $O^{\bullet-}$ with acetaldehyde. The primary purpose of the study was to investigate HCCHO via electron detachment of the formylmethylene anion. This approach provides an alternate pathway to generation of HCCHO, unlike the traditional decomposition of diazoketones. In addition, we investigate several other reactive intermediates formed in the $O^{\bullet-}$ + H_3CCHO reaction, including vinoxide, H_2CCHO^-, and an apparent two-step reaction product, $CCO^{\bullet-}$. Both intermediates are characterized in comparison with previously recorded photoelectron spectra reported in Ref. [134,242,243] and Ref. [244,245], respectively.

11.2. Experimental and theoretical methods

The experiments were carried out using a pulsed negative-ion time-of-flight photoelectron imaging spectrometer described previously.[37] A mixture of room-temperature acetaldehyde vapor in N_2O carrier gas at a pressure of 30 psi was expanded into a vacuum chamber using a General Valve (series 99) pulsed supersonic nozzle. Anions were generated by collisions of 1 keV electrons from an electron gun, creating slow secondary electrons. The slow electrons undergo dissociative attachment to N_2O to form $O^{\bullet-}$. The nascent $O^{\bullet-}$ reacts further via chemical ionization, as in equations 11.1 – 11.3.

The anions were mass selected in a linear time-of-flight mass spectrometer and intersected by a pulsed linearly polarized laser beam (Nd:YAG, 10 ns, 30 mJ at 532 nm

or 10 mJ at 355 nm) within a velocity-map[26] imaging[24] assembly. Photodetached electrons were projected onto a microchannel-plate detector, coupled to a phosphor screen. The resulting images were recorded by a charge-coupled device camera. The images were accumulated for statistics and analyzed by inverse Abel transformation using the BASEX program.[40] Transformed images yield intensities in radial and angular coordinates with respect to the image center, $I(r,\theta)$, where angle θ is defined relative to the laser polarization direction. Photoelectron spectra are obtained by integrating the transformed images with respect to the angular coordinate. The spectra were calibrated using the known photoelectron spectrum of $O^{\bullet -}$.[41,42] Photoelectron angular distributions (PADs) were obtained by integration over r. The angular distributions were fit using the standard equation[31] and characterized in terms of the anisotropy parameter β.[29,30]

Electronic structure calculations were carried out using the Gaussian 03 program.[130] Unless stated otherwise, the geometry optimizations and frequency calculations reported in this work were performed at the B3LYP/aug-cc-pVDZ level of theory. Other basis sets, aug-cc-pVQZ and 6-311++G(3df,3pd), were also used, for comparison, but only small differences were found. For the $HCCHO^{\bullet -}$ and HCCHO, we also employed the Møller-Plesset second-order perturbation theory (MP2), in order to compare the predictions of different methods. Frequency calculations were used to confirm that the optimized structures corresponded to local minima. Transition state structures were identified as structures with a single imaginary frequency.

11.2. Experimental results and analysis

A representative mass spectrum of the ions formed by the reaction of O^- with H_3CCHO seeded in N_2O is shown in Figure 11.2. The $O^{\bullet -}$ + H_3CCHO reaction products

are indicated with red arrows and labels. Similar to the high-pressure flow-tube results,[233] we observe the vinoxide anion, H_2CCHO^- (*m/z* = 43 a.m.u.) and the formylmethylene anion, $HCCHO^{\bullet-}$ (*m/z* = 42 a.m.u.). In addition, we observe an *m/z* = 40 a.m.u. peak assigned to the ketenylidene anion, $CCO^{\bullet-}$. The peaks marked with asterisks are possible addition/elimination products, HCO_2^- and $H_3CCO_2^-$, similar to those observed in the high-pressure flow-tube reactor.[233] However, these ions could not be investigated spectroscopically, because of their low intensities and large electron affinities.

The primary products of the reaction of $O^{\bullet-}$ with H_3CCHO are formed via the following pathways:

$$O^{\bullet-} + H_3CCHO \rightarrow HO^{\bullet} + H_2CCHO^- \quad (11.4)$$

$$O^{\bullet-} + H_3CCHO \rightarrow H_2O + HCCHO^{\bullet-} \quad (11.5)$$

$$2O^{\bullet-} + H_3CCHO \rightarrow 2H_2O + CCO^{\bullet-} + e^- \quad (11.6)$$

Formation of $CCO^{\bullet-}$ requires removal of all four H centers (three H atoms and a proton, H^+) in H_3CCHO. Such elimination must be at least a two-step process and a possible mechanism is proposed in Section 11.4.2.

The product anions were characterized individually by photoelectron imaging. The $HCCHO^{\bullet-}$ anion had not been previously studied by photoelectron spectroscopy and we carried out both spectroscopic and theoretical investigations of $HCCHO^{\bullet-}$ and HCCHO in the ground and excited states. The experimental results for this ion are presented in Section 11.3.1 and discussed in detail in Section 11.4.1. The H_2CCHO^- and $CCO^{\bullet-}$ ions, on the other hand, have been the targets of several previous experiments[134,242-247] and only

brief discussions of their photoelectron spectra are included in Sections 11.3.2 and 11.3.3, respectively. These analyses are necessary not only for completeness of the present study, but also because the resulting energetics are used in determining several thermochemical properties in Section 11.4.3.

11.3.1. Formylmethylene anion, $HCCHO^-$

The 532 and 355 nm photoelectron images and spectra of formylmethylene anion, $HCCHO^-$ (m/z = 42 in Figure 11.2), are shown in Figure 11.3. The 532 nm image (a) shows a single feature assigned to the $X\,^3A''$ ground state of HCCHO. To analyze the partially resolved vibrational structure, we performed a Fourier transform of the spectrum: $f(\text{eBE}) \rightarrow F(q)$, where q is signal frequency (in units of 1/eV), conjugate to electron binding energy (eBE). The result, $F(q)$, is plotted in Figure 11.4(a). The high-q part of the Fourier spectrum (red dotted line) corresponds to noise in the experimental data, while other dominant features of $F(q)$ (blue solid line) reflect the periodic components present in the original spectrum in Figure 11.3(a). In particular, the peak at q = 17.7 eV^{-1}, marked in Figure 11.4(a) with an asterisk, corresponds to the dominant vibrational progression discerned in the photoelectron spectrum in Figure 11.3(a). The features near q = 0 in Figure 11.4(a) define the overall envelope of the $X\,^3A''$ spectral band in Figure 11.3(a).

Figure 11.4(b) shows the same Fourier spectrum, but plotted as a function of ω, defined as the periodic spectral interval corresponding to signal frequency q: $\hbar\omega = 1/q$. $F(\omega)$ is obtained from $F(q)$ via a Jacobian transformation: $F(\omega) = F(q)\,|dq/d\omega|$, where $|dq/d\omega| \propto q^2$. $F(\omega)$ is the spectrum of (vibrational) mode frequencies present in the

experimental spectrum *f*(eBE). The high-*q* (noise) part of the Fourier spectrum in Figure 11.4(a) corresponds to the low-ω part of $F(\omega)$, while the dominant vibrational peak at q = 17.7 eV^{-1} transforms into the corresponding peak, also marked with an asterisk, in Figure 11.4(b). From the maximum position and width of this peak, we determine the average spacing of the partially resolved vibrational progression in Figure 11.3(a) as 456 ± 28 cm^{-1}.

We further used the Fourier analysis as a low-pass filter for the 532 nm experimental spectrum shown in Figure 11.3(a). Specifically, the high-*q* (low-ω) noise part of the Fourier spectrum was eliminated (replaced by zeroes) and the resulting cleaned up spectrum, consisting only of the blue solid part in Figure 11.4, was used for inverse Fourier transform. This procedure yielded the filtered photoelectron spectrum shown as a solid red line in Figure 11.3(a). The vibrational progression with the average spacing determined above is unmistakable in the filtered spectrum. Assigning the first peak of the filtered X $^3A''$ spectral band as the band origin yields the adiabatic electron affinity of HCCHO, EA = 1.87 ± 0.02 eV.

The 355 nm image in Figure 11.3(b) shows a second spectral feature, with a maximum around 3.05 eV. This feature is assigned to an excited state of HCCHO, $A\,^3A''$. Both bands, $X\,^3A''$ and $A\,^3A''$, have maximum intensities parallel to the laser polarization, corresponding to $\beta > 0$.

11.3.2. Vinoxide anion, H_2CCHO^-

The vinoxide anion, H_2CCHO^-, has been the subject of several previous studies.[248-251] Most recently, a high-resolution slow-electron velocity-map imaging (SEVI) study

gave an adiabatic electron affinity EA($H_2CCHO^{\bullet}$) = 1.8250 ± 0.0012 eV.[242] This result is compared to the EA values of 1.8248 eV,[250] 1.817 ± 0.023 eV,[248] and 1.8240 ± 0.0050 eV,[251] obtained in earlier studies. A photoelectron image of H_2CCHO^- has also been reported previously,[134] giving an EA = 1.795 ± 0.015 eV.[243] Our results for this species are consistent with the previous studies and hence only a brief account is given here.

The 355 and 532 nm photoelectron images and spectra of H_2CCHO^- (corresponding to *m/z* = 43 in Figure 11.2) are shown in Figure 11.5. The 355 nm image shows two major features, a low energy band assigned to the $X\,^2A''$ state of vinoxy and a higher energy feature assigned to the first excited state, $A\,^2A'$. The 532 nm spectrum shows a vibrational progression for the ground state only. Its onset allows for an unambiguous determination of adiabatic electron affinity, EA($H_2CCHO^{\bullet}$) = 1.82 ± 0.01 eV (42.0 ± 0.2 kcal/mol), is in good agreement with the above SEVI experiment[242] and other previous studies.[134,243,248,250,251] It also agrees with the theoretical prediction of 1.84 eV [B3LYP/6-311++G(3df,3pd)]. The 557 ± 70 cm^{-1} spacing between the partially resolved peaks in the $X\,^2A''$ band (532 nm) is assigned to the CCO bending mode. Contributions from other modes (primarily due to CC and CO stretches) overlap with the main progression, resulting in additional structure and broadening of the bands in Figure 11.5.[242,243]

The first excited state of $H_2CCHO^{\bullet}$, $A\,^2A'$, also shows vibrational structure, with an onset at 2.80 ± 0.01 eV and an apparent spacing of about 1500 cm^{-1}. The band origin corresponds to a 0.98 ± 0.02 eV term energy for the A^2A' excited state of vinoxy radical, in agreement with the SEVI result of 0.996 ± 0.003 eV.[242] The ~1500 cm^{-1} vibrational progression for the $A\,^2A'$ state at 355 nm (Figure 11.5) is in good agreement with the 1595 cm^{-1} (unscaled) frequency of the CC stretch calculated at the B3LYP/6-

311++G(3df,3pd) level. Several other modes, primarily the CO stretch, also contribute to the overall band shape.[242,243]

The $X\,^2\mathrm{A}''$ transition exhibits perpendicular angular distributions at both wavelengths studied, corresponding to β = –0.64(5) at 355 nm. The excited state has a parallel distribution, with β = 0.51(5) determined for the first two vibrational features in the 355 nm image. Continetti and co-workers[134] interpreted the photoelectron angular distributions in H_2CCHO^- photodetachment using symmetry-based arguments.[32] In the dominant electron configuration of H_2CCHO^-, [core](10a′)^2(2a″)^2, the 2a″ HOMO is a non-bonding π orbital, while the 10a′ HOMO–1 is essentially an oxygen lone-pair with significant "s" character in the plane of the molecule. Electron detachment from the 10a′ orbital is expected to yield a predominantly parallel angular distribution, while detachment from 2a″ should yield a perpendicular distribution. Thus, the perpendicular and parallel features seen in Figure 11.5 are consistent with the formation of H_2CCHO in the $X\,^2\mathrm{A}''$ and $A\,^2\mathrm{A}'$ states, respectively.

11.3.3. Ketenylidene anion, $CCO^{\bullet-}$

The 355 nm photoelectron image and photoelectron spectrum of $CCO^{\bullet-}$ (*m*/z = 40 in Figure 11.2) are shown in Figure 11.6. The results are in excellent agreement with previous findings for $CCO^{\bullet-}$ (not involving the title reaction),[244-246] leaving no doubt about the identity of the observed species. All image features peak in the direction perpendicular to the laser polarization, corresponding to negative β values, as expected for electron emission from a *d*-like π* HOMO of $CCO^{\bullet-}$.

The spectrum shows a number of well resolved vibrational peaks. The first set of

peaks is assigned to the ground state of CCO, $X\,^3\Sigma^-$, and the origin yields EA = 2.31 ± 0.01 eV, in agreement with the previously reported values of 2.3207 ± 0.0006 eV (SEVI)[244] and 2.310 ± 0.012 eV (photoelectron spectroscopy).[247] The higher-energy peaks are assigned to the first, $a^1\Delta$, and second, $b^1\Sigma^+$, excited states of CCO. The sharp origin transitions are used to assign the adiabatic detachment energies: 2.95 ± 0.01 eV for the $a^1\Delta$ state and 3.33 ± 0.01 eV for $b^1\Sigma^+$. The corresponding term energies are 0.64 ± 0.01 and 1.02 ± 0.01 eV, respectively, compared to the SEVI values 0.6539 ± 0.0006 and 1.0170 ± 0.0006 eV.[244] The major progressions comprising the $X\,^3\Sigma^-$ and $a^1\Delta$ bands, spaced by about 1970 cm^{-1} in both cases, are assigned to CO stretch.

11.4. Discussion

The major products formed from the reaction of $O^{\bullet-}$ with H_3CCHO are $CCO^{\bullet-}$, $HCCHO^{\bullet-}$ and H_2CCHO^-. Of these, $HCCHO^{\bullet-}$ and H_2CCHO^- were observed previously,[235] but $CCO^{\bullet-}$ was not. Although $HCCHO^{\bullet-}$ was previously detected in the above reaction, it has not been studied by photoelectron spectroscopy. In Section 11.4.1, we discuss our findings for $HCCHO^{\bullet-}$ and the corresponding neutral molecule. In Section 11.4.2, a mechanism of $CCO^{\bullet-}$ formation is proposed. Section 11.4.3 summarizes the thermochemical properties derived from our measurements.

11.4.1. Formylmethylene: anion and neutral structures and the Wolff rearrangement

The formation of $HCCHO^{\bullet-}$ in the $O^{\bullet-}$ + H_3CCHO reaction was reported by Grabowski and Melly.[235] The photodetachment of this anion gives formylmethylene, an intermediate in the Wolff rearrangement (see Figure 11.1).

The electronic structures of three lowest-energy electronic states of HCCHO, the ground-state triplet (^{3}HCCHO), the singlet (^{1}HCCHO), and the excited-state triplet, are illustrated in Figure 11.7 for a planar molecular geometry with the H atoms in the *cis* configuration. In the ground state, the carbene structure has one electron in a σ and one in a π orbital. There is also a resonance structure with the unpaired π electron on the oxygen atom; this structure is best described as a σ, π biradical. Qualitative predictions suggest the carbene form is the primary resonance structure, so the biradical character of $X\,^3\mathrm{A}''$ is usually ignored.

In the singlet carbene at a planar geometry (corresponding to the $a\,^1\mathrm{A}'$ state), both electrons are paired in the carbon σ orbital, while the corresponding resonance structure with a C=C double bond is zwitterionic (Figure 11.7). However, the planar geometry is not the lowest energy structure of ^{1}HCCHO. It twists around the C–C bond, forming the lower energy non-planar structure. The non-planarity is an important property of singlet formylmethylene.[252-254]

The excited triplet state, $A\,^3\mathrm{A}''$, results from removal of an electron from the oxygen lone pair in the anion, producing a zwitterionic species best described as a σ, π biradical. In this state, there is an unpaired electron in the π system, which is resonance stabilized in a carbene zwitterionic structure. However, the σ, π biradical form is expected to be the primary resonance structure of the $A\,^3\mathrm{A}''$ state.

The geometries of precursors are known to play a role in determining the rearrangement products of carbonyl-carbenes.[236,237] In our investigation of $HCCHO^{\bullet-}$, both B3LYP and MP2 methods predict the non-planar *syn* geometry of $HCCHO^{\bullet-}$ is the global minimum, while the *anti* equilibrium is predicted to lie about 0.05 eV (1.1

kcal/mol) higher in energy.[255] To guide our analysis, we performed an inexpensive, albeit admittedly crude, relaxed potential energy surface scan with respect to the H-C-C(O)-H dihedral angle at the B3LYP/aug-cc-pVDZ level of theory. The result, plotted in Figure 11.8, shows a 0.15 eV (3.5 kcal/mol) barrier to interconversion. The dihedral angle corresponding to the minimum-energy structure is approximately 40°. Based on these findings, we expect the *syn* conformation of $HCCHO^{\bullet-}$ to be favored.

The ground state of neutral formylmethylene is a planar-geometry triplet. A similar potential energy surface scan (Figure 11.8) shows that the global minimum of HCCHO corresponds to a *trans* geometry, with the *cis* structure as a local minimum about 0.04 eV (1 kcal/mol) higher in energy. The barrier to *cis–trans* interconversion is predicted to be 0.30 eV (7 kcal/mol). Hence, we expect vertical electron detachment from the *syn* global minimum of the anion (VDE = 2.22 eV at the B3LYP/aug-cc-pVDZ level of theory) to yield the higher-energy *cis*-^{3}HCCHO isomer with a calculated adiabatic electron affinity (relative to *syn*-$HCCHO^{\bullet-}$) of about 1.93 eV. Vertical detachment from the slightly higher-energy *anti* anion (VDE = 2.18 eV at the B3LYP/aug-cc-pVDZ level of theory) would lead to the lower-energy *trans*-^{3}HCCHO, with a calculated adiabatic electron affinity (relative to *anti*-$HCCHO^{\bullet-}$) of about 1.83 eV.

The 532 nm photoelectron spectrum of $HCCHO^{\bullet-}$ in Figure 11.3(a) is congested, because of the overlap of many vibrational modes of ^{3}HCCHO excited upon $HCCHO^{\bullet-}$ photodetachment. The electron affinity of ^{3}HCCHO is determined to be 1.87 ± 0.02 eV, in good agreement with the calculated values for both the *trans*- and *cis*- forms of ^{3}HCCHO (1.83 and 1.93 eV, respectively). The spectrum in Figure 11.3(a) does show a vibrational progression, with an average spacing of 456 ± 28 cm^{-1}, as determined by the

Fourier analysis described in Section 11.3.1. The major geometry difference between the anion and neutral is the H-CC(O)-H dihedral angle, and so we expect the H-CC(O)-H out-of-plane bend to be the primary vibration excited upon photodetachment. The observed spectral interval is in good agreement with the fundamental frequency of this mode in *cis*-^{3}HCCHO, calculated to be 492 cm^{-1} (unscaled, B3LYP/aug-cc-pVQZ level of theory). This observation suggest the predominant presence of *syn*-HCCHO$^{\bullet-}$, consistent with the lower energy of the *syn* (compared to *anti*) conformation, as predicted by theory.

The same mode for the *trans*-^{3}HCCHO structure has a 626 cm^{-1} frequency, which is intriguingly close to the location of a secondary spectral feature at 608 ± 30 cm^{-1} in Figure 11.4(b), just to the right of the main (*) peak. Although the intensity of this secondary feature is too small to draw solid conclusions, we find that the integrated intensity ratio of the two peaks (~20:1) is consistent with a statistical distribution of the *syn*- and *anti*-HCCHO$^{\bullet-}$ isomers, given the predicted energy difference (1.1 kcal/mol) and assuming an ion-beam (vibrational) temperature of ~200 K.

The higher-energy feature in the 355 nm photoelectron spectrum of HCCHO$^{\bullet-}$ in Figure 11.3(b) is attributed to the excited triplet state, $A\,^3\mathrm{A}''$, which arises from electron detachment of an oxygen lone-pair in HCCHO$^{\bullet-}$ (see Figure 11.7) with a calculated VDE of 3.00 eV (B3LYP/aug-cc-pVDZ). This prediction compares well with the band maximum observed at about 3.05 eV.

Based on various theoretical predictions, the HCCHO$^{\bullet-}$ → ^{1}HCCHO photodetachment transition is expected at eBE ≥ 2.60 eV – slightly higher in energy than ^{3}HCCHO, but below the excited triplet, $A\,^3\mathrm{A}''$. The photoelectron spectrum shows no

clear evidence for ^{1}HCCHO. The expected location of this transition, based on B3LYP/aug-cc-pVDZ, is indicated in Figure 11.3(b) by a dashed line. Although there is spectral intensity in this region, it is impossible to conclude if it is due to ^{1}HCCHO or the $X\,^3$A″ band, or both.

Geometry optimization for ^{1}HCCHO, starting from the global-minimum *syn* structure of HCCHO$^{\bullet-}$, at all levels of theory used in this study, leads to ketene, H_2CCO. This result is in accord with previous observations that *syn*-ketocarbenes preferentially form ketene products. It also agrees with the time-resolved studies[239,240,256] that indicated a fast, direct rearrangement for *syn* ketocarbenes. On the other hand, optimization of ^{1}HCCHO geometry starting from the *anti*-HCCHO$^{\bullet-}$ structure yielded a stable minimum corresponding to *anti*-^{1}HCCHO, separated from ketene by a small barrier. Figure 11.9 summarizes the neutral product correlations for *syn*- and *anti*-HCCHO$^{\bullet-}$ photodetachment, including the *anti*-^{1}HCCHO → H_2CCO transition state. At the B3LYP/aug-cc-pVDZ level of theory, vertical detachment of *anti*-HCCHO$^{\bullet-}$ yields ^{1}HCCHO with an energy approximately equivalent to the transition state and the resulting neutral molecule is likely to undergo a 1,2-H atom shift to ketene. Overall, detachment to the singlet state is expected to result in a fast Wolff rearrangement to H_2CCO, regardless of the starting geometry of HCCHO$^-$. The transient nature of ^{1}HCCHO contrasts that of ^{3}HCCHO, which is a long-lived species, not subject to the Wolff rearrangement.

Although both HCCHO$^{\bullet-}$ and ^{1}HCCHO are non-planar at their respective equilibria, the geometry difference between the two is more significant than that of the anion and ^{3}HCCHO (see Figure 11.9). Because of the large difference between the equilibrium geometries of HCCHO$^{\bullet-}$ and ^{1}HCCHO (or H_2CCO), we expect these transitions to have

poor Franck-Condon overlap and hence low intensity, compared to ^{3}HCCHO. Photoelectron (transition-state) spectroscopy, is often a powerful tool for probing short-lived intermediates. For example, this utility is clearly born out in the studies of vinylidenes[108,184] and oxyallyl.[257-259] However, to observe a short-lived intermediate, it must either be well separated in the photoelectron spectrum from other transitions or exhibit identifiable characteristic vibrational structure. In this study, the ^{1}HCCHO transition is expected to have low intensity due to a poor Franck-Condon overlap, while lying in the same spectral range as the congested triplet band. For this reason, the photodetachment signal due to ^{1}HCCHO is probably buried underneath the $X\,^3$A″ band in Figure 11.3(b). Often, the angular distributions corresponding to different photodetachment transitions can be used to identify the ground and excited states, but in the present study the broad congested band from the triplet overwhelms any possible intensity from the singlet.

11.4.2. Ketenylidene anion: formation mechanism

The photoelectron image and spectrum of the *m/z* = 40 anion presented in Figure 11.6 are in excellent agreement with previous results for $CCO^{\bullet-}$,[244-247] as discussed in Section 11.3.3, leaving no doubt about the identity of the observed species. However, the formation of this anion in our ion source is both novel and interesting, because it must involve at least a two-step process that removes a net $H_4^{\bullet+}$ from H_3CCHO.

In Figure 11.10, we suggest a mechanism that assumes an initial $H_2^{\bullet+}$ abstraction to form either stable formylmethylene anion, $HCCHO^{\bullet-}$, via path (a), or a metastable ketene anion $[H_2CCO^{\bullet-}]^*$, path (b). Evidence that $H_2CCO^{\bullet-}$ is not stable is provided by the

photoelectron spectra of the *m/z* = 42 ion (Figure 11.3), which does not show any low electron binding energy features expected for a weakly bound anion such as $H_2CCO^{\bullet-}$. The $[H_2CCO^{\bullet-}]^*$ intermediate is expected to undergo rapid autodetachment to form $H_2CCO + e^-$. A second $H_2^{\bullet+}$ abstraction from the nascent H_2CCO by a second $O^{\bullet-}$ would yield then $CCO^{\bullet-}$, via step (c) in Figure 11.10.

We recognize that the evidence to support this proposal is scarce. Indeed, the electron/ion-molecule chemistry in our ion source could conceivably involve alternative reactions and the mechanism in Figure 11.10 is but one way to rationalize the formation of $CCO^{\bullet-}$ in our experiment. The principal weakness of the proposed explanation is the very low probability expected for a multi-step process in a pulsed ion source. However, such processes are not unknown and the low intensity of the observed $CCO^{\bullet-}$ ions (see Figure 11.2) is consistent with a low-probability mechanism. In another example of such a process, vinoxide anion can be synthesized by the reaction of $O^{\bullet-}$ with ethanol,[134,243,248] which requires a multi-step mechanism that removes a net H_3^+ from CH_3CH_2OH. In the course of the present project, we confirmed this reaction by measuring photoelectron spectra of the *m/z* = 43 anion prepared from the reaction of $O^{\bullet-}$ and ethanol. The spectra were identical to those shown in Figure 11.5. In this case, the reaction probably proceeds via an initial $H_2^{\bullet+}$ abstraction from ethanol that produces a metastable acetaldehyde anion, $[H_3CCHO^{\bullet-}]^*$, which decays via electron emission to H_3CCHO. A secondary proton abstraction by $O^{\bullet-}$ then gives the vinoxide anion, H_2CCHO^-.

11.4.3. Thermochemistry

The electron affinities determined in this study can be used to calculate

thermodynamic properties of the corresponding anions and radicals. Of primary interest are heats of formation ($\Delta_f H_{298}$) and bond dissociation energies (denoted here as BDE, but also commonly referred to as DH_{298}).

The R–H BDEs are calculated using the acidity/electron affinity cycle:[6,139]

$$\mathrm{BDE(R–H)} = \Delta_{acid}H_{298}(\mathrm{RH}) + \mathrm{EA(R)} - \mathrm{IP(H)} + [\text{thermal correction}], \quad (11.7)$$

where IP(H) is the ionization potential of the hydrogen atom. The [thermal correction] term arises from integrated (0 to 298 K) differential heat capacities (ΔC_p) of the reactants and products. This term is small, typically about 0.3 kcal/mol. It is absorbed by other, larger uncertainties involved in the calculations and, therefore, disregarded from this point on. The thermochemical parameters used in our calculations and the results are summarized in Table 11.1. The source column either gives references for the previously known values or specifies how the new values were determined. Although multiple paths to a given quantity are possible within the self-consistent framework of thermodynamics, only selected one or two are identified in each case.

For example, from the experimentally determined EA(H_2CCHO) = 1.82 ± 0.01 eV = 42.0 ± 0.2 kcal/mol (line XI in Table 11.1), we calculate, using Eq. (11.7), the C–H bond dissociation energy on the methyl group of acetaldehyde, BDE(H–CH_2CHO) = 94.3 ± 2.2 kcal/mol (line XVII). From the same calculation using the more precise SEVI value for the electron affinity (1.8250 ± 0.0012 eV),[242] we obtain a BDE = 94.4 ± 2.2 kcal/mol, which is indistinguishable from our value. This comparison is, nonetheless, quite instructive, as it serves to emphasize that the main contribution to the uncertainty comes from the measured acidity of acetaldehyde, $\Delta_{acid}H_{298}(H_3CCHO)$ (line XV in Table 11.1), and not the spectroscopic determination of electron affinity of the corresponding

radical.

Bond dissociation energies and gas-phase acidities are related to the corresponding heats of formation:

$$\Delta_f H_{298}(R) = BDE(R–H) + \Delta_f H_{298}(RH) – \Delta_f H_{298}(H) \quad (11.8)$$

$$\Delta_f H_{298}(R^-) = \Delta_{acid} H_{298}(RH) + \Delta_f H_{298}(RH) – \Delta_f H_{298}(H^+) \quad (11.9)$$

Substituting the above result, BDE(H–CH_2CHO) = 94.3 ± 2.2 kcal/mol in Eq. (11.8), we obtain the formation enthalpy of the vinoxy radical, $\Delta_f H_{298}(H_2CCHO^{\bullet})$ = 1.4 ± 2.2 kcal/mol (line IV).

The first C–H bond dissociation energy on the methyl group of acetaldehyde (94.3 kcal/mol, as determined above), is slightly smaller than many typical C–H BDEs. For comparison, in propane, the H-$CH_2CH_2CH_3$ BDE is calculated to be 100.4 ± 3.4 kcal/mol.[139] The small difference can be partially attributed to resonance stabilization of the unpaired electron in the vinoxy radical resulting from acetaldehyde dissociation.

Vinoxy radical has a planar structure, with the unpaired electron on the carbon radical center stabilized by resonance with the π electrons in the carbonyl bond. This radical can be regarded as an allyl radical ($H_2CCHCH_2^{\bullet}$) with one of the methylene groups replaced by an oxygen atom. Allyl radical is formed by methyl C–H cleavage in propene (CH_3CHCH_2) and the corresponding BDE(H–CH_2CHCH_2) = 88.8 ± 0.4 kcal/mol[139] is distinctly lower than the BDE(H–CH_2CHO) = 94.3 ± 2.2 kcal/mol obtained above. Allyl radical has two equivalent resonance structures, with the radical site located on either of the terminal methylene groups. The double-resonance stabilization is reflected in the low BDE of propene. In vinoxy radical, on the other hand, the resonance structures are not equivalent: the configuration with a π bond on the more electronegative

oxygen atom is dominant, while the structure with a π bond connecting the carbon atoms has a smaller contribution. As a result of the decreased resonance stabilization of the unpaired electron, acetaldehyde has a larger BDE, compared to propene.

In contrast, BDE($H_2CC(O)$–H), i.e. the C–H BDE of $H_2CCHO^{\bullet}$ on the central carbon, to give H_2CCO, is determined to be only 39.3 ± 2.2 kcal/mol (line XVIII in Table 11.1). This is less than half the energy of a C–H bond on the methylene and reflects the stability of ketene, in which the two unpaired electrons couple to form a CC π bond.

The thermochemistry of ketenylidene is obtained from the EA of CCO. Using our experimental EA(CCO), Eq. (11.7), and the thermochemical values in Table 11.1, we calculate BDE(H–$CCO^{\bullet}$) = 99.9 ± 3.6 kcal/mol (line XIX). The bond energy calculated using the SEVI value[244] for EA(CCO) is 100.1 ± 3.6 kcal/mol, which is, again, indistinguishable from our value (within the uncertainly limits). We also obtained $\Delta_f H_{298}$(CCO) = 90.2 ± 4.2 kcal/mol (line VIII). This result is in agreement with the previously reported value $\Delta_f H_{298}$(CCO) = 92.0 ± 4.6 kcal/mol,[246] although the agreement could be expected due to the use of similar thermochemical cycles. However, both of these values differ significantly from the value presently reported in the NIST Chemistry WebBook database, $\Delta_f H_{298}$(CCO) = 68.499 kcal/mol (line IX).[144]

The correct value $\Delta_f H_{298}$(CCO) is important both in itself and as a parameter used in calculating the thermodynamic properties of other species. In order to examine the above discrepancy, we used B3LYP/6-31+G(d) to estimate BDE(H–CCO) and BDE(C–CO), and compared the results with the corresponding BDE values obtained from Eq. (11.9) using $\Delta_f H_{298}$(CCO) = 90.2 kcal/mol (this work) and 68.499 kcal/mol (NIST Chemistry WebBook[144]).

Substituting $\Delta_f H_{298}$(CCO) = 90.2 kcal/mol in Eq. (11.9), we obtain BDE(H–CCO) = 99.9 kcal/mol (Table 11.1, line XIX) – in excellent agreement with the DFT prediction of 98 kcal/mol. Using Eq. (11.8) with $\Delta_f H_{298}$(CCO) = 68.499 kcal/mol,[144] on the other hand, gives a much lower BDE(H–CCO) value of 78 kcal/mol. Theory also predicts BDE(C–CO) = 60 kcal/mol, in good agreement with the BDE(C–CO) of 54.7 kcal/mol, obtained using $\Delta_f H_{298}$(CCO) = 90.2 ± 4.2 kcal/mol (this work) and the standard heats of formation of C and CO, 171.30 and –26.41 kcal/mol,[260] respectively. The same calculation using $\Delta_f H_{298}$(CCO) = 68.499 kcal/mol predicts a C–CO bond energy of 76.4 kcal/mol, which differs significantly from the DFT prediction. While DFT BDEs are not indisputable, the calculations support the findings based on our experimental measurements. Therefore, we recommend $\Delta_f H_{298}$(CCO) = 90.2 ± 4.2 kcal/mol.

11.5. Conclusions

We used photoelectron imaging spectroscopy to characterize the $HCCHO^{\bullet-}$, H_2CCHO^-, and $CCO^{\bullet-}$ products of the reaction of $O^{\bullet-}$ with H_3CCHO. From photoelectron spectra of the formylmethylene anion, the electron affinity of HCCHO (1.87 ± 0.02 eV) and the detachment energies for two triplet bands are determined, but no unambiguous assignment for the singlet state of HCCHO could be made. This is attributed to the singlet being an intermediate in the Wolff rearrangement, which results in formation of ketene; we therefore expect large geometry change (thus, poor Franck-Condon overlap) and fast rearrangement upon photodetachment to the singlet surface. The title reaction also provides a unique method for synthesizing $CCO^{\bullet-}$, whose formation in our ion source is both novel and intriguing. A possible two-step mechanism for $CCO^{\bullet-}$ formation is suggested, involving an $[H_2CCO^{\bullet-}]^*$ intermediate. From the

measured electron affinities of HCCHO, H_2CCHO, and CCO, several new thermochemical properties have been determined, such as the C–H bond dissociation energies and heats of formation of some organic molecules and/or their anion. In particular, we determine the heat of formation of CCO, $\Delta_f H_{298}$(CCO) = 90.2 ± 4.2 kcal/mol, and recommend revising the presently accepted value. Overall, the high reactivity of $O^{\bullet-}$ with organic molecules demonstrates the utility of this reagent in the formation of a variety of reactive intermediates via a single process.

Acknowledgements. This work was supported by the U.S. National Science Foundation (grants CHE-071380 and CHE-1011895).

Table 11.1 Thermochemical quantities either used or obtained in this work. All values in kcal/mol.

#	**Property**	**Value**	**Source**
I.	$\Delta_f H_{298}(H)$	52.103 ± 0.001	Ref. [148]
II.	$\Delta_f H_{298}(H_3CCHO)$	–40.80 ± 0.35	Ref. [261]
III.	$\Delta_f H_{298}(H_2CCO)$	–11.4 ± 0.4	Ref. [245]
IV.	$\Delta_f H_{298}(H_2CCHO^{\bullet})$	1.4 ± 2.2	*This work:* Eq. (8), I, II, XVII
V.	$\Delta_f H_{298}(HCCO^{\bullet})$	42.4 ± 2.1	Ref. [245]
VI.	$\Delta_f H_{298}(H^+)$	365.696 ± 0.001	Ref. [262,263]
VII.	$\Delta_f H_{298}(H_2CCHO^-)$	–40.6 ± 2.2	*This work:* Eq. (9), II, VI, XV
VIII.	$\Delta_f H_{298}(CCO)$	90.2 ± 4.2[a]	*This work:* Eq. (8), I, V, XIX
IX.	$\Delta_f H_{298}(CCO)$	*68.499*[b]	Ref. [144]
X.	$\Delta_f H_{298}(CCO^{\bullet-})$	36.9 ± 4.2	*This work:* VII, XIII or Eq. (9), V, VI, XVI
XI.	$EA(H_2CCHO^{\bullet})$	42.0 ± 0.2	*This work:* experiment (Fig. 5)
XII.	EA(HCCHO)	43.1 ± 0.5	*This work:* experiment (Fig. 3)
XIII.	EA(CCO)	53.3 ± 0.2	*This work:* experiment (Fig. 6)
XIV.	IP(H)	313.6	Ref. [144,262,263]
XV.	$\Delta_{acid} H_{298}(H_3CCHO)$	365.9 ± 2.2	Ref. [143]
XVI.	$\Delta_{acid} H_{298}(HCCO^{\bullet})$	360.2 ± 3.6	Ref. [264]
XVII.	$BDE(H–CH_2CHO)$	94.3 ± 2.2	*This work:* Eq. (7), XI, XIV, XV
XVIII.	$BDE(H_2CC(O)–H)$	39.3 ± 2.2	*This work:* Eq. (8), I, III, IV
XIX.	$BDE(H–CCO^{\bullet})$	99.9 ± 3.6	*This work:* Eq. (7), XIII, XIV, XVI

[a] Recommended value. [b] Presently reported on NIST website[144] (not recommended).

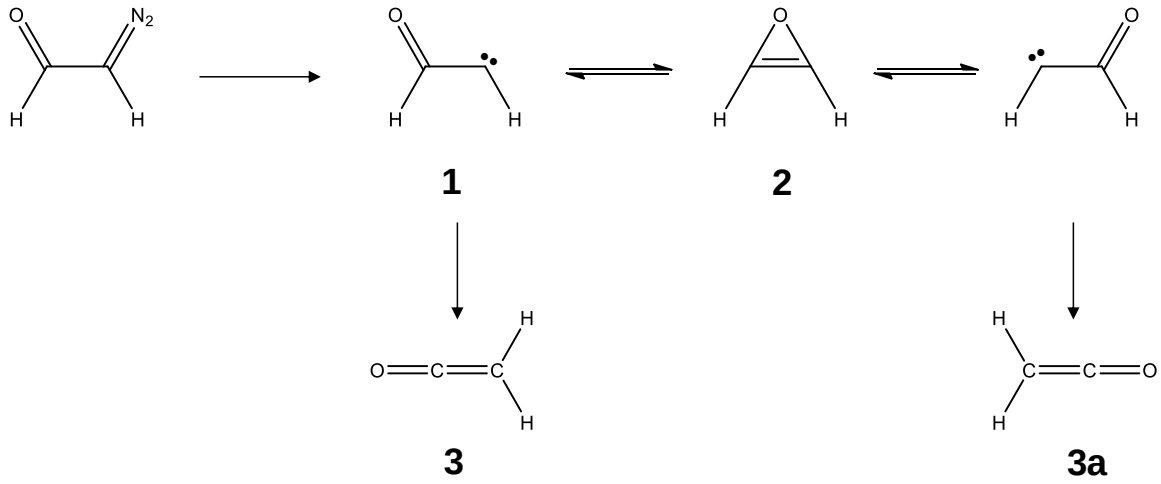

Figure 11.1 General mechanism for the Wolff rearrangement of formylmethylene, **1**, to ketene, **3**, via the oxirene intermediate, **2**, allowing carbon atom scrambling.

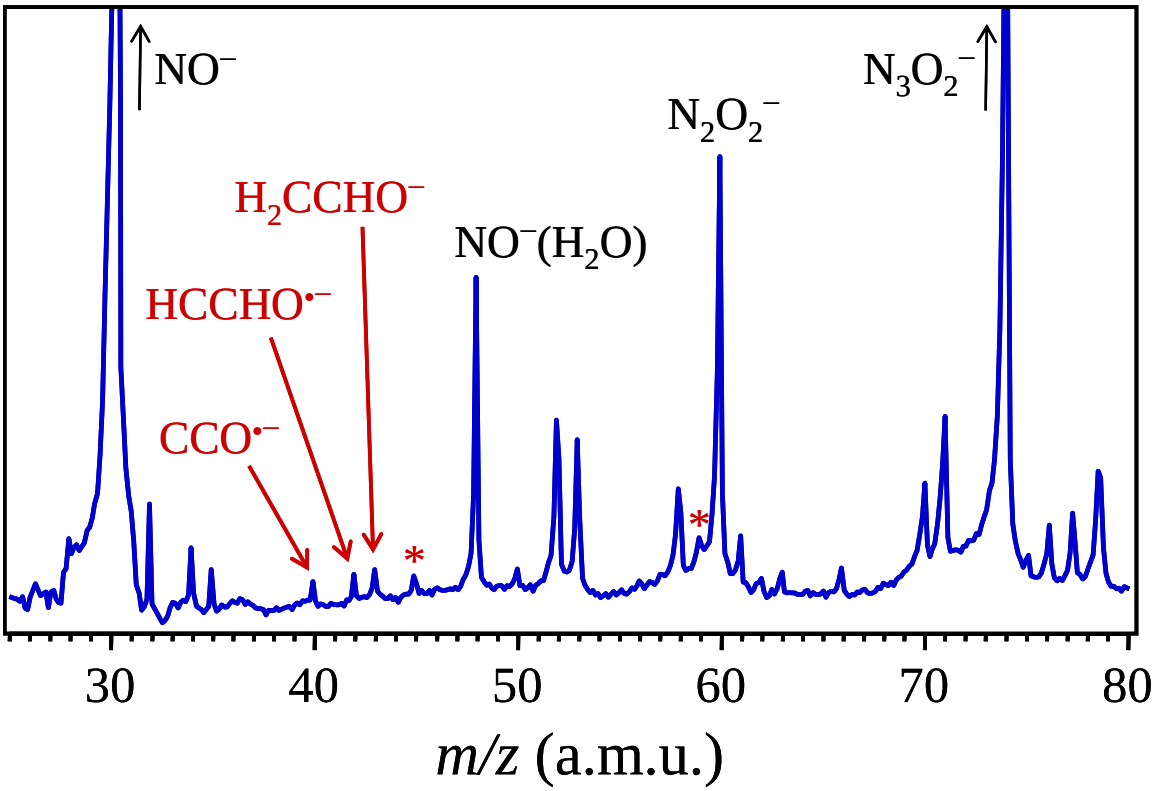

Figure 11.2 Time-of-flight mass-spectrum of the negative ions formed in the reaction of $O^{\bullet-}$ with H_3CCHO seeded in N_2O carrier gas at a backing pressure of 30 psi. The vertical scale is magnified to emphasize the low-intensity peaks. The major peaks (black labels) correspond to $N_xO_y^-$ species resulting from the reaction of $O^{\bullet-}$ with N_2O. The $O^{\bullet-}$ + H_3CCHO reaction products, CCO^- (*m/z* = 40), $HCCHO^-$ (*m/z* = 42) and H_2CCHO^- (*m/z* = 43) are indicated with red arrows and corresponding labels. The peaks marked with red asterisks could correspond to the addition/elimination products HCO_2^- (*m/z* = 45) and $CH_3CO_2^-$ (*m/z* = 59); however, due to low ion intensity, we could not obtain photoelectron spectra of these ions to confirm the assignment.

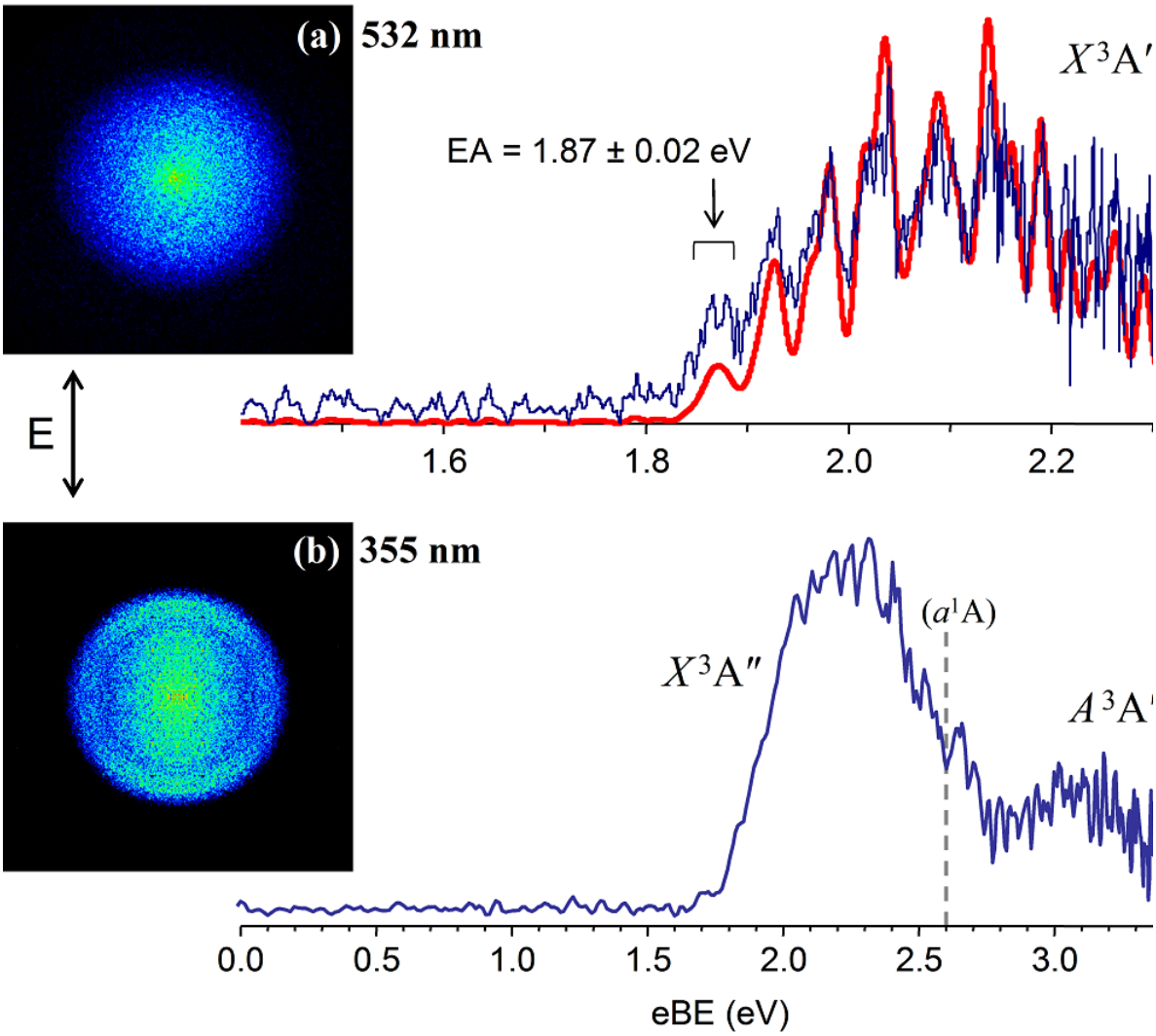

Figure 11.3 Photoelectron images and spectra of formylmethylene anion, $HCCHO^{\bullet -}$, measured at 532 and 355 nm. In (a), the 532 nm experimental spectrum (blue) corresponding to the ground X^3A'' state of HCCHO, is superimposed with the filtered spectrum (red), obtained using a low-pass Fourier filter, as described in the text. In (b), the 355 nm image and spectrum show two bands corresponding to the X^3A'' and A^3A'' states of HCCHO. The vertical dashed line indicates the approximate location of the a^1A state, expected based on the calculations described in the text.

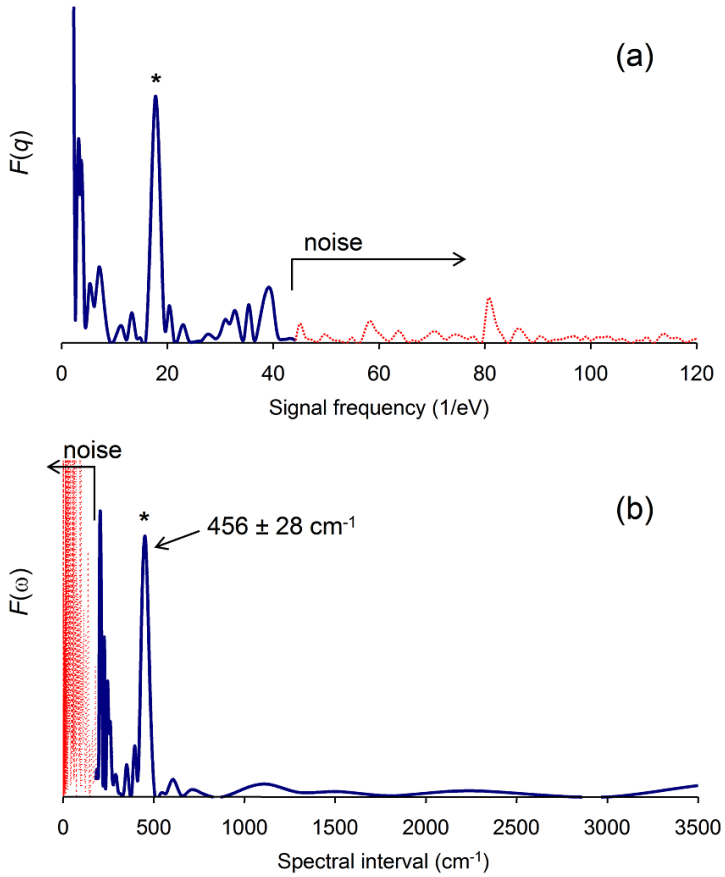

Figure 11.4 (a) Fourier transform $F(q)$ of the experimental 532 nm photoelectron spectrum of $HCCHO^{\bullet-}$ in Figure 11.3(a). The Fourier spectrum is arbitrarily divided into the low-q (true signal) and high-q (noise) parts, shown as a solid blue and red dotted lines, respectively. The high-q (noise) part is discarded in calculating the filtered spectrum shown in Figure 11.3(a). **(b)** The same Fourier spectrum as in (a), but plotted as a function of periodic spectral interval ω, related to signal frequency q by $\hbar\omega = 1/q$. $F(\omega)$ is obtained from $F(q)$ via a Jacobian transformation $F(\omega) = F(q)\,|dq/d\omega|$, with $|dq/d\omega| \propto q^2$. The blue solid and red dotted lines have the same meaning as in (a). Asterisks mark the same dominant vibrational peak at $q = 17.7$ eV^{-1} in (a), corresponding to $\omega = 456$ cm^{-1} in (b), reflecting the average spacing of the partially resolved vibrational progression seen in the experimental spectrum in Figure 3(a).

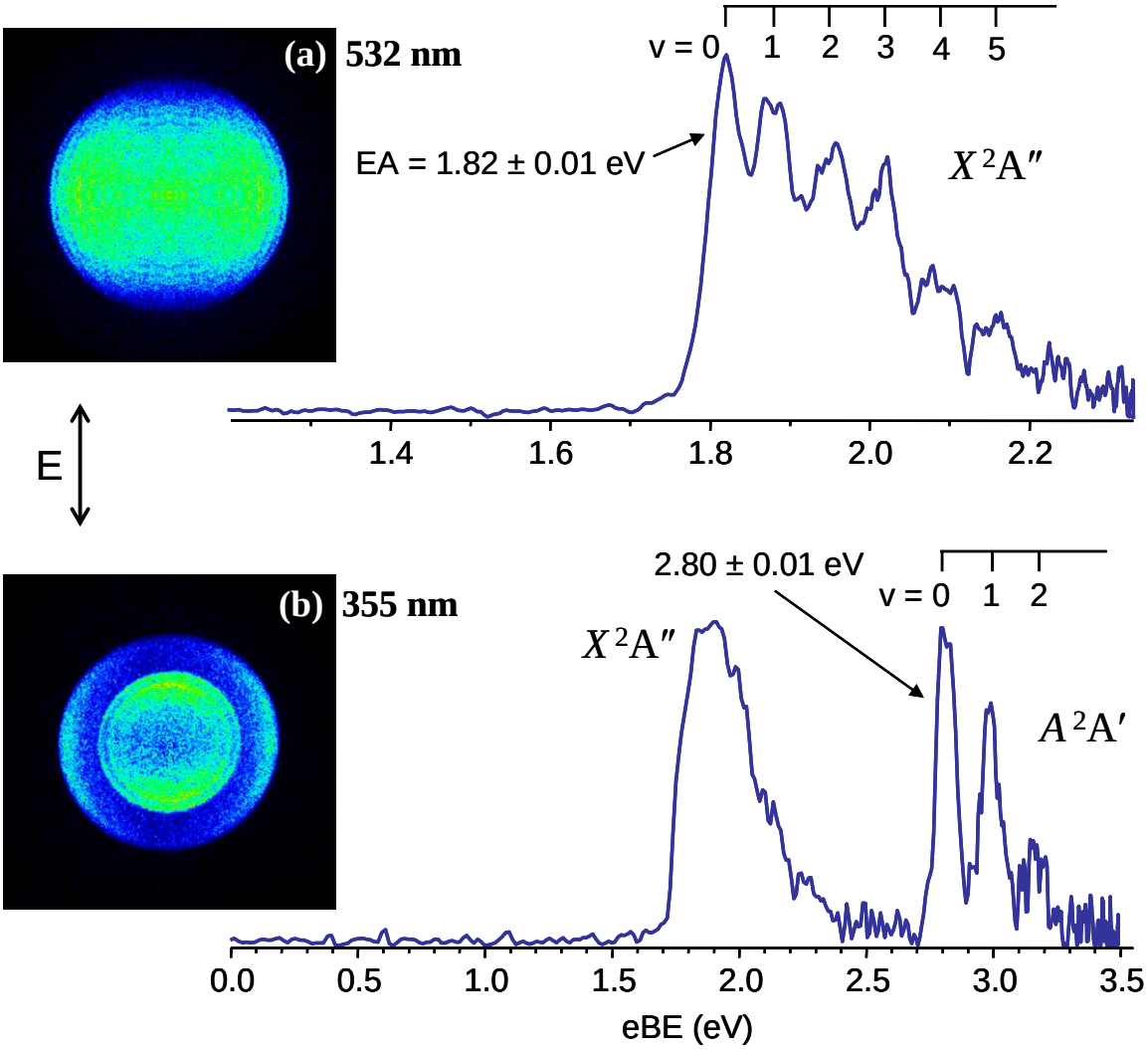

Figure 11.5 Photoelectron images and spectra of vinoxide, $H2CCHO^-$, measured at (a) 532 and (b) 355 nm. The 532 nm spectrum shows the ground X $^2A''$ state and a vibrational progression with the peaks labeled v = 0 – 5. The 355 nm spectrum also show the X $^2A''$ state and the excited A $^2A'$ state with a vibrational progression labeled v = 0 – 2.

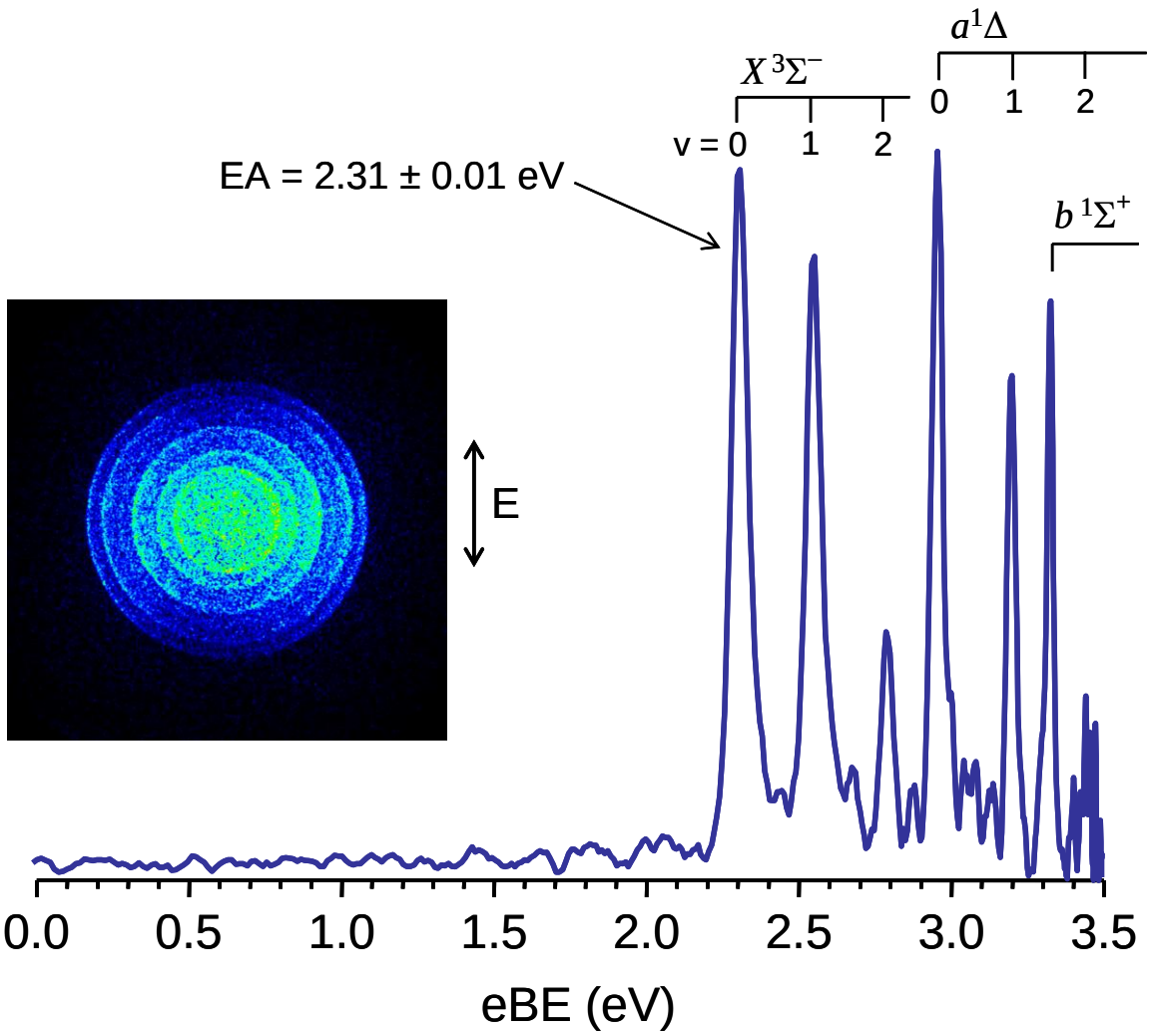

Figure 11.6 Photoelectron image and spectrum of $CCO^{\bullet-}$ obtained at 355 nm. The $X\,^3\Sigma^-$, $a\,^1\Delta$, and $b\,^3\Sigma^+$ electronic states are observed, with the well-resolved vibrational progressions corresponding to the C=O stretch. Lower intensity peaks are due to the C=C stretch mode.

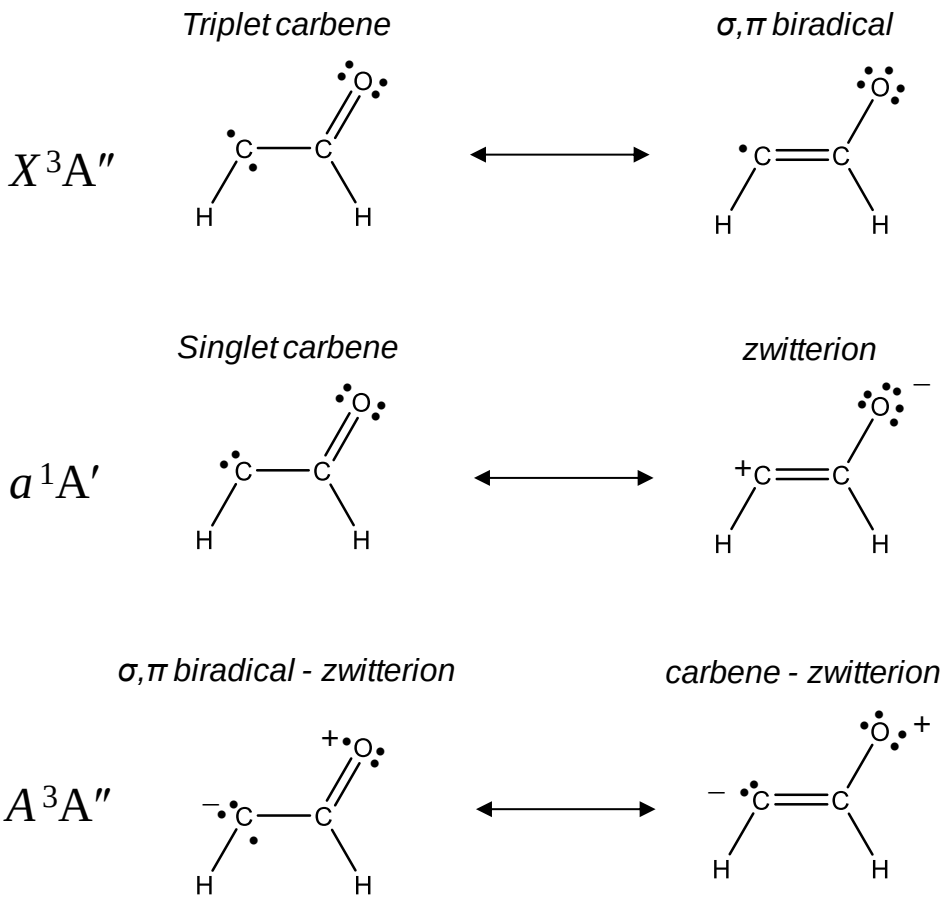

Figure 11.7 The lowest electronic states of HCCHO, $X\,^3\mathrm{A}''$, $a^1\mathrm{A}'$, and $A\,^3\mathrm{A}''$ in order of increasing energy. The primary resonance structures for each state are labeled to best describe the electron arrangement.

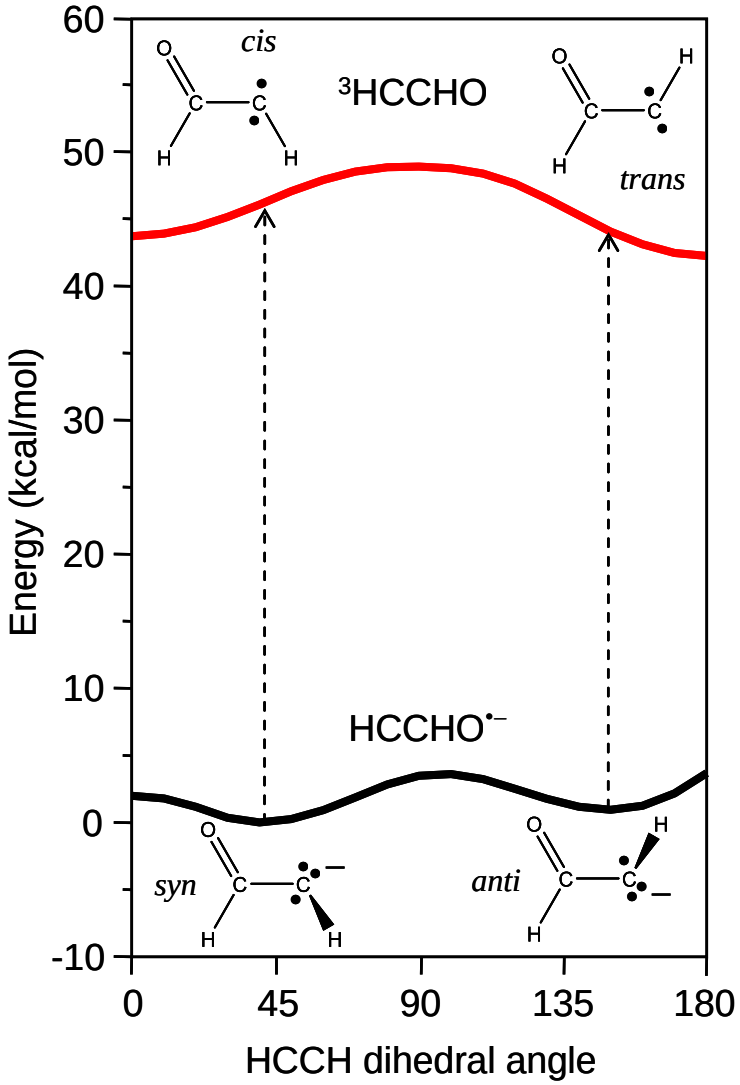

Figure 11.8 Relaxed potential energy surface scan of the HCCH dihedral for $HCCHO^{\bullet -}$ and $^{3}HCCHO$ calculated at the B3LYP/aug-cc-pVDZ level of theory. The predicted lowest-energy structure for $HCCHO^{\bullet -}$ is the *syn* geometry, while the *anti* structure is about 1 kcal/mol higher in energy. The lowest energy structure of $^{3}HCCHO$ is the *trans* isomer, with a barrier of about 3.5 kcal/mol separating the *cis* and *trans* isomers.

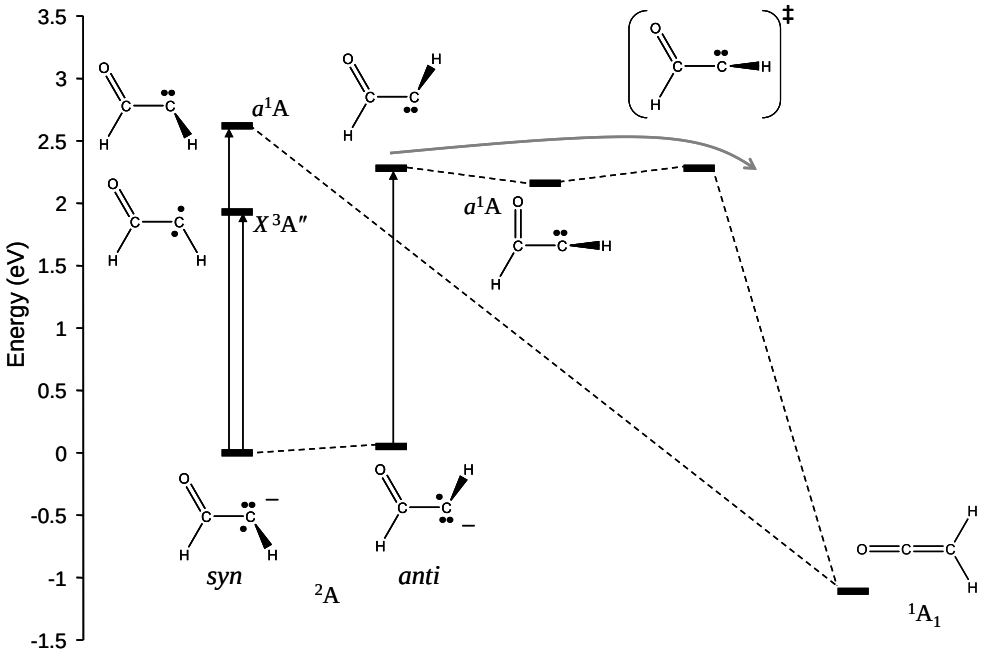

Figure 11.9 Schematic correlation diagram for $HCCHO^{\bullet-}$ photodetachment at the B3LYP/aug-cc-pVDZ level of theory. Detachment of $HCCHO^{\bullet-}$ from either *syn* or *anti* geometries leads to the Wolff rearrangement product H_2CCO.

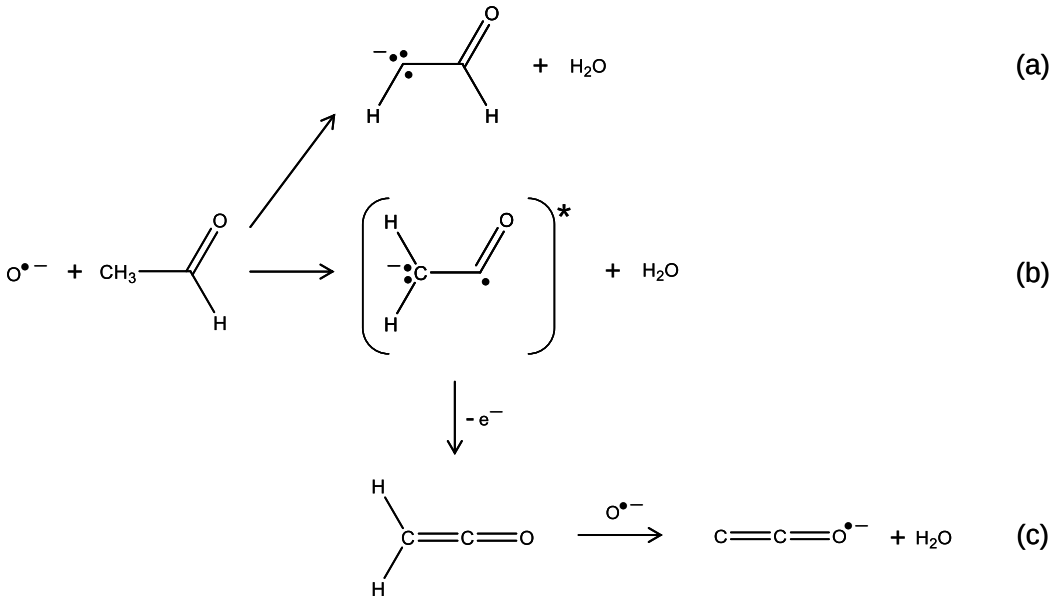

Figure 11.10 Proposed mechanism for the formation of $CCO^{\bullet-}$ in the reaction of $O^{\bullet-}$ with acetaldehyde, H_3CCHO, via a two step process involving the ketene anion intermediate, $[H_2CCO^{\bullet-}]^*$.

CHAPTER 12

LOW LYING ELECTRONIC STATES OF CYCLOPENTADIENONE VIA PHOTOELECTRON IMAGING SPECTROSCOPY

12.1. Introduction

Cyclopentadienone (C_5H_4O) is an important intermediate in the combustion of benzene and phenol, and biomass pyrolysis.[265] It is extremely reactive due to its anti-aromatic electronic resonance character, however it was shown to have a sufficient lifetime in gas phase[266] for rotational[267] spectroscopy studies. An accurate assignment of the vibrational frequencies of C_5H_4O has recently been reported[265] using infrared absorbance spectroscopy of cyclopentadienone frozen in solid rare gas matrices and backed up by high-level ab initio anharmonic force field calculations.

There are not a lot of previous studies on the excited state ordering of neutral C_5H_4O. Theoretical studies[268] of a series of conjugated, cyclic ketones suggest the lowest spin allowed transition of C_5H_4O to be $X^1A_1 \rightarrow {}^1B_2$, with the excitation energy of 3.00 eV, while the most intense band of the theoretical spectrum is calculated to be at 5.98 eV, corresponding to a transition to ${}^1A_1$ state. This is in good agreement with the UV/VIS spectrum[269] that shows band maxima at 195 and 360 nm (6.35 and 3.44 eV respectively). The first excited triplet state is theoretically predicted to be a ${}^3B_2$ state with an excitation energy of 1.97 eV.[268] Access to low lying triplet excited states however is forbidden due to spin selection rules and therefore has not been observed experimentally. Photoelectron spectroscopy of negative ions is not bound by the same selection rules as optical

spectroscopy and thus uniquely suited for studying both singlet and triplet excited states simultaneously.

Atomic oxygen radical anion ($O^{\cdot -}$) reactivity, described in detail elsewhere, can be utilized to synthesize a number of important anion intermediates in the gas-phase. These intermediates can be than characterized using spectroscopic tools in order to obtain their thermochemical, as well as molecular and electronic properties. The $O^{\cdot -}$ anions are formed in the gas phase by employing N_2O as a carrier gas, which along with a sample vapor is introduced in high vacuum chamber via pulsed supersonic nozzle. The gas mixture is intersected with high energy (1 keV) electron beam generated by electron gun, creating slow secondary electrons which undergo dissociative attachment to N_2O to form $O^{\cdot -}$. The nascent $O^{\cdot -}$ reacts further with sample of interest usually via single or double deprotonation reactions.

In this work, we have produced cyclopentadienone anion ($C_5H_4O^-$) via unusual 4 H abstraction reaction of $O^{\cdot -}$ with cyclopentanone (C_5H_8O) neutral precursor. Using photoelectron imaging spectroscopy we were able to gain access to several low-lying electronic excited states of the C_5H_4O and report first measurements of its electron affinity and singlet-triplet splitting.

12.2. Experimental

The experiments were performed using the negative-ion photoelectron spectrometer described in detail elsewhere.[37] In brief, a mixture of room temperature cyclopentanone vapor with N_2O carrier gas at a backing pressure of 30 psi was expanded into vacuum chamber through a pulsed supersonic nozzle (General Valve, series 99). The

anions are formed via deprotonation process described above and extracted into Willey-McLaren time-of-flight mass spectrometer where they are separated by mass-to-charge ratio. The mass-selected anions are intersected with linearly polarized laser pulses, within a velocity-map imaging assembly, timed to coincide only with the ions of interest. Anion photodetachment was performed at 355, 532, 808, and 1064 nm. The 808 nm radiation was the fundamental output of a Continuum, Inc., Surelight II-20 Nd:YAG pumped (532 nm) ND6000 dye laser, operating on the LDS821 dye and delivering 10 mJ, ~ 10 ns duration pulses. The 1064, 532, and 355 nm radiation was the output of fundamental, second or third harmonics of Spectra Physics, Inc. Lab-130 Nd:YAG (neodymium-doped yttrium aluminum garnet) laser with ~ 6 ns pulse duration and 5 mJ/pulse.

The photodetached electrons are accelerated by a series of velocity-map imaging electrodes onto a 40 mm position sensitive microchannel plate detector coupled to a P43 phosphorus screen (Burle, Inc.). The resulting images are recorded by a charge-coupled device camera (Photometrics CoolSNAP MYO) and accumulated for ~10^6 experimental cycles. The images were analyzed by means of the inverse Abel transformation[25] using the BASEX software package.[40] The energy scale in the resulting spectra is calibrated using the well-known photodetachment transition of O^-.[41]

A representative mass-spectrum of the anions generated with cyclopentanone seeded in N_2O is presented in Figure 12.1(b) along with the similar spectrum obtained for the fluoroacetonitrile (CH_2FCN) mixture with N_2O (a) to indicate the sample sensitive nature of the peak of interest, 80 a.m.u. The intensity of the mass spectrum peak is in arbitrary units, and is dependent on the instrument settings – backing pressure, nozzle duration and electron gun current, however it can be adjusted to produce peak intense

enough for photodetachment experiments. The peak is assigned to $C_5H_4O^-$, with the proposed mechanism of its formation presented in Figure 12.2. The loss of four hydrogens is highly unusual and is attributed to unstable nature of 1,3-cyclopentadienyl, 2-oxo (C_5H_6O) intermediate diradical.

12.3. Results

Photoelectron images and corresponding photoelectron spectra of $C_5H_4O^-$ obtained at 1064, 808, 532, and 355 nm are shown in Figure 12.3. The photoelectron spectra are plotted versus electron binding energy, eBE = hν – eKE. Vibrational resolution in the 1064 and 808 nm data allows for accurate determination of the adiabatic electron affinity of the corresponding neutral, EA(C_5H_4O, $^1A_1$) = 1.06 ± 0.01 eV. This is the first determination of this important property of the cyclopentadienone. The spacing between two peaks in the 1064 nm spectrum, ~645 cm^{-1}, corresponds to the excitation of the ν9 in plane ring-distorting vibrational mode of the neutral, which agrees perfectly with the IR spectrum recently obtained by Ormond et. al.[265] The 808 nm data shows an additional progression with an average spacing of 825 ± 44 cm^{-1} which correspond to a ν8 mode of the neutral excited upon the photodetachment from anion. This is also in excellent agreement with the study by Ormond and co-workers.[265]

In contrast to lower energy (higher wavelength) spectra, 532 nm data shows ground state transition as a broad vibrationally unresolved feature due to resolution limitation of our instrument for the high-eKE electrons. However, the low-eKE transition (corresponding to the feature in the center of the image) is partially vibrationally resolved with a spacing of ~400 cm^{-1}. This transition corresponds to the first excited state of the

C_5H_4O neutral and we assign it to a triplet state, $^3A_2$. This allows for an accurate assignment of the EA of the triplet state, EA($^3A_2$) = 2.18 ± 0.02 eV and subsequently the singlet-triplet splitting, ΔE_{ST} = 1.12 ± 0.05 eV, for the neutral cyclopentadienone.

There are three prominent transitions visible at 355 nm spectrum. In addition to ground singlet state, $^1A_1$, and excited triplet, $^3A_2$, there is another sharp transition at the higher binding energy. This transition is assigned to a first excited singlet state (open-shell singlet) with an EA($^1B_2$) = 3.45 ± 0.01 eV. This is in good agreement with the theoretical prediction by Borin and co-workers[268] for the lowest singlet-singlet transition to be at 3.00 eV (which would imply EA($^1B_2$) = EA(X^2A_1) + 3.00 = 4.06 eV). The triplet transition is vibrationally resolved with an average spacing of 1290 ± 20 cm^{-1}. The highest peak corresponds to a largest Franck-Condon factor and allows the determination of the vertical detachment energy, VDE($^3B_2$) = 2.56 ± 0.02 eV. The lower eBE peaks of the same triplet transition observed for the 532 nm data are not visible at the 355 nm spectrum possibly due to a low Franck-Condon overlap for the 0-0 transition.

Geometry optimization calculations have been performed for anion, and singlet, and triplet states of the neutral at CCSD/aug-cc-pVDZ level of theory. Figure 12.4 shows optimized structures of the $^2B_1$, $^1A_1$, and $^3A_2$ states. There is a large geometry difference between anion and singlet, which is consistent with the convoluted $^1A_1$ transition in 532 nm spectrum in Figure 12.2. For the triplet state, the biggest geometry difference is in C=C bond length, which will manifest itself in ring breathing vibrational mode being active.

Single point energy calculations were also performed on the optimized geometries for all three states and electron affinity along with vertical detachment energy was calculated. The results for all the levels of theory employed along with the experimental assignment are shown in the Table 12.1. The EA and VDE calculated at the highest level of theory (CCSD/aug-cc-pVDZ) are in good agreement with the experiment, however higher basis set calculations, in particular using aug-cc-pVTZ with diagonal triples corrections, are required for higher chemical accuracy.

12.4. Conclusions and future directions

We reported the first spectroscopic observation of the cyclopentadienone anion ($C_5H_4O^-$) in the gas phase. Using photoelectron imaging technique, we were able to accurately measure the adiabatic electron affinity of neutral cyclopentadienone (C_5H_4O) in the gas phase, EA($^1A_1$) = 1.06 ± 0.01 eV. Additionally, two excited states of the neutral C_5H_4O were observed and assigned to a triplet ($^3A_2$) and open-shell singlet ($^1B_2$) states, with the adiabatic EAs of 2.18 ± 0.02 eV and 3.45 ± 0.01 eV respectively. These results are in relatively good agreement with theoretical predictions for the state ordering done by Borin et. al. Considering the discrepancy between experiment and theory, there might be another state of the neutral cyclopentadienone accessible at the highest laser wavelength available in our laboratory, 266 nm (4.66 eV). Imaging of $C_5H_4O^-$ at this wavelength will go a long way in validating of this prediction.

EA and VDE calculations done in our laboratory are in good agreement with experiment, however highest level of theory available for us at a time, for system as big as cyclopentadienone, was coupled cluster method with single and double excitations

using Dunning's augmented correlation-consistent polarized valence double-ξ basis set (aug-cc-pVDZ). Triple-ξ analogue of this basis set in conjunction with diagonal triples corrections, CCSD(dT), are required to achieve higher chemical accuracy. The low-lying electronic states of C_5H_4O can also be explored using equation-of-motion (EOM) spin-flip (SF) methodology, combined with coupled cluster theory. This approach can provide more accurate description of the multiconfigurational excited states.[197,198]

Table 12.1 Calculated and experimental VDE and adiabatic EA corresponding to the detachment to the $^1A_1$, $^3A_2$, and $^1B_2$ states of the neutral C_4H_4O

Method/basis set	VDE			Adiabatic EA (eV)		
	$^2B_1 \rightarrow {}^1A_1$	$^2B_1 \rightarrow {}^3A_2$	$^2B_1 \rightarrow {}^1B_2$	$^2B_1 \rightarrow {}^1A_1$	$^2B_1 \rightarrow {}^3A_2$	$^2B_1 \rightarrow {}^1B_2$
B3LYP/aug-cc-pVDZ	1.610	2.742		1.302	2.520	
B3LYP/aug-cc-pVTZ	1.585	2.755		1.269	2.524	
CCSD/aug-cc-pVDZ	1.168	2.550		0.866	2.281	
experiment	1.21(5)	2.74(2)	-	1.06(1)	2.56(2)	3.45(1)

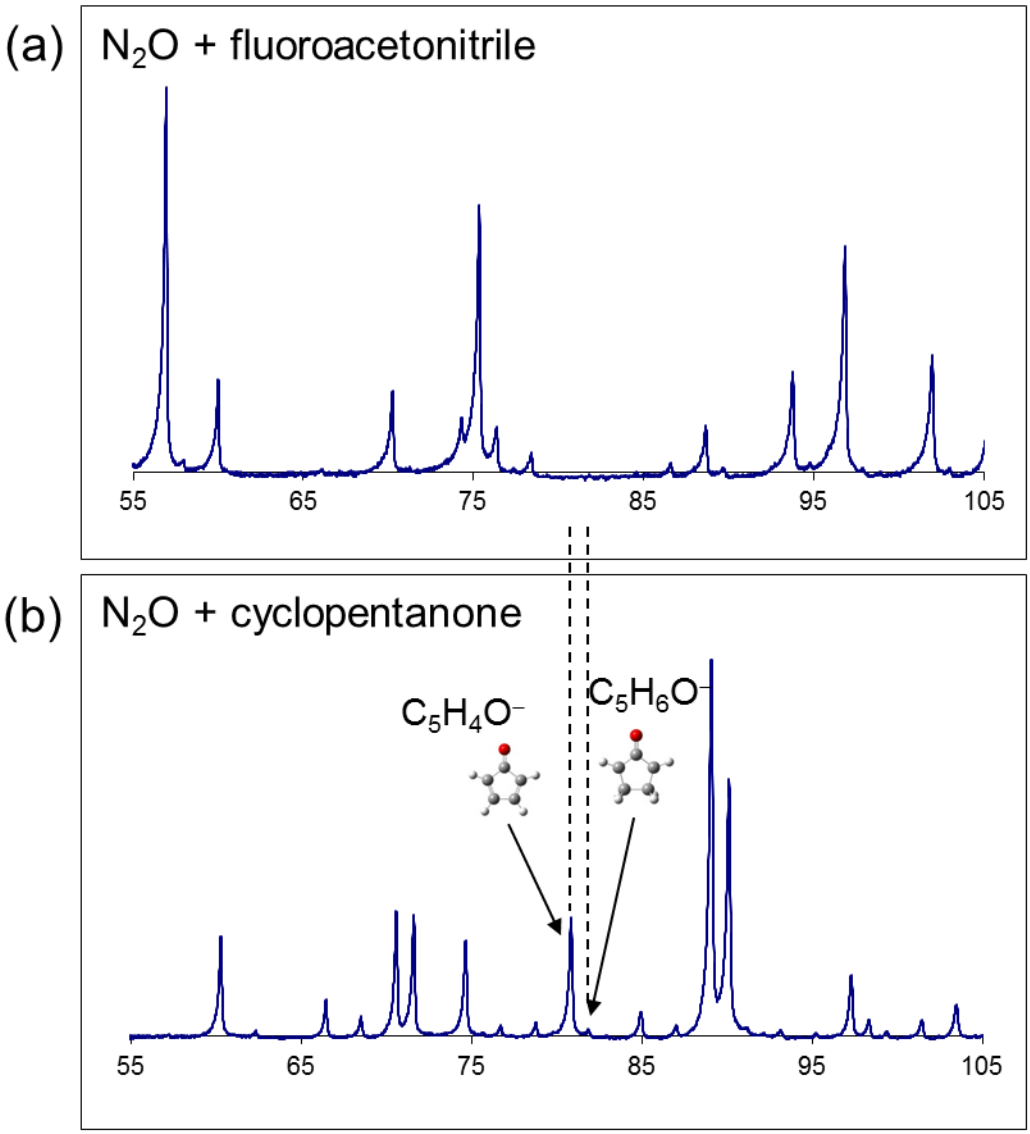

Figure 12.1 Representative time-of-flight mass spectrum for a (b) cyclopentanone (C_5H_8O) and (a) fluoroacetonitrile (CH_2FCN). Spectra are plotted on the same scale on top of each other in order to highlight the sample sensitive nature of the $C_5H_4O^-$ peak of interest.

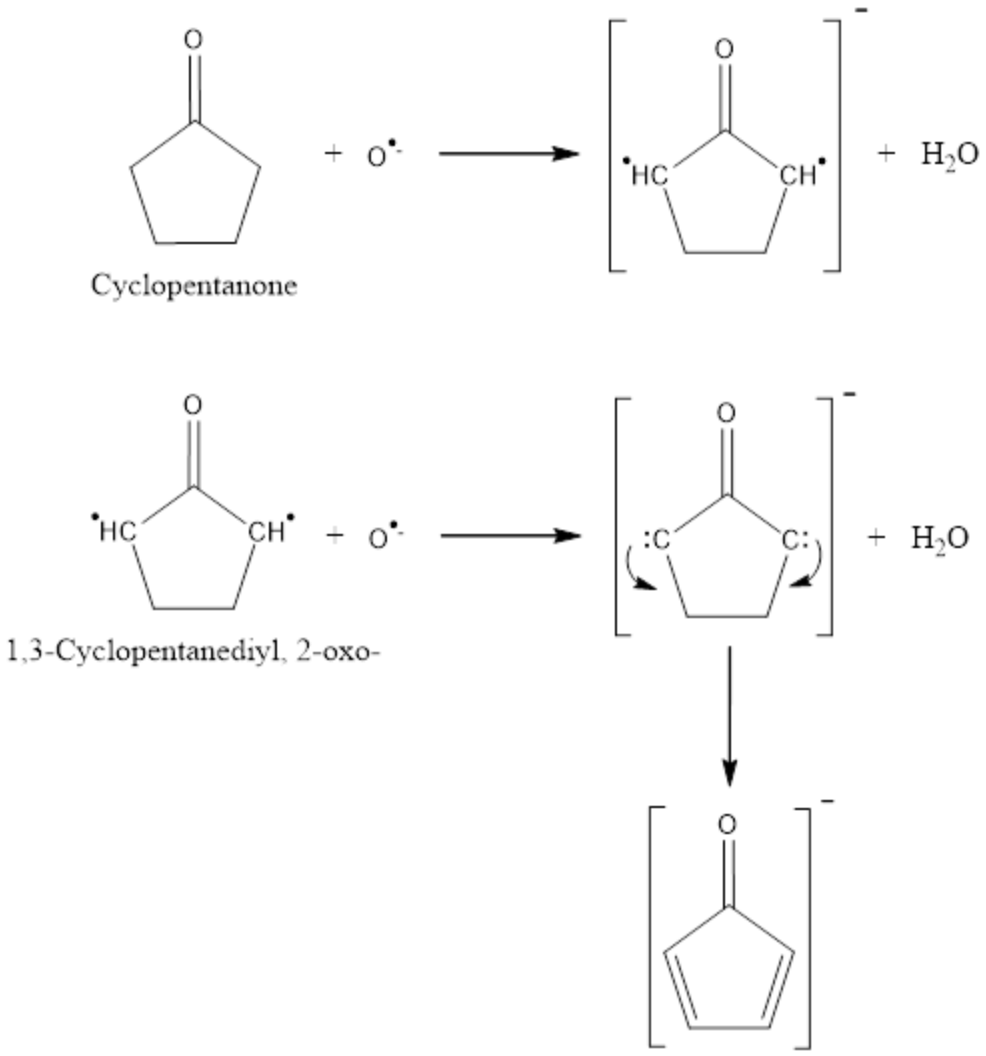

Figure 12.2 Proposed mechanism of formation for 1,3-cyclopentadienyl, 2-oxo diradical (C_5H_6O) and cyclopentadienone (C_5H_4O) via 2 or 4 hydrogen abstraction by $O^{\cdot -}$ radical anion.

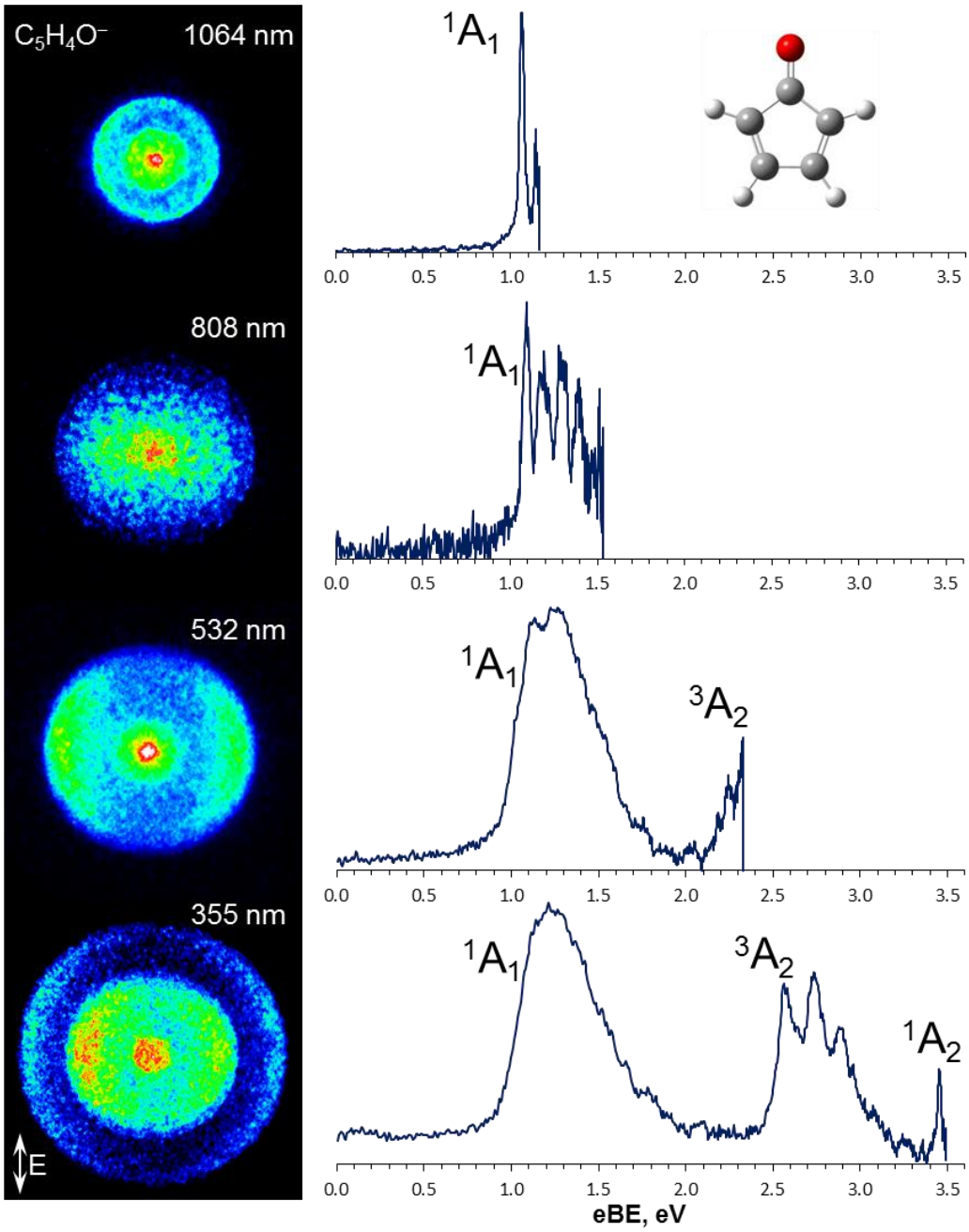

Figure 12.3 Raw photoelectron images (left) and corresponding photoelectron spectra (right) of $C_5H_4O^-$ obtained at 1064, 808, 532, and 355 nm. The laser polarization vector is vertical in the plane of the images, as indicated by the double arrow on the bottom left corner.

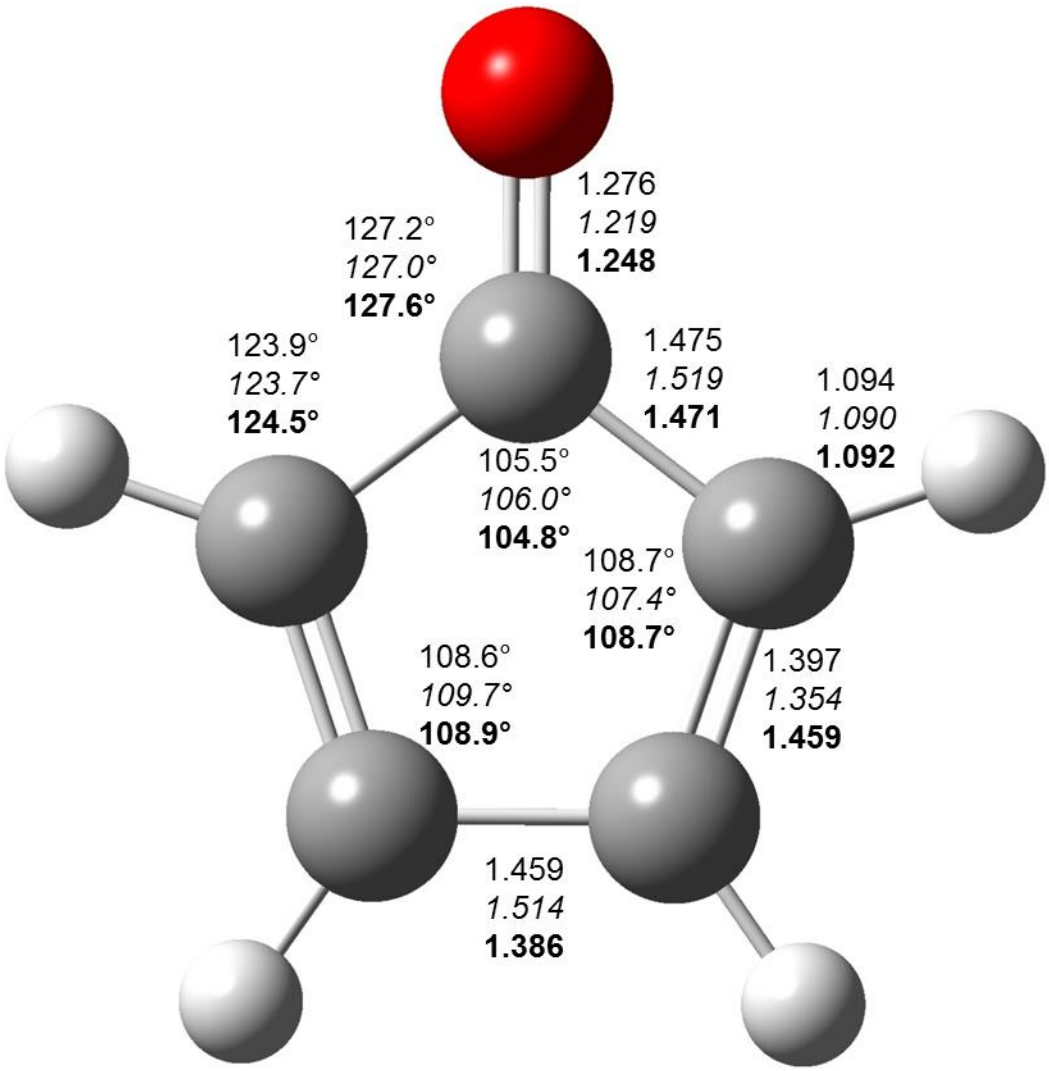

Figure 12.4 Bond length (Å) and angles (degree) of the C_{2v} optimized structure of the $^2B_1$ (anion), $^1A_1$, and $^3A_2$ (neutral) states of C_5H_4O shown in normal, italic and bold fonts respectively. All optimization calculations were performed at CCSD/aug-cc-pVDZ level of theory.

CHAPTER 13

LOW LYING EXCITED ELECTRONIC STATES OF C_7H_5N VIA PHOTOELECTRON IMAGING OF CYANOBENZENE ANION AND ITS CLUSTERS

13.1. Introduction

Benzonitrile (C_6H_5CN, also known as cyanobenzene) is a relatively simple aromatic molecule with a cyano group that affects many interesting electronic properties. It serves as a synthetic reagent in production of explosives and pharmaceuticals. It is also a well-known charge transfer acceptor species in solution[270] and it was shown to be a potential precursor to self-assembled thin films on metal surfaces.[271,272] Similar cyanobenzene derivatives show promise as bridging groups between bulk metals and complexes for electron transfer.[273,274] To understand and predict the electronic properties of such derivatives, it is important to have a clear picture of the parent species and its simple clusters.

The benzonitrile molecule has a large dipole moment, with the experimentally determined magnitude ranging from 4.14 D[275] to 4.48 D[276] in its ground state, which is sufficient for the formation of dipole bound anions.[277] Formation of various dipole-bound neutral complexes of benzonitrile with water and other solvents, including benzonitrile itself, is well documented and has been a topic of extensive research both experimentally and computationally.[270,278-285] These studies have attempted to elucidate the mechanism of the electron transfer by studying the electronic properties and molecular structures of benzonitrile and its complexes in the ground and electronically excited states. However, only the first excited singlet state (S_1) has been studied due to limitation of the laser

induced fluorescent (LIF) spectroscopy, bound by optical selection rules. The origin of the first excited singlet is reported to be 36512.938(6) cm^{-1} (about 4.527 eV)[282], 36442.118(30) cm^{-1} (about 4.518 eV)[280] and 36420.10(1) cm^{-1} (about 4.516 eV)[279] higher in energy than the ground state for benzonitrile, benzonitrile-water and benzonitrile dimer respectively.

In this work, we examine and assign several excited states of benzonitrile (singlet and triplet) and its clusters with water and itself using photoelectron imaging of the corresponding anions. Anion photoelectron spectroscopy allows access to both the singlet and triplet states of the neutral molecule.

13.2. Experimental

The experiments were performed using the anion photoelectron imaging spectrometer described in detail elsewhere.[37] A mixture of cyanobenzene vapor and Ar carrier gas at a backing pressure of ~30 psi was introduced into a high-vacuum chamber through a pulsed supersonic nozzle (General Valve Series 9), operated at a 50 Hz repetition rate. The gas expansion was crossed with a collimated 1 keV electron beam and ions of interest were formed by secondary electron attachment. The resulting anions were further extracted into Willey-McLaren time of flight mass spectrometer and accelerated to a kinetic energy of about 3 keV. Mass selected anions were crossed with a linearly-polarized pulsed laser beam, timed to coincide only with the ions of interest. The fundamental output, second, third, and forth harmonics of the Nd:YAG (yttrium aluminum garnet) laser were used to produce 1064, 532, 355, and 266 nm radiation respectively (~10 ns pulse duration, 5 mJ/pulse).

Photodetached electrons were projected onto a 40 mm diameter MCP detector coupled with a P43 phosphor screen (Burle, Inc.) using static electric fields within the velocity-map[26] photoelectron[24,25] imaging assembly.[37] The resulting images were recorded by a charge-coupled device camera (Photometrics CoolSNAP MYO) and accumulated for ~10^6 experimental cycles. Kinetic energy and angular distributions of the photodetached electrons were obtained via inverse Abel transform[25,56] as implemented in the BASEX program.[40] The kinetic energy scale was calibrated using the well-known photodetachment transition of O^-.[41,42]

Geometry optimization calculations were performed for the anion and neutral ground and excited states of benzonitrile at the coupled-cluster level of theory with single and double excitations, CCSD, using the Gaussian 09[195] and Q-chem[199] suites of programs. The normal mode analysis was performed to confirm that structure corresponds to true potential minimum. Due to the size of the molecule and computational limitations, highest basis set used for both Gaussian and Q-Chem calculations was aug-cc-pVDZ.

13.3. Results and discussion

The photoelectron images of cyanobenzene anion, $(cb)^-$ and its clusters, $cb^-(H_2O)$, and $(cb)_2^-$, obtained at 1064, 532, 355, and 266 nm are presented in Figure 13.1. Corresponding photoelectron spectra are shown in Figure 13.2. All spectra are plotted with respect to binding energy, eBE = hν – eKE, where hν is the photon energy and eKE is electron kinetic energy.

Overall the photoelectron spectra exhibit four easily distinguishable features, marked with upper-case letters (see Figure 13.2). All the peaks are assigned were fit with Gaussian function and the resulting VDE values are reported in Table 13.1. The lowest eBE feature, A, corresponds to the ground state anion (doublet) to ground state neutral (singlet) transition and provides the value for the adiabatic electron affinity, EA = 0.058 ± 0.005 eV. This result is significantly different than the currently accepted value of EA = 0.26 ± 0.10,[286] obtained via electron capture detector method. However, a small EA is consistent with the dipole bound anionic state, predicted due to a high dipole moment of benzonitrile molecule. The assignment of EA with such precision was made possible only due to use of relatively low energy IR photons (1064 nm). With the increase of photon energy used, peak A gets progressively broader (see Figure 13.2) reflecting not only vibrational congestion of the transition, but also the lower resolution of the instrument for high eKE electrons.

The photoelectron band of anionic benzonitrile clusters are shifted towards higher binding energy. This shift corresponds to the solvation energy that can be calculated by the means of the thermodynamic cycle: $D_0(A^-\cdot X) = EA(A\cdot X) + D_0(A\cdot X) - EA(A)$. To a first approximation, $D_0(A\cdot X) << D_0(A^-\cdot X)$, so $D_0(A^-\cdot X) = EA(A\cdot X) - EA(A)$. Solvation energies for all the clusters studied in this work are presented in Table 13.2. The solvation energy of water (hydration energy) of 0.32 eV is significantly smaller than that of many smaller anions, but similar to tetracyanoethylene (TCNE) and fumaronitrile anions with hydration energies of 0.35 eV[231] and 0.32 eV (Chapter 10) respectively. Similarly to previous cases, we attribute the low first hydration energy to the delocalized charge structure of benzonitrile, whereas the water molecule is effectively interacting

with only part of the charge. This is in general agreement with the previous studies on benzonitrile-water neutral complex done using microwave spectroscopy[281] and density functional theory (DFT),[287] that suggest a cyclic structure of the water cluster with oxygen atom bound to the ortho-hydrogen of the ring and hydrogen atom bound to nitrogen of the cyano group.

The maximum of band A in the benzonitrile dimer spectrum is shifted to a higher binding energy by a significantly higher value than the water cluster, 0.54 eV. This shift reflects the approximate $(C_6H_5CN)_2^- \rightarrow C_6H_5CN^- + C_6H_5CN$ dissociation energy and suggests high degree of interaction between two benzonitrile molecules. The neutral benzonitrile dimer has been studied by laser induced fluorescence (LIF) spectroscopy[278,284,285] and rotationally resolved LIF[279] suggesting a planar structure of the neutral dimer with two hydrogen bonds between nitrogens of cyano groups and ortho-hydrogens of the aromatic rings. A dipole-dipole interaction between two neutral benzonitriles was estimated by Borst et. al. to be 572 cm^{-1}, while double hydrogen bonding was predicted computationally to be on the order of 800 cm^{-1}. The dipole moment of the anionic benzonitrile is only slightly different than its neutral counterpart, thus the strength of the dipole-dipole bond can be expected to be of a similar magnitude. These interactions only account for a fraction of the solvation energy determined in our experiment. A different structure of the benzonitrile dimer, in particular the π stacking configuration, may account for this discrepancy. The structure of the benzonitrile complexes however cannot be discerned from our experiment and the exact way the monomers bind remains an open question.

The second lowest eBE feature, peak B, corresponds to a first excited state of neutral C_6H_5CN (^3A) and is accessible at photon energies of 355 nm and higher (see Figure 13.2). This sharp transition is almost at the energy cut-off and allows for an accurate assignment of the triplet state electron affinity, EA(^3A) = 3.415 ± 0.001 eV. This is the first spectroscopic measurement of this important property of the benzonitrile. Analogous peaks have been observed for the benzonitrile clusters and exhibit the shifts of the similar magnitude towards higher binding energy due to solvent induced stabilization.

The first excited singlet state of neutral C_6H_5CN (^1A) is accessible at 266 nm and can only be seen for the bare benzonitrile. The transition, labeled peak C, is well resolved and its electron affinity is assigned to EA(^1A) = 4.455 ± 0.001 eV. This is in excellent agreement with the previously reported value of 4.527 eV based on the LIF spectroscopy studies.[282] Similar peaks for the benzonitrile cluster anions are not accessible due to an energy cut-off at 266 nm (4.66 eV). Lastly, low eKE structureless peaks that are seen in some of the photoelectron spectra (and labeled D), specifically the ones obtained at 1064 nm, are assigned to an autodetachment from electronically excited cyanobenzene anion.

Ab initio calculations were performed for the anion and the singlet and triplet states of neutral benzonitrile. The geometries were optimized using DFT (B3LYP) and CCSD methods with Dunning's augmented correlation-consistent polarized valence double (and triple)-ζ basis set (aug-cc-pVDZ and aug-cc-pVTZ). Due to the size of the molecule and limited computational power, the highest level of theory available for geometry optimization was CCSD/aug-cc-pVDZ. The resulting structures of the ^2A ground state of the anion and the closed-shell singlet (^1A) and the triplet (^3A) states of the corresponding neutral are similar between the levels of theory and suggest planar

geometry for all of the states calculated. This is in agreement with previous experimental and theoretical geometries obtained for the neutral benzonitrile.

The adiabatic EAs of the ^{1}A and ^{3}A states of the neutral benzonitrile, as well as the corresponding anion VDEs were computed[195] using the DFT and coupled-cluster theory and the results are summarized in Table 13.3. While values for the triplet state are in good agreement with the experiment, it is clear that within the theoretical methods applied none can accurately describe the dipole bound anion. This is possibly due to dipole-bound nature of the state, where the additional electron is not within the molecular frame as assumed by the methodologies used. A different method should be implemented in order to better describe the energetic properties of this state.

Additionally, a better description of the inherently multiconfigurational nature of the low-lying electronic states, in particular the open-shell singlet, can be achieved by using the equation-of-motion (EOM) spin-flip (SF) or ionization potential (IP) methodology[177,227,228] combined with the coupled-cluster theory, including diagonal triples corrections (dT).[198] Using higher basis sets, especially the ones including more diffuse functions, will also be beneficial; however the use of larger basis sets is limited by computational capabilities.

In conclusion, more computational work needs to be done in order to correctly predict the electronic structure of the benzonitrile anion and its corresponding neutral.

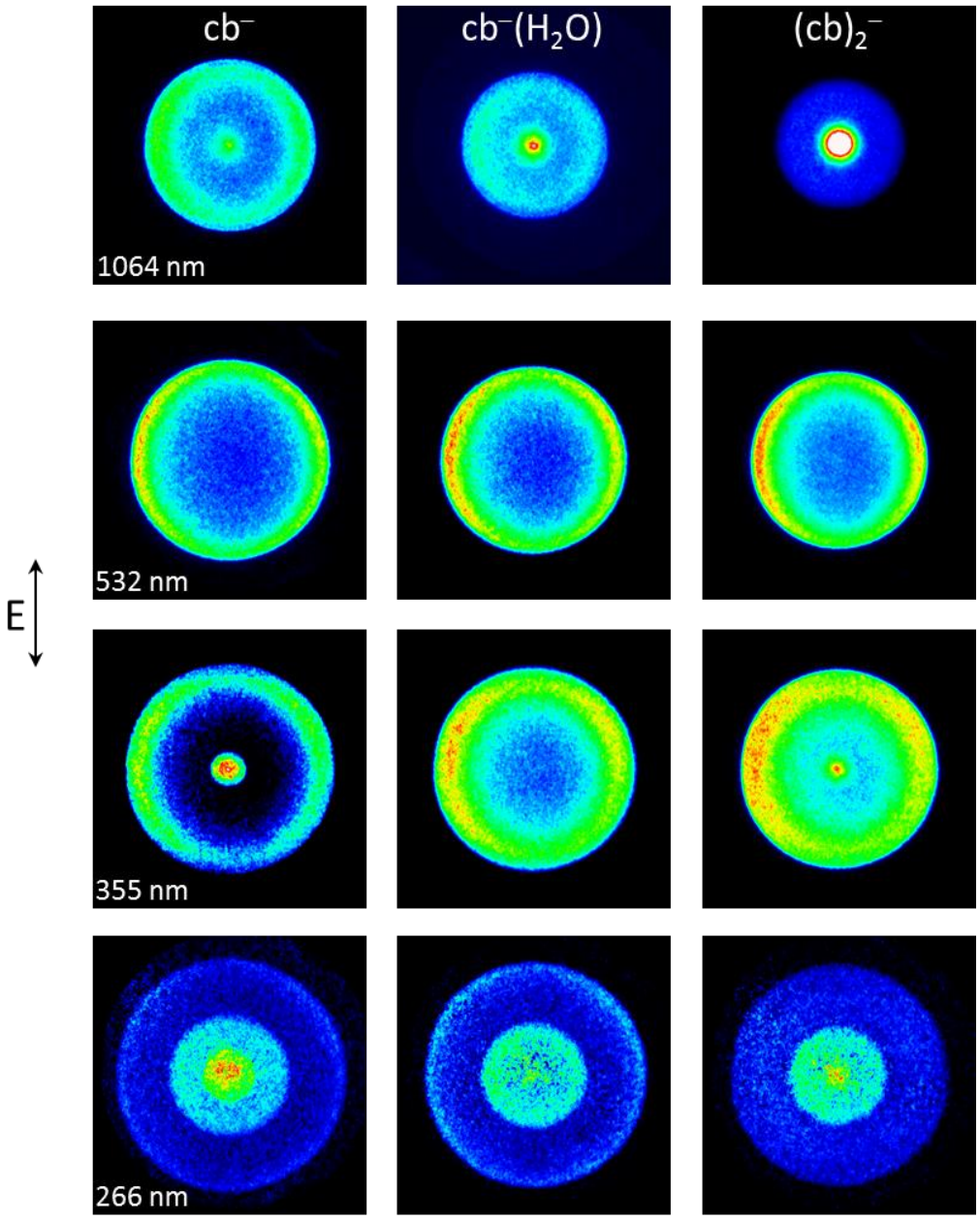

Figure 13.1 Photoelectron images of cyanobenzene, cb^-, and its clusters, $cb^-(H_2O)$ and $(cb)_2^-$ obtained at 1064, 532, 355, and 266 nm.

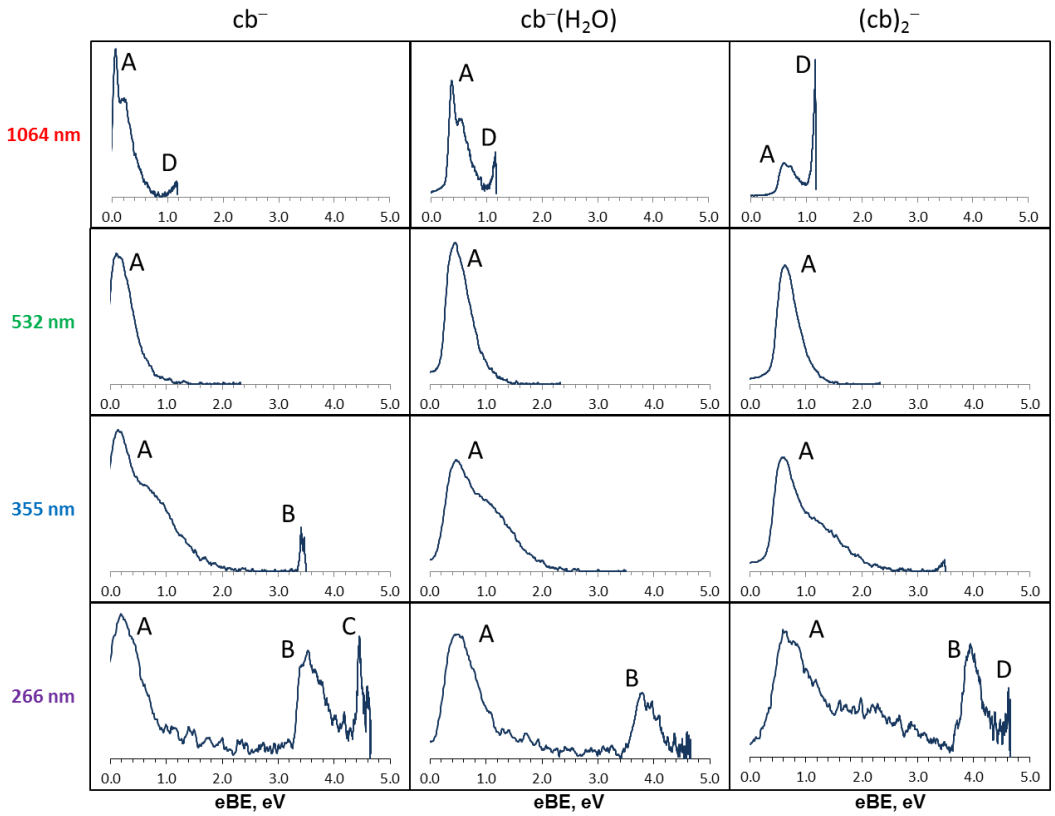

Figure 13.2 Photoelectron spectra corresponding to images in Fig. 13.1 of cyanobenzene and its clusters. See text and Table 13.1 for details of the band assignment.

Table 13.1 Photoelectron band energy values determined from cyanobenzene photoelectron images and spectra in Figures 13.1–13.2. See text for details of the band assignments.

Wavelength	Peak	eBE, eV		
		cb^-	$cb^-(H_2O)$	$(cb)_2^-$
1064 nm	A	0.058(5)	0.374(5)	0.596(5)
532 nm	A	0.11(1)	0.44(1)	0.61(1)
355 nm	A	0.14(2)	0.46(2)	0.59(2)
	B	3.415(1)	–	–
266 nm	A	0.19(5)	0.49(5)	0.64(5)
	B	3.43(2)	3.80(2)	3.99(2)
	C	4.455(1)	–	–

Table 13.2 Benzonitrile cluster dissociation energies. The binding energy is derived from the thermochemical cycle $D_0(AX^-) = EA(AX) + D_0(AX) - EA(A)$, where EA = electron affinity and D_0 = dissociation energy. To a first approximation $D_0(AX) \approx 0$, so $D_0(AX^-) = EA(AX) - EA(A)$. Due to approximate nature of calculations we do not assign absolute uncertainties.

Reaction	Energy (eV)
$C_6H_5CN^-(H_2O) \rightarrow C_6H_5CN^- + H_2O$	0.32
$C_6H_5CN^-(C_6H_5CN) \rightarrow C_6H_5CN^- + C_6H_5CN$	0.54

Table 13.3 Calculated VDE and adiabatic EA corresponding to the detachment to the X^1A and ^3A states of the neutral

Method/basis set	VDE (eV)		Adiabatic EA (eV)	
	$^2A \rightarrow X^1A$	$^2A \rightarrow {}^3A$	$^2A \rightarrow X^1A$	$^2A \rightarrow {}^3A$
B3LYP/aug-cc-pVDZ	0.358	4.397	0.165	3.490
B3LYP/aug-cc-pVTZ	0.315	3.644	0.135	3.499
CCSD/aug-cc-pVDZ	-0.4535	3.489	-0.4541	2.902
CCSD/aug-cc-pVDZ (via Q-Chem)			-0.211	3.154
experiment			0.058(5)	3.415(1)

CHAPTER 14

PHOTOELECTRON ANGULAR DISTRIBUTIONS FOR STATES OF ANY MIXED CHARACTER: A PRACTICAL MODEL FOR ATOMIC, MOLECULAR AND CLUSTER ANIONS

14.1. Introduction

Photoelectron imaging spectroscopy is a versatile and powerful experimental technique for probing the electronic structure of atoms and molecules. The photoelectron energy spectrum contains information about electronic, vibrational, and possibly even rotational energy levels of the species involved.[288] The photoelectron angular distributions (PAD) resulting from one-photon detachment reflect the symmetry of the parent orbitals and are closely related to the differential photodetachment cross-sections.[34]

The laboratory-frame PADs in one-photon detachment (or ionization) using linearly polarized light are given, in general, by:[289]

$$\sigma'(\theta) = (\sigma/4\pi)[1 + \beta P_2(\cos\theta)], \qquad (14.1)$$

where θ is the angle between the photoelectron velocity vector and the light's electric field vector, $P_2(\cos\theta) = (1/2)(3\cos^2\theta - 1)$ is the second-order Legendre polynomial, σ is the total (integrated) photodetachment cross-section, $\sigma' \equiv d\sigma/d\Omega$ is the differential cross-section with respect to the solid angle Ω ($d\Omega = \sin\theta d\theta$), and β is the anisotropy parameter, ranging from -1 to 2 for purely perpendicular and parallel transitions, respectively.

In the case of atomic species, the initial state of the electron can usually be described, within the orbital approximation, by a definite value of the orbital angular momentum quantum number, *l*. Due to the momentum conservation, the electrons emitted in a one-photon detachment or ionization process are represented by superposition of partial waves with angular momentum quantum numbers $l \pm 1$. According to the original derivations by Bethe,[290] generalized by Cooper and Zare,[29,30] the anisotropy parameter β for atomic ionization or photodetachment is given by the following expression, commonly referred to as the Cooper-Zare central-potential formula:

$$\beta_l = \frac{l(l-1)\chi^2_{l,l-1} + (l+1)(l+2)\chi^2_{l,l+1} - 6l(l+1)\chi_{l,l+1}\chi_{l,l-1}\cos\delta_{l+1,l-1}}{(2l+1)[l\chi^2_{l,l-1} + (l+1)\chi^2_{l,l+1}]}. \qquad (14.2)$$

In this equation, $\chi_{l,l\pm1}$ are the magnitudes of the radial transition dipole matrix elements for the ($l \pm 1$) partial waves originating from the initial atomic orbital with the orbital angular momentum quantum number *l*, and $\delta_{l+1,l-1}$ is the corresponding phase shift induced by interactions with the remaining neutral or ion.

Equation (14.14.2) is generally not applicable to molecular or cluster species, for which *l* is not defined.[291,292] In some cases, however, when the molecular orbital (MO) resembles an atomic-like wavefunction, an effective-*l* description may be adopted. For example, the $2p\pi_g^*$ highest-occupied MO (HOMO) of O_2^- is a *d*-like function. Thus, the photodetachment of O_2^- can be modeled approximately using the central-potential model with $l = 2$.[57,59,293] As another example, photodetachment from CH^-,[294,295] effectively involves the non-bonding 2*p* orbitals of the carbon atom and can be modeled with the Cooper-Zare formula with $l = 1$.[296] As most MOs cannot be described by a single *l* value,

many attempts have been made to develop a general Cooper-Zare-like equation for molecular species.[297-302] One such development is the theory for PADs of diatomic molecules by Buckingham et al.,[301,302] discussed in Section 14.4.4 of this work. Unfortunately, none of the previous formulations are both general and straightforward.

As the direct precursor to the present work, our group has recently developed an analogue of the Cooper-Zare formula for photodetachment from mixed *s*-*p* orbitals of polyatomic molecules.[209,303,304] Although the approach used to derive the model is general (at least in principle),[304] the mixed *s*-*p* formula itself is not. Specifically, the mixed *s*-*p* model assumes that the initial state of the electron is a linear combination of one *s* and one *p*-type functions localized on the same center:[209,304]

$$|\psi_{sp}\rangle = \sqrt{1-\gamma_p}\,|s\rangle + \sqrt{\gamma_p}\,|p\rangle, \tag{14.3}$$

where γ_p is the fractional *p* character, $0 \le \gamma_p \le 1$. Any relative phase factors for the *s* and *p* components are absorbed into the corresponding kets. [Originally, *f* (for fractional) was used in Eq. (14.14.3) instead of γ_p.[34,209,303-305] Here, we change the notation to make it amenable to any general mixing case, including those with *f*-orbital contributions.] The key equation of the mixed *s*-*p* model, expressed in the form analogous to Eq. (14.14.2), is:

$$\beta_{sp} = \frac{2(1-\gamma_p)\chi_{0,1}^2 + \gamma_p(2\chi_{1,2}^2 - 4\chi_{1,0}\chi_{1,2}\cos\delta_{2,0})}{(1-\gamma_p)\chi_{0,1}^2 + \gamma_p(\chi_{1,0}^2 + 2\chi_{1,2}^2)}. \tag{14.4}$$

Although it does not contain *l* explicitly, the *l* values corresponding to the *s* and *p* components of the initial orbital have been assumed in the derivation of the model.[303,304] Although the Cooper-Zare formula was not used in the derivation, in the limiting cases of a pure *s* (γ_p = 0) and pure *p* (γ_p = 1) orbitals, Eq. (14.14.4) reduces exactly to the

corresponding Cooper-Zare predictions, i.e. Eq. (14.14.2) with $l = 0$ and $l = 1$, respectively. With some additional approximations[306] (see Section 14.3), the mixed *s-p* model has been shown to predict correctly the behavior of the anisotropy parameter with respect to electron kinetic energy (eKE) for several polyatomic anions, particularly those with hybrid sp^n orbitals.[305,307] It also performs well for atomic and atomic-like anions perturbed by cluster solvation.[20,304]

In general, any MO can be formally represented as a linear combination of atomic-orbital functions centered at a chosen point in space. This is the central idea of this work. The objective is to generalize the Cooper-Zare central-potential model,[29,30,290] as well as the mixed *s-p* model,[304] to molecular or cluster states of any mixed character. We develop a transparent mathematical approach, which allows one to construct an analogous expression for photodetachment from any MO. We use the same assumptions as those underlying the Cooper-Zare central-potential model, but do not use the Cooper-Zare formula explicitly. Instead, we show that in the limiting cases of photodetachment/photoionization of atomic species the Cooper-Zare formula naturally follows from the present work. The present approach also differs from the original derivation of the mixed *s-p* model by Emily R. Grumbling et al.:[303,304] while the original formulation considered only the so-called principal molecular orientations, instead of complete orientation averaging, no such approximation is used here.

Section 14.2 presents the general model formalism and first considers its application to the *s-p* mixing case, as a test case for comparison with the previous formulation.[303,304] We confirm that the previous approximate approach yielded the exact same *s-p* mixing result, which follows from the more general approach described here.

We then follow through with an analogous derivation for the *p-d* mixing case and subsequently introduce a general expression for photoelectron anisotropy for any mixed MO. Although we refer specifically to anion photodetachment, most results in Section 14.2 are also applicable to the photoionization of neutral molecules. In Section 14.3, we employ additional approximations, valid for negative ions only, and develop a practical adaptation of the model specifically to anion photodetachment. Section 14.4 considers the photodetachment of NO^- as a benchmark case for the *p-d* mixing variant of the theory.

14.2. Generalized mixing model

The differential cross-section for one-photon detachment (ionization) is calculated through the corresponding transition dipole matrix element:[290]

$$\sigma'(\theta) = \frac{d\sigma}{d\Omega} = \frac{4\pi^2 E}{c} \int \left| \vec{\varepsilon} \cdot \langle k | \vec{r} | \psi_{MO} \rangle \right|^2 d\alpha d\beta d\gamma , \tag{14.5}$$

where the integral taken over all molecular orientations (specified by Euler angles α, β, and γ) accounts for the orientation averaging, $\vec{r}$ is the position operator, ψ_{MO} and $|k\rangle$ are the parent MO and the free (outgoing) electron wave, respectively, *c* is the speed of light, E is the photon energy, while the unit vector $\vec{\varepsilon}$ defines the laser polarization direction. Assuming no interaction between the remaining neutral molecule and the detached electron, one may use the plane-wave description for free electrons.

By expanding the outgoing photoelectron wavefunction in a spherically-symmetric basis, the expression for the differential cross-section, Eq. (14.14.5), becomes a sum over all possible angular-momentum components:[135]

$$\sigma'(\theta) = \frac{4\pi^2 E}{c} \frac{1}{2\pi k^2} \sum_{l,l'=0}^{\infty} \sum_{m=-l}^{l} \sum_{m'=-l'}^{l'} C_{\ell,m} C^*_{\ell',m'} \Theta_{\ell,m}(\theta) \Theta^*_{\ell',m'}(\theta) . \tag{14.6}$$

The energy (or k) dependent $C_{l,m}$ coefficients define the differential cross-sections of the partial waves described by $\Theta_{l,m}(\theta)$, i.e. the spherical harmonics integrated over azimuth angle.

As follows from Eq. (14.14.1), the complete differential cross-section function $\sigma'(\theta)$ is not required for the calculation of β. It is sufficient to know the relative differential cross-sections for just two emission angles, e.g. $\theta = 0$ and $\pi/2$:

$$\beta = \frac{2\left(\sigma'(0) - \sigma'(\pi/2)\right)}{\sigma'(0) + 2\sigma'(\pi/2)}. \qquad (14.7)$$

This realization simplifies the following derivation, as many of the spherical harmonics in Eq. (14.14.6) vanish at these angles.

14.2.1. Photodetachment from orbitals with definite *l* values

In this sub-section, we derive the expressions for the differential cross-sections corresponding to $\theta = 0$ and $\pi/2$ that will be used in Section 14.2.2 for anisotropy parameter calculations for the photodetachment from various mixed MOs. We first consider photodetachment from a p orbital ($l = 1$, $m = 0, \pm 1$), as the simplest case where the PAD is dictated by nontrivial partial-wave interference.

Taking into account the selection rules, $\Delta l = \pm 1$, $\Delta m = 0$ (linearly polarized light), the outgoing waves in p orbital detachment are described by harmonics $\Theta_{0,0}(\theta)$, $\Theta_{2,0}(\theta)$, and $\Theta_{2,\pm1}(\theta)$. At $\theta = 0$ and $\pi/2$, $\Theta_{2,\pm1} = 0$; hence, the corresponding waves do not contribute to the parallel and perpendicular cross sections. Therefore, for these two angles *only*, Eq. (14.14.6) takes the form:

$$\sigma'_p(\theta) = N\left(C_{0,0}^2\Theta_{0,0}^2(\theta) + 2C_{0,0}C_{2,0}\cos(\delta_2 - \delta_0)\Theta_{0,0}(\theta)\Theta_{2,0}(\theta) + C_{2,0}^2\Theta_{2,0}^2(\theta)\right), \qquad (14.8)$$

where $\theta = 0$ or $\pi/2$, $N = 2\pi E/(ck^2)$ is the pre-factor in Eq. (14.14.6), which is independent of θ and will cancel out upon substitution into Eq. (14.14.7). Throughout this work, σ'_l, l = 0, 1, 2, … or *s*, *p*, *d*, …, denotes the differential cross-section for detachment from an l orbital, accounting for the interference of the ($l \pm 1$) partial waves. It should not be confused with the differential cross-section corresponding to the l partial-wave. Substituting $\Theta_{0,0}(\theta) = \frac{1}{2\sqrt{\pi}}$ and $\Theta_{2,0}(\theta) = \frac{1}{4}\sqrt{\frac{5}{\pi}}(3\cos^2\theta - 1)$ into Eq. (14.14.8), we obtain the parallel ($\theta = 0$) and perpendicular ($\theta = \pi/2$) differential cross-sections for detachment from a *p* orbital:

$$\sigma'_p(\theta) = \frac{N}{4\pi}\left(C_{0,0}^2 + \sqrt{5}C_{0,0}C_{2,0}\cos\delta_{2,0}(3\cos^2\theta - 1) + \frac{5}{4}C_{2,0}^2(3\cos^2\theta - 1)^2 \right). \qquad (14.9)$$

Although this equation is valid only at $\theta = 0$ and $\theta = \pi/2$, it is sufficient for our purpose. Substituting (sequentially) $\theta = 0$ and $\theta = \pi/2$ into Eq. (14.14.9) and using the results in Eq. (14.14.7), we obtain the following expression for the anisotropy parameter in *p* orbital photodetachment:

$$\beta_p = \frac{\frac{15}{8\pi}C_{2,0}^2 + \frac{3\sqrt{5}}{2\pi}C_{0,0}C_{2,0}\cos\delta_{2,0}}{\frac{3}{4\pi}C_{0,0}^2 + \frac{15}{8\pi}C_{2,0}^2}. \qquad (14.10)$$

Even though we only used $\theta = 0$ and $\pi/2$ to arrive at this result, it defines the entire PAD through Eq. (14.14.1). Using an approach similar to that described elsewhere,[135] we compare Eq. (14.14.10) to the corresponding Cooper-Zare expression, i.e. Eq. (14.14.2) with $l = 1$:

$$\beta_p = \frac{2\chi_{1,2}^2 - 4\chi_{1,0}\chi_{1,2}\cos\delta_{2,0}}{\chi_{1,0}^2 + 2\chi_{1,2}^2}. \tag{14.11}$$

Since Eqs. (14.14.10) and (14.14.11) describe the same physics, they must be identical. We hence deduce the proportionality $C_{2,0}/C_{0,0} = -(2/\sqrt{5})\,\chi_{1,2}/\chi_{1,0}$, which we re-write, for convenience, as two equations with a common coefficient M_1 (the subscript indicates l = 1 for a *p* orbital):

$$\begin{cases} C_{0,0} = -2M_1\sqrt{\pi}\chi_{1,0} \\ C_{2,0} = 4M_1\dfrac{\sqrt{\pi}}{\sqrt{5}}\chi_{1,2} \end{cases} \tag{14.12}$$

Substituting Eq. (14.14.12) into Eq. (14.14.9), we obtain the expressions for the parallel and perpendicular differential cross-sections for detachment from a *p* orbital:

$$\begin{cases} \sigma'_p(0) = M_1^2 N(\chi_{1,0}^2 + 4\chi_{1,2}^2 - 4\chi_{1,0}\chi_{1,2}\cos\delta_{2,0}) \\ \sigma'_p(\pi/2) = M_1^2 N(\chi_{1,0}^2 + \chi_{1,2}^2 + 2\chi_{1,0}\chi_{1,2}\cos\delta_{2,0}) \end{cases}. \tag{14.13}$$

As a matter of verification, substituting Eq. (14.14.13) into Eq. (14.14.7) yields Eq. (14.14.11), i.e. the Cooper-Zare expression for *p* orbital photodetachment.

Similar derivations can be carried out for detachment from any orbital with a definite l value. In the trivial case of detachment from an *s* orbital (l = 0, m = 0), only the $\Theta_{1,0}$ wave is emitted and Eq. (14.14.6) simplifies to:

$$\sigma'_s(\theta) = NC_{1,0}^2\Theta_{1,0}^2(\theta) = NC_{1,0}^2\frac{3}{4\pi}\cos^2\theta, \tag{14.14}$$

Using Eq. (14.14.14) with θ = 0 and θ = π/2 in Eq. (14.14.7), we obtain the expected result for the anisotropy parameter in *s* orbital photodetachment:

$$\beta_s = \frac{2C_{1,0}^2 \dfrac{3}{4\pi}}{C_{1,0}^2 \dfrac{3}{4\pi}} = 2. \tag{14.15}$$

Although the Cooper-Zare equation does not apply, in a rigorous sense, to $l = 0$, because the $(l - 1)$ partial wave and its phase do not exist in this case, substituting $l = 0$ into Eq. (14.14.2) formally leads to zeroing out the nonexistent terms and yields the correct result:

$$\beta_s = \frac{2\chi_{0,1}^2}{\chi_{0,1}^2} = 2. \tag{14.16}$$

Comparing the middle parts of Eqs. (14.14.15) and (14.14.16), in a manner consistent with the above formulations for *p* orbital photodetachment, we set $C_{1,0} = 2M_0\sqrt{\dfrac{\pi}{3}}\chi_{0,1}$. This allows us to express the parallel and perpendicular differential cross-sections for detachment from an *s* orbital, similar to Eq. (14.14.13) for *p*. Using Eq. (14.14.14), we obtain:

$$\begin{cases} \sigma_s'(0) = M_0^2 N\chi_{0,1}^2 \\ \sigma_s'(\pi/2) = 0 \end{cases} \tag{14.17}$$

Analogous derivations become progressively more complex for larger values of *l*. For example, for a *d* orbital ($l = 2$, $m = 0, \pm1, \pm2$), there are eight outgoing waves, described by harmonics $\Theta_{1,0}(\theta)$, $\Theta_{1,\pm1}(\theta)$, $\Theta_{3,0}(\theta)$, $\Theta_{3,\pm1}(\theta)$, and $\Theta_{3,\pm2}(\theta)$. Although $\Theta_{3,\pm2}(\theta)$ vanish for $\theta = 0$ and $\theta = \pi/2$ and, therefore, do not contribute to the parallel and perpendicular cross-sections, the remaining harmonics still result in 21 terms that must be considered in Eq. (14.14.6). The complete, rather cumbersome derivation is included in Supplementary Materials.[308] Here, we give only the final result [analogous to Eq. (14.14.13) for a *p*

orbital] for the parallel and perpendicular differential detachment cross-sections for a *d* orbital:

$$\begin{cases} \sigma'_d(0) = M_2^2 N(4\chi_{2,1}^2 + 9\chi_{2,3}^2 - 12\chi_{2,1}\chi_{2,3}\cos\delta_{3,1}) \\ \sigma'_d(\pi/2) = M_2^2 N(3\chi_{2,1}^2 + 3\chi_{2,3}^2 + 6\chi_{2,1}\chi_{2,3}\cos\delta_{3,1}) \end{cases} \tag{14.18}$$

The differential cross-sections for parallel and perpendicular detachment from higher-order atomic orbitals are not discussed here, but can be easily derived (with some patience) following the procedure detailed in this sub-section.

14.2.2. Photodetachment from mixed-character states

The above derivations have been performed for atomic orbitals and yield expressions that are equivalent to the Cooper-Zare formulae for the corresponding *l* values. We now show that the differential cross-sections for $\theta = 0$ and $\theta = \pi/2$, expressed as explicit functions of the corresponding radial dipole elements $\chi_{l,l\pm1}$, lead to a straightforward method for constructing the formulae for the anisotropy parameter in the detachment from *any* mixed state. We begin with a re-derivation of the mixed *s*-*p* model, obtained previously using a slightly different approach.[34,209,303,304] This will serve as an initial test of the generalized mixing theory presented below.

In calculations of cross-sections, one sums over the final states [hence Eq. (14.14.6)], but averages over the degenerate initial states. For a mixed *s*-*p* state described by Eq. (14.14.3), the orientation-averaged differential cross-sections can thus be shown to be the weighted average of the contributions of the *s* and *p* components of the initial state:

$$\sigma_{sp}'(\theta) = (1 - \gamma_p)\,\sigma_s'(\theta) + \gamma_p\,\sigma_p'(\theta). \tag{14.19}$$

In this expression, interference between the $p \rightarrow s$ and $p \rightarrow d$ channels is included in σ_p',

per Eq. (14.14.8), while the cross-terms for the $s \rightarrow p$ and $p \rightarrow s$, as well as $s \rightarrow p$ and $p \rightarrow d$ channels are zeroed out by orientation averaging, as discussed previously,[304] upon the integration with respect to the Euler angles in Eq. (14.14.5). Substituting Eqs. (14.14.17) and (14.14.13) into Eq. (14.14.19) yields:

$$\begin{cases} \sigma'_{sp}(0) = M_0^2 N(1-\gamma_p)\chi_{0,1}^2 + M_1^2 N\gamma_p(\chi_{1,0}^2 + 4\chi_{1,2}^2 - 4\chi_{1,0}\chi_{1,2}\cos\delta_{2,0}) \\ \sigma'_{sp}(\pi/2) = M_1^2 N\gamma_p(\chi_{1,0}^2 + \chi_{1,2}^2 + 2\chi_{1,0}\chi_{1,2}\cos\delta_{2,0}) \end{cases} \tag{14.20}$$

Upon substitution of Eq. (14.14.20) into Eq. (14.14.7), we obtain:

$$\beta_{sp} = \frac{2M_0^2 N(1-\gamma_p)\chi_{0,1}^2 + 2M_1^2 N\gamma_p(3\chi_{1,2}^2 - 6\chi_{1,0}\chi_{1,2}\cos\delta_{2,0})}{M_0^2 N(1-\gamma_p)\chi_{0,1}^2 + M_1^2 N\gamma_p(3\chi_{1,0}^2 + 6\chi_{1,2}^2)}. \tag{14.21}$$

While the N coefficient in Eq. (14.14.21) cancels out, the ratio of M_0 and M_1 does not. In general, M_l depends on l, for the following reason. The differential and total cross-sections, which are proportional to M_l^2, include a sum over all final states and an average over the $(2l + 1)$ degenerate initial states. Hence, both σ_l' and σ_l must be proportional to the dipole elements squared, divided by $(2l + 1)$.[302] Hence, $M_l^2 \propto (2l + 1)^{-1}$, which can be expressed as $M_l^2 = M^2/(2l + 1)$, where M is a factor independent of l. It follows then that $M_0^2 = 3M_1^2$. Using this proportionality in Eq. (14.14.21) yields the already familiar *s*-*p* mixing formula, Eq. (14.14.4). Previously, Eq. (14.14.4) was obtained using a different approach, based on the analysis of the geometric properties of the relevant partial waves.[304] The agreement of the new derivation with the previous result is an important validation point.

A similar procedure can be applied to the detachment from a superposition of *p* and *d* orbitals,

$$|\psi_{pd}\rangle = \sqrt{1-\gamma_d}\,|p\rangle + \sqrt{\gamma_d}\,|d\rangle, \tag{14.22}$$

where γ_d is the fractional *d* character. Using the *p*-*d* mixing analogue of Eq. (14.14.19) and referring to Eqs. (14.14.7), (14.14.13), (14.14.18), and $M_l^2 = M^2/(2l + 1)$, we obtain the anisotropy parameter for mixed *p*-*d* state photodetachment:

$$\beta_{pd} = \frac{(1-\gamma_d)(2\chi_{1,2}^2 - 4\chi_{1,0}\chi_{1,2}\cos\delta_{2,0}) + \gamma_d(2\chi_{2,1}^2 + 12\chi_{2,3}^2 - 36\chi_{2,1}\chi_{2,3}\cos\delta_{3,1})/5}{(1-\gamma_d)(\chi_{1,0}^2 + 2\chi_{1,2}^2) + \gamma_d(2\chi_{2,1}^2 + 3\chi_{2,3}^2)} . \quad (14.23)$$

In the limiting cases of $\gamma_d = 0$ and $\gamma_d = 1$, Eq. (14.14.23) reduces exactly to the Cooper-Zare predictions for the detachment from pure *p* and pure *d* states, i.e. Eq. (14.14.2) with $l = 1$ and $l = 2$, respectively. This property of Eq. (14.23.14), is similar to that of Eq. (14.14.4) for *s*-*p* mixing,

The above approach allows us to construct analogous expressions for the detachment from *any* mixed orbital, and therefore, at least in principle, from anything or everything. It can be easily generalized for any number of different *l* components, not necessarily just one, as in the Cooper-Zare formula, Eq. (14.14.2), or two, as in the *s*-*p* and *p*-*d* mixing cases discussed above.

Since atomic orbitals form a complete basis set, any MO can be expanded as their linear combination. We assume

$$|\psi_{\mathrm{MO}}\rangle = \sum_l \sqrt{\gamma_l}\,|l\rangle , \quad (14.24)$$

where $|l\rangle$ are suitable linear combinations of atomic orbitals of a given type (defined *l* value and $m = -l \ldots l$) adapted to the system at hand. The phase factors are absorbed into the kets, while γ_l are the fractional *l* characters ($l = s, p, d$, etc.) that satisfy the normalization requirement $\sum_l \gamma_l = 1$. Generalizing the approach used to obtain the *s*-*p*

and *p-d* mixing formulae, Eqs. (14.14.4) and (14.14.23), the anisotropy parameter for the detachment from the mixed orbital defined by Eq. (14.14.24) is expressed as:

$$\beta = \frac{\sum_l \gamma_l \left[l(l-1)\chi_{l,l-1}^2 + (l+1)(l+2)\chi_{l,l+1}^2 - 6l(l+1)\chi_{l,l-1}\chi_{l,l+1}\cos\delta_{l+1,l-1} \right]/(2l+1)}{\sum_l \gamma_l [l\chi_{l,l-1}^2 + (l+1)\chi_{l,l+1}^2]}. \quad (14.25)$$

14.2.3. Simple empirical rule for MOs of any mixed character

Equation (14.14.25) allows us to formulate a simple empirical rule for writing the Cooper-Zare-like equation for any specific mixing case.

First, it is convenient to express the Cooper-Zare formula,[29,30] Eq. (14.14.2), as a ratio:

$$\beta_l = v_l / w_l, \quad (14.26)$$

where

$$v_l = \frac{l(l-1)\chi_{l,l-1}^2 + (l+1)(l+2)\chi_{l,l+1}^2 - 6l(l+1)\chi_{l,l-1}\chi_{l,l+1}\cos\delta_{l+1,l-1}}{2l+1},$$
$$w_l = l\chi_{l,l-1}^2 + (l+1)\chi_{l,l+1}^2. \quad (14.27)$$

We shall refer to v_l and w_l as the Cooper-Zare numerator and denominator, respectively, even though the $(2l + 1)$ divider in v_l is usually included in the denominator of the Cooper-Zare formula,[29,30] as it is commonly written [Eq. (14.14.2)]. The denominator w_l is related to the photodetachment cross-section σ_l for an atomic orbital with orbital angular momentum l, via $\sigma_l \propto (2l + 1)^{-1} w_l$.[301,302] The $(2l + 1)^{-1}$ factor in this expression accounts for the averaging over the degenerate states with quantum number l. It is for this reason that in Sichel's work[302] the Cooper-Zare formula is written with $(2l + 1)^{-1}$ in the denominator, offset by $(2l + 1)^{-2}$ in the numerator, in contrast to the more common format

of Eq. (14.14.2),[29,30] which has a (2*l* + 1) factor in the denominator only.

Using Eq. (14.14.27), the *s*-*p* mixing formula, Eq. (14.14.4), may be written compactly as:

$$\beta_{sp} = \frac{(1-\gamma_p)v_0 + \gamma_p v_1}{(1-\gamma_p)w_0 + \gamma_p w_1}. \tag{14.28}$$

The *p*-*d* mixing formula, Eq. (14.14.23), can be expressed in a similar form:

$$\beta_{pd} = \frac{(1-\gamma_d)v_1 + \gamma_d v_2}{(1-\gamma_d)w_1 + \gamma_d w_2}. \tag{14.29}$$

Finally, comparing the general mixing formula, Eq. (14.14.25), to the definitions in Eq. (14.14.27), the former may be written simply as:

$$\beta = \frac{\sum_l \gamma_l v_l}{\sum_l \gamma_l w_l}. \tag{14.30}$$

Hence, the general mixing formula, Eq. (14.14.25), is a ratio of the Cooper-Zare numerators and denominators, individually averaged over all *l* components of the parent MO with the respective fractional characters γ_l. When "mixing" the respective Cooper-Zare numerators and denominators in such an empirical way, the (2*l* + 1) degeneracy factor (commonly appearing in the denominator of the Cooper-Zare formula)[29,30] must be treated as part of the numerator, per Eq. (14.14.27).

For example, the Cooper-Zare formulae for the detachment from a pure *s* or *p* orbital are given by Eqs. (14.14.16) and (14.14.11), respectively. Mixing (averaging) the respective numerators, $v_0 = 2\chi_{0,1}^2$ and $v_1 = [\,2\chi_{1,2}^2 - 4\chi_{1,0}\chi_{1,2}\cos(\delta_2 - \delta_0)\,]$, and denominators, $w_0 = \chi_{0,1}^2$ and $w_1 = (\chi_{1,0}^2 + 2\chi_{1,2}^2)$, using $(1 - \gamma_p)$ and γ_p for the *s* and *p*

fractional characters, yields the *s-p* mixing equation, Eq. (14.14.4). We have just obtained the final *s-p* mixing result in an empirical fashion, without going through the intermediate derivation steps described in Section 14.2.1 and earlier in this section, or in Ref. [304].

Turning to *p-d* mixing, the Cooper-Zare formula for *p* orbital photodetachment is expressed by Eq. (14.14.11), with the numerator v_1 and denominator w_1 given in the preceding paragraph. The Cooper-Zare expression for *d* orbital photodetachment is obtained by substituting $l = 2$ into Eq. (14.14.2):

$$\beta_d = \frac{(2\chi_{2,1}^2 + 12\chi_{2,3}^2 - 36\chi_{2,1}\chi_{2,3}\cos\delta_{3,1})/5}{2\chi_{2,1}^2 + 3\chi_{2,2}^2}, \tag{14.31}$$

i.e. $v_2 = (2\chi_{2,1}^2 + 12\chi_{2,3}^2 - 36\chi_{2,1}\chi_{2,3}\cos\delta_{3,1})/5$ and $w_2 = 2\chi_{2,1}^2 + 3\chi_{2,2}^2$. Using $(1 - \gamma_d)$ and γ_d for the fractional *p* and *d* characters, respectively, yields the *p-d* mixing equation, Eq. (14.14.23), also skipping all the intermediate steps described in Section 14.2.2 and in Part A of Supplementary Materials.[308]

As another illustration of the empirical approach, we shall write the anisotropy equation for detachment from a mixed *d-f* state with a fractional *f* character γ_f, avoiding the exceedingly tedious derivation altogether. Since the Cooper-Zare formula for a *d* orbital is given by Eq. (14.14.31), while that for an *f* orbital [substituting $l = 3$ into Eq. (14.14.2)] is:

$$\beta_f = \frac{(6\chi_{3,2}^2 + 20\chi_{3,4}^2 - 72\chi_{3,2}\chi_{3,4}\cos\delta_{4,2})/7}{3\chi_{3,2}^2 + 4\chi_{3,4}^2}, \tag{14.32}$$

the above procedure yields the formal *d-f* mixing result in one simple step:

$\beta_{df} =$ (14.33)

$$\frac{(1-\gamma_f)(2\chi_{2,1}^2+12\chi_{2,3}^2-36\chi_{2,1}\chi_{2,3}\cos\delta_{3,1})/5+\gamma_f(6\chi_{3,2}^2+20\chi_{3,4}^2-72\chi_{3,2}\chi_{3,4}\cos\delta_{4,2})/7}{(1-\gamma_f)(2\chi_{2,1}^2+3\chi_{2,3}^2)+\gamma_f(3\chi_{3,2}^2+4\chi_{3,4}^2)}$$

.

Analogous equations can be similarly formulated for any other mixing scenario, including cases of more than one type of functions contributing to the MO expansion in Eq. (14.14.24).

14.2.4 Comparison to Buckingham et al.'s theory for diatomics

Before continuing with the practical adaptation of the generalized mixing theory, we discuss the results obtained so far in the context of Buckingham et al.'s theory for PADs of diatomic molecules.[301,302] The bulk of their work accounts for rotational structure within different angular-momentum coupling cases. They showed, however, [Eq. (30) in Ref. [301]] that in the absence of rotational resolution (averaging over the rotational levels), the photoelectron anisotropy parameter for a linear molecule is given by (adapting the notation to that used in the present work):

$$\beta=\frac{\sum_{l=|\Delta\Lambda|}^{\infty}|c_{nl}|^2\,(2l+1)^{-2}[l(l-1)\chi_{l,l-1}^2+(l+1)(l+2)\chi_{l,l+1}^2-6l(l+1)\chi_{l,l-1}\chi_{l,l+1}\cos\delta_{l+1,l-1}]}{\sum_{l=|\Delta\Lambda|}^{\infty}|c_{nl}|^2\,(2l+1)^{-1}[l\chi_{l,l-1}^2+(l+1)\chi_{l,l+1}^2]},$$

(14.34)

where c_{nl} are the parent MO expansion coefficients with respect to the central-potential basis and $\Delta\Lambda$ is the change in the projection of the electronic orbital angular momentum on the internuclear axis due to the photoionization or photodetachment transition. Within the MO approximation, $\Delta\Lambda$ corresponds to the projection of angular momentum of the parent orbital (λ). For a single l value, Eq. (14.14.34) reduces to the corresponding

Cooper-Zare formula, Eq. (14.14.2).

There is revealing similarity between the general mixing equation, Eq. (14.14.25), and Buckingham et al.'s[301] rotation-averaged result for diatomic molecules, Eq. (14.14.34). To emphasize this point further, Eq. (14.14.34) may be rewritten in the following form, using the definitions of Eq. (14.14.27):

$$\beta = \frac{\sum_{l=|\Delta\Lambda|}^{\infty} |c_{nl}|^2 (2l+1)^{-1} v_l}{\sum_{l=|\Delta\Lambda|}^{\infty} |c_{nl}|^2 (2l+1)^{-1} w_l} . \tag{14.35}$$

This equation is similar to the general mixing formula obtained here, in the form of Eq. (14.14.30), with two distinctions.

First, the weight factors under the sums are different, but the difference is easily reconciled. The $|c_{nl}|^2$ coefficients in Eq. (14.14.34) or Eq. (14.14.35) represent the weights of different l components of the initial MO. In Eq. (14.14.25) or, equivalently, Eq. (14.14.30) these weights are expressed in the equivalent form of fractional l character, γ_l. Further, the $(2l + 1)$ dividers in Eq. (14.14.35) account for the averaging over the m_l components of the degenerate states with defined l values.[301] Similar factors do not appear in Eq. (14.14.30), because of how the initial state is defined in our derivation, per Eq. (14.14.24). For example, in the *s*-*p* mixing variant of the model, the initial state is defined as a superposition of one *s*- and one *p*-type function, while other *m* components of the *p* state do not contribute to the detachment MO. All necessary averaging is hence accounted for by γ_p in Eq. (14.14.3) or, generally, γ_l in Eq. (14.14.24).

The second distinction between Eq. (14.14.30) and Eq. (14.14.35) is the respective summation ranges. In Eq. (14.14.30), we sum (average) over all l components of the

initial MO included in the consideration. In Eq. (14.14.35), the sum starts, effectively, at $l = |\lambda|$, where λ is the projection of l of the parent MO on the linear molecule's axis. Hence, this distinction reflects the different scopes of applicability of the two models (polyatomics vs. linear molecules), while the conceptual foundation behind the basis-set expansions is the same in both cases.

Overall, the approach taken in the present work is distinct from that used by Buckingham et al.[301,302] In 14.2.1-14.2.3, the averaging over the rotational structure is included implicitly, rather than explicitly, as part of orientation averaging. The disregard of rotational structure has led to tremendous simplifications in the formalism presented here. The final result is more general than Buckingham et al.'s theory,[301,302] as it applies to any polyatomic system, yet it coincides with Buckingham et al's[301] rotation-averaged formula in the partial case of diatomics.

14.3. The Hanstorp approximation

14.3.1. Applications to the central-potential and s-p mixing models

The direct application of the Cooper-Zare model,[29,30] or the generalized mixing theory (14.2.1-14.2.3), as well as the theory of Buckingham et al.[301,302] (14.2.4), requires the evaluation of the transition matrix elements $\chi_{l,l\pm1}$. That being a nontrivial undertaking in its own right,[293] an alternative approach, applicable only to anion photodetachment, was proposed by Hanstorp and co-workers.[306] They assumed that the relative scaling of the partial-wave cross-sections and, therefore, the transition dipole elements, follows the Wigner law.[200] The Cooper-Zare formula, Eq. (14.14.2), can be rearranged to show that β_l is dependent not on the matrix elements themselves, but the $\chi_{l,l+1}/\chi_{l,l-1}$ ratio.

Assuming the ratio of the (l + 1) and (l – 1) partial wave cross-sections to be proportional to ε^2,[200] where $\varepsilon \equiv$ eKE, and, therefore, $\chi_{l,l+1}/\chi_{l,l-1} = A_l\varepsilon$, where A_l is a proportionality coefficient, Eq. (14.14.2) can be rearranged to allow the calculation of β_l as an explicit function of eKE:[306]

$$\beta_l(\varepsilon) = \frac{l(l-1) + (l+1)(l+2)A_l^2\varepsilon^2 - 6l(l+1)A_l\,\varepsilon\cos\delta_{l+1,l-1}}{(2l+1)[l + (l+1)A_l^2\varepsilon^2]}. \tag{14.36}$$

In a similar vein, all applications of the *s*-*p* mixing model published to date[34,209,295,304,305,307] have used the Hanstorp-like[306] form of Eq. (14.14.4), namely:[209,304]

$$\beta_{sp}(\varepsilon) = \frac{2(1-\gamma_p)B_1\varepsilon + \gamma_p(2A_1^2\varepsilon^2 - 4A_1\varepsilon\cos\delta_{2,0})}{(1-\gamma_p)B_1\varepsilon + \gamma_p(1+2A_1^2\varepsilon^2)}. \tag{14.37}$$

Equation (14.14.37) gives the explicit eKE dependence of the anisotropy parameter in a manner analogous to Eq. (14.14.36) for defined-l states. The A_1 coefficient in Eq. (14.14.37) describes the relative scaling of the $p \rightarrow d$ and $p \rightarrow s$ detachment channels; it is but a specific (l = 1) case of A_l used in Eq. (14.14.36), which describes the same for the $l \rightarrow l \pm 1$ channels originating from the initial l orbital. The B_1 coefficient in Eq. (14.14.37) was first introduced (originally as simply B) in the *s*-*p* mixing model;[209,304] it describes, in a similar[306] Wigner-like[200] fashion, the "crossed" $s \rightarrow p$ and $p \rightarrow s$ channel ratio. Specifically,

$$\frac{\chi_{1,2}^2}{\chi_{1,0}^2} = A_1^2\varepsilon^2, \quad \frac{\chi_{0,1}^2}{\chi_{1,0}^2} = B_1\varepsilon. \tag{14.38}$$

14.3.2. Application to new cases

A similar approach can be applied to any of the new mixing cases discussed in

Section II. First, the definitions of the A_1 and B_1 coefficients in Eq. (14.14.38) must be generalized to any values of $l \geq 1$:

$$\frac{\chi^2_{l,l+1}}{\chi^2_{l,l-1}} = A_l^2 \varepsilon^2 , \; \frac{\chi^2_{l-1,l}}{\chi^2_{l,l-1}} = B_l \varepsilon . \tag{14.39}$$

Since these definitions follow the original approximation of Hanstorp et al.,[306] we shall refer to A_l and B_l as the Hanstorp coefficients. Using these definitions, it is convenient to redefine the Cooper-Zare numerator and denominator expressions in Eq. (14.14.27) in the following form:

$$\begin{aligned} v_l &= \chi^2_{l,l-1} V_l \\ w_l &= \chi^2_{l,l-1} W_l \end{aligned} \tag{14.40}$$

where

$$\begin{aligned} V_l &= \frac{l(l-1) + (l+1)(l+2) A_l^2 \varepsilon^2 - 6l(l+1) A_l \varepsilon \cos\delta_{l+1,l-1}}{2l+1} \\ W_l &= l + (l+1) A_l^2 \varepsilon^2 \end{aligned} \tag{14.41}$$

are the respective numerator and denominator of Eq. (14.14.36),[306] defined in a manner consistent with the definitions of v_l and w_l in Eq. (14.14.27).

We now consider a particularly important class of mixing cases, applicable to any sequential binary mixing of the (l – 1) and l components of the initial state (e.g., *s-p*, *p-d*, etc.), so that $\gamma_{l\text{-}1} + \gamma_l = 1$. Substituting the definitions in Eqs. (14.14.40) and (14.14.41), into the general mixing formula, Eq. (14.14.25), or, equivalently, Eq. (14.14.30), the anisotropy parameter for photodetachment from an (l – 1, l) mixed state is expressed as:

$$\beta_{l-1,l} = \frac{(1-\gamma_l) v_{l-1} + \gamma_l v_l}{(1-\gamma_l) w_{l-1} + \gamma_l w_l} = \frac{(1-\gamma_l) \chi^2_{l-1,l-2} V_{l-1} + \gamma_l \chi^2_{l,l-1} V_l}{(1-\gamma_l) \chi^2_{l-1,l-2} W_{l-1} + \gamma_l \chi^2_{l,l-1} W_l} ,$$

$$\beta_{l-1,l}(\varepsilon) = \frac{(1-\gamma_l)B_l\varepsilon V_{l-1} + \gamma_l A_{l-1}^2 \varepsilon^2 V_l}{(1-\gamma_l)B_l\varepsilon W_{l-1} + \gamma_l A_{l-1}^2 \varepsilon^2 W_l}. \quad (14.42)$$

Equation (14.14.42) gives an explicit eKE-dependence of the anisotropy parameter for any sequential binary mixing case (l – 1, l). For l = 1, Eq. (14.14.42) reduces to the familiar *s-p* mixing formula, Eq. (14.14.37).[209,304] Although the A_0 coefficient is not defined, it formally cancels out upon the substitution of Eq. (14.14.41) into Eq. (14.42) with l = 1.

The next sequential binary case corresponds to the detachment from a mixed *p-d* state. It is described by Eq. (14.14.42) with l = 2, which gives:

$$\beta_{pd}(\varepsilon) = \frac{(1-\gamma_d)B_2\varepsilon(2A_1^2\varepsilon^2 - 4A_1\varepsilon\cos\delta_{2,0}) + \gamma_d A_1^2\varepsilon^2(2+12A_2^2\varepsilon^2 - 36A_2\varepsilon\cos\delta_{3,1})/5}{(1-\gamma_d)B_2\varepsilon(1+2A_1^2\varepsilon^2) + \gamma_d A_1^2\varepsilon^2(2+3A_2^2\varepsilon^2)}. \quad (14.43)$$

A practical application of the *p-d* mixing formalism in the form of Eq. (14.14.43) is discussed in 14.4.

14.3.3. Examples of binary mixing curves

As discussed previously, the *s-p* mixing equation with the Hanstorp coefficients, Eq. (14.14.37), can be rearranged as follows:[34,209]

$$\beta_{sp}(\varepsilon) = \frac{2Z_1(A_1\varepsilon) + 2(A_1\varepsilon)^2 - 4(A_1\varepsilon)\cos\delta_{2,0}}{Z_1(A_1\varepsilon) + 1 + 2(A_1\varepsilon)^2}, \quad (14.44)$$

where Z_1 is a specific (l = 1) case of the composite mixing parameter Z_l, defined as:

$$Z_l = \frac{1-\gamma_l}{\gamma_l}\frac{B_l}{A_l}. \quad (14.45)$$

Neglecting $\delta_{2,0}$ and staying aware other model constraints, Z_1 can be said to reflect both the physics and chemistry of a mixed *s-p* photodetachment process, by combining the

relative channel cross-sections (via A_1 and B_1) with the character of the parent MO (via $\gamma_1 \equiv \gamma_p$).[209] Furthermore, Eq. (14.14.44) reveals that for a given value of Z_1, β_{sp} is a unique function of $A_1\varepsilon$. Hence, if the energy scale is normalized with regard of the "size" of the initial orbital (as determined by A_1),[34,306] the anisotropy trend is completely determined by Z_1. This is illustrated in Figure 14.1, where the anisotropy parameter, per Eq. (14.14.44), is plotted versus $A_1\varepsilon$ for different values of Z_1, ranging from $Z_1 = 0$ (pure *p* orbital limit) to $Z_1 = \infty$ (pure *s* limit).

Figure 14.1 is a complete summary of the mixed *s*-*p* model.[34,304] It shows that the mixed *s*-*p* anisotropy trends show a broad variation from the pure *s* limit to the qualitatively different pure *p* limit, depending on the character of the detachment orbital. In particular, even small deviations from the pure *s* limit (e.g., a solvation-induced polarization of an *s* orbital)[304] are predicted to have a large effect on the photodetachment anisotropy. It is for this reason that PADs can be used as a sensitive probe of *s*-*p* hybridization.[309]

The *p*-*d* mixing case is notably different. Using the composite *p*-*d* mixing parameter Z_2, defined by Eq. (14.14.45), Eq. (14.14.43) can be re-written in a form analogous to Eq. (14.14.44):

$$\beta_{pd}(\varepsilon) = \frac{Z_2[2(A_2\varepsilon) - 4(A_2/A_1)\cos\delta_{2,0}] + [2 + 12(A_2\varepsilon)^2 - 36(A_2\varepsilon)\cos\delta_{3,1}]/5}{Z_2(A_2\varepsilon)^{-1}[(A_2/A_1)^2 + 2(A_2\varepsilon)^2] + [2 + 3(A_2\varepsilon)^2]}. \quad (14.46)$$

In contrast to *s*-*p* mixing, this equation cannot be summarized in a single graph of β_{pd} vs. $A_2\varepsilon$ for different Z_2 values, because of the additional Hanstorp coefficient, A_1, present in the formula. To illustrate the anisotropy trends, in Figure 14.2 several β_{pd} curves for varying Z_2 values are plotted vs. $A_2\varepsilon$, all assuming (arbitrarily) $A_1 = 2A_2$. While the

appearance of the graph will change with A_1, the key point remains clear, as illuminated by the limited representation of Eq. (14.14.46) in Figure 14.2: at moderate eKEs, the variation among the different *p*-*d* mixing curves is less striking than in the case of *s*-*p* mixing (Figure 14.1). This is not surprising, considering that the limiting pure-*p* and pure-*d* curves exhibit qualitatively similar behaviors, both showing a $\beta = -1$ minimum. A more-shallow ($\beta > -1$) minimum can result only from a non-zero phase-shift between the partial waves. The *p*-*d* mixing curves, on the other hand, predict, in general, more shallow minima ($\beta > -1$), as a consequence of interference, even with zero phase-shifts. This is illustrated by the intermediate-Z_2 (e.g., $Z_2 = 1$) curves in Figure 14.2.

14.4. Benchmark application to NO^- photodetachment

The photodetachment of NO^-, whose HOMO is a $2p\pi^*$ orbital shared between the nitrogen and the oxygen atoms, is a benchmark test for the *p*-*d* mixing case described in Section 14.3.2. As illustrated in Figure 14.3, the lopsided HOMO (a, left) can be described approximately, per Eq. (14.14.22), as a linear combination of a single 3*d* and a single 2*p* type functions, centered halfway between N and O (b).

The photodetachment of nitric oxide anion has been the subject of numerous experimental and theoretical studies,[310-312] including several investigations of NO^- and its cluster anions by our group.[194,309,313,314] The β values were recorded for the $NO(X\,^2\Pi, v' = 0 - 6) \leftarrow NO^-(X\,^3\Sigma^-, v'' = 0)$ photodetachment band at several wavelengths ranging between 1064 and 266 nm. Attempts were made to fit the experimental $\beta(\varepsilon)$ dependence using the central-potential model [Eq. (14.14.36)] with an effective $l = 2$. Similar to O_2^- photodetachment,[58,59] the optimal values of the fit parameters (A_2 and $\delta_{3,1}$) depend on the

vibrational state of neutral NO.[313] In the present work, we consider only the data corresponding, as closely as possible, to vertical photodetachment, as such transitions are most appropriate for comparisons with the model, which does not include vibronic effects.

The vibrational state of NO that has the largest Franck-Condon overlap with the ground state of the anion is v′ = 2.[310] This is clearly borne out in the photoelectron imaging data, such as, for example, the 612 nm results for NO^- shown in Figure 14.4. Both the photoelectron image and the spectrum exhibit a clearly resolved vibrational progression, with v′ = 2 corresponding to the most intense peak. In Figure 14.5, the experimental β values for v′ = 2 transitions, obtained in several independent measurements at various wavelengths (ranging from 1064 to 266 nm),[303,309] are plotted versus eKE.

Shown as a dashed curve in Figure 14.5 is the least-squares fit to these data using the Hanstorp formulation of the Cooper-Zare model, Eq. (14.14.36), with an effective l = 2, A_2 = 0.36 eV^{-1}, and $\cos\delta_{3,1}$ = 0.88. Although the fit reproduces the observed anisotropy trend quite well, the agreement is not satisfying, because it is based on an unphysical assumption. The NO^- HOMO [Figure 14.3(a), left] does not have the same symmetry properties as a *d* orbital. The significant phase shift necessary to reproduce the observed $\beta(\varepsilon)$ trend points to the flaws inherent in the central potential description. In general, the interaction of the departing electron with the remaining neutral in anion photodetachment is much weaker than the Coulomb attraction in neutral-molecule ionization and the resulting phase shifts tend to be small. Additionally, both l = 1 and l = 3 waves turn to zero at the origin (r = 0), which decreases the effect of the (weak) core interactions on

their individual phases. The above phase shift, necessary to reproduce the $\beta > -1$ minimum in the experimental $\beta(\varepsilon)$ dependence using Eq. (14.14.36), is inconsistent with these expectations.

The analysis can be improved by describing the lopsided $2p\pi^*$ HOMO of NO^- as a polarized *d* orbital, which is done with the addition of some *p* character, as illustrated in Figure 14.3. We constructed a *p*-*d* model function, per Eq. (14.14.22), as a superposition of one 2*p* and one 3*d* atomic-orbital functions centered in the middle of the N–O bond. The spatial extents of these hydrogenic functions are controlled, per Eq. (S.16) in Supplementary Materials,[308] by the respective nuclear-charge parameters, ζ_{2p} and ζ_{3d}. In the present case, these charges do not correspond directly to any physical atom in NO^-. For this reason, in contrast to our work on carbon-centered *s*-*p* hybrid orbitals,[209,305,307,315] these two charges cannot be assumed to be equal á priori.

Overall, the mixed *p*-*d* model function is defined by three parameters: the above charges, ζ_{2p} and ζ_{3d}, and the fractional *d* character γ_d. In order to optimize the model function's *d* character, we carried out a least-squares fit (in three spatial dimensions) of the *p*-*d* model function to the NO^- HOMO determined from CCSD/aug-cc-pVTZ calulations[195] [Figure 14.3(a), left]. The procedure yielded $\gamma_d = 0.985$, with $\zeta_{2p} = 1.63$ and $\zeta_{3d} = 5.20$. The γ_d value corresponds to only a 1.5% (probability based) *p* character, but a non-trivial 0.12 coefficient for the *p* component in Eq. (14.14.22) ($\sqrt{1-\gamma_d} = 0.12$). The resulting mixed *p*-*d* model orbital is shown in Figure 14.3(a), right. The ab initio HOMO and the model orbital are very similar.

The *p*-*d* mixing formula, Eq. (14.14.43), can now be used to model the observed anisotropy trend. The Hanstorp coefficients depend sensitively on the details of the parent

orbital[209] and more work is needed to derive their values in a pure ab initio fashion. One feature is clear, however: the A_1, A_2, and B_2 coefficients in Eq. (14.14.43) are not independent. Among the three of them, they contain only two degrees of freedom, analogous to the *s*-*p* mixing case, where the A_1 and B_1 coefficients in Eq. (14.14.37) are generally related to each other.[209] If the *p* and *d* components of the mixed model orbital [Figure 14.3(a), right] are described by respective 2*p* and 3*d* hydrogenic functions with effective charges ζ_{2p} and ζ_{3d} (as above), the coefficients can be calculated (in atomic units) as:

$$A_1 = \frac{16}{\xi_{2p}^2}, \qquad A_2 = \frac{144}{5\xi_{3d}^2}, \qquad B_2 = \frac{2^9 \xi_{3d}^7}{5 \cdot 3^6 \xi_{2p}^2}. \tag{14.47}$$

The derivation of these equations is given in part B of Supplementary Materials.[308]

Given the above *d* character (γ_d = 0.985), the anisotropy trend per Eq. (14.14.43) is determined by only two independent parameters, ζ_{2p} and ζ_{3d}. We neglect the expected-to-be-small phase shifts (by setting $\cos\delta_{2,0}$ = $\cos\delta_{3,1}$ = 1) and fit Eq. (14.14.43) to the experimental data in Figure 14.5. The fit yields the $\beta(\varepsilon)$ dependence plotted in the same figure as a solid curve, with the fit parameter values ζ_{2p} = 1.46 and ζ_{3d} = 5.94. These charges are only slightly different from the respective values obtained above by fitting the *p*-*d* model orbital to the ab initio HOMO (ζ_{2p} = 1.63 and ζ_{3d} = 5.20). The slight discrepancy is not surprising, given the assumption of the hydrogenic functions to describe the *d* and *p* components of the orbital.

14.5. Summary

A generalized mixing model for molecular and molecular-anion PADs has been developed in a form which is both practical and consistent with the Cooper-Zare central-

potential formula[29,30] and the previously reported mixed *s*-*p* model.[304] The generalized model was derived from the differential cross-sections for photodetachment from mixed-character parent orbitals. From the rigorous derivation, a simple empirical form emerged, allowing for an easy description of the mixing of any number of atomic orbitals of any type.

Although the model specifically targets anion photodetachment, the results obtained in Section 14.2 are also applicable to the photoionization of neutral molecules. However, the results obtained using Hanstorp et al.'s approximation[306] (Section 14.3) and the assumption of zero phase-shifts apply to negative ions only. The use of these approximations yields a practical description of the anisotropy parameter in anion photodetachment as a function of electron kinetic energy, which can be compared to the experiment.

While the model allows the calculation of the anisotropy parameters in the photodetachment from atomic, molecular, or cluster anion states of any mixed character, the specific scenarios considered explicitly include the *s*-*p* and *p*-*d* mixing cases. The *s*-*p* mixing predictions are completely consistent with the previous mixed *s*-*p* model[304] results. The newly-derived *p*-*d* mixing variant of the general model is shown to reproduce the observed anisotropy trend in NO^- photodetachment with physically meaningful parameter values. The successful modeling of this benchmark system further validates both the *p*-*d* mixing equation and the generalized mixing model from which it was obtained.

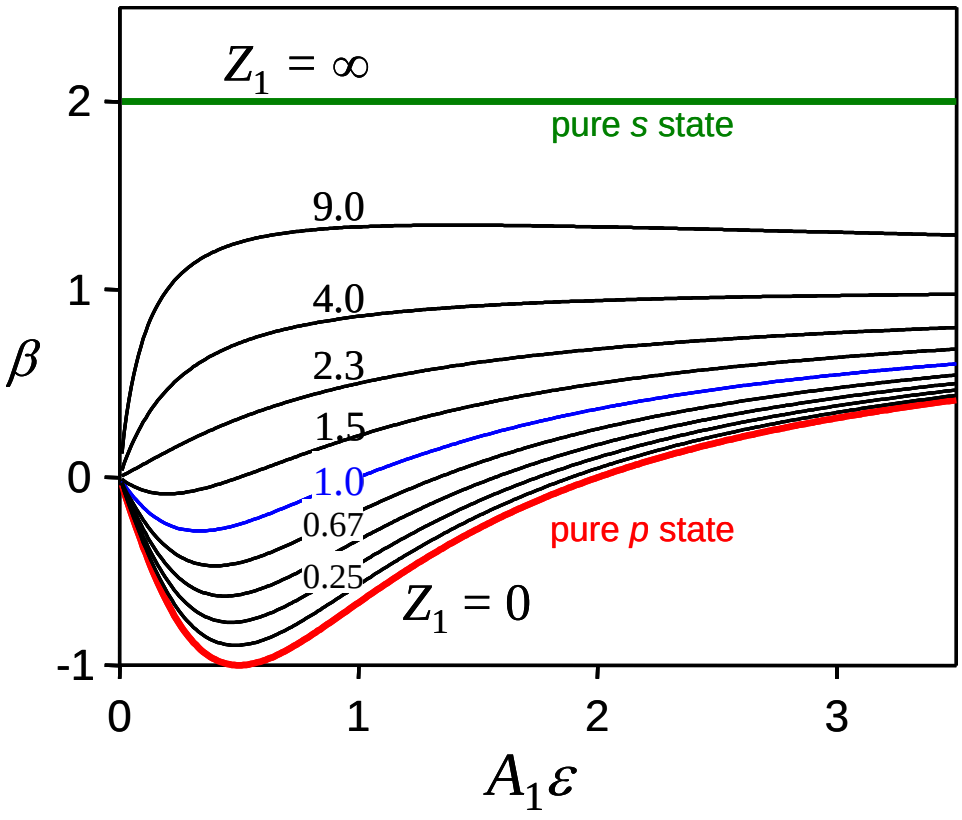

Figure 14.1 The electron kinetic energy dependence of the anisotropy parameter for photodetachment from mixed *s*-*p* states, as given by Eq. (14.44), for different values of Z_1 [defined by Eq. (14.45)]. All mixing curves shown assume no phase shift ($\delta_{2,0} = 0$). The horizontal axis ($A_1\varepsilon$) corresponds to eKE (ε) normalized for the "size" of the *p* component of the initial state, as expressed by the Hanstorp coefficient A_1. For example, if $A_1 = 1$ eV^{-1}, the axis corresponds to eKE in units of eV. The blue curve corresponds to $Z_1 = 1$. The green and red curves correspond to the respective pure *s* ($Z_1 = \infty$) and pure *p* ($Z_1 = 0$) limiting cases of the mixed *s*-*p* model and coincide exactly with the predictions of the Cooper-Zare central-potential model [Eq. (14.36)] for $l = 0$ and $l = 1$.

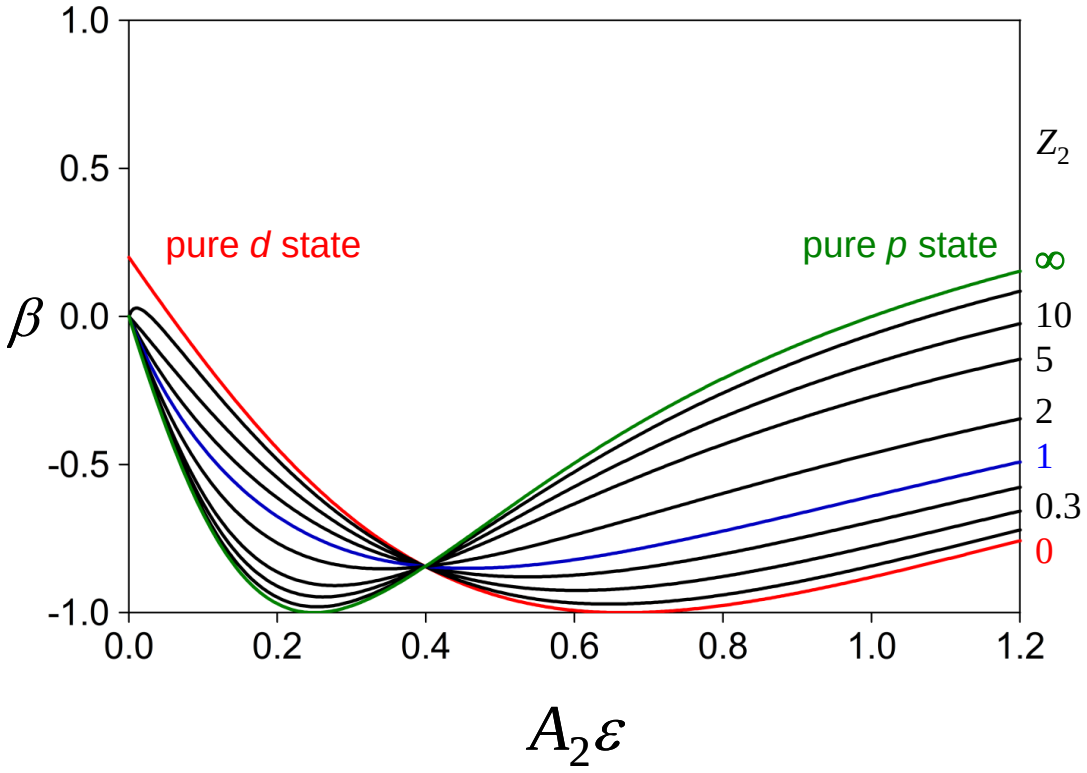

Figure 14.2 Energy dependence of the anisotropy parameter for photodetachment from mixed *p*-*d* states, as given by Eq. (14.46) for different values of Z_2 between 0 (pure *d* state, red curve) and ∞ (pure *p* state, green curve) assuming no phase shifts ($\delta_{2,0} = \delta_{3,1} = 0$) and $A_1 = 2A_2$. See the text and Figure 14.1 caption for details. The blue curve corresponds to $Z_2 = 1$.

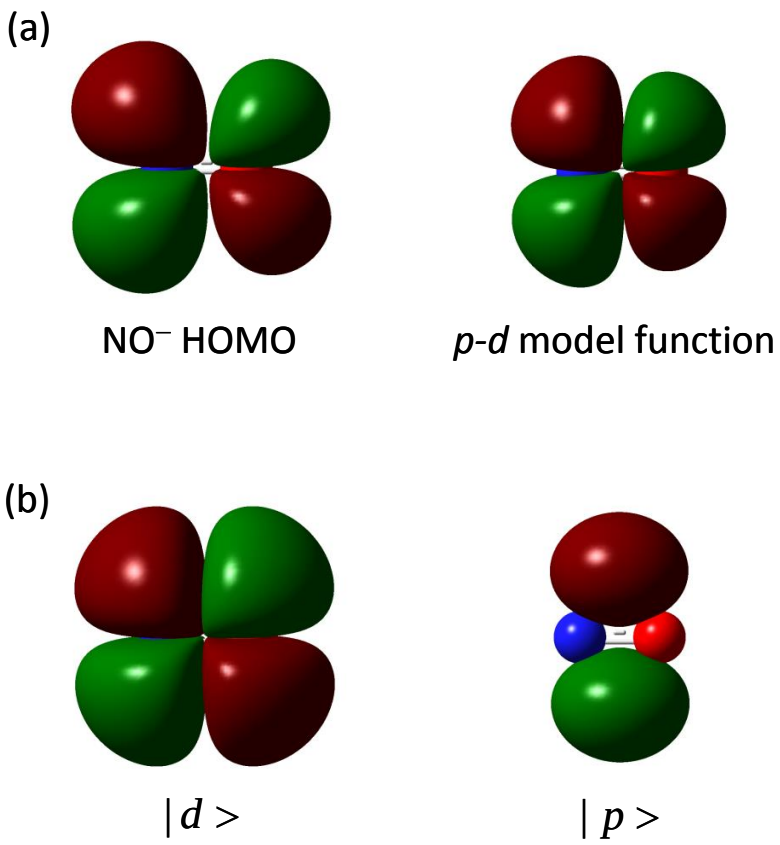

Figure 14.3 (a) Left: NO^- HOMO from CCSD/aug-cc-pVTZ calculations. Right: the *p*-*d* model function obtained as a least-squares fit of the linear combination [Eq. (14.22)] of a single 3*d* and a single 2*p* hydrogenic functions, centered halfway between N and O. The optimized fit parameters are: $\gamma_d = 0.985$, $\zeta_{2p} = 1.63$, and $\zeta_{3d} = 5.20$. (b) The individual *d* and *p* components of the model function shown on the right in (a). All plots correspond to an isosurface value of 0.02.

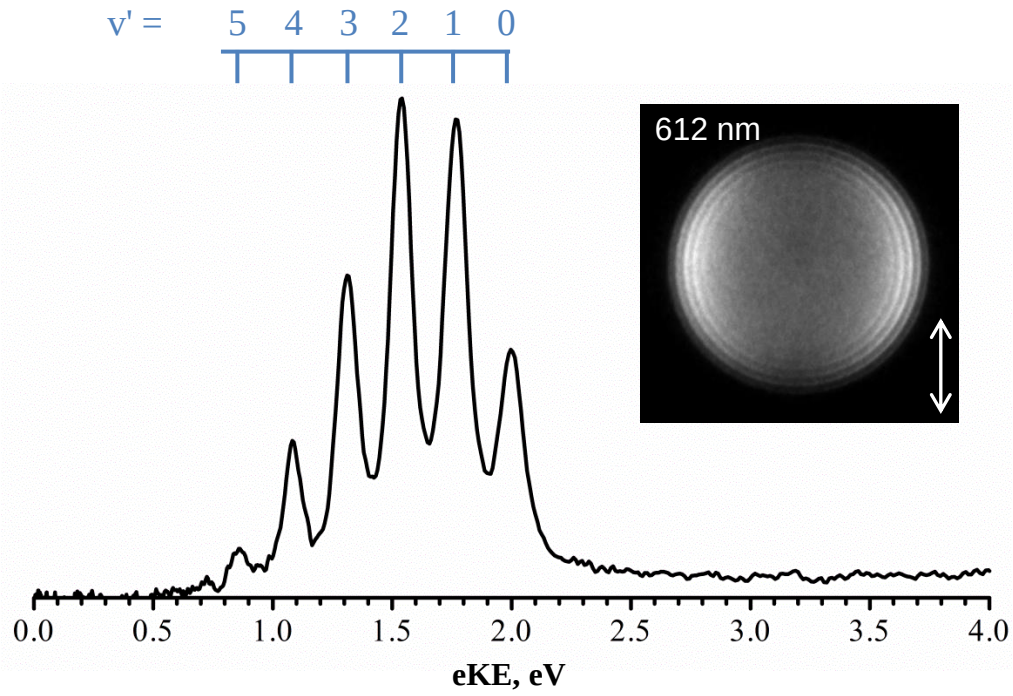

Figure 14.4 The NO($X\,^2\Pi$, v′) ← NO^-($X\,^3\Sigma^-$, v″ = 0) photoelectron spectrum obtained at 612 nm. The comb above the spectrum indicates the peak assignments to the vibrational states of neutral NO. The inset on the right shows the corresponding photoelectron image. The double-sided vertical arrow indicates the laser polarization direction.

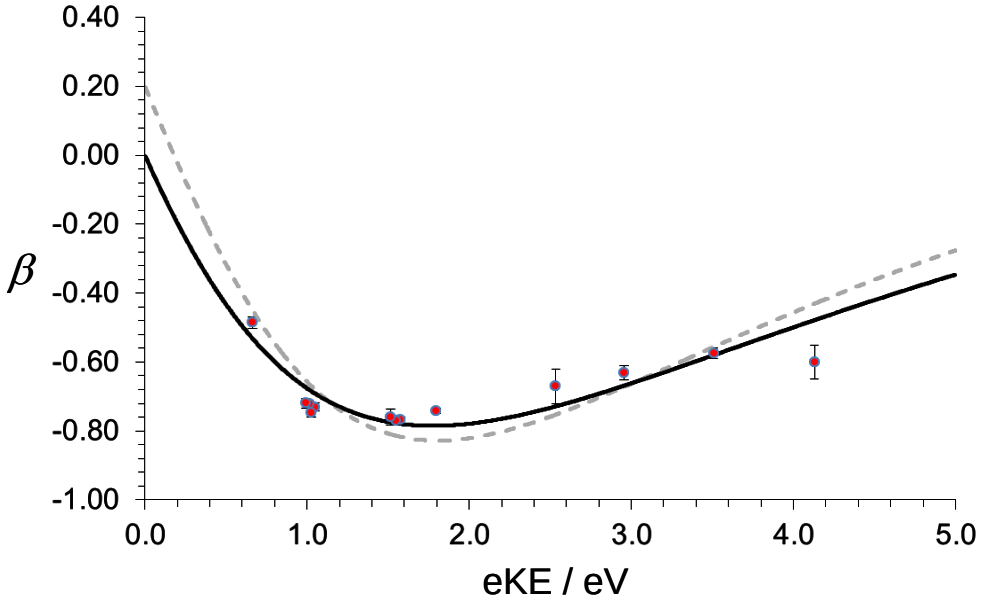

Figure 14.5 Symbols: experimental energy dependence of the photoelectron anisotropy parameter for the NO($X\,^2\Pi$, v′ = 2) ← NO^-($X\,^3\Sigma^-$, v″ = 0) photodetachment transition at several wavelengths ranging between 1064 nm (the leftmost data point) and 266 nm (the rightmost point). Dashed curve: the least-squares fit to these data using the Cooper-Zare central-potential model [Eq. (14.36)] with an effective l = 2. The optimal fit parameters are: A_2 = 0.36 eV^{-1} and $\cos\delta_{3,1}$ = 0.88. Solid curve: the *p*-*d* mixing model prediction using Eq. (14.43) with $\cos\delta_{2,0} = \cos\delta_{3,1} = 1$, γ_d = 0.985 (determined from the analysis of the NO^- HOMO), A_1, A_2, and B_2 calculated from ζ_{2p} and ζ_{3d} via Eq. (14.47), while ζ_{2p} and ζ_{3d} are used as adjustable parameters to fit the curve to the experimental data (optimal values: ζ_{2p} = 1.46 and ζ_{3d} = 5.94).

SUPPLEMENT A: Photodetachment from a d-orbital

In this supplement, we derive the expressions for the differential cross-sections corresponding to $\theta = 0$ and $\pi/2$ for the photodetachment from a *d* orbital ($l = 2$, $m = 0, \pm1, \pm2$).

Taking into account the selection rules, $\Delta l = \pm1$, $\Delta m = 0$ (linearly polarized light), the outgoing waves in *d* orbital detachment are described by spherical harmonics $\Theta_{1,0}(\theta)$, $\Theta_{3,0}(\theta)$, $\Theta_{1,\pm1}(\theta)$, $\Theta_{3,\pm1}(\theta)$, and $\Theta_{3,\pm2}(\theta)$. At $\theta = 0$ and $\pi/2$, $\Theta_{3,\pm2} = 0$ and thus the corresponding partial wave does not contribute to the parallel and perpendicular cross sections. Therefore, for these two angles only, Eq. (6) takes the form:

$$
\begin{aligned}
&\sigma'_p(\theta,\varphi) = \\
&= N\{C_{1,0}^2\Theta_{1,0}^2(\theta,\varphi) + 2C_{1,0}C_{3,0}\cos(\delta_3-\delta_1)\Theta_{1,0}(\theta,\varphi)\Theta_{3,0}(\theta,\varphi) + C_{3,0}^2\Theta_{3,0}^2(\theta,\varphi) + \\
&+ 2C_{1,0}C_{1,1}\Theta_{1,0}(\theta,\varphi)\Theta_{1,1}(\theta,\varphi) + C_{1,0}C_{1,-1}\Theta_{1,0}(\theta,\varphi)\Theta_{1,-1}(\theta,\varphi) + \\
&+ 2C_{1,0}C_{3,1}\Theta_{1,0}(\theta,\varphi)\Theta_{3,1}(\theta,\varphi) + C_{1,0}C_{3,-1}\Theta_{1,0}(\theta,\varphi)\Theta_{3,-1}(\theta,\varphi) + \\
&+ 2C_{3,0}C_{1,1}\Theta_{3,0}(\theta,\varphi)\Theta_{1,1}(\theta,\varphi) + C_{3,0}C_{1,-1}\Theta_{3,0}(\theta,\varphi)\Theta_{1,-1}(\theta,\varphi) + \\
&+ 2C_{3,0}C_{3,1}\Theta_{3,0}(\theta,\varphi)\Theta_{3,1}(\theta,\varphi) + C_{3,0}C_{3,-1}\Theta_{3,0}(\theta,\varphi)\Theta_{3,-1}(\theta,\varphi) + \\
&+ C_{1,1}^2\Theta_{1,1}^2(\theta,\varphi) + 2C_{1,1}C_{1,-1}\Theta_{1,1}(\theta,\varphi)\Theta_{1,-1}(\theta,\varphi) + C_{1,-1}^2\Theta_{1,-1}^2(\theta,\varphi) + \\
&+ C_{3,1}^2\Theta_{3,1}^2(\theta,\varphi) + 2C_{3,1}C_{3,-1}\Theta_{3,1}(\theta,\varphi)\Theta_{3,-1}(\theta,\varphi) + C_{3,-1}^2\Theta_{3,-1}^2(\theta,\varphi) + \\
&+ 2C_{1,1}C_{3,1}\cos(\delta_3-\delta_1)\Theta_{1,1}(\theta,\varphi)\Theta_{3,1}(\theta,\varphi) + \\
&+ 2C_{1,1}C_{3,-1}\cos(\delta_3-\delta_1)\Theta_{1,1}(\theta,\varphi)\Theta_{3,-1}(\theta,\varphi) + \\
&+ 2C_{1,-1}C_{3,1}\cos(\delta_3-\delta_1)\Theta_{1,-1}(\theta,\varphi)\Theta_{3,1}(\theta,\varphi) + \\
&+ 2C_{1,-1}C_{3,-1}\cos(\delta_3-\delta_1)\Theta_{1,-1}(\theta,\varphi)\Theta_{3,-1}(\theta,\varphi)\}
\end{aligned}
\quad , \qquad \text{(S.1)}
$$

where *N* is the same pre-factor as in Eq. (7). By integrating over φ, only terms that do not have φ component explicitly will remain, resulting in the following expression:

$$\sigma'_p(\theta) = N\{C_{1,0}^2\Theta_{1,0}^2(\theta) + 2C_{1,0}C_{3,0}\cos(\delta_3-\delta_1)\Theta_{1,0}(\theta)\Theta_{3,0}(\theta) + C_{3,0}^2\Theta_{3,0}^2(\theta) +$$
$$+ 2C_{1,1}C_{1,-1}\Theta_{1,1}(\theta,\varphi)\Theta_{1,-1}(\theta,\varphi) + 2C_{3,1}C_{3,-1}\Theta_{3,1}(\theta,\varphi)\Theta_{3,-1}(\theta,\varphi) + \quad .(S.2)$$
$$+ 2C_{1,1}C_{3,-1}\cos(\delta_3-\delta_1)\Theta_{1,1}(\theta,\varphi)\Theta_{3,-1}(\theta,\varphi) + 2C_{1,-1}C_{3,1}\cos(\delta_3-\delta_1)\Theta_{1,-1}(\theta,\varphi)\Theta_{3,1}(\theta,\varphi)\}$$

The expressions for the spherical harmonics are given by:

$$\begin{cases} \Theta_{1,0}(\theta) = \dfrac{1}{2}\sqrt{\dfrac{3}{\pi}}\cos\theta, \\ \Theta_{3,0}(\theta) = \dfrac{1}{4}\sqrt{\dfrac{7}{\pi}}(5\cos^3\theta - 3\cos\theta), \\ \Theta_{1,\pm1}(\theta,\varphi) = \mp\dfrac{1}{2}\sqrt{\dfrac{3}{2\pi}}e^{\pm i\varphi}\sin\theta, \\ \Theta_{3,\pm1}(\theta,\varphi) = \mp\dfrac{1}{8}\sqrt{\dfrac{21}{\pi}}e^{\pm i\varphi}\sin\theta(5\cos^2\theta - 1). \end{cases} \quad (S.3)$$

Substituting the above formulas into Eq. (S.2), we obtain the differential cross-section for the detachment from a *d* orbital:

$$\sigma'_p(\theta) = N\{\frac{3}{4\pi}C_{1,0}^2\cos^2\theta + \frac{\sqrt{21}}{4\pi}C_{1,0}C_{3,0}\cos(\delta_3-\delta_1)(5\cos^4\theta - 3\cos^2\theta) +$$
$$+ \frac{7}{16\pi}C_{3,0}^2(5\cos^3\theta - 3\cos\theta)^2 - \frac{3}{4\pi}C_{1,1}C_{1,-1}\sin^2\theta -$$
$$- \frac{21}{32\pi}C_{3,1}C_{3,-1}(5\cos^2\theta - 1)^2\sin^2\theta - \quad .$$
$$- \frac{3\sqrt{7}}{8\pi\sqrt{2}}C_{1,1}C_{3,-1}\cos(\delta_3-\delta_1)(5\cos^2\theta - 1)\sin^2\theta -$$
$$- \frac{3\sqrt{7}}{8\pi\sqrt{2}}C_{1,-1}C_{3,1}\cos(\delta_3-\delta_1)(5\cos^2\theta - 1)\sin^2\theta\} \quad (S.4)$$

Substituting $\theta = 0$ and $\theta = \pi/2$ angles into Eq. (S.4) and using the results in Eq. (14.7), we obtain the following formula for the anisotropy parameter in detachment from a *d* orbital:

$$\beta_d = \frac{\begin{array}{l}\frac{3}{2\pi}C_{1,0}^2 + \frac{7}{2\pi}C_{3,0}^2 + \frac{3}{2\pi}C_{1,1}C_{1,-1} + \frac{21}{16\pi}C_{3,1}C_{3,-1} + \\ + \cos(\delta_3 - \delta_1)\left\{\frac{\sqrt{21}}{\pi}C_{1,0}C_{3,0} - \frac{3\sqrt{7}}{4\pi\sqrt{2}}(C_{1,1}C_{3,-1} + C_{1,-1}C_{3,1})\right\}\end{array}}{\begin{array}{l}\frac{3}{4\pi}C_{1,0}^2 + \frac{7}{4\pi}C_{3,0}^2 - \frac{3}{2\pi}C_{1,1}C_{1,-1} - \frac{21}{16\pi}C_{3,1}C_{3,-1} + \\ + \cos(\delta_3 - \delta_1)\left\{\frac{\sqrt{21}}{2\pi}C_{1,0}C_{3,0} - \frac{3\sqrt{7}}{4\pi\sqrt{2}}(C_{1,1}C_{3,-1} + C_{1,-1}C_{3,1})\right\}\end{array}}. \qquad \text{(S.5)}$$

Using the same approach as in the main article, we compare Eq. (S.5) to the corresponding Cooper-Zare expression, i.e. Eq. (14.2) with $l = 2$:

$$\beta_p = \frac{2\chi_{2,1}^2 + 12\chi_{2,3}^2 - 36\chi_{2,1}\chi_{2,3}\cos(\delta_3 - \delta_1)}{10\chi_{2,1}^2 + 15\chi_{2,3}^2}. \qquad \text{(S.6)}$$

Since Eqs. (S.5) and (S.6) describe the same physics, they must be identical. We thus obtain the following system of equations for the $C_{n,m}$ coefficients:

$$\begin{cases} \frac{3}{2\pi}C_{1,0}^2 + \frac{7}{2\pi}C_{3,0}^2 + \frac{3}{2\pi}C_{1,1}C_{1,-1} + \frac{21}{16\pi}C_{3,1}C_{3,-1} = M_2^2(2\chi_{2,1}^2 + 12\chi_{2,3}^2), \\ \frac{3}{4\pi}C_{1,0}^2 + \frac{7}{4\pi}C_{3,0}^2 - \frac{3}{2\pi}C_{1,1}C_{1,-1} - \frac{21}{16\pi}C_{3,1}C_{3,-1} = M_2^2(10\chi_{2,1}^2 + 15\chi_{2,3}^2), \\ \frac{\sqrt{21}}{\pi}C_{1,0}C_{3,0} - \frac{3\sqrt{7}}{4\pi\sqrt{2}}(C_{1,1}C_{3,-1} + C_{1,-1}C_{3,1}) = -36M_2^2\chi_{2,1}\chi_{2,3}, \\ \frac{\sqrt{21}}{2\pi}C_{1,0}C_{3,0} - \frac{3\sqrt{7}}{4\pi\sqrt{2}}(C_{1,1}C_{3,-1} + C_{1,-1}C_{3,1}) = 0. \end{cases} \qquad \text{(S.7)}$$

By adding or subtracting equations in (S.7) to and from each other with necessary coefficients we can simplify the above system of equation to the following:

$$\begin{cases} \frac{9}{4\pi}C_{1,0}^2 + \frac{21}{4\pi}C_{3,0}^2 = M_2^2(12\chi_{2,1}^2 + 27\chi_{2,3}^2), \\ \frac{9}{2\pi}C_{1,1}C_{1,-1} + \frac{63}{16\pi}C_{3,1}C_{3,-1} = -M_2^2(18\chi_{2,1}^2 + 18\chi_{2,3}^2), \\ \frac{3\sqrt{21}}{2\pi}C_{1,0}C_{3,0} = -36M_2^2\chi_{2,1}\chi_{2,3}, \\ \frac{9\sqrt{7}}{4\pi\sqrt{2}}(C_{1,1}C_{3,-1} + C_{1,-1}C_{3,1}) = 36M_2^2\chi_{2,1}\chi_{2,3}. \end{cases} \quad \text{(S.8)}$$

From here we derive the expressions for the $C_{n,m}$ coefficients in terms of the dipole matrix elements:

$$\begin{cases} C_{1,0} = 4M_2\frac{\sqrt{\pi}}{\sqrt{3}}\chi_{2,1}, \\ C_{3,0} = -6M_2\frac{\sqrt{\pi}}{\sqrt{7}}\chi_{2,3}), \\ C_{1,\pm1} = \pm 2M_2\sqrt{\pi}\chi_{2,1}, \\ C_{3,\pm1} = \mp 4M_2\frac{\sqrt{2\pi}}{\sqrt{7}}\chi_{2,3}. \end{cases} \quad \text{(S.9)}$$

Substituting Eq. (S.8) into Eq. (S.4), we obtain the expressions for the parallel and perpendicular differential cross-sections for detachment from a *d* orbital:

$$\begin{cases} \sigma_d'(0) = M_2^2 N[4\chi_{2,1}^2 + 9\chi_{2,3}^2 - 12\chi_{2,1}\chi_{2,3}\cos(\delta_3 - \delta_1)] \\ \sigma_d'(\pi/2) = M_2^2 N[3\chi_{2,1}^2 + 3\chi_{2,3}^2 + 6\chi_{2,1}\chi_{2,3}\cos(\delta_3 - \delta_1)] \end{cases} \quad \text{(S.10)}$$

SUPPLEMENT B: Analytical evaluation of A and B coefficients for the p-d mixing case

According to the Eq. (43) from the main article, there are three coefficients that need to be defined in order to correctly predict the anisotropy parameter β_{pd} dependence on eKE, namely A_1, A_2, and B_1. In what follows, we evaluate those coefficients analytically based on their generalized definition (Eq. (37)) and radial dipole integrals defined in reference 21 of the main article.

$$A_1\varepsilon = \frac{\chi_{1,2}}{\chi_{1,0}} = \frac{\int_0^\infty j_2(kr)r^3R_{2p}(r)dr}{\int_0^\infty j_0(kr)r^3R_{2p}(r)dr}, \tag{S.11}$$

$$A_2\varepsilon = \frac{\chi_{2,3}}{\chi_{2,1}} = \frac{\int_0^\infty j_3(kr)r^3R_{3d}(r)dr}{\int_0^\infty j_0(kr)r^3R_{3d}(r)dr}, \tag{S.12}$$

$$B_2\varepsilon = \frac{\chi_{1,2}^2}{\chi_{2,1}^2} = \frac{\left(\int_0^\infty j_2(kr)r^3R_{2p}(r)dr\right)^2}{\left(\int_0^\infty j_1(kr)r^3R_{3d}(r)dr\right)^2}. \tag{S.13}$$

In the Wigner limit ($kr \to 0$), the behavior of the spherical Bessel functions is determined by the first term of their Maclaurin series expansion, thus

$$j_l(kr) \cong \frac{(kr)^l}{(2l+1)!!}, \quad \text{for } kr \to 0. \tag{S.14}$$

In particular, the specific $l = 0 - 3$ functions will be required for evaluation of the A and B coefficients, $j_0(kr) \cong 1$, $j_1(kr) \cong kr/3$, $j_2(kr) \cong (kr)^2/15$, and $j_3(kr) \cong (kr)^3/105$.

Substituting the above approximations for the Bessel functions into Eqs. (S.10 – S.13) and taking into account that $\varepsilon = k^2/2$ (atomic units) we obtain the following expressions for the A and B coefficients:

$$A_1 = \frac{2}{15}\frac{\int_0^\infty r^5 R_{2p}(r)dr}{\int_0^\infty r^3 R_{2p}(r)dr}, \quad A_2 = \frac{2}{35}\frac{\int_0^\infty r^6 R_{3d}(r)dr}{\int_0^\infty r^4 R_{3d}(r)dr}, \quad B_2 = \frac{2}{25}\frac{\left(\int_0^\infty r^5 R_{2p}(r)dr\right)^2}{\left(\int_0^\infty r^4 R_{3d}(r)dr\right)^2} \tag{S.15}$$

Standard normalized p and d hydrogenic radial functions from Eqs. (S.14) are well-known:

$$R_{2p} = \frac{1}{2\sqrt{6}}\xi_{2p}^{5/2} r e^{-\xi_{2p} r/2}, \quad R_{3d} = \frac{2\sqrt{2}}{81\sqrt{15}}\xi_{3d}^{7/2} r^2 e^{-\xi_{3d} r/3}. \tag{S.16}$$

After substituting Eq. (S.15) into (S.14) the corresponding integrals can be accurately evaluated analytically, yielding final expressions for the desired coefficients:

$$A_1 = \frac{16}{\xi_{2p}^2}, \tag{S.17}$$

$$A_2 = \frac{144}{5\xi_{3d}^2}, \tag{S.18}$$

$$B_2 = \frac{2^9 \xi_{3d}^7}{5 \cdot 3^6 \xi_{2p}^2}. \tag{S.19}$$

CHAPTER 15

ONGOING PROJECTS AND FUTURE DIRECTIONS

In this section the ideas for future projects are discussed. Some of these ideas have already been pursued to a certain extent either computationally or experimentally, while others are experiments with interesting potential that grew from the work presented in this dissertation.

15.1. Another O^- + Cyclopentanone reaction product

Atomic oxygen radical anion ($O^{\cdot -}$) reactivity, described in detail elsewhere (see for instance Chapter 11) can be utilized to synthesize a number of important anion intermediates in the gas-phase. These intermediates can be then characterized using spectroscopic tools in order to obtain their thermochemical properties, as well as their molecular and electronic properties.

The reaction of $O^{\cdot -}$ with cyclopentanone, C_5H_8O, was examined in our laboratory via mass spectrometry. The experimental procedure is identical to that described in Chapter 12 for production of cyclopentadienone anion; in fact the product discussed below was obtained under the same experimental conditions as highlighted in Chapter 12. The typical mass spectrum is presented in Figure 12.1(a) along with a similar spectrum obtained for the fluoroacetonitrile (CH_2FCN) mixture with N_2O to indicate the sample sensitive nature of the 82 and 80 a.m.u. peaks. The peaks are assigned to the $C_5H_6O^-$ and $C_5H_4O^-$, with the proposed mechanism of their formation presented in Figure 12.1(b).

The relative intensities of the produced anions are dependent on the instrument settings in the ion chamber – backing pressure, nozzle duration and electron gun current, which can be adjusted to produce peaks intense enough for photoelectron imaging experiments.

1,3-Cyclopentanediyl, 2-oxo (C_5H_6O) is a diradical in which two nearly degenerate, nonbonding molecular orbitals (MOs) are occupied by two electrons. The relative state ordering depends on the energy gap between the frontier MOs as well as their character and is of great interest. The lone pairs on oxygen give rise to a second diradical manifold, which can interact with the other states. This is similar to the other oxygen-containing diradicals, with one of the examples being the oxyallyl studied previously in our lab.[257,258,316]

In order to study the complex electronic structure of these highly reactive intermediates we employed photoelectron imaging spectroscopy on the corresponding anions. The mass selected anion of interest was intersected with the laser pulse of specific energy and polarization. In this particular study we used second harmonics (532 nm) of Nd:YAG laser (Quanta Ray, Lab 50). The photodetached electrons are projected onto position sensitive detector via velocity map imaging electrodes[24] where raw images are recorded using a charge-coupled device (CCD) camera and accumulated for ~10^6 experimental cycles.

The photoelectron image and corresponding photoelectron spectrum of $C_5H_6O^-$ obtained at 532 nm are presented in Figure 15.1. Despite the relatively high noise levels and an energy cut-off at ~2.3 eV, we can see two (or more) overlapping transitions with possible vibrational progression. Bands are labeled with lower case letters and the

binding energy corresponding to every transition labeled is presented in the Table 15.1. The assignment of those transitions however is complicated due to the rich manifold of diradical states. Imaging at different laser wavelengths may prove useful in helping to resolve convoluted transitions, due to higher resolution at the threshold energy.

In order to assist in the assignment, geometry optimization calculations have been performed for the anion, and singlet and triplet states of neutral using Gaussian suite of programs at CCSD/aug-cc-pVDZ level of theory. Figure 15.2 shows optimized structures of the anion's $^2A_2$ state, singlet $^1A_1$, and triplet $^3B_1$. In all three states, the geometry of the ring is approximately the same, with only two internal coordinates showing large differences between the states, i.e., the C=O bond and C-C=O angle. We therefore expect C=O stretch vibrational mode, with a typical IR frequency of ~1700 cm^{-1} or 0.22 eV, to be excited upon photodetachment.

Single point energy calculations were performed on the optimized geometries for all three states and the electron affinity along with vertical detachment energy was calculated. The results for the two levels of theory used (shown in Table 15.2) predict a near overlap of the singlet and triplet states, making it harder to assign the energy difference between states or even ground state multiplicity. However, due to the inherent multiconfigurational nature of diradicals, the single reference calculations cannot adequately describe the energetic properties of the system (especially the excited states). A more appropriate description based on a spin-flip method needs to be adopted.[177,197,227,228] Although also rooted in a nominally single-reference formalism, the EOM-SF strategy allows us to calculate the energies of the low-spin excited states starting from a robust high-spin reference, thus providing a more accurate description of

the multiconfigurational target states.[197] Additionally, higher chemical accuracy can be achieved by using larger basis sets, e.g. aug-cc-pVTZ, and by including diagonal triples corrections (dT).[198]

In conclusion, more work needs to be done both computationally and experimentally in order to gain an insight on relative state ordering of 1,3-Cyclopentanediyl, 2-oxo diradical.

15.2. Photoelectron angular distribution for the detachment from nitrobenzene anion

Nitrobenzene anion (NB^-) has been previously studied in our lab as a model system for understanding the detachment from larger, doubly substituted aromatics, such as para- and meta-dinitrobenzene anions (p-, m- DNB^-). Those systems are of great interest due to their high symmetry and π-conjugated delocalized nature of the highest occupied molecular orbital (HOMO), and to the first approximation can be thought of as a superposition of the molecular orbitals of two NO_2 groups. Thus understanding the photodetachment process from the nitrobenzene anion will help to shed light on the more complicated case of dinitrobenzene anion detachment.

In the previous work by Pichugin et al, NB^- was imaged at 780, 532, 390, 355, and 266 nm.[11] Images were analyzed and anisotropy parameter β was determined for the $X^2B_1 \rightarrow X^1A_1$ transition and plotted with respect to electron kinetic energy (see Figure 15.3(a)). The observed anisotropy distribution was interpreted in terms of a group theoretical approach and modeled with the Bethe-Cooper-Zare (BCZ) model[29-31] for the s and d waves emission in the detachment of p-shell electron from atomic anions (see

dotted line in Figure 15.3(a)). However, in fitting of the experimental data, the researchers excluded one of the data points (532 nm data point at eKE = 1.2 eV, β = -0.10, shown in red) on the basis of the limited data statistics. The rest of the data is in a good agreement with the predicted curve, which makes the outlier seem especially peculiar. It is also worth mentioning that in general the BCZ model is not applicable for the detachment from molecular anions, thus agreement with the experiment is not a trivial result. In order to improve the pervious modeling, we decided to further examine photoelectron angular distribution for the detachment from NB^- and not only get better statistics for the 532 nm data point but to obtain more data points for other eKE.

The representative photoelectron images and corresponding photoelectron spectra of NB^- obtained at 1064, 781, 612 and 532 nm are presented in Figure 15.4. The peak A in the spectra is assigned to a direct photodetachment from the ground X^2B_1 state of the anion to the ground X^1A_1 state of the neutral nitrobenzene. The band is vibrationally resolved with a spacing of 1260 ± 20 cm^{-1} for 781 nm and 1310 ± 50 cm^{-1} for 612 nm spectra respectively. This excited vibrational mode corresponds to a symmetric stretch of the NO_2 group.[317,318] The electron affinity is defined by the lowest eBE peak in 1064 nm spectrum to be EA = 0.983 ± 0.001 eV which is in good agreement with the previously reported EA of 1.00 ± 0.01 eV,[319] but reflects the order of magnitude improvement in the uncertainty range.

Perhaps the most interesting observation is in angular distribution behavior. The anisotropy parameter for every vibrationally resolved transition was determined and plotted with respect to electron kinetic energy in Figure 15.3 (b). The most striking result is the same almost isotropic character of the 532 nm image, with β = –0.147 ± 0.006.

Improved resolution was obtained for that particular data point, allowing for higher confidence in the obtained anisotropy parameters. This clear oscillatory behavior of the β parameter with respect to eKE, outlined schematically with the dotted line in Figure 15.3 (b), can be possibly explained by interference effects. This is possible due to π conjugation of the NB^- HOMO, where electron is highly delocalized along the molecule and can be ejected from different "centers" upon interaction with the photon, resulting in interference of outgoing electron waves. Interference model, described in detail in Chapter 14 of this dissertation can be employed in order to understand the anisotropy parameter behavior; however, it will have to be adapted for the detachment from more than two possible "centers".

In conclusion, the experimental data for the nitrobenzene anion exhibits the oscillatory behavior of anisotropy parameter with respect to photoelectron kinetic energy. One possible explanation could be the quantum interference effects due to delocalization of the NB^- molecular orbital. The multiple (more than two) center interference model needs to be developed in order to model a coherent photoelectron emission from nitrobenzene anion. Additionally, more data points can be obtained, especially for the region of interest around eKE of 1.3 eV (532 nm laser wavelength), in order to map out the exact positions of the anisotropy parameter maxima and minima. The use of a tunable laser system will go a long way in pursuing these goals.

15.3. Dicyanoacetylene anion

Neutral dicyanoacetylene molecule (NCCCCN) is an important organic molecule which is postulated (along with many other carbon-nitrogen chains[320]) to be present in the

interstellar medium. It has been previously observed on Titan and Neptune via infrared spectroscopy.[321] However it has never been detected in the interstellar medium because of the nonexistence of its microwave spectrum due to its symmetry and zero dipole moment. The anionic states of NCCCCN are of further importance as a possible intermediate state in a formation of astrophysically relevant anions. CCCN and CN fragment anions have been shown to form upon electron attachment to dicyanoacetylene.[322]

However the anion produced via electron attachment to NCCCCN is metastable with a relatively short lifetime due to the linear equilibrium geometry of the neutral dicyanoacetylene. The antibonding character of the low-lying vacant orbitals of cyanoacetylene results in significant geometric distortions in the anion, rendering NCCCCN a poor choice of the starting reactant for generating $NCCCCN^-$. Similar to a cyanoacetylene, recently observed in our laboratory for the first time,[120] we propose using fumaronitrile ($C_4N_2H_2$) as a precursor in formation of dicyanoethylene anion. The anion of interest can be generated via H_2^+ abstraction reaction of O^- with fumaronitrile, whose bent CCCC skeleton structure could be the key to the formation of the $NCCCCN^-$.

In order to support the possibility of the existence of bent dicyanoethylene anion, geometry optimization calculations have been performed for the anion, and singlet and triplet states of neutral using Gaussian suite of programs at CCSD/aug-cc-pVDZ and CCSD/aug-cc-pVTZ levels of theory. Figure 15.5 shows optimized structures of the anion's ^2A_g state, singlet $^1\Sigma$, and triplet ^3A_u. The optimized anion geometry was shown to be of C_{2h} symmetry, with a bent CCCC skeleton similar to a fumaronitrile structure, supporting the possibility of above mechanism of formation. Moreover, the single point

energy calculations performed on optimized geometries, suggest relatively high EA of ~1.2 eV, with a predicted vertical detachment energy of ~2.2 eV. This further supports the existence of a bent dicyanoacetylene anion. The results for all of the levels of theory employed are shown in Table 15.4, where EOM-IP formalism has been used along with the Gaussian calculations.

The usual strategy for the high abundance O^- production in the supersonic gas jet (via dissociative electron attachment to N_2O carrier gas) is not possible however, due to overlap of the expected mass spectrum peak, corresponding to a doubly deprotonated fumaronitrile (m/z = 76 a.m.u.), with another peak of the same mass, possibly $O^-(N_2O_2)$. Therefore, another reagent source is necessary for the experiments on $NCCCCN^-$. One of the possible ways is to use O_2 as a carrier gas.

In conclusion, based on the previous experimental data and supported by the theoretical calculations, it may be possible to produce dicyanoacetylene anion using fumaronitrile as a precursor. The key to the formation of adiabatically weakly bound $NCCCCN^-$ is the bent ≡C−C≡C–C≡ skeleton of the reactant.

15.4 Quantum interference effects in photodetachment of dinitroaromatics revisited

Electronic through-bond coherence of delocalized charge distributions in negative ions is essential in determining the fundamentals of charge transfer and conductivity in a variety of systems, including photovoltaic devices and carbon nanotubes.[323-325] This topic is of great interest in material sciences and electronics industry as well as in fundamental chemistry and has been studied previously in our laboratory with an example of I_2^- [326,327] and dinitrobenzenes.[11]

Dinitrobenzene (DNB) anions are a perfect model system to study the coherence of delocalized electron orbitals, due to their π-conjugation and high-symmetry structures. Photoelectron imaging spectroscopy is a powerful technique ideally suited to probe the electronic structure of negative ions since it provides the information about both the energies and the symmetries of parent anion orbitals from which an electron has been removed. Photodetachment of an excess electron from a molecular orbital delocalized over two or more equivalent structural moieties of an anion leads to a coherent superposition of emitted electron waves. The phenomenon of multi-center interference in photodetachment is directly related to the quantum interference effect observed in the classical double-slit experiment with electrons.[328] In the case of photodetachment from an isolated molecular anion of dinitrobenzene, two nitro groups act as emission centers and an outgoing electron is a result of the interference of two electron waves simultaneously emitted from both centers.

To test this assumption, gas-phase photoelectron imaging experiments were performed previously[11] on the meta- and para-dinitrobenzene anions. However, there was a concern of contamination of the meta-dinitrobenzene sample, resulting in low vibrational resolution and overall questionable results. In this work we have decided to repeat the experiment and higher quality images and corresponding spectra were obtained. We also performed photoelectron imaging on the ortho-dinitrobenzene isomer using various laser photon energies. The experimental data for para- and meta-dinitrobenzene anions clearly show oscillatory behavior of the anisotropy parameter with respect to the photoelectron kinetic energy due to quantum interference. This indicates that these dinitrobenzene anions retain their high symmetry electronic and geometrical

structure in the gas phase. Ortho-dinitrobenzene data, however, does not show similar anisotropy parameter behavior, probably due to much shorter distance between the nitro groups and lower symmetry.

In addition, we report the adiabatic electron affinities of 1.62 ± 0.01 eV and 1.96 ± 0.01 eV for meta- and para- dinitrobenzene molecules respectively. These measurements refine the values obtained previously from the gas phase electron transfer equilibrium experiments.[329]

Photoelectron images and spectra of p-DNB collected in the range of 532-266 nm are presented in Fig.15.6. Overall the photoelectron data exhibit three easily distinguishable features, marked with upper case letters in the corresponding spectra. The highest eKE feature A is assigned to the transition from ground state anion X^2B_{3u} to the ground state neutral X^1A_g of p-DNB. The apparent vibrational progression in band A is best resolved for the 532 nm data due to improved energy resolution for the low kinetic energy photoelectrons. Peak separation of 1280 ± 110 cm^{-1} is in a good agreement with symmetric stretch of NO_2 group.[317-319] The position of the peak with the lowest eBE corresponds to (0,0) transition and provides the value for adiabatic electron affinity (AEA) of 1.96 ± 0.01 eV. This result is in excellent agreement with the previous indirect determination of EA = 2.00 ± 0.10 eV, but reflects an order of magnitude improvement in uncertainty range.

Feature B, visible in the 266 nm spectrum is attributed to direct photodetachment from the ground state of anion to an uncharacterized excited electronic state of neutral p-DNB. Finally, the lowest kinetic energy band C which correspond to the almost isotropic

high intensity spot in the middle of the image, is assigned to the autodetachment process from a temporary excited state(s) of p-DNB$^-$ anion.[330] The electron binding energies for the p-DNB$^-$ are listed in Table 15.5 along with the anisotropy parameters for each wavelength. Photoelectron angular distribution for band A is highly dependent on the electron kinetic energy of the peak and shows oscillatory behavior, similar to the one observed for the detachment from nitrobenzene.

Photoelectron images and spectra of m-DNB collected in the range of 532-355 nm are presented in Fig.15.7. Analogous to p-DNB$^-$, three separate features can be discerned from the data. Vibrationally resolved band A is assigned to $X^1A_1 \leftarrow X^2A_2$ transition, with vibrational frequency of 1300 ± 60 cm^{-1} corresponding to the NO_2 symmetric stretch. The lowest eBE peak yields AEA of 1.62 ± 0.01 eV which is in excellent agreement with the previous measurement of EA = 1.66 ± 0.10 eV indirectly obtained through gas phase electron transfer equilibrium experiments. Feature B has also been assigned to the direct photodetachment from anion ground state to some excited state(s) of the neutral m-DNB, while sharp low-eKE band C represents autodetachment. Corresponding electron binding energies and anisotropy parameters are listed in Table 15.6. Band A exhibits same variational trend of photoelectron angular distribution as was observed in the photodetachment of p-DNB$^-$.

Selected photoelectron images and corresponding spectra of o-DNB collected in the range of 612–266 nm are presented in Figure 15.8. Band A, corresponding to a ground state anion to ground state neutral transition is not vibrationally resolved as in other dinitrobenzene isomers, due to the large geometry difference between the anion and

neutral. This is expected because of the close proximity of the nitro-groups, where addition of an electron to the neutral species results in the out-of-plane twist of the nitro-groups due to repulsion of the partial charge. Feature B, prominent only in the 355 nm spectrum corresponds to some excited state(s) of the neutral. Band C is assigned to an autodetachment, similar to other dinitrobenzenes. Adiabatic electron affinity is determined as a lowest eBE peak to be 1.76 ± 0.05 eV and is in good agreement with the previously reported value of 1.65 ± 0.1 eV.[329] Corresponding electron binding energies and anisotropy parameters are listed in Table 15.7.

Anisotropy parameter trends are plotted with respect to eKE for all three of the isomers in Figure 15.9. The experimental data for para- and meta- DNB anions exhibit the oscillatory behavior of anisotropy parameter with respect to the photoelectron kinetic energy due to the quantum interference effect, indicating that these anions retain their high symmetry electronic and geometrical structure in the gas phase. In order to understand the coherent nature of photoelectron emission of dinitrobenzene anions, multiple center interference model needs to be developed based on the "theory of everything" described in detail in Chapter 14 of this dissertation. Additionally, more data points can be obtained for all of the anions, especially in the higher photon energy region, using a tunable laser system.

Table 15.1 Electron binding energy assignment, based on the experimental photoelectron spectrum of C_5H_6O anion shown in Figure 15.1

Peak	VDE, eV
a	1.46 ± 0.02
b	1.69 ± 0.05
c	1.79 ± 0.05
d	1.91 ± 0.02
e	1.99 ± 0.05
f	2.07 ± 0.05

Table 15.2 Calculated VDE and adiabatic EA corresponding to the detachment to the ^{1}B and ^{3}C states of the neutral C_5H_6O diradical

Method/basis set	VDE(eV)		Adiabatic EA (eV)	
	$^2A_2 \rightarrow {}^1A_1$	$^2A_2 \rightarrow {}^3B_1$	$^2A_2 \rightarrow {}^1A_1$	$^2A_2 \rightarrow {}^3B_1$
B3LYP/aug-cc-pVDZ	1.710	1.877	1.612	1.805
CCSD/aug-cc-pVDZ	1.665	1.637	1.558	1.554

Table 15.3 Photoelectron band energy and anisotropy parameter (β_2) values determined from NB^- photoelectron images in Figure 16.4. See text for details of the band assignments.

Wavelength	Peak	eKE, eV	β_2
1064 nm	A_0	0.178(1)	-0.078(19)
	A_1	0.095(1)	-0.045(60)
781 nm	A_0	0.595(1)	-0.505(35)
	A_1	0.434(2)	-0.460(14)
	A_2	0.276(1)	-0.283(39)
612 nm	A_0	1.023(2)	-0.422(31)
	A_1	0.864(1)	-0.488(18)
	A_2	0.707(1)	-0.457(11)
	A_3	0.538(1)	-0.356(10)
532 nm	A_0	1.323(2)	-0.029(7)
	A_1	1.178(2)	-0.147(6)

Table 15.4 Calculated VDE and adiabatic EA corresponding to the detachment to the $^1\Sigma$ and ^3A_u states of the neutral dicyanoacetylene (C_4N_2)

Method/basis set	VDE(eV)		Adiabatic EA (eV)	
	$^2A_g \rightarrow {}^1\Sigma$	$^2A_g \rightarrow {}^3A_u$	$^2A_g \rightarrow {}^1\Sigma$	$^2A_g \rightarrow {}^3A_u$
CCSD/aug-cc-pVDZ	2.294	4.938	1.214	4.818
CCSD/aug-cc-pVTZ	2.229	5.110	1.156	4.983
EOM-IP-CCSD/aug-cc-pVDZ	2.339	4.874		
EOM-IP-CCSD(dT)/aug-cc-pVDZ	2.220	4.602		
EOM-IP-CCSD/aug-cc-pVTZ	2.310	5.035		
EOM-IP-CCSD(dT)/aug-cc-pVTZ	2.197	4.781		

Table 15.5 Electron binding energies and the anisotropy parameters (β) determined from the corresponding spectral features observed in the photodetachment of p-dinitrobenzene anion at different photon energies. See Figure 15.6 and the text for the band assignments.

Wavelength	Peak	eBE, eV	β
532	A_0	1.96 ± 0.01[a]	-0.56 ± 0.07[b]
	A_1	2.15 ± 0.01	-0.22 ± 0.03
	A_2	2.30 ± 0.01	0.04 ± 0.01
390	A_0	1.98 ± 0.01	-0.08 ± 0.03
	A_1	2.14 ± 0.01	-0.14 ± 0.03
	A_2	2.30 ± 0.01	-0.18 ± 0.05
	A_3	2.47 ± 0.01	-0.19 ± 0.05
	C	3.17 ± 0.05	-0.10 ± 0.05[c]
355	A_0	1.97 ± 0.01	-0.03 ± 0.03
	A_1	2.13 ± 0.01	-0.01 ± 0.05
	A_2	2.30 ± 0.01	-0.06 ± 0.07
	C	3.48 ± 0.05	-0.10 ± 0.02
266	A	2.63 ± 0.05	-0.17 ± 0.02
	B	3.69 ± 0.05	-0.10 ± 0.03
	C	4.65 ± 0.05	-0.12 ± 0.22

[a] The uncertainties are determined as a standard deviation between different sets of measurements taken under the same conditions [b] The anisotropy parameter is determined for each individual vibrational peak [c] The anisotropy parameter is obtained for the entire Frank-Condon region of the band. Vertical detachment energy of the transition is obtained via Gaussian fit.

Table 15.6 Electron binding energies and the anisotropy parameters (β) determined from the corresponding spectral features observed in the photodetachment of m-dinitrobenzene anion at different photon energies. See Figure 15.7 and the text for the band assignments.

Wavelength	Peak	eBE, eV	β
	A_0	1.62 ± 0.01[a]	-0.38 ± 0.03[b]
	A_1	1.80 ± 0.01	-0.47 ± 0.05
532	A_2	1.97 ± 0.01	-0.54 ± 0.01
	A_3	2.13 ± 0.01	-0.24 ± 0.02
	A_4	2.31 ± 0.01	0.03 ± 0.03
	A_2	2.00 ± 0.01	-0.15 ± 0.03
	A_3	2.16 ± 0.01	-0.12 ± 0.05
390	A_4	2.31 ± 0.01	-0.16 ± 0.06
	A_5	2.47 ± 0.01	-0.24 ± 0.03
	C	3.17 ± 0.05	-0.11 ± 0.07[c]
	A_1	1.96 ± 0.01	-0.15 ± 0.03
	A_2	2.14 ± 0.01	-0.06 ± 0.03
355	A_3	2.31 ± 0.01	-0.12 ± 0.01
	A_4	2.45 ± 0.01	-0.11 ± 0.04
	C	3.39 ± 0.05	-0.11 ± 0.02

[a] The uncertainties are determined as a standard deviation between different sets of measurements taken under the same conditions [b] The anisotropy parameter is determined for each individual vibrational peak [c] The anisotropy parameter is obtained for the entire Frank-Condon region of the band. Vertical detachment energy of the transition is obtained via Gaussian fit.

Table 15.7 Electron binding energies and the anisotropy parameters (β) determined from the corresponding spectral features observed in the photodetachment of o-dinitrobenzene anion at different photon energies. See Figure 15.8 and the text for the band assignments.

Wavelength	eBE, eV	β
612	1.87 ± 0.01	0.09 ± 0.07[a]
532	2.00 ± 0.01	0.13 ± 0.06
407	2.01 ± 0.02	-0.20 ± 0.02
355	1.96 ± 0.01	-0.31 ± 0.02
306	1.95 ± 0.05	-0.27 ± 0.02
266	1.96 ± 0.05	-0.22 ± 0.02

[a] The anisotropy parameter is obtained for the entire Frank-Condon region of the band. Vertical detachment energy of the transition is obtained via Gaussian fit.

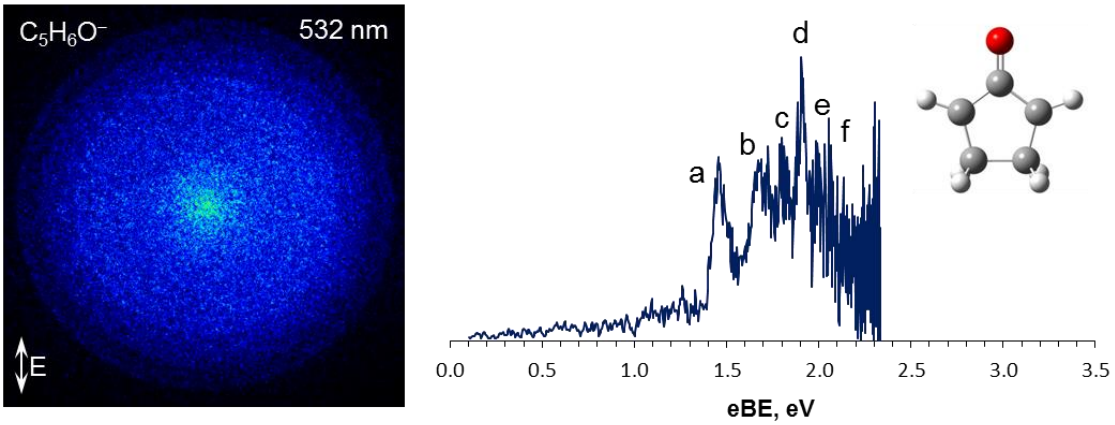

Figure 15.1 Photoelectron image and spectrum of $C_5H_6O^-$ obtained at 532 nm. Peaks are labeled with a lower case letters and energetics are presented in Table 16.1

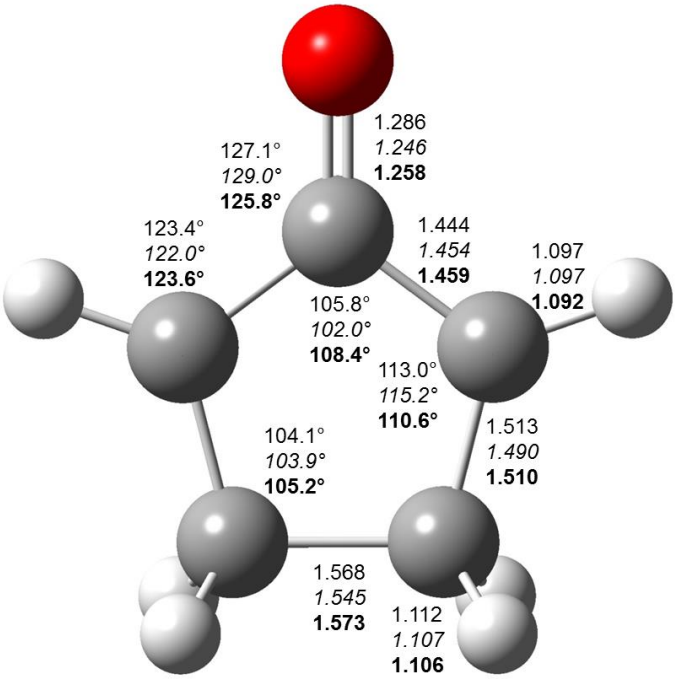

Figure 15.2 Bond length (Å) and angles (degree) of the C_{2v} optimized structure of the $^2A_2$, $^1A_1$, and $^3B_1$ states shown in normal, italic, and bold fonts, respectively.

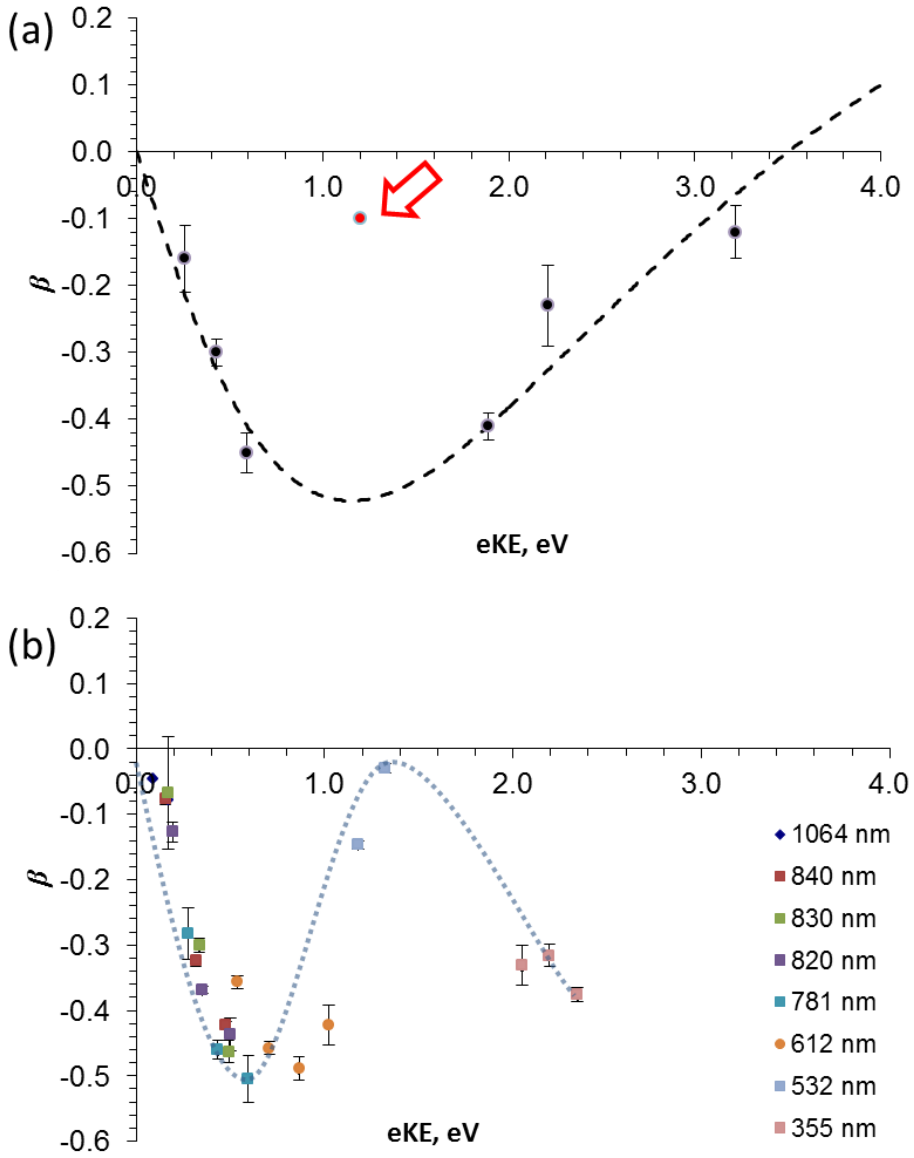

Figure 15.3 (a) Previously[11] obtained data for anisotropy parameter (β) dependence on electron kinetic energy for the detachment from NB^-. The long-dash curve represents the BCZ model fit. Red dot correspond to the 532 nm data and was considered an outlier (see text for details). **(b)** Newly acquired anisotropy data at different wavelengths and with better statistics for the 532 nm specifically. Dotted line represents schematic outline of the oscillatory behavior of the anisotropy parameter and is intended to guide the eye.

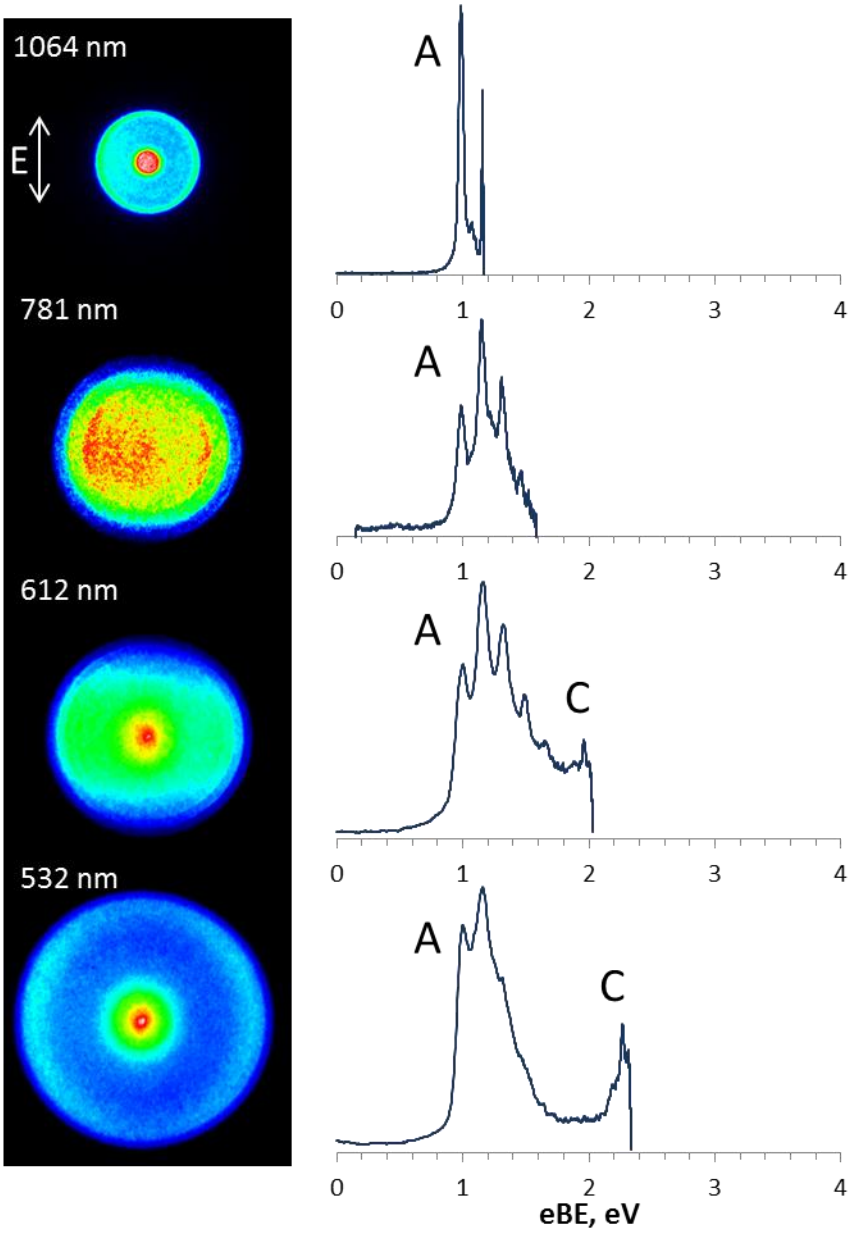

Figure 15.4 Representative photoelectron images and corresponding photoelectron spectra for the detachment from NB^- obtained at 1064 nm, 781 nm, 612 nm, and 532 nm. Laser polarization is indicated with the double arrow.

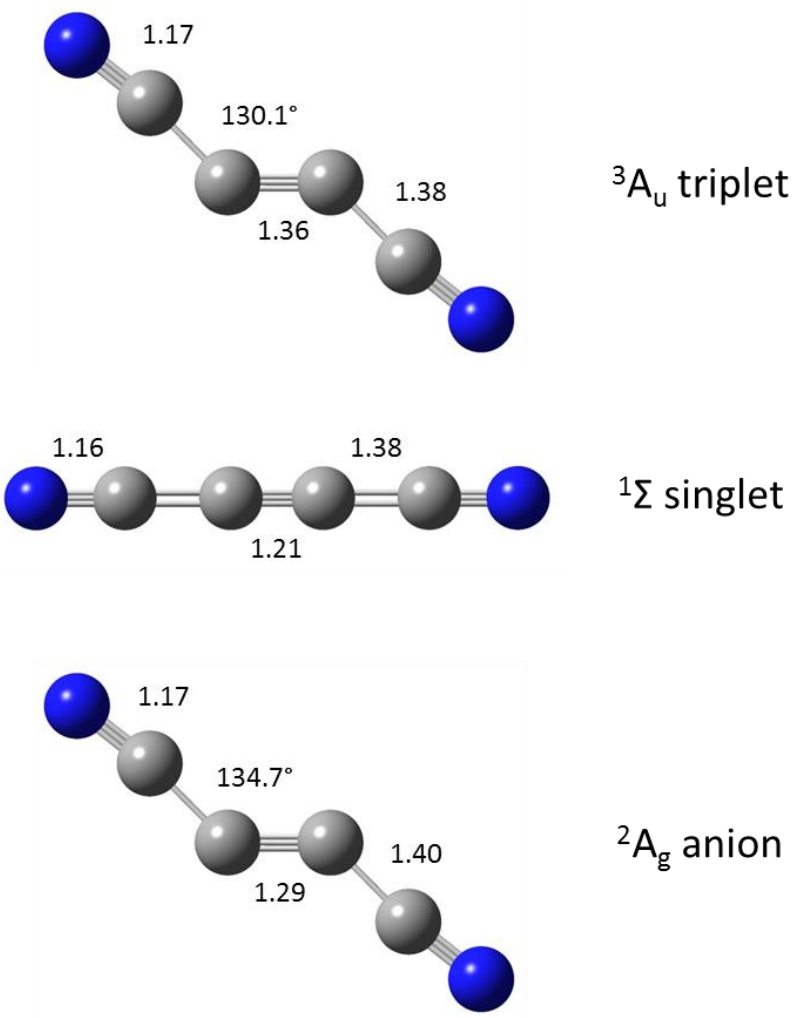

Figure 15.5 C_{2h} optimized structure of the ^2A_g anion and ^3A_u state of neutral C_4N_2, along with the $C_{\infty v}$ structure of the $^1\Sigma$ neutral state. All the bond lengths are given in Å, while angles are in degrees.

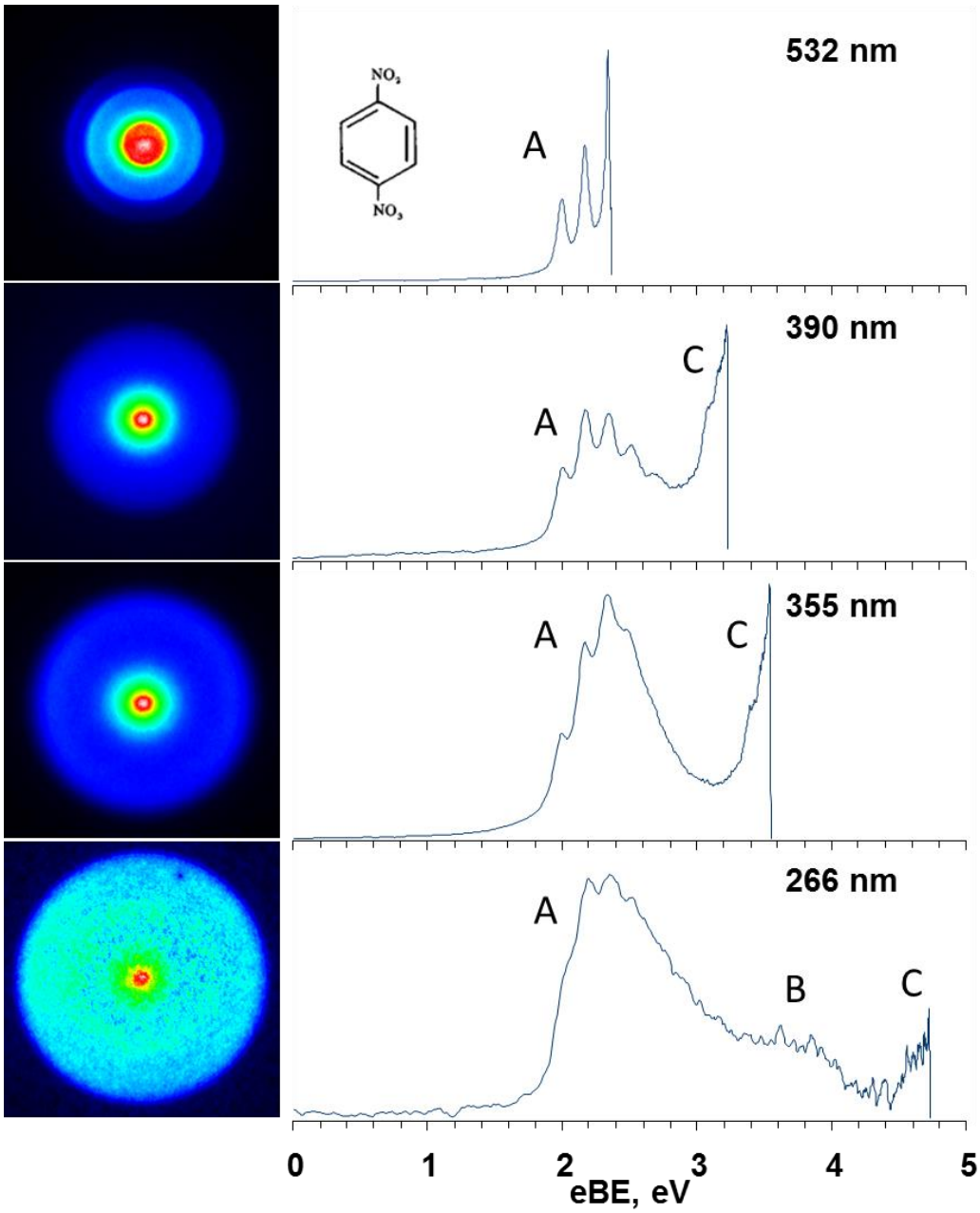

Figure 15.6 Photoelectron images and the corresponding photoelectron spectra of para-dinitrobenzene obtained at selected wavelengths. The laser polarization direction is vertical in the image plane.

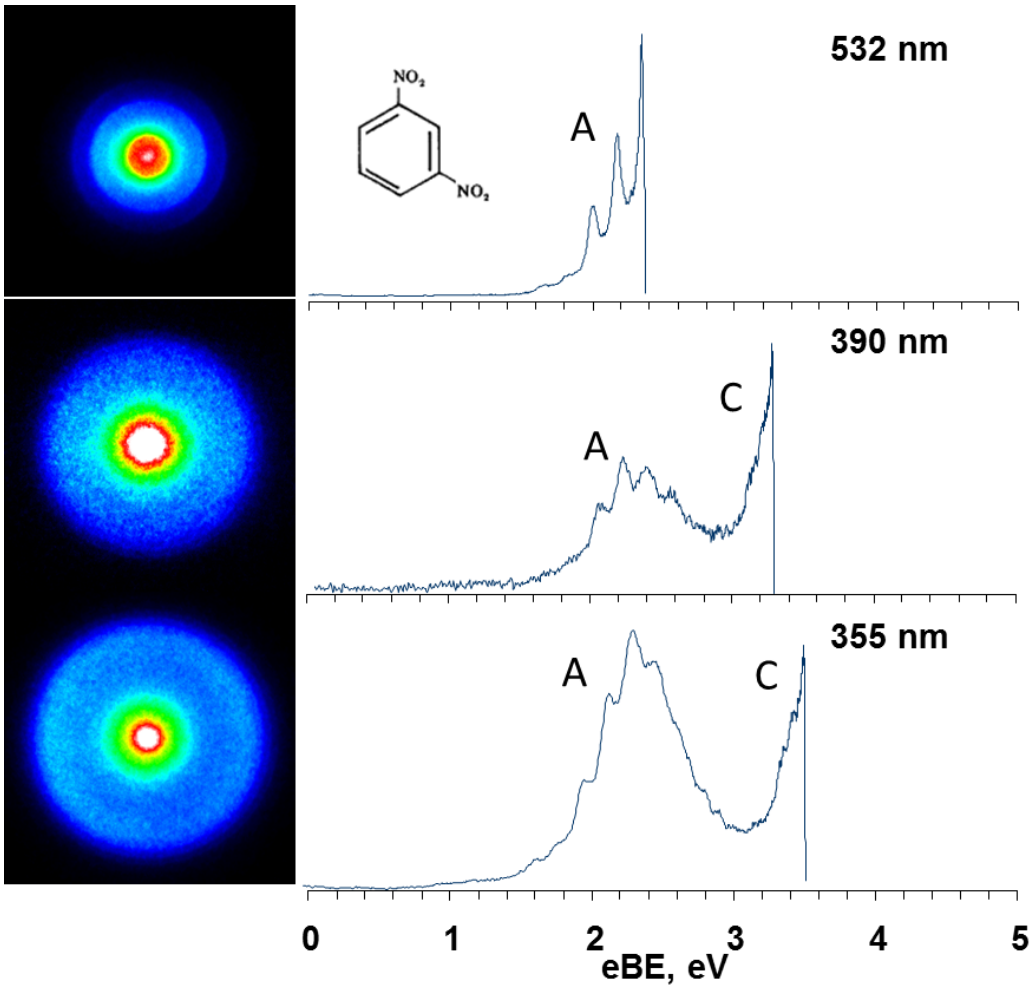

Figure 15.7 Photoelectron images and the corresponding photoelectron spectra of meta-dinitrobenzene obtained at selected wavelengths. The laser polarization direction is vertical in the image plane.

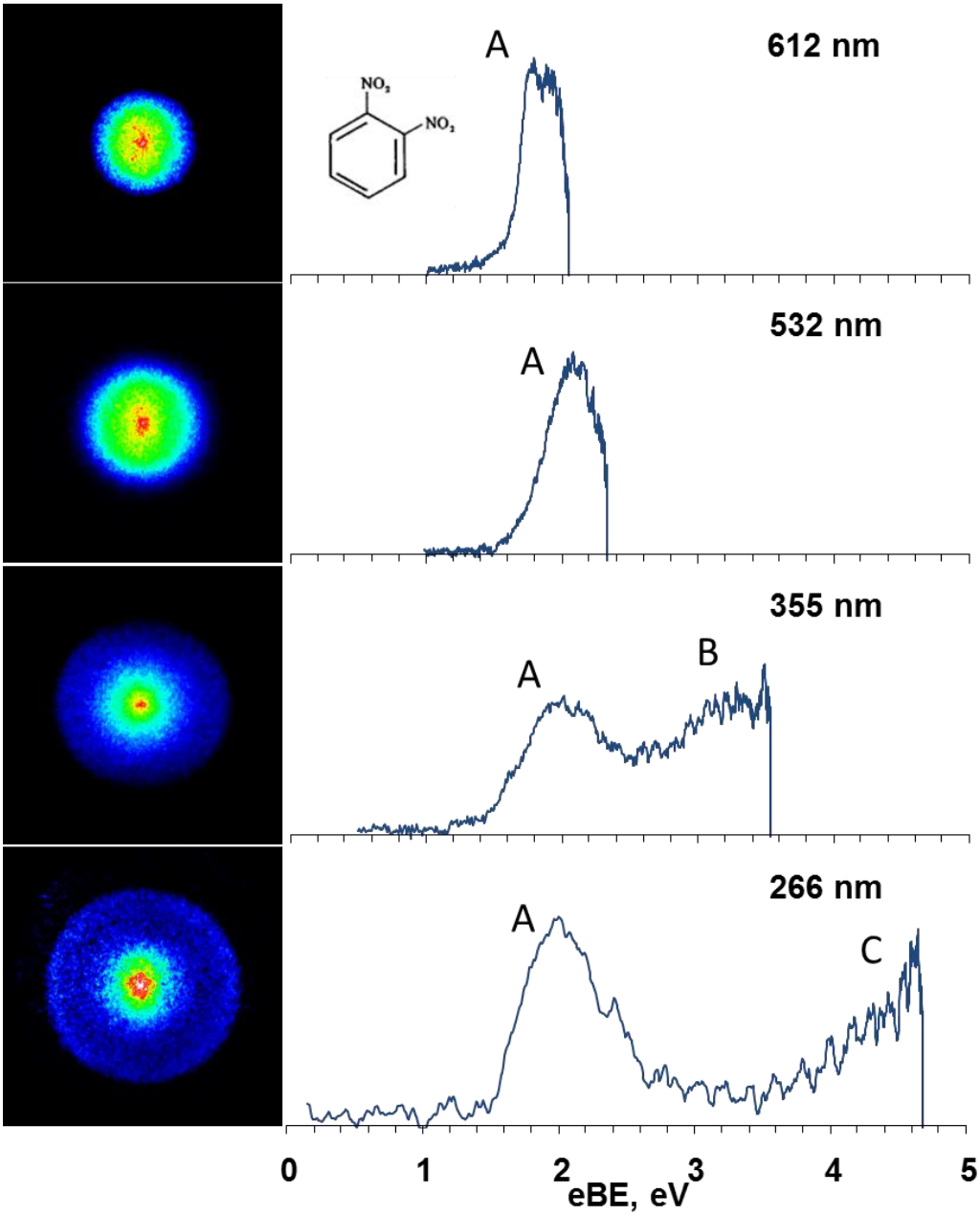

Figure 15.8 Photoelectron images and the corresponding photoelectron spectra of ortho-dinitrobenzene obtained at selected wavelengths. The laser polarization direction is vertical in the image plane.

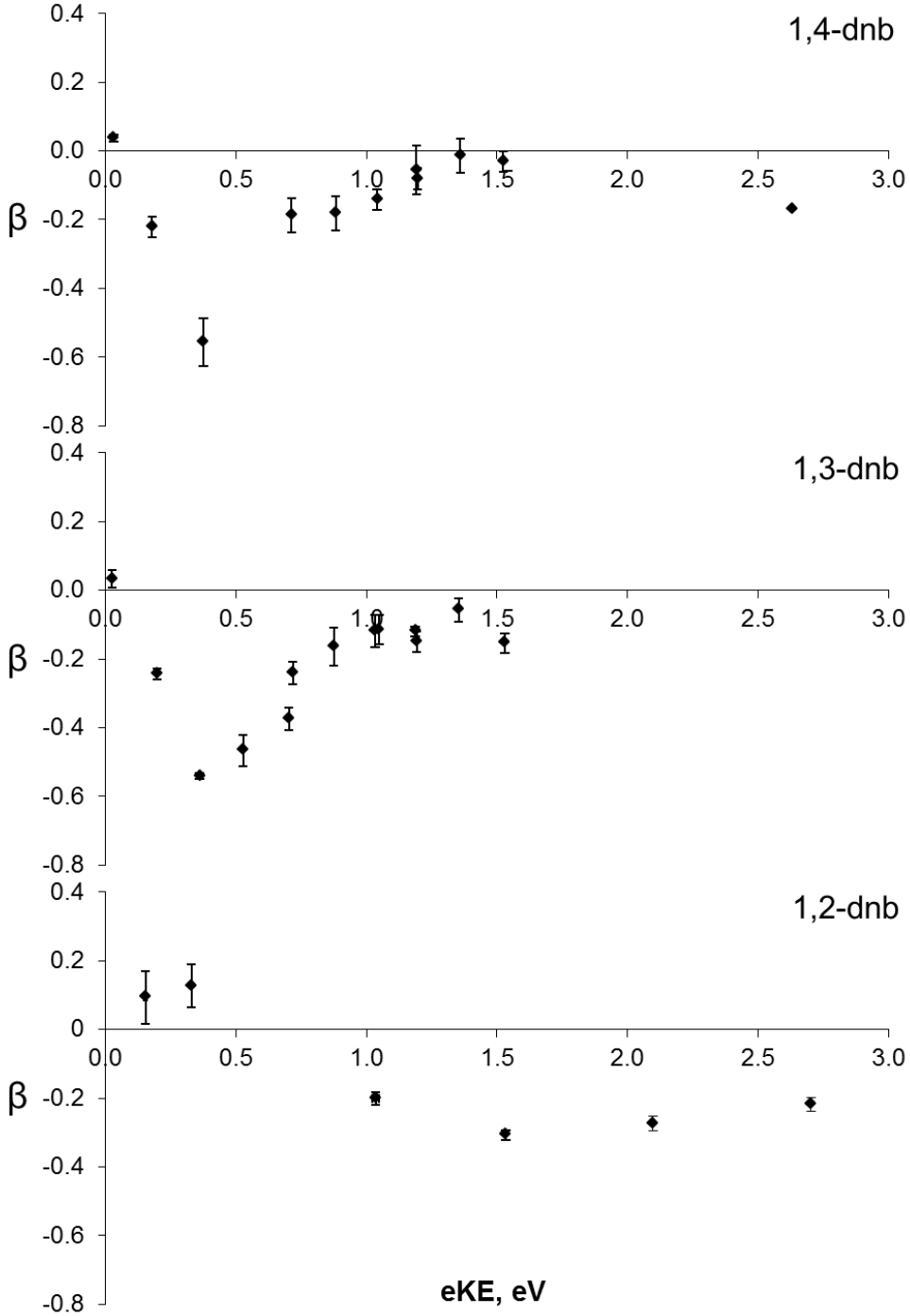

Figure 15.9 Anisotropy parameter (β) dependence on the electron kinetic energy in photodetachment of p-DNB (top), m-DNB (center), and o-DNB (bottom)

REFERENCES

(1) Krupenie, P. H. *Journal of Physical and Chemical Reference Data* **1972**, *1*, 423.

(2) Cheung, A. S. C.; Yoshino, K.; Esmond, J. R.; Parkinson, W. H. *Journal of Molecular Spectroscopy* **1996**, *178*, 66.

(3) Ervin, K. M.; Anusiewicz, W.; Skurski, P.; Simons, J.; Lineberger, W. C. *Journal of Physical Chemistry A* **2003**, *107*, 8521.

(4) Aquino, A. J. A.; Taylor, P. R.; Walch, S. P. *Journal of Chemical Physics* **2001**, *114*, 3010.

(5) Sommerfeld, T.; Knecht, S. *European Physical Journal D* **2005**, *35*, 207.

(6) Goebbert, D. J.; Velarde, L.; Khuseynov, D.; Sanov, A. *Journal of Physical Chemistry Letters* **2010**, *1*, 792.

(7) Goebbert, D. J.; Pichugin, K.; Khuseynov, D.; Wenthold, P. G.; Sanov, A. *Journal of Chemical Physics* **2010**, *132*, 224301.

(8) Wren, S. W.; Vogelhuber, K. M.; Ervin, K. M.; Lineberger, W. C. *Physical Chemistry Chemical Physics* **2009**, *11*, 4745.

(9) Milian, B.; Pou-Amerigo, R.; Viruela, R.; Orti, E. *Chemical Physics Letters* **2003**, *375*, 376.

(10) Milian, B.; Pou-Amerigo, R.; Merchan, M.; Orti, E. *ChemPhysChem* **2005**, *6*, 503.

(11) Pichugin, K. Electronic Structure and Reaction Dynamics of Molecular and Cluster Anions via Photoelectron Imaging. Ph.D. dissertation, University of Arizona, 2010.

(12) Fleming, G. R.; Wolynes, P. G. *Physics Today* **1990**, *43*, 36.

(13) Castleman, A. W.; Bowen, K. H. *Journal Of Physical Chemistry* **1996**, *100*, 12911.

(14) Velarde, L. Ph. D. dissertation. Ph.D. dissertation, University of Arizona, 2008.

(15) Sanov, A.; Mabbs, R. *International Reviews in Physical Chemistry* **2008**, *27*, 53.

(16) Young, R. M.; Yandell, M. A.; King, S. B.; Neumark, D. M. *Journal of Chemical Physics* **2012**, *136*.

(17) Young, R. M.; Yandell, M. A.; Neumark, D. M. *Journal of Chemical Physics* **2011**, *134*.

(18) Young, R. M.; Neumark, D. M. *Chemical Reviews* **2012**, *112*, 5553.

(19) Goebbert, D. J.; Sanov, A. *Journal of Chemical Physics* **2009**, *131*, 104308.

(20) Grumbling, E.; Sanov, A. *Journal of Chemical Physics* **2011**, *135*, 164301.

(21) Grumbling, E. R.; Sanov, A. *Journal of Chemical Physics* **2011**, *135*.

(22) Mabbs, R.; Surber, E.; Velarde, L.; Sanov, A. *Journal of Chemical Physics* **2004**, *120*, 5148.

(23) Pichugin, K.; Grumbling, E.; Velarde, L.; Sanov, A. *Journal of Chemical Physics* **2008**, *129*, 044311.

(24) Chandler, D. W.; Houston, P. L. *Journal of Chemical Physics* **1987**, *87*, 1445.

(25) Heck, A. J. R.; Chandler, D. W. *Annual Review of Physical Chemistry* **1995**, *46*, 335.

(26) Eppink, A. T. J. B.; Parker, D. H. *Review of Scientific Instruments* **1997**, *68*, 3477.

(27) Parker, D. H.; Eppink, A. T. J. B. *Journal Of Chemical Physics* **1997**, *107*, 2357.

(28) Mabbs, R.; Surber, E.; Sanov, A. *Analyst* **2003**, *128*, 765.

(29) Cooper, J.; Zare, R. N. *J. Chem. Phys.* **1968**, *48*, 942.

(30) Cooper, J.; Zare, R. N. *J. Chem. Phys.* **1968**, *49*, 4252.

(31) Cooper, J.; Zare, R. N. Photoelectron angular distributions. In *Atomic collision processes*; Geltman, S., Mahanthappa, K. T., Brittin, W. E., Eds.; Gordon and Breach, Science Publishers: New York, London, Paris, 1968; Vol. XI-C; pp 317.

(32) Surber, E.; Mabbs, R.; Sanov, A. *J. Phys. Chem. A* **2003**, *107*, 8215.

(33) Mabbs, R.; Grumbling, E. R.; Pichugin, K.; Sanov, A. *Chemical Society Reviews* **2009**, *38*, 2169.

(34) Sanov, A. *Annual Review of Physical Chemistry* **2014**, *65*, 341.

(35) Johnson, M. A.; Lineberger, W. C. Pulsed Methods for Cluster Ion Spectroscopy. In *Techniques for the Study of Ion Molecule Reactions*; Farrar, J. M., Saunders, W. H., Eds.; Wiley: New York, 1988; pp 591.

(36) Alexander, M. L.; Levinger, N. E.; Johnson, M. A.; Ray, D.; Lineberger, W. C. *Journal of Chemical Physics* **1988**, *88*, 6200.

(37) Velarde, L.; Habteyes, T.; Sanov, A. *Journal of Chemical Physics* **2006**, *125*, 114303.

(38) Posey, L. A.; DeLuca, M. J.; Johnson, M. A. *Chemical Physics Letters* **1986**, *131*, 170.

(39) Surber, E. Photoelectron imaging of molecular and cluster anions. Ph.D. dissertation, University of Arizona, 2005.

(40) Dribinski, V.; Ossadtchi, A.; Mandelshtam, V. A.; Reisler, H. *Review of Scientific Instruments* **2002**, *73*, 2634.

(41) Neumark, D. M.; Lykke, K. R.; Andersen, T.; Lineberger, W. C. *Physical Review A* **1985**, *32*, 1890.

(42) Cavanagh, S. J.; Gibson, S. T.; Gale, M. N.; Dedman, C. J.; Roberts, E. H.; Lewis, B. R. *Physical Review A* **2007**, *76*, 052708.

(43) Sanov, A.; Lineberger, W. C. *PhysChemComm* **2002**, *5*, 165.

(44) Sanov, A.; Lineberger, W. C. *Physical Chemistry Chemical Physics* **2004**, *6*, 2018.

(45) DeLuca, M. J.; Han, C.-C.; Johnson, M. A. *Journal of Chemical Physics* **1990**, *93*, 268.

(46) Sherwood, C. R.; Garner, M. C.; Hanold, K. A.; Strong, K. M.; Continetti, R. E. *Journal Of Chemical Physics* **1995**, *102*, 6949.

(47) Sherwood, C. R.; Continetti, R. E. *Chemical Physics Letters* **1996**, *258*, 171.

(48) Sherwood, C. R.; Hanold, K. A.; Garner, M. C.; Strong, K. M.; Continetti, R. E. *Journal Of Chemical Physics* **1996**, *105*, 10803.

(49) Hanold, K. A.; Continetti, R. E. *Chemical Physics* **1998**, *239*, 493.

(50) Li, R. J.; Hanold, K. A.; Garner, M. C.; Luong, A. K.; Continetti, R. E. *Faraday Discussions* **1997**, *108*, 115.

(51) Hanold, K. A.; Luong, A. K.; Continetti, R. E. *Journal of Chemical Physics* **1998**, *109*, 9215.

(52) Antonchenko, V. Y.; Kryachko, E. S. *Journal of Physical Chemistry A* **2005**, *109*, 3052.

(53) Conway, D. C. *Journal of Chemical Physics* **1969**, *50*, 3864.

(54) Hiraoka, K. *Journal of Chemical Physics* **1988**, *89*, 3190.

(55) Bopp, J. C.; Alexandrova, A. N.; Elliott, B. M.; Herden, T.; Johnson, M. A. *International Journal of Mass Spectrometry* **2009**, *283*, 94.

(56) Grumbling, E. R.; Mabbs, R.; Sanov, A. *Journal of Chemical Education* **in press**.

(57) Akin, F. A.; Schirra, L. K.; Sanov, A. *Journal of Physical Chemistry A* **2006**, *110*, 8031.

(58) Mabbs, R.; Mbaiwa, F.; Wei, J.; Van Duzor, M.; Gibson, S. T.; Cavanagh, S. J.; Lewis, B. R. *Physical Review A* **2010**, *82*, 011401.

(59) Van Duzor, M.; Mbaiwa, F.; Wei, J.; Singh, T.; Mabbs, R.; Sanov, A.; Cavanagh, S. J.; Gibson, S. T.; Lewis, B. R.; Gascooke, J. R. *Journal of Chemical Physics* **2010**, *133*, 174311.

(60) Clements, T. G.; Continetti, R. E. *Physical Review Letters* **2002**, *89*, 033005.

(61) Kelley, J. A.; Robertson, W. H.; Johnson, M. A. *Chemical Physics Letters* **2002**, *362*, 255.

(62) Hanold, K. A.; Sherwood, C. R.; Continetti, R. E. *Journal Of Chemical Physics* **1995**, *103*, 9876.

(63) Nandi, S.; Sanov, A.; Delaney, N.; Faeder, J.; Parson, R.; Lineberger, W. C. *Journal of Physical Chemistry A* **1998**, *102*, 8827.

(64) Sanov, A.; Sanford, T.; Nandi, S.; Lineberger, W. C. *Journal of Chemical Physics* **1999**, *111*, 664.

(65) Delaney, N.; Faeder, J.; Parson, R. *Journal of Chemical Physics* **1999**, *111*, 651.

(66) Sheps, L.; Miller, E. M.; Horvath, S.; Thompson, M. A.; Parson, R.; McCoy, A. B.; Lineberger, W. C. *Science* **2010**, *328*, 220.

(67) Sheps, L.; Miller, E. M.; Horvath, S.; Thompson, M. A.; Parson, R.; McCoy, A. B.; Lineberger, W. C. *Journal of Chemical Physics* **2011**, *134*, 184311.

(68) Brooks, P. R.; Harland, P. W.; Redden, C. E. *Journal of the American Chemical Society* **2006**, *128*, 4773.

(69) Brooks, P. R.; Harland, P. W.; Redden, C. E. *Journal of Physical Chemistry A* **2006**, *110*, 4697.

(70) Compton, R. N.; Carman, H. S.; Desfrancois, C.; Abdoulcarmine, H.; Schermann, J. P.; Hendricks, J. H.; Lyapustina, S. A.; Bowen, K. H. *Journal Of Chemical Physics* **1996**, *105*, 3472.

(71) Walker, I. C.; Fluendy, M. A. D. *International Journal of Mass Spectrometry* **2001**, *205*, 171.

(72) Stockdale, J. A.; Davis, F. J.; Compton, R. N.; Klots, C. E. *J. Chem. Phys.* **1974**, *60*, 4279.

(73) Compton, R. N.; Reinhardt, P. W.; Cooper, C. D. *J. Chem. Phys.* **1978**, *68*, 4360.

(74) Adams, C. L.; Schneider, H.; Ervin, K. M.; Weber, J. M. *Journal of Chemical Physics* **2009**, *130*, 074307.

(75) Goebbert, D. J.; Pichugin, K.; Sanov, A. *Journal of Chemical Physics* **2009**, *131*, 164308.

(76) Sommerfeld, T. *Physical Chemistry Chemical Physics* **2002**, *4*, 2511.

(77) Alizadeh, E.; Ferreira da Silva, F.; Zappa, F.; Mauracher, A.; Probst, M.; Denfil, S.; Bacher, A.; Maerk, T. D.; Limao-Viera, P.; Scheier, P. *International Journal of Mass Spectrometry and Ion Processes* **2008**, *271*, 15.

(78) Sailer, W.; Pelc, A.; Matejcik, S.; Illenberger, E.; Scheier, P.; Maerk, T. D. *J. Chem. Phys.* **2002**, *117*, 7989.

(79) Wincel, H. *International Journal of Mass Spectrometry* **2003**, *226*, 341.

(80) Dessent, C. E. H.; Kim, J.; Johnson, M. A. *Faraday Discussions* **2000**, *115*, 395.

(81) Nakanishi, R.; Nagata, T. *Journal of Chemical Physics* **2009**, *130*, 224309.

(82) Bull, J. N.; Maclagan, R. G. A. R.; Harland, P. W. *Journal of Physical Chemistry A* **2010**, *114*, 3622.

(83) Gutsev, G. L.; Jena, P.; Bartlett, R. J. *Journal of Chemical Physics* **1999**, *110*, 403.

(84) Arenas, J. F.; Otero, J. C.; Pelaez, D.; Soto, J.; Serrano-Andres, L. *Journal of Chemical Physics* **2004**, *121*, 4127.

(85) Guo, Y. Q.; Bhattacharya, A.; Bernstein, E. R. *Journal of Physical Chemistry A* **2009**, *113*, 85.

(86) Butler, L. J.; Krajnovich, D.; Lee, Y. T.; Ondrey, G.; Bersohn, R. *Journal of Chemical Physics* **1983**, *79*, 1708.

(87) Kwok, H. S.; He, G. Z.; Sparks, R. K.; Lee, Y. T. *International Journal of Chemical Kinetics* **1981**, *13*, 1125.

(88) Moss, D. B.; Trentelman, K. A.; Houston, P. L. *J. Chem. Phys.* **1992**, *96*, 237.

(89) Blais, N. C. *J. Chem. Phys.* **1983**, *79*, 1723.

(90) Frisch, M. J.; Trucks, G. W.; Schlegel, H. B.; Scuseria, G. E.; Robb, M. A.; Cheeseman, J. R.; Montgomery, J. J. A.; Vreven, T.; Kudin, K. N.; Burant, J. C.; Millam, J. M.; Iyengar, S. S.; Tomasi, J.; Barone, V.; Mennucci, B.; Cossi, M.; Scalmani, G.; Rega, N.; Petersson, G. A.; Nakatsuji, H.; Hada, M.; Ehara, M.; Toyota, K.; Fukuda, R.; Hasegawa, J.; Ishida, M.; Nakajima, T.; Honda, Y.; Kitao, O.; Nakai, H.; Klene, M.; Li, X.; Knox, J. E.; Hratchian, H. P.; Cross, J. B.; Bakken, V.; Adamo, C.; Jaramillo, J.; Gomperts, R.; Stratmann, R. E.; Yazyev, O.; Austin, A. J.; Cammi, R.; Pomelli, C.; Ochterski, J. W.; Ayala, P. Y.; Morokuma, K.; Voth, G. A.; Salvador, P.; Dannenberg, J. J.; Zakrzewski, V. G.; Dapprich, S.; Daniels, A. D.; Strain, M. C.; Farkas, O.; Malick, D. K.; Rabuck, A. D.; Raghavachari, K.; Foresman, J. B.; Ortiz, J. V.; Cui, Q.; Baboul, A. G.; Clifford, S.; Cioslowski, J.; Stefanov, B. B.; Liu, G.; Liashenko, A.; Piskorz, P.; Komaromi, I.; Martin, R. L.; Fox, D. J.; Keith, T.; Al-Laham, M. A.; Peng, C. Y.; Nanayakkara, A.; Challacombe, M.; Gill, P. M. W.; Johnson, B.; Chen, W.; Wong, M.

W.; Gonzalez, C.; Pople, J. A. Gaussian 03; Rev. B.01 ed.; Gaussian, Inc.: Wallingford CT, 2004.

(91) Stratmann, R. E.; Scuseria, G. E.; Frisch, M. J. *J Chem Phys* **1998**, *109*, 8218.

(92) Bauernschmitt, R.; Ahlrichs, R. *Chem Phys Lett* **1996**, *256*, 454.

(93) Casida, M. E.; Jamorski, C.; Casida, K. C.; Salahub, D. R. *J Chem Phys* **1998**, *108*, 4439.

(94) Nadal, M. E.; Kleiber, P. D.; Lineberger, W. C. *Journal Of Chemical Physics* **1996**, *105*, 504.

(95) Vorsa, V.; Campagnola, P. J.; Nandi, S.; Larsson, M.; Lineberger, W. C. *Journal Of Chemical Physics* **1996**, *105*, 2298.

(96) Vorsa, V.; Nandi, S.; Campagnola, P. J.; Larsson, M.; Lineberger, W. C. *Journal of Chemical Physics* **1997**, *106*, 1402.

(97) Sanov, A.; Nandi, S.; Jordan, K. D.; Lineberger, W. C. *Journal of Chemical Physics* **1998**, *109*, 1264.

(98) Sanford, T.; Han, S. Y.; Thompson, M. A.; Parson, R.; Lineberger, W. C. *Journal of Chemical Physics* **2005**, *122*, 054307.

(99) Habteyes, T.; Velarde, L.; Sanov, A. *Chemical Physics Letters* **2006**, *424*, 268.

(100) Zadoyan, R.; Li, Z.; Martens, C. C.; Apkarian, V. A. *Journal of Chemical Physics* **1994**, *101*, 6648.

(101) Arenas, J. F.; Otero, J. C.; Peláez, D.; Soto, J. *Journal of Chemical Physics* **2005**, *122*, 084324.

(102) Wodtke, A. M.; Hintsa, E. J.; Lee, Y. T. *J. Phys. Chem.* **1986**, *90*, 3549.

(103) Arenas, J. F.; Otero, J. C.; Pelaez, D.; Soto, J. *Journal of Chemical Physics* **2003**, *119*, 7814.

(104) McMillen, D. F.; Golden, D. M. *Annual Review of Physical Chemistry* **1982**, *33*, 493.

(105) Ervin, K. M.; Ho, J.; Lineberger, W. C. *Journal of Physical Chemistry* **1988**, *92*, 5405.

(106) Lykke, K. R.; Murray, K. K.; Neumark, D. M.; Lineberger, W. C. *Phil. Trans. R. Soc. Lond. A* **1988**, *324*, 179.

(107) Burnett, S. M.; Stevens, A. E.; Feigerle, C. S.; Lineberger, W. C. *Chemical Physics Letters* **1983**, *100*, 124.

(108) Ervin, K. M.; Ho, J.; Lineberger, W. C. *Journal of Chemical Physics* **1989**, *91*, 5974.

(109) Carrington, T.; Hubbard, L. M.; Schaefer, H. F.; Miller, W. H. *Journal of Chemical Physics* **1984**, *80*, 4347.

(110) Dykstra, C. E.; Schaefer, H. F. *Journal of the American Chemical Society* **1978**, *100*, 1378.

(111) Conrad, M. P.; Schaefer, H. F. *Journal of the American Chemical Society* **1978**, *100*, 7820.

(112) Osamura, Y.; Schaefer, H. F.; Gray, S. K.; Miller, W. H. *Journal of the American Chemical Society* **1981**, *103*, 1904.

(113) Gallo, M. M.; Hamilton, T. P.; Schaefer, H. F. *Journal of the American Chemical Society* **1990**, *112*, 8714.

(114) Hu, C. H.; Schaefer, H. F. *Journal of Physical Chemistry* **1993**, *97*, 10681.

(115) Gilles, M. K.; Lineberger, W. C.; Ervin, K. M. *Journal of the American Chemical Society* **1993**, *115*, 1031.

(116) Gunion, R. F.; Koppel, H.; Leach, G. W.; Lineberger, W. C. *Journal of Chemical Physics* **1995**, *103*, 1250.

(117) Gunion, R. F.; Lineberger, W. C. *Journal Of Physical Chemistry* **1996**, *100*, 4395.

(118) Deleeuw, B. J.; Fermann, J. T.; Xie, Y. M.; Schaefer, H. F. *Journal of the American Chemical Society* **1993**, *115*, 1039.

(119) Collins, C. L.; Hu, C. H.; Yamaguchi, Y.; Schaefer, H. F. *Israel Journal of Chemistry* **1993**, *33*, 317.

(120) Goebbert, D. J.; Khuseynov, D.; Sanov, A. *Journal of Chemical Physics* **2009**, *131*, 161102.

(121) Graupner, K.; Merrigan, T. L.; Field, T. A.; Youngs, T. G. A.; Marr, P. C. *New Journal of Physics* **2006**, *8*, 117.

(122) Kolos, R.; Gronowski, M.; Botschwina, P. *Journal of Chemical Physics* **2008**, *128*, 154305.

(123) Thaddeus, P.; Gottlieb, C. A.; Gupta, H.; Brunken, S.; McCarthy, M. C.; Agundez, M.; Guelin, M.; Cernicharo, J. *Astrophysical Journal* **2008**, *677*, 1132.

(124) Botschwina, P.; Oswald, R. *Journal of Chemical Physics* **2008**, *129*, 044305.

(125) Kolos, R.; Gronowski, M.; Dobrowolski, J. C. *Astrophysical Journal* **2009**, *701*, 488.

(126) Dawson, J. H. J.; Nibbering, N. M. M. *Int. J. Mass Spectrom. and Ion Physics* **1980**, *33*, 3.

(127) Heni, M.; Illenberger, E. *Int. J. Mass Spectrom. and Ion Processes* **1986**, *73*, 127.

(128) Duschinsky, F. *Acta Physicochimica Urss* **1937**, *7*, 551.

(129) Dawson, J. H. J.; Jennings, K. R. *Journal of the Chemical Society-Faraday Transactions II* **1976**, *72*, 700.

(130) Frisch, M. J.; Trucks, G. W.; Schlegel, H. B.; Scuseria, G. E.; Robb, M. A.; Cheeseman, J. R.; Montgomery, J. J. A.; Vreven, T.; Kudin, K. N.; Burant, J. C.; Millam, J. M.; Iyengar, S. S.; Tomasi, J.; Barone, V.; Mennucci, B.; Cossi, M.; Scalmani, G.; Rega, N.; Petersson, G. A.; Nakatsuji, H.; Hada, M.; Ehara, M.; Toyota, K.; Fukuda, R.; Hasegawa, J.; Ishida, M.; Nakajima, T.; Honda, Y.; Kitao, O.; Nakai, H.; Klene, M.; Li, X.; Knox, J. E.; Hratchian, H. P.; Cross, J. B.; Bakken, V.; Adamo, C.; Jaramillo, J.; Gomperts, R.; Stratmann, R. E.; Yazyev, O.; Austin, A. J.; Cammi, R.; Pomelli, C.; Ochterski, J. W.; Ayala, P. Y.; Morokuma, K.; Voth, G. A.; Salvador, P.; Dannenberg, J. J.; Zakrzewski, V. G.; Dapprich, S.; Daniels, A. D.; Strain, M. C.; Farkas, O.; Malick, D. K.; Rabuck, A. D.; Raghavachari, K.; Foresman, J. B.; Ortiz, J. V.; Cui, Q.; Baboul, A. G.; Clifford, S.; Cioslowski, J.; Stefanov, B. B.; Liu, G.; Liashenko, A.; Piskorz, P.; Komaromi, I.; Martin, R. L.; Fox, D. J.; Keith, T.; Al-Laham, M. A.; Peng, C. Y.; Nanayakkara, A.; Challacombe, M.; Gill, P. M. W.; Johnson, B.; Chen, W.; Wong, M. W.; Gonzalez, C.; and Pople, J. A. Gaussian 03, Revision C.02; Gaussian, Inc.: Wallingford CT, 2004.

(131) Kohn, D. W.; Robles, E. S. J.; Logan, C. F.; Chen, P. *Journal of Physical Chemistry* **1993**, *97*, 4936.

(132) Sharp, T. E.; Rosenstock, H. M. *Journal of Chemical Physics* **1964**, *41*, 3453.

(133) Ervin, K. M.; Ramond, T. M.; Davico, G. E.; Schwartz, R. L.; Casey, S. M.; Lineberger, W. C. *Journal of Physical Chemistry A* **2001**, *105*, 10822.

(134) Bowen, M. S.; Continetti, R. E. *Journal of Physical Chemistry A* **2004**, *108*, 7827.

(135) Oana, C. M.; Krylov, A. I. *Journal of Chemical Physics* **2009**, *131*, 124114.

(136) Blanksby, S. J.; Ellison, G. B. *Accounts of Chemical Research* **2003**, *36*, 255.

(137) Moran, S.; Ellis Jr., H. E.; DeFrees, D. J.; McLean, A. D.; Ellison, G. B. *J. Am. Chem. Soc.* **1987**, *109*, 5996.

(138) Bickelhaupt, F. M.; Ziegler, T.; Schleyer, P. V. *Organometallics* **1996**, *15*, 1477.

(139) Blanksby, S. J.; Ellison, G. B. *Accounts of Chemical Research* **2003**, *36*, 255.

(140) Wagman, D. D.; Evans, W. H.; Parker, V. B.; Schumm, R. H.; Halow, I.; Bailey, S. M.; Churney, K. L.; Nuttall, R. L. *J. Phys. Chem. Ref. Data, Supl. 1* **1982**, 11.

(141) Ervin, K. M. *Chem. Rev.* **2001**, *101*, 391.

(142) Fujio, M.; McIver, R. T.; Taft, R. W. *J. Am. Chem. Soc.* **1981**, *103*, 4017.

(143) Bartmess, J. E.; Scott, J. A.; McIver, R. T. *J. Am. Chem. Soc.* **1979**, *101*, 6047.

(144) Bartmess, J. E. "Negative Ion Energetics Data". In *NIST Chemistry WebBook, NIST Standard Reference Database Number 69*; Linstrom, P. J., Mallard, W. G., Eds.; National Institute of Standards and Technology: Gaithersburg MD, 20899, http://webbook.nist.gov (retrieved January 12, 2010), 2009.

(145) Luo, Y.-R. *Handbook of Bond Dissociation Energies in Organic Compounds*; CRC Press: Boca Raton, Florida, 2003.

(146) Bak, B.; Svanholt, H. *J. Mol. Struct.* **1977**, *37*, 153.

(147) Bak, B.; Bjorkman, C. *J. Mol. Struct.* **1975**, *25*, 131.

(148) Cox, J. D.; Wagman, D. D.; Medvedev, V. A. *CODATA Key Values for Thermodynamics*; Hemisphere Publishing Corp.: New York, 1984.

(149) Beckhaus, H. D.; Dogan, B.; Pakusch, J.; Verekin, S.; Ruechardt, C. *Chem. Ber.* **1990**, *123*, 2153.

(150) An, X.; Mansson, M. *J. Chem. Thermodyn.* **1983**, *15*, 287.

(151) King, K. D.; Goddard, R. D. *Int. J. Chem. Kinet.* **1975**, *7*, 837.

(152) Engelking, P. C.; Corderman, R. R.; Wendoloski, J. J.; Ellison, G. B.; ONeil, S. V.; Lineberger, W. C. *Journal of Chemical Physics* **1981**, *74*, 5460.

(153) Leopold, D. G.; Murray, K. K.; Miller, A. E. S.; Lineberger, W. C. *Journal of Chemical Physics* **1985**, *83*, 4849.

(154) Rauk, A. *Orbital Interaction Theory of Organic Chemistry*; John Wiley & Sons Inc.: New York, NY, 1994.

(155) Schwartz, R. L.; Davico, G. E.; Ramond, T. M.; Lineberger, W. C. *Journal of Physical Chemistry A* **1999**, *103*, 8213.

(156) Tomioka, H. *Acc. Chem. Res.* **1997**, *30*, 315.

(157) Bowling, N. P.; Halter, R. J.; Hodges, J. A.; Seburg, R. A.; Thomas, P. S.; Simmons, C. S.; Stanton, J. F.; McMahon, R. J. *Journal of the American Chemical Society* **2006**, *128*, 3291.

(158) Thomas, P. S.; Bowling, N. P.; McMahon, R. J. *Journal of the American Chemical Society* **2009**, *131*, 8649.

(159) Nimlos, M. R.; Davico, G.; Geise, C. M.; Wenthold, P. G.; Lineberger, W. C.; Blanksby, S. J.; Hadad, C. M.; Petersson, G. A.; Ellison, G. B. *Journal of Chemical Physics* **2002**, *117*, 4323.

(160) Kalcher, J. *Chem. Phys. Lett.* **2005**, *403*, 146.

(161) Morter, C. L.; Farhat, S. K.; Curl, R. F. *Chem Phys Lett* **1993**, *207*, 153.

(162) Bernheim, R. A.; Kempf, R. J.; Reichenbecher, E. F. *J Magetic Resonance* **1970**, *3*, 5.

(163) Bernheim, R. A.; Kempf, R. J.; Gramas, J. V.; Skell, P. S. *J Chem Phys* **1965**, *43*, 196.

(164) Bernheim, R. A.; Kempf, R. J.; Humer, P. W.; Skell, P. S. *J Chem Phys* **1964**, *41*, 1156.

(165) Wasserman, E.; Yager, W. A.; Kuck, V. J. *Chem Phys Lett* **1970**, *7*, 409.

(166) Kim, K. S.; Schaefer III, H. F.; Radom, L.; Pople, J. A.; Binkley, J. S. *J Am Chem Soc* **1983**, *105*, 4148.

(167) Poutsma, J. C.; Upshaw, S. D.; Squires, R. R.; Wenthold, P. G. *J Phys Chem A* **2002**, *106*, 1067.

(168) Wasserman, E.; Barash, L.; Yager, W. A. *Journal of the American Chemical Society* **1965**, *87*, 2075.

(169) Dunkin, I. R.; McCluskey, A. *Spectrochimica Acta* **1994**, *54*, 209.

(170) Blanksby, S. J.; Dua, S.; Bowie, J. H.; Schroeder, D.; Schwarz, H. *J. Phys. Chem. A* **2000**, *104*, 11248.

(171) Hajgato, B.; Flamming, R.; Veszpremi, T.; Nguyen, M. T. *Mol. Phys.* **2002**, *100*, 1693.

(172) Maier, G.; Reisenauer, H. P.; Ruppel, R. *Eur. J. Org. Chem.* **2003**, *2003*, 2695.

(173) Lucchese, R. R.; Schaefer, H. F. *J. Am. Chem. Soc.* **1977**, *99*, 13.

(174) Valli, C.; Blondel, C.; Delsart, C. *Physical Review A* **1999**, *59*, 3809.

(175) Levchenko, S. V.; Krylov, A. I. *J Chem Phys* **2004**, *120*, 175.

(176) Krylov, A. I. *Chem Phys Lett* **2001**, *338*, 522.

(177) Slipchenko, L. V.; Krylov, A. I. *Journal of Chemical Physics* **2005**, *123*, 084107.

(178) Levchenko, S. V.; Reisler, H.; Krylov, A. I.; Gessner, O.; Stolow, A.; Shi, H. C.; East, A. L. L. *Journal of Chemical Physics* **2006**, *125*, 084301.

(179) Slipchenko, L. V.; Krylov, A. I. *Journal of Chemical Physics* **2002**, *117*, 4694.

(180) Shao, Y.; Fusti-Molnar, L.; Jung, Y.; Kussmann, J.; Ochsenfeld, C.; Brown, S. T.; Gilbert, A. T. B.; Slipchenko, L. V.; Levchenko, S. V.; O'Neill, D. P.; Distasio Jr., R. A.; Lochan, R. C.; Wang, T.; Beran, G. J. O.; Besley, N. A.; Herbert, J. M.; Lin, C. Y.; Van Voorhis, T.; Chien, S. H.; Sodt, A.; Steele, R. P.; Rassolov, V. A.; Maslen, P. E.; Korambath, P. P.; Adamson, R. D.; Austin, B.; Baker, J.; Byrd, E. F. C.;

Dachsel, H.; Doerksen, R. J.; Dreuw, A.; Dunietz, B. D.; Dutoi, A. D.; Furlani, T. R.; Gwaltney, S. R.; Heyden, A.; Hirata, S.; Hsu, C.-P.; Kedziora, G.; Khalliulin, R. Z.; Klunzinger, P.; Lee, A. M.; Lee, M. S.; Liang, W.; Lotan, I.; Nair, N.; Peters, B.; Proynov, E. I.; Pieniazek, P. A.; Rhee, Y. M.; Ritchie, J.; Rosta, E.; Sherrill, C. D.; Simmonett, A. C.; Subotnik, J. E.; Woodcock III, H. L.; Zhang, W.; Bell, A. T.; Chakraborty, A. K.; Chipman, D. M.; Keil, F. J.; Warshel, A.; Hehre, W. J.; Schaefer III, H. F.; Kong, J.; Krylov, A. I.; Gill, P. M. W.; Head-Gordon, M. *Phys Chem Chem Phys* **2006**, *8*, 3172.

(181) Although the open-shell singlet in NCCCN is calculated to be linear, the state can be bent in other systems, including methylene, CH2.

(182) Hrovat, D. A.; Borden, W. T. *private communication*.

(183) Wijeratne, N. R.; Da Fonte, M.; Ronemus, A.; Wyss, P. J.; Tahmassebi, D.; Wenthold, P. G. *J Phys Chem A* **2009**, *113*, 9467.

(184) Goebbert, D. J.; Khuseynov, D.; Sanov, A. *Journal of Physical Chemistry A* **2010**, *114*, 2259.

(185) Deyerl, H. J.; Alconcel, L. S.; Continetti, R. E. *Journal of Physical Chemistry a* **2001**, *105*, 552.

(186) Menon, A. S.; Henry, D. J.; Bally, T.; Radom, L. *Organic & Biomolecular Chemistry* **2011**, *9*, 3636.

(187) Tomioka, H. *Accounts of Chemical Research* **1997**, *30*, 315.

(188) Gilles, M. K.; Ervin, K. M.; Ho, J.; Lineberger, W. C. *Journal Of Physical Chemistry* **1992**, *96*, 1130.

(189) Harrison, A. G.; Jennings, K. R. *Journal of the Chemical Society-Faraday Transactions I* **1976**, *72*, 1601.

(190) Lee, J.; Grabowski, J. J. *Chemical Reviews* **1992**, *92*, 1611.

(191) Vogelhuber, K. M.; Wren, S. W.; McCoy, A. B.; Ervin, K. M.; Lineberger, W. C. *Journal of Chemical Physics* **2011**, *134*, 184306.

(192) Wiley, W. C.; McLaren, I. H. *Review of Scientific Instruments* **1955**, *26*, 1150.

(193) Hiraoka, K.; Fujimaki, S.; Aruga, K.; Yamabe, S. *Journal of Physical Chemistry* **1994**, *98*, 8295.

(194) Grumbling, E. R.; Pichugin, K.; Velarde, L.; Sanov, A. *Journal of Physical Chemistry A* **2010**, *114*, 1367.

(195) Frisch, M. J.; Trucks, G. W.; Schlegel, H. B.; Scuseria, G. E.; Robb, M. A.; Cheeseman, J. R.; Scalmani, G.; Barone, V.; Mennucci, B.; Petersson, G. A.; Nakatsuji, H.; Caricato, M.; Li, X.; Hratchian, H. P.; Izmaylov, A. F.; Bloino, J.; Zheng, G.; Sonnenberg, J. L.; Hada, M.; Ehara, M.; Toyota, K.; Fukuda, R.; Hasegawa, J.; Ishida, M.; Nakajima, T.; Honda, Y.; Kitao, O.; Nakai, H.; Vreven, T.; Montgomery, J., J. A.; Peralta, J. E.; Ogliaro, F.; Bearpark, M.; Heyd, J. J.; Brothers, E.; Kudin, K. N.; Staroverov, V. N.; Kobayashi, R.; Normand, J.; Raghavachari, K.; Rendell, A.; Burant, J. C.; Iyengar, S. S.; Tomasi, J.; Cossi, M.; Rega, N.; Millam, N. J.; Klene, M.; Knox, J. E.; Cross, J. B.; Bakken, V.; Adamo, C.; Jaramillo, J.; Gomperts, R.; Stratmann, R. E.; Yazyev, O.; Austin, A. J.; Cammi, R.; Pomelli, C.; Ochterski, J. W.; Martin, R. L.; Morokuma, K.; Zakrzewski, V. G.; Voth, G. A.; Salvador, P.; Dannenberg, J. J.; Dapprich, S.; Daniels, A. D.; Farkas, Ö.; Foresman, J. B.; Ortiz, J. V.; Cioslowski, J.; Fox, D. J. Gaussian 09; Revision A.1 ed.; Gaussian, Inc.: Wallingford, CT, 2009.

(196) Levchenko, S. V.; Krylov, A. I. *Journal of Chemical Physics* **2004**, *120*, 175.

(197) Krylov, A. I. *Annual Review of Physical Chemistry* **2008**, *59*, 433.

(198) Manohar, P. U.; Krylov, A. I. *Journal of Chemical Physics* **2008**, *129*, 194105.

(199) Shao, Y.; Molnar, L. F.; Jung, Y.; Kussmann, J.; Ochsenfeld, C.; Brown, S. T.; Gilbert, A. T. B.; Slipchenko, L. V.; Levchenko, S. V.; O'Neill, D. P.; DiStasio, R. A.; Lochan, R. C.; Wang, T.; Beran, G. J. O.; Besley, N. A.; Herbert, J. M.; Lin, C. Y.; Van Voorhis, T.; Chien, S. H.; Sodt, A.; Steele, R. P.; Rassolov, V. A.; Maslen, P. E.; Korambath, P. P.; Adamson, R. D.; Austin, B.; Baker, J.; Byrd, E. F. C.; Dachsel, H.; Doerksen, R. J.; Dreuw, A.; Dunietz, B. D.; Dutoi, A. D.; Furlani, T. R.; Gwaltney, S. R.; Heyden, A.; Hirata, S.; Hsu, C. P.; Kedziora, G.; Khalliulin, R. Z.; Klunzinger, P.; Lee, A. M.; Lee, M. S.; Liang, W.; Lotan, I.; Nair, N.; Peters, B.; Proynov, E. I.; Pieniazek, P. A.; Rhee, Y. M.; Ritchie, J.; Rosta, E.; Sherrill, C. D.; Simmonett, A. C.; Subotnik, J. E.; Woodcock, H. L.; Zhang, W.; Bell, A. T.; Chakraborty, A. K.; Chipman, D. M.; Keil, F. J.; Warshel, A.; Hehre, W. J.; Schaefer, H. F.; Kong, J.; Krylov, A. I.; Gill, P. M. W.; Head-Gordon, M. *Physical Chemistry Chemical Physics* **2006**, *8*, 3172.

(200) Wigner, E. P. *Physical Review* **1948**, *73*, 1002.

(201) Mead, R. D.; Lykke, K. R.; Lineberger, W. C. Photodetachment Threshold Laws. In *Electronic and Atomic Collisions*; Eichler, J., Hertel, I. V., Stolterfoht, N., Eds.; Elsevier, 1984; pp 721.

(202) Surber, E.; Sanov, A. *Phys. Rev. Lett.* **2003**, *90*, 093001.

(203) Surber, E.; Sanov, A. *J. Chem. Phys.* **2003**, *118*, 9192.

(204) Feller, D.; Peterson, K. A. *Journal of Chemical Physics* **2007**, *126*, 114105.

(205) Goebbert, D. J.; Khuseynov, D.; Sanov, A. *Journal of Physical Chemistry A* **2011**, *115*, 3208.

(206) Poutsma, J. C.; Upshaw, S. D.; Squires, R. R.; Wenthold, P. G. *Journal of Physical Chemistry A* **2002**, *106*, 1067.

(207) Moran, S.; Ellis, H. B.; Defrees, D. J.; Mclean, A. D.; Ellison, G. B. *Journal of the American Chemical Society* **1987**, *109*, 5996.

(208) Viehe, H. G.; Janousek, Z.; Merenyi, R.; Stella, L. *Accounts of Chemical Research* **1985**, *18*, 148.

(209) Sanov, A.; Grumbling, E. R.; Goebbert, D. J.; Culberson, L. M. *Journal of Chemical Physics* **2013**, *138*, 054311.

(210) A positive sign of ΔE_{S-T} corresponds to the triplet lying above the singlet (i.e., the singlet is the ground state).

(211) Gronert, S.; Keeffe, J. R.; O'Ferrall, R. A. M. *Journal of the American Chemical Society* **2011**, *133*, 3381.

(212) Miller, J. S. *Inorganic Chemistry* **2000**, *39*, 4392.

(213) Kaplan, M. L.; Haddon, R. C.; Bramwell, F. B.; Wudl, F.; Marshall, J. H.; Cowan, D. O.; Gronowitz, S. *Journal of Physical Chemistry* **1980**, *84*, 427.

(214) Fatiadi, A. J. *Synthesis-Stuttgart* **1987**, 959.

(215) Fatiadi, A. J. *Synthesis-Stuttgart* **1986**, 249.

(216) Blundell, S. J. *Applied Magnetic Resonance* **1997**, *13*, 155.

(217) Fox, J. R.; Foxman, B. M.; Guarrera, D.; Miller, J. S.; Calabrese, J. C.; Reis, A. H. *Journal of Materials Chemistry* **1996**, *6*, 1627.

(218) Fukuzumi, S.; Mochida, K.; Kochi, J. K. *Journal of the American Chemical Society* **1979**, *101*, 5961.

(219) Chowdhury, S.; Kebarle, P. *Journal of the American Chemical Society* **1986**, *108*, 5453.

(220) Miller, J. S. *Angewandte Chemie-International Edition* **2006**, *45*, 2508.

(221) Luong, A. K.; Clements, T. G.; Resat, M. S.; Continetti, R. E. *Journal of Chemical Physics* **2001**, *114*, 3449.

(222) Mabbs, R.; Surber, E.; Sanov, A. *The Journal of Chemical Physics* **2005**, *122*, 054308.

(223) Robertson, W. H.; Price, E.; Weber, J. M.; Shin, J.-W.; Weddle, G. M.; Johnson, M. A. *J. Phys. Chem. A* **2003**, *107*, 6527.

(224) Hendricks, J. H.; De Clercq, H. L.; Freidhoff, C. B.; Arnold, S. T.; Eaton, J. G.; Fancher, C.; Lyapustina, S. A.; Snodgrass, J. T.; Bowen, K. H. *Journal of Chemical Physics* **2002**, *116*, 7926.

(225) Brinkmann, N. R.; Rienstra-Kiracofe, J. C.; Schaefer, H. F. *Molecular Physics* **2001**, *99*, 663.

(226) Wong, P. C. *Canadian Journal of Chemistry-Revue Canadienne De Chimie* **1982**, *60*, 339.

(227) Krylov, A. I. *Chemical Physics Letters* **2001**, *350*, 522.

(228) Levchenko, S. V.; Krylov, A. I. *Journal of Chemical Physics* **2004**, *120*, 175.

(229) Miller, F. A.; Sala, O.; Devlin, P.; Overend, J.; Lippert, E.; Luder, W.; Moser, H.; Varchmin, J. *Spectrochimica Acta* **1964**, *20*, 1233.

(230) Jensen, J. O. *Journal of Molecular Structure-Theochem* **2003**, *631*, 231.

(231) Khuseynov, D.; Fontana, M.; Sanov, A. *Chem. Phys. Lett.* **2012**, *550*, 15.

(232) Mabbs, R.; Surber, E.; Sanov, A. *Chemical Physics Letters* **2003**, *381*, 479.

(233) Lin, M. X.; Grabowski, J. J. *International Journal of Mass Spectrometry* **2004**, *237*, 149.

(234) Guo, Y.; Grabowski, J. J. *Abstracts of Papers of the American Chemical Society* **1990**, *199*, 147.

(235) Grabowski, J. J.; Melly, S. J. *International Journal of Mass Spectrometry* **1987**, *81*, 147.

(236) Kirmse, W. *European Journal of Organic Chemistry* **2002**, 2193.

(237) Meier, H.; Zeller, K. P. *Angew. Chem. Int. Ed.* **1975**, *14*, 32.

(238) Kaplan, F.; Mitchell, M. L. *Tetrahedron Letters* **1979**, *9*, 759.

(239) Wang, J.; Burdzinski, G.; Kubicki, J.; Platz, M. S. *J Am Chem Soc* **2009**, *130*, 11195.

(240) Burdzinski, G.; Wang, J.; Gustafson, T. L.; Platz, M. S. *J Am Chem Soc* **2008**, *130*, 3746.

(241) Litovitz, A. E.; Keresztes, I.; Carpenter, B. K. *Journal of the American Chemical Society* **2008**, *130*, 12085.

(242) Yacovitch, T. I.; Garand, E.; Neumark, D. M. *J Chem Phys* **2009**, *130*, 244309.

(243) Alconcel, L. S.; Deyerl, H. J.; Zengin, V.; Continetti, R. E. *J Phys Chem A* **1999**, *103*, 9190.

(244) Garand, E.; Yacovitch, T. I.; Neumark, D. M. *J Chem Phys* **2008**, *129*, 074312.

(245) Oakes, J. M.; Jones, M. E.; Bierbaum, V. M.; Ellison, G. B. *Journal of Physical Chemistry* **1983**, *87*, 4810.

(246) Zengin, V.; Persson, B. J.; Strong, K. M.; Continetti, R. E. *Journal Of Chemical Physics* **1996**, *105*, 9740.

(247) Choi, H.; Mordaunt, D. H.; Bise, R. T.; Taylor, T. R.; Neumark, D. M. *Journal Of Chemical Physics* **1998**, *108*, 4070.

(248) Ellison, G. B.; Engelking, P. C.; Lineberger, W. C. *Journal of Physical Chemistry* **1982**, *86*, 4873.

(249) Zimmerman, A. H.; Reed, K. J.; Brauman, J. I. *Journal of the American Chemical Society* **1977**, *99*, 7203.

(250) Mead, R. D.; Lykke, K. R.; Lineberger, W. C.; Marks, J.; Brauman, J. I. *Journal of Chemical Physics* **1984**, *81*, 4883.

(251) Jackson, R. L.; HIberty, P. C.; Brauman, J. I. *Journal of Chemical Physics* **1981**, *71*, 3705.

(252) Tanaka, K.; Yoshimine, M. *Journal of the American Chemical Society* **1980**, *102*, 7655.

(253) Scott, A. P.; Nobes, R. H.; Schaefer III, H. F.; Radom, L. *J Am Chem Soc* **1994**, *116*, 10159.

(254) Scott, A. P.; Platz, M. S.; Radom, L. *Journal of the American Chemical Society* **2001**, *123*, 6069.

(255) Holland, D. M. P.; Karlsson, L.; von Niessen, W. *Journal of Electron Spectroscopy and Related Phenomena* **2001**, *113*, 221.

(256) Toscano, J. P.; Platz, M. S. *J Am Chem Soc* **1995**, *117*, 4712.

(257) Ichino, T.; Villano, S. M.; Gianola, A. J.; Goebbert, D. J.; Velarde, L.; Sanov, A.; Blanksby, S. J.; Zhou, X.; D. A. Hrovat; Borden, W. T.; Lineberger, W. C. *Angew. Chem. Int. Ed.* **2009**, *48*, 8509.

(258) Mozhayskiy, V.; Goebbert, D. J.; Velarde, L.; Sanov, A.; Krylov, A. I. *Journal of Physical Chemistry A* **2010**, *114*, 6935.

(259) Ichino, T.; Villano, S. M.; Gianola, A. J.; Goebbert, D. J.; Velarde, L.; Sanov, A.; Blanksby, S. J.; Zhou, X.; Hrovat, D. A.; Borden, W. T.; Lineberger, W. C. *Journal of Physical Chemistry A* **in press**, *48*.

(260) *CRC Handbook of Chemistry and Physics*, 90 ed.; CRC Press: Boca Raton, Florida, 2009-2010.

(261) Wiberg, K. B.; Crocker, L. S.; Morgan, K. M. *J. Am. Chem. Soc.* **1991**, *113*, 3447.

(262) Goebbert, D. J.; Wenthold, P. G. *Int. J. Mass Spectrom.* **2006**, *257*, 1.

(263) *NIST Chemistry WebBook, NIST Standard Reference Database No. 69*; NIST Standard Reference Database Number 69, June 2005 Release ed.; Linstrom, P. J.; Mallard, W. G., Eds.; National Institute of Standards and Technology: Gaitnersburg, MD, 2005.

(264) Van Doren, J. M.; Miller, T. M.; Stevens-Miller, A. E.; Viggiano, A. A.; Morris, A.; Paulson, J. F. *J. Am. Chem. Soc.* **1993**, *115*, 7407.

(265) Ormond, T. K.; Scheer, A. M.; Nimlos, M. R.; Robichaud, D. J.; Daily, J. W.; Stanton, J. F.; Ellison, G. B. *Journal of Physical Chemistry A* **2014**, *118*, 708.

(266) Gavina, F.; Costero, A. M.; Gil, P.; Luis, S. V. *Journal of the American Chemical Society* **1984**, *106*, 2077.

(267) Baron, P. A.; Brown, R. *Chemical Physics* **1973**, *1*, 444.

(268) Serrano-Andres, L.; Pou-Amerigo, R.; Fulscher, M. P.; Borin, A. C. *Journal of Chemical Physics* **2002**, *117*, 1649.

(269) Maier, G. *Pure and Applied Chemistry* **1986**, *58*, 95.

(270) Klaboe, P. *Journal of the American Chemical Society* **1962**, *84*, 3458.

(271) Solomun, T.; Christmann, K.; Baumgartel, H. *Journal of Physical Chemistry* **1989**, *93*, 7199.

(272) Tao, F.; Wang, Z. H.; Xu, G. Q. *Journal of Physical Chemistry B* **2002**, *106*, 3557.

(273) Schaffer, L. J.; Taube, H. *Journal of Physical Chemistry* **1986**, *90*, 3669.

(274) Mishchenko, A.; Zotti, L. A.; Vonlanthen, D.; Burkle, M.; Pauly, F.; Cuevas, J. C.; Mayor, M.; Wandlowski, T. *Journal of the American Chemical Society* **2011**, *133*, 184.

(275) Wlodarczak, G.; Burie, J.; Demaison, J.; Vormann, K.; Csaszar, A. G. *Journal of Molecular Spectroscopy* **1989**, *134*, 297.

(276) Borst, D. R.; Korter, T. M.; Pratt, D. W. *Chemical Physics Letters* **2001**, *350*, 485.

(277) Desfrancois, C.; Abdoul-Carime, H.; Schermann, J. P. *International Journal Of Modern Physics B* **1996**, *10*, 1339.

(278) Borst, D. R.; Pratt, D. W.; Schaeffer, M. *Physical Chemistry Chemical Physics* **2007**, *9*, 4563.

(279) Schmitt, M.; Bohm, M.; Ratzer, C.; Siegert, S.; van Beek, M.; Meerts, W. L. *Journal of Molecular Structure* **2006**, *795*, 234.

(280) Schafer, M.; Borst, D. R.; Pratt, D. W.; Brendel, K. *Molecular Physics* **2002**, *100*, 3553.

(281) Melandri, S.; Consalvo, D.; Caminati, W.; Favero, P. G. *Journal of Chemical Physics* **1999**, *111*, 3874.

(282) Helm, R. M.; Vogel, H. P.; Neusser, H. J. *Chemical Physics Letters* **1997**, *270*, 285.

(283) Helm, R. M.; Vogel, H. P.; Neusser, H. J.; Storm, V.; Consalvo, D.; Dreizler, H. *Zeitschrift Fur Naturforschung Section a-a Journal of Physical Sciences* **1997**, *52*, 655.

(284) Kobayashi, T.; Kajimoto, O. *Journal of Chemical Physics* **1987**, *86*, 1118.

(285) Kobayashi, T.; Honma, K.; Kajimoto, O.; Tsuchiya, S. *Journal of Chemical Physics* **1987**, *86*, 1111.

(286) Ziatkis, A.; Lee, C. K.; Wentworth, W. E.; Chen, E. C. M. *Analytical Chemistry* **1983**, *55*, 1596.

(287) Kryachko, E. S.; Nguyen, M. T. *Journal of Chemical Physics* **2001**, *115*, 833.

(288) Ervin, K. M.; Lineberger, W. C. Photoelectron Spectroscopy of Negative Ions. In *Advances in Gas Phase Ion Chemistry*; Adams, N. G., Babcock, L. M., Eds.; JAI Press: Greenwich, 1992; Vol. 1; pp 121.

(289) Zare, R. N. *Molecular Photochemistry* **1972**, *4*, 1.

(290) Bethe, H. A.; Salpeter, E. E. *Quantum Mechanics of One- and Two-Electron Atoms*; Springer-Verlag; Academic Press Inc.: Berlin; New York, 1957.

(291) Fano; Dill, D. *Physical Review A* **1972**, *6*, 185.

(292) Park, H.; Zare, R. N. *Journal of Chemical Physics* **1996**, *104*, 4554.

(293) Reed, K. J.; Zimmerman, A. H.; Andersen, H. C.; Brauman, J. I. *Journal of Chemical Physics* **1976**, *64*, 1368.

(294) Goebbert, D. J. *Chemical Physics Letters* **2012**, *551*, 19.

(295) Bandyopadhyay, B.; Pruitt, C. J. M.; Goebbert, D. J. *Journal of Chemical Physics* **2013**, *138*.

(296) Kasdan, A.; Herbst, E.; Lineberger, W. C. *Chemical Physics Letters* **1975**, *31*, 78.

(297) Ritchie, B. *Journal of Chemical Physics* **1974**, *60*, 898.

(298) Ritchie, B. *Journal of Chemical Physics* **1974**, *61*, 3279.

(299) Ritchie, B. *Journal of Chemical Physics* **1974**, *61*, 3291.

(300) Schweig, A.; Thiel, W. *Journal of Chemical Physics* **1974**, *60*, 951.

(301) Buckingham, A. D.; Orr, B. J.; Sichel, J. M. *Philosophical Transactions of the Royal Society of London Series a-Mathematical and Physical Sciences* **1970**, *268*, 147.

(302) Sichel, J. M. *Molecular Physics* **1970**, *18*, 95.

(303) Grumbling, E. R. Electronic Structure, Intermolecular Interactions and Electron Emission Dynamics via Anion Photoelectron Imaging. Ph.D. dissertation, University of Arizona, 2010.

(304) Grumbling, E.; Sanov, A. *Journal of Chemical Physics* **2011**, *135*, 164302.

(305) Culberson, L. M.; Blackstone, C. C.; Sanov, A. *Journal of Physical Chemistry A* **2013**, *117*, 11760.

(306) Hanstorp, D.; Bengtsson, C.; Larson, D. J. *Physical Review A* **1989**, *40*, 670.

(307) Culberson, L. M.; Blackstone, C. C.; Wysocki, R.; Sanov, A. *Physical Chemistry Chemical Physics* **2014**, *16*, 527.

(308) See Supplementary Material Document No._____ for the following additional information. Part A: The derivation of the parallel and perpendicular differential cross-sections in *d* orbital photodetachment. Part B: Analytical evaluation of the Hanstorp coefficients for the 2*p*-3*d* mixing case. For information on Supplementary Material, see http://www.aip.org/pubservs/epaps.html.

(309) Culberson, L. M. Molecular Electronic Structure via Photoelectron Imaging Spectroscopy. Ph.D. dissertation, University of Arizona, 2013.

(310) Siegel, M. W.; Bennett, R. A.; Celotta, R. J.; Hall, J. L.; Levine, J. *Physical Review A* **1972**, *6*, 607.

(311) Maricq, M. M.; Tanguay, N. A.; O'Brien, J. C.; Rodday, S. M.; Rinden, E. *Journal of Chemical Physics* **1989**, *90*, 3136.

(312) McCarthy, M. C.; Allington, J. W. R.; Griffith, K. S. *Chemical Physics Letters* **1998**, *289*, 156.

(313) Velarde, L.; Habteyes, T.; Grumbling, E. R.; Pichugin, K.; Sanov, A. *Journal of Chemical Physics* **2007**, *127*, 084302.

(314) Grumbling, E. R.; Mabbs, R.; Sanov, A. *Journal of Chemical Education* **2011**, *88*, 1515.

(315) Culberson, L. M.; Blackstone, C. C.; Wallace, A. A.; Sanov, A. **in preparation**.

(316) Ichino, T.; Villano, S. M.; Gianola, A. J.; Goebbert, D. J.; Velarde, L.; Sanov, A.; Blanksby, S. J.; Zhou, X.; Hrovat, D. A.; Borden, W. T.; Lineberger, W. C. *Journal of Physical Chemistry A* **2011**, *115*, 1634.

(317) Green, J. H. S.; Harrison, D. J. *Spectrochimica Acta Part a-Molecular Spectroscopy* **1970**, *A 26*, 1925.

(318) Baronetskii, A. O.; Kuzyants, G. M. *Bulletin of the Academy of Sciences of the Ussr Division of Chemical Science* **1980**, *29*, 1267.

(319) Desfrancois, C.; Periquet, V.; Lyapustina, S. A.; Lippa, T. P.; Robinson, D. W.; Bowen, K. H.; Nonaka, H.; Compton, R. N. *Journal of Chemical Physics* **1999**, *111*, 4569.

(320) Kolos, R.; Grabowski, Z. R. *Astrophysics and Space Science* **2000**, *271*, 65.

(321) Samuelson, R. E.; Mayo, L. A.; Knuckles, M. A.; Khanna, R. J. *Planetary and Space Science* **1997**, *45*, 941.

(322) Graupner, K.; Field, T. A.; Saunders, G. C. *Astrophysical Journal Letters* **2008**, *685*, L95.

(323) Scholes, G. D.; Rumbles, G. *Nature Materials* **2006**, *5*, 683.

(324) Kilina, S.; Tretiak, S. *Advanced Functional Materials* **2007**, *17*, 3405.

(325) Emberly, E.; Kirczenow, G. *Nanotechnology* **1999**, *10*, 285.

(326) Mabbs, R.; Pichugin, K.; Sanov, A. *Journal of Chemical Physics* **2005**, *123*, 054329.

(327) Mabbs, R.; Pichugin, K.; Sanov, A. *Journal of Chemical Physics* **2005**, *122*, 174305.

(328) Joensson, C. *Zeitschrift Fur Physik* **1961**, *161*, 454.

(329) Chowdhury, S.; Heinis, T.; Grimsrud, E. P.; Kebarle, P. *The Journal of Physical Chemistry* **1986**, *90*, 2747.

(330) Mock, R. S.; Grimsrud, E. P. *Journal of the American Chemical Society* **1989**, *111*, 2861.